Photoionizaion as a Probe of Ultrafast Molecular Dynamics

A Dissertation presented

by

Spencer Lourdes Horton

to

The Graduate School

in Partial Fulfillment of the

Requirements

for the Degree of

Doctor of Philosophy

in

Physics

Stony Brook University

August 2018

Stony Brook University

The Graduate School

Spencer Lourdes Horton

We, the dissertation committe for the above candidate for the
Doctor of Philosophy degree, hereby recommend
acceptance of this dissertation

Thomas C. Weinacht - Dissertation Advisor
Professor, Department of Physics and Astronomy, Stony Brook University

---

Thomas Allison - Chairperson of Defense
Assistant Professor, Department of Physics and Astronomy
and Department of Chemistry, Stony Brook University

Marivi Fernández-Serra - Committee Member
Associate Professor, Department of Physics and Astronomy, Stony Brook University

---

Paul Hocket - External Committee Member
Research Officer, National Research Council of Canada, Ottawa, Canada

This dissertation is accepted by the Graduate School

Abstract of the Dissertation

Photoionization as a Probe of Ultrafast Molecular Dynamics

by

Spencer Lourdes Horton

Doctor of Philosophy

in

Physics

Stony Brook University

2018

Ionization can serve as a universal probe of excited state dynamics in molecules, such as internal conversion, dissociation, and isomerization. These processes are of fundamental importance to a wide array of dynamics in biology, chemistry and physics. In this thesis the topic of how to best construct a "molecular movie" of these photoinduced exited state molecular dynamics is addressed. Directly measuring a molecular structure or wave function amplitude as a function of time in order to construct a "molecular movie" is arguably impossible. Rather, the most insight is typically gained by comparing experiment with theoretical calculations of observables in order to verify the calculations, and then generating the "molecular movie" from calculations. Thus, an important criterion in evaluating different measurement approaches is how easily they can be compared with theoretical calculations of the measured observable.

Arguments are presented for why time-resolved ionization spectroscopy with a weak-field ionization probe is ideally suited for this goal. For the work conducted in this thesis, an ultrafast weak-field ionization pump-probe time-resolved ionization spectrometer is constructed utilizing UV (260 nm) and Vacuum-UV (156 nm) light to measure neutral excited state dynamics. Time-resolved VUV-pump UV-probe measurements were conducted to study of the highly excited states of pyrrole, where rapid internal conversion to the ground state appears to be the dominate relaxation channel. Time-resolved UV-pump and VUV-probe measurements in internal conversion of 1,3-cyclohexadiene are also performed. The measurements

reveal a substantial ionization of the "hot" ground state following internal conversion despite the fact that our probe photon energy is below the ionization potential of the molecule. With the aid of electronic structure calculations, the results are interpreted in terms of vibrationally assisted below threshold ionization, where vibrational energy is converted to electronic energy. A comparison of time-resolved ionization spectroscopy is done using weak and strong field ionization as probes of these dynamics. It is found that though the two probes capture the same general dynamics only the weak-field ionization probe can be quantitatively compared to dynamics calculations. Lastly, weak-field ionization time-resolved photoelectron spectroscopy experiments are conducted on halogenated methanes. The high degree of agreement between the experiment and calculation enables us to construct "molecular movies" of the dynamics.

To my family.

Contents

List of Figures

Acknowledgements

The work presented in this thesis would not have been possible without the incredible support I had from both my family and my friends. It is impossible for me to convey how much I appreciate everyone for all their support, but here is my attempt.

First and foremost, I would like to thank my family. My Mother was always there to supported me and without her I would never have been able to complete this work. She was always there to lend a sympathetic ear, while also encouraging me to "Soldier on Through". Chad, whose academic approach to life has always been an inspiration to me. Meredith, one of the smartest persons I will ever know, has always been there for me. My best-friend Joseph, the best brother a person could ever ask for, really helped to remind me to not be so serious all the time. Emily, the kindest person you will ever meet, kept me humble. Abbagale's sense of humor has always a breath of fresh air.

I would like to give a special thanks to my lab members. Péter Sándor was my first real friend I made at Stony Brook and I will always cherish our friendship. We had our foosball o'clock where we would show the Physics Department what team Cougar Baits was all about, and our "crummy" movie nights in the AMO seminar room to relax after a particularly stressful day in the lab. Arthur Zhao was a fantastic office mate. He was always willing to talk physics and help brainstorm solutions to problems I had in the lab. A very special thanks has to be given to Yusong Liu, who worked directly with me on the projects presented in this thesis. I am not exaggerating when I say that Yusong and I made the perfect team, and that in this case the sum was most definitely greater than the parts. Gayle Gerschwind was a fantastic undergraduate that really completed Team VUV. Gayle also introduced our lab to the wonders of Yao's Diner, a contribution that can never be overlooked. I would also like to thank Brian Kaufman and Chuan Cheng, who were fantastic additions to the lab and made my last years here much more fun.

I would also like to take a moment now to thank my fellow AMO community here at Stony Brook. The AMO community, us "Basement Dwellers", really came together during my time here at Stony Brook. We really created something special! Ludwig Krinner and Bertus Jordaan were two of my dearest friends here at Stony

Brook. Bertus and my coffee breaks were some of the best times, our endless political and economic debates were the highlight of my day. Ludwig Krinner has always been an amazing friend who you can alway rely on, and is a true “Bro”. Melanie Reber was both a mentor and a friend whose knowledge and experience were invaluable to me. Brian and Melissa Arnold are easily two of the kindest people you will ever meet. They were always there for me when I needed them and I will forever be grateful to them for that. Mehdi Namazi really helped make the time here at Stony Brook fun...I will never forget our obsessive bowling and Catan period. Without Yuning Chen’s support the thesis writing might have very well have gotten the better of me. Alessia Scriminich, even with our short overlap time, really helped me survive the dreaded thesis writing months and became a cherished friend.

Outside the AMO community I would like to say thank you to my dear friends: Oumarou Njoya, Yiqian Xu, and Hans Niederhausen. Oumarou and I made some of the best BBQ on Long Island, and without Hans I would never have been able to pass my comprehensive exam.

I would also like to say a very special thanks to Patrick Hawkins. Our weekends of aimlessly walking around and talking about history and politics, watching documentaries, eating Chinese food, and drinking iced coffee from Dunkin’ Donuts were critical for me in order to keep my sanity.

Chapter 1

Introduction

A fundamental goal of ultrafast time-resolved molecular dynamics is to make a "molecular movie" of photoinduced exited state molecular dynamics. These photoinduced excited state molecular dynamics, such as internal conversion, dissociation, and isomerization, play a central role in many fundamental processes in nature. They are of critical importance to a wide array of dynamics in biology, chemistry, and physics, such as: vision, photosynthesis, and the photoprotection of DNA/RNA. In reality, it is arguably impossible that one can directly measure a molecular structure or wave function amplitude as a function of time in order to construct a "molecular movie". (It is important to note here that the definition of a "molecular movie" is not well defined, hence the quotation marks. Measuring molecular structure versus time is a 3D real-space picture of the dynamics and can be performed with a semi-classical treatment, whereas following a wave function amplitude as a function of time requires up to 3N dimensions and a fully quantum mechanical treatment). Rather, the most insight is typically gained by comparing experiment with theoretical calculations of observables in order to verify the calculations, and then generating the "molecular movie" from calculations. Thus, an important criterion in evaluating different measurement approaches is how easily they can be compared with theoretical calculations of the measured observable. In other words, the measured observable should be computationally tractable and not too computationally expensive in order for the calculations to be feasibly performed for multiple molecular geometries.

Many different experimental approaches have been developed in order to follow these dynamics in real time. Each time-resolved experimental approach has advantages and disadvantages. For example, ultrafast electron diffraction [1, 2, 3, 4, 5] holds the promise of providing direct structural information as a function of time, but suffers from orientational averaging over the sample, repulsion between the electrons in a short pulse, and the group velocity mismatch between electrons and

light. Ultrafast x-ray diffraction [6, 7, 8, 9] overcomes the last two disadvantages of electron diffraction, but suffers from low scattering cross sections, and requires a large number of photons in the probe pulse - typically only available at free electron laser light sources. Optical spectroscopy approaches such as transient absorption [10, 11, 12, 13, 14] can provide high time resolution with a compact apparatus, but require detailed knowledge of the potential energy surfaces (electronic energies as a function of nuclear coordinates) along the reaction coordinate in order to be interpreted. They are also limited by transition dipole moments, which can change with coordinate, leading to varying sensitivity, which vanishes on dark states. Time-resolved ionization spectroscopy [15, 16, 17, 18, 19, 20] offers the advantage over optical spectroscopies that it is always possible to ionize, regardless of the character of the excited state, provided the photon energy is sufficient (or the field strong enough for multiphoton cases). The near threshold ionization of valence electrons from excited states (for which the cross section is large) can be accomplished either in the weak field regime, with the absorption of a single ultraviolet (UV) or vacuum ultraviolet (VUV) photon ($\sim$ 6-10 eV), or in the strong field regime, with the absorption of multiple low energy near infrared photons ($\sim$ 1-3 eV) [21, 22, 23, 24, 19, 20, 25].

In this thesis, time-resolved ionization spectroscopy is favored to study ultrafast neutral excited state dynamics, because of its above mentioned advantages. The question left to answer is if one should perform these experiments in the weak field regime or the strong field regime? Strong field ionization (SFI) has the advantage of using wavelengths that are relatively easy to generate, and one can always ionize the molecule with sufficient intensity. However, for SFI it is difficult to calculate observables, such as the time dependent ion yield, since the calculations of an N electron molecule in a strong field are computationally expensive and difficult to carry out for multiple molecular geometries. For SFI, perturbation theory cannot be used, and there is no analog for the Dyson Norm as a good predictor of the population distribution across the ionic states. Because of this, SFI requires computationally costly calculations to determine the ionization rate as a function of molecular geometry. Weak field ionization (WFI) has the advantage that calculations of observables are tractable and that perturbation theory can be used to accurately describe the ionization step. It can be shown that the first-order one-photon ionization probability is directly proportional to the norm of the Dyson orbital formed by projecting the N-1 electron wave function of the final (ionic) state onto the N electron wave function of the initial (neutral) state of the molecule [26, 27]:

$$\phi^D = \sqrt{N} \int \psi_i^N(r_1, \ldots, r_N) \psi_f^{N-1}(r_2, \ldots, r_N) dr_2 \ldots dr_N, \tag{1.1}$$

where ψ_i^N is the initial, N-electron wave function of the neutral, and ψ_f^{N-1} is the final, N-1 electron wave function of the ion. The integral is over N-1 dimensions, leaving a one-electron function or orbital for ϕ^D. The total ion yield for each molecular geometry in the WFI perturbative regime produced by a dynamics calculation can be expressed in terms of this Dyson orbital as:

$$\text{Ion Yield} \propto \left| \left\langle \psi_k^e \right| \hat{\epsilon} \cdot \mathbf{r} \left| \phi^D \right\rangle \right|^2 \left\langle \phi^D \right| \left. \phi^D \right\rangle, \tag{1.2}$$

where $\hat{\epsilon}$ is the polarization direction of the light, $\mathbf{r}$ the position operator, ψ_k^e the free (continuum) electron wave function with momentum k, and $\left\langle \phi^D \right| \left. \phi^D \right\rangle$ is the Dyson norm. WFI also has its disadvantages, the generation and implementation of the appropriate wavelengths (photon energies) for WFI can be challenging, and the fixed energy of the probe can lead to technical complications in following the dynamics from excited states back down to the ground state.

It is argued that the best experimental apparatus for measuring molecular dynamics is one that can be most easily compared to calculations in order to verify the "molecular movies" they generate. The experimental observable for WFI are routine, accurate, and cheap, whereas for SFI the calculations are extremely computationally expensive and less well explored in general. Because of this a new time-resolved ionization spectrometer was developed that utilizes a probe in the WFI regime. The photon energy this WFI probe had to be chosen with some care. A 5 eV UV-photon as the WFI probe would be relatively easy to generate and propagate for the use in experiments, but the photon energy is too low to ionize a typical molecule, with ionization potentials of approximately 10 eV, from anywhere on the neutral excited state potential energy surface, as shown in Fig. 1.1. A probe with a photon energy above the ionization potential of the target molecule would create a large background single photon ionization signal from ground state ionization, and would make extracting the pump-probe dynamics extremely difficult. An 8 eV VUV-probe is ideally suited for the studying neutral excited state dynamics, although is is difficult to generate and propagate. The photon energy of 8 eV is just below the ionization potential for most organic molecules, so one has sufficient photon energy to follow the neutral excited state dynamics while not generating background ionization signal from the ground state.

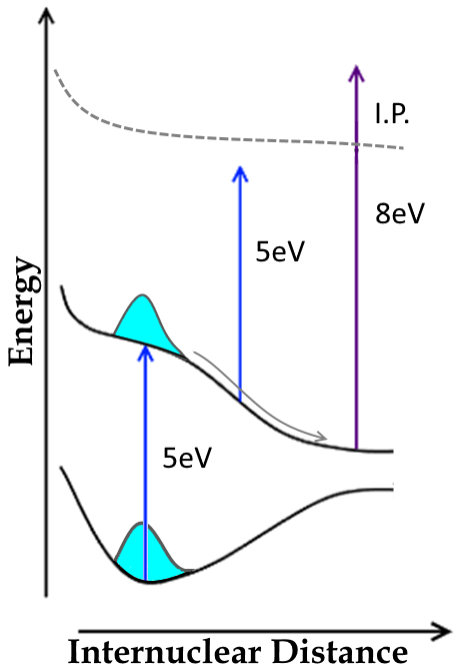

Figure 1.1: A cartoon of a generic molecules' potential energy surface, depicting the differences between using a WFI UV and a WFI VUV probe to study the dynamics.

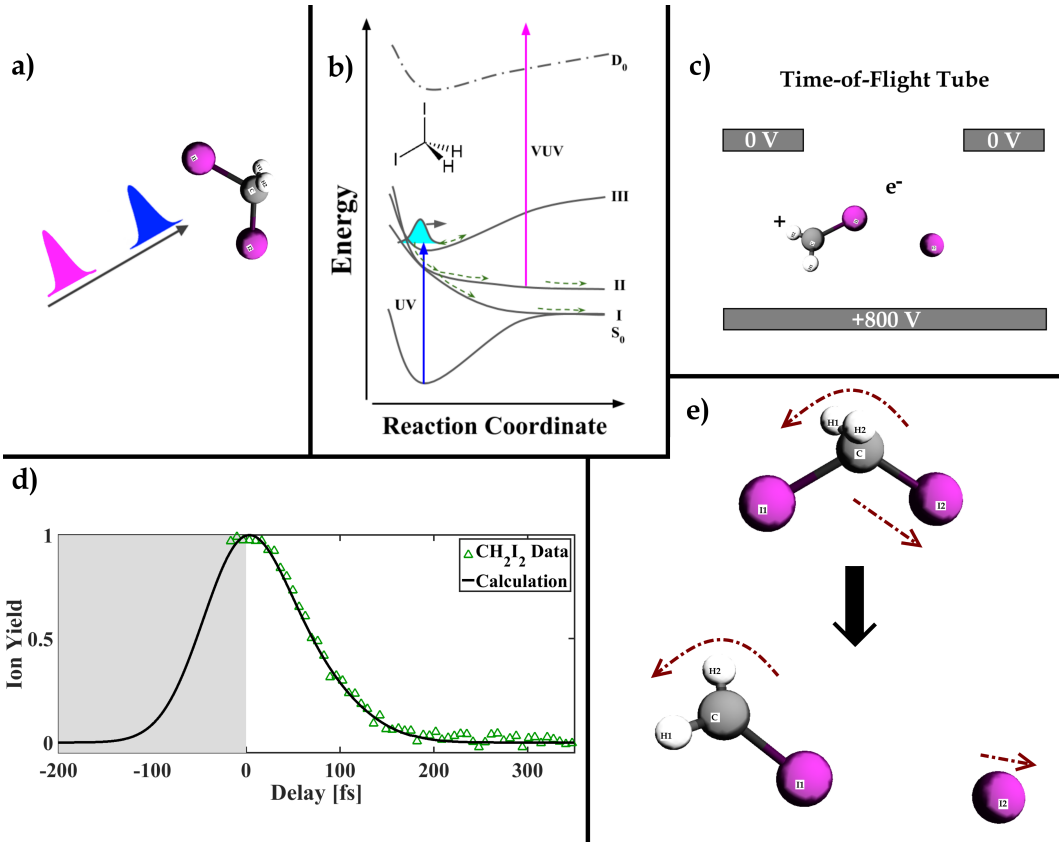

Figure 1.2: Schematic depicting how a typical measurement is conducted and used to generate a "molecular movie" in this thesis. a) A cartoon depicting a pump-pulse, blue, and a probe pulse, pink, incident on a target molecule (diiodomethane in this cartoon). b) A cartoon of the potential energy surface for the molecule. The molecular dynamics are initiated by the pump-pulse and subsequently ionized by the probe pulse. c) A cartoon depicting the products resulting from the pump and probe interaction with the molecule. The figure shows the repeller plates, bottom plate at +800 V and the top plate at 0 V, that generate the static electric field that sends the ions into the time-of-flight tube. Once in the time-of-flight tube the different ion masses become temporally separated and measured by a microchannel plate (MCP) stack detector. d) The measured and calculated ion signal from the pump-probe experiment. e) Snapshots of the actual "molecular movie" generated through calculations that were verified with experiment.

Fig. 1.2 is a schematic depicting how a general pump-probe measurement is carried out for the experiments presented in this thesis, and how they can be related to a "molecular movie". Panel a is a cartoon of the UV-pump pulse, blue, followed by a VUV-probe pulse, pink, incident on a target molecule (diiodomethane for this specific example), where the delay between the pump and probe pulse can be controlled. Panel b shows a cartoon of the potential energy surface of diiodomethane, where the pump pulse launches a wave packet on the excited state surface that is subsequently ionized by the probe pulse. The relative delay between the pump and the probe pulse can be used to probe the complete neutral excite state dynamics. Panel c shows the products from the pump and probe pulse interaction with the molecular system. The products are generated between a pair of repeller plates that utilize a static electric field to send the ions into a time-of-flight tube. In the time-of-flight tube the different mass fragments have different flight times and are temporally separated when they arrive at the detector (microchannel plate (MCP) stack). Panel d shows the results for the total ion yield of the experiment versus pump-probe delay. The results of the dynamics calculations are also shown alongside the experimental data. The high level of agreement between the theory and the experiment enables one to verify the accuracy of the theory. Panel e shows the results of a "molecular movie" that are generated from the calculation.

Chapter 2

Experimental Apparatus

2.1 Laser System

The majority of the work discussed in this thesis was performed with the use of a Kerr-lens modelocked oscillator (KM Labs), pumped with a Coherent V5 continuous wave laser, and a multi-pass ring cavity amplifier (KM Labs, HAP-AMP), pumped with a Photonics DM-20 Q-switched 170 ns Nd:YLF laser. The output of the amplifier is a 1.5 mJ pulse with a 1 kHz repetition rate, 30 fs pulse duration, and a central wavelength of 780 nm.

2.2 Harmonic Generation

2.2.1 Overview

Throughout this thesis extensive use is made of nonlinear optics, and hence it is useful to give a brief overview. In nonlinear optics, the polarization, $P(t)$, is generally expressed in terms of a power series in the field strength $E(t)$ as

$$P(t) = \epsilon_0 \left[\chi^{(1)} E(t) + \chi^{(2)} E^2(t) + \chi^{(3)} E^3(t) + \dots \right]. \tag{2.1}$$

The terms $\chi^{(2)}$ and $\chi^{(3)}$ are known as the second and third order nonlinear optical susceptibilities, respectively [28]. The wave equation in nonlinear optics generally takes the form

$$\nabla^2 E - \frac{n^2}{c^2} \frac{\partial^2 E}{\partial t^2} = \frac{1}{\epsilon_0 c^2} \frac{\partial^2 P^{NL}}{\partial t^2}, \tag{2.2}$$

where n is the index of refraction, c is the speed of light in vacuum, ϵ_0 is the permittivity of free space, $E(t)$ is the electric field, and $P^{NL}(t)$ is the nonlinear portion of

the polarization ($P = P^{(1)} + P^{NL}$, where $P^{(1)}$ is the part of the polarization that depends linearly on the electric field strength E). From Eq. 2.2 it is evident that the nonlinear polarization, $P^{NL}(t)$, acts as a driving force for the electric field, $E(t)$.

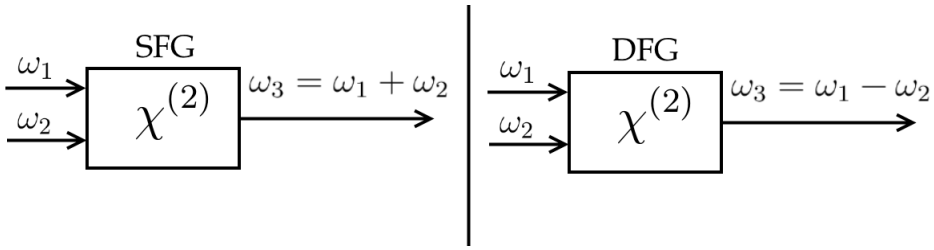

Figure 2.1: Schematic depicting sum-frequency generation (SFG) on the left-hand side and difference-frequency generation (DFG) on the right-hand side of the figure, [28].

In the work discussed in this thesis both the $\chi^{(2)}$ and $\chi^{(3)}$ susceptibility terms are used in order to generate desired wavelengths. The second term in the expansion of the polarization in Eq. 2.1 depends on the square of the electric field. Now, assume that one has an electric field that consists of two distinct frequency components

$$E(t) = E_1 e^{-i\omega_1 t} + E_2 e^{-i\omega_2 t} + c.c., \tag{2.3}$$

where E_1 and E_2 are the amplitudes of the field, ω_1 and ω_2 are the frequencies, and $c.c$ is the complex conjugate. Looking at the second term in the expansion of the polarization with field strength

$$P^{(2)} = \epsilon_0 \chi^{(2)} E(t)^2, \tag{2.4}$$

and plugging in the assumed electric field of Eq. 2.3 one gets

$$\begin{aligned} P^{(2)}(t) = \epsilon_0 \chi^{(2)} [E_1^2 e^{-2i\omega_1 t} + E_2^2 e^{-2i\omega_2 t} + 2E_1 E_2 e^{-i(\omega_1+\omega_2)t} + \\ 2E_1 E_2^* e^{-i(\omega_1-\omega_2)t} + c.c.] + 2\epsilon_0 \chi^{(2)} \left[E_1 E_1^* + E_2 E_2^*\right]. \end{aligned} \tag{2.5}$$

From Eq. 2.5 it becomes evident how $\chi^{(2)}$ can be used for three-wave mixing, examples are shown in Fig. 2.1. The first two terms in Eq. 2.5 oscillate at twice the frequency of ω_1 and ω_2, and lead to second harmonic generation (SHG) of the input frequencies ω_1 and ω_2, respectively. The third term gives rise to sum-frequency generation (SFG), where the input frequencies ω_1 and ω_2 can result in the generation of a new frequency, ω_3, that is equal to the sum of the two input frequencies. The fourth term gives rise to difference-frequency generation (DFG),

where the input frequencies can result in the generation of a new frequency that is equal to the difference of the two input frequencies.

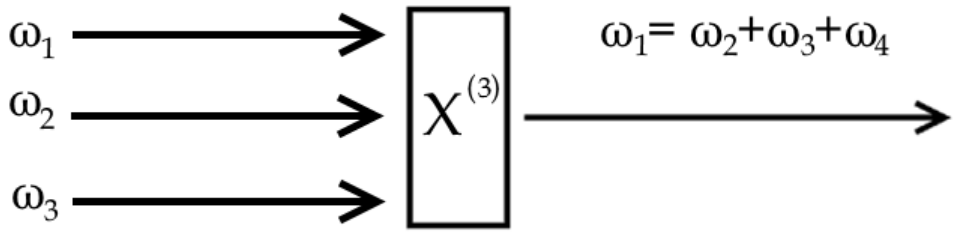

Figure 2.2: Four wave mixing schematic, [28]

The third term in the expansion of the polarization, Eq. 2.1, depends on the cube of the electric field. Following the same procedure for $\chi^{(2)}$, assuming this time that the incident field is composed of three distinct frequencies, yields many terms [28]. Some of those terms give rise to four-wave mixing, and an example of a four-wave mixing process is given in Fig. 2.2.

2.2.2 Third Harmonic Generation

In order to generate the third harmonic (260 nm, 4.77 eV) of the laser pulse one first needs to generate the second harmonic and then perform sum-frequency generation with the fundamental frequency and the second harmonic to generate the third harmonic. Second harmonic generation (SHG) is performed in a 250 μm thick beta barium borate (BBO) crystal cut for second harmonic generation ($\theta = 30°$, $\phi = 0°$, Type I SHG). Then the pulse passes through a 1 mm thick calcite crystal ($\theta = 41°$, $\phi = 0°$) to compensate for the group velocity mismatch between the fundamental and the second harmonic in the third harmonic generation (THG) crystal. The pulses then pass through a 100μm thick BBO crystal cut for THG ($\theta = 57°$, $\phi = 30°$, Type II SFG). After the THG crystal high reflectivity dielectric mirrors for the third harmonic are used to separate out the third harmonic from the fundamental and the second harmonic.

2.2.3 Fifth Harmonic Generation

The generation of the fifth harmonic (156 nm, 7.95 eV) is more challenging than the generation of the second and third harmonics. The fifth harmonic sits in the vacuum-ultraviolet (VUV) region of the electromagnetic spectrum. This region

of the electromagnetic spectrum corresponds to a major absorption band in oxygen, therefore these wavelengths are readily absorbed in atmosphere and need to be generated and propagated in vacuum, hence the name. The fifth harmonic is also readily absorbed in any standard crystal used in harmonic generation. So, in order to generate the fifth harmonic a process pioneered by Noack et. al., [29, 30], was used. Since it is not possible for the fifth harmonic to be generated in a crystal one has to move to a gaseous medium. Gases are centrosymmetric and lack $\chi^{(2)}$, so without a $\chi^{(2)}$ three-wave mixing cannot be performed in the medium. Because of this one has to look to $\chi^{(3)}$ and a four-wave mixing process in order to generate the fifth harmonic. In the work outlined in this thesis non-collinear four-wave mixing in argon gas that satisfies the phase matching condition

$$\vec{k}_{5\omega} = 2\vec{k}_{3\omega} - \vec{k}_{\omega} \tag{2.6}$$

is used to generate the fifth harmonic.

A schematic of this non-collinear four-wave mixing can be seen in Fig. 2.3, were θ and ϕ are the non-collinear angles that need to be satisfied for the generation of the fifth harmonic. In order to calculate the angles needed for the correct

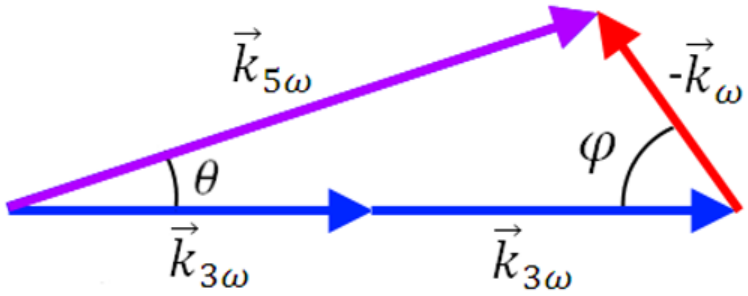

Figure 2.3: Phase matching diagram for the fifth harmonic generation.

phase matching conditions to be met one has to calculate the wavevector, k, for each wavelength. The wavevector is defined as $k = \frac{2\pi n}{\lambda}$, where n is the index of refraction and λ is the wavelength. A pressure dependent Sellmeier-type formula for the index of refraction of a femtosecond laser in argon gas is used to calculate the magnitude of the wavevectors [31]. Generically this equation is

$$n^2(\lambda, P, T) - 1 = \frac{P}{P_0} \cdot \frac{T_0}{T} \cdot \left[\frac{B_1 \lambda^2}{\lambda^2 - C_1} + \frac{B_2 \lambda^2}{\lambda^2 - C_2} \right], \tag{2.7}$$

where λ is in μm, B_1, B_2, C_1, and C_2 are coefficients at P_0 = 1000 mbars and T_0 = 273K. For argon, $B_1 = 20332.29 \times 10^{-8}$, $C_1 = 206.12 \times 10^{-6}$, $B_2 = 34458.31 \times$

10^{-8}, and $C_2 = 8.066 \times 10^{-3}$, [31]. One can then calculate the phase matching angles for different argon pressures, as seen in Fig. 2.4.

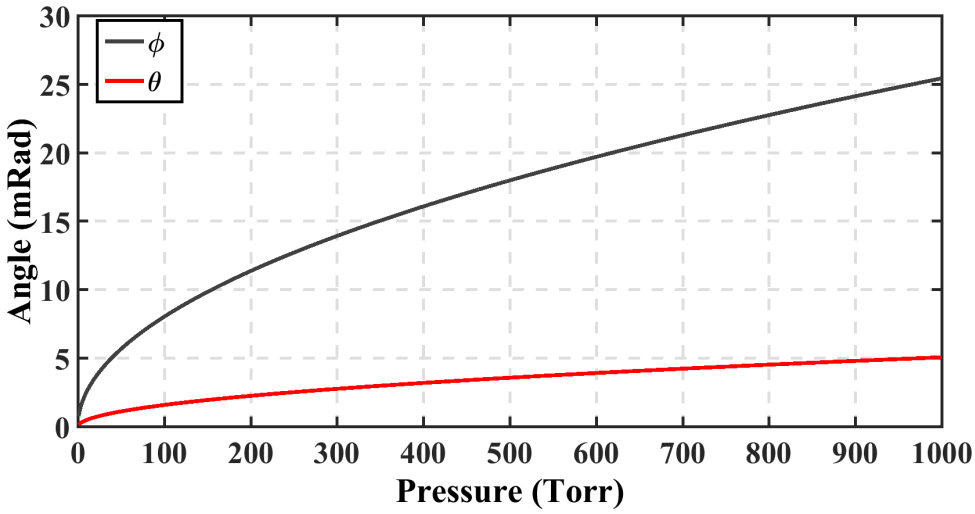

Figure 2.4: Phase matching angles versus pressure.

Experimentally the pressure of the argon gas cell and the phase matching angles of the pulses were optimized. It was found that after an argon gas cell pressure of 300 Torr is reached that the generation process saturates, consistent with what was found in [29, 30].

2.3 Self-Focusing

2.3.1 Measurements

The initial setup for SHG and THG can be seen in Fig. 2.5, where the distances between the crystals is indicated. The incident IR is focused in oder to increase the intensity and maximize the SHG and THG output from the BBO crystals. The generated UV was very poor and the UV mode was donut shaped.

In order to diagnose the system all of the harmonic generation crystals were removed and the IR beam was imaged in the position of the THG crystal. Inserting the SHG crystal, a flat 250 μm thick piece of BBO crystal, caused the beam to shrink dramatically in the position of the THG crystal, as seen in Fig. 2.6. Since the BBO crystal is flat, the only explanation for the dramatic shrinking of the beam waist was self-focusing. To test this hypothesis the pulse duration was changed in order to change the intensity of the pulse, thus increasing or decreasing the self-focusing

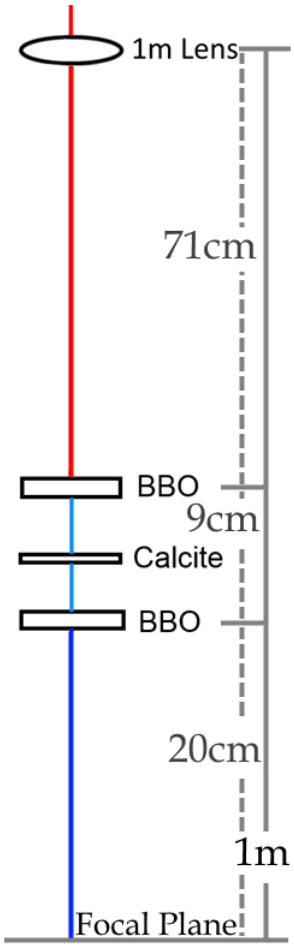

Figure 2.5: Initial THG Setup.

effect. A simple way of changing the pulse duration is to move the perpendicular distance between the two gratings in the grating compressor. The perpendicular grating separation is linearly proportional to the second and third order phases of the pulse, hence it can be used to compensate for any dispersion in the pulse and compress the pulse at a given location. Details of the grating compressor can be found in Appendix A.

Scanning the compressors perpendicular separation dramatically changed the size of the IR beam at the location of the THG crystal after passing through the one meter lens and the SHG crystal. The results of the compressor scan on the beam waist can be seen in Fig. 2.7 for the horizontal and vertical waists of the beam. This size dependence of the beam on the compressor setting gave strong evidence that this was a self-focusing effect.

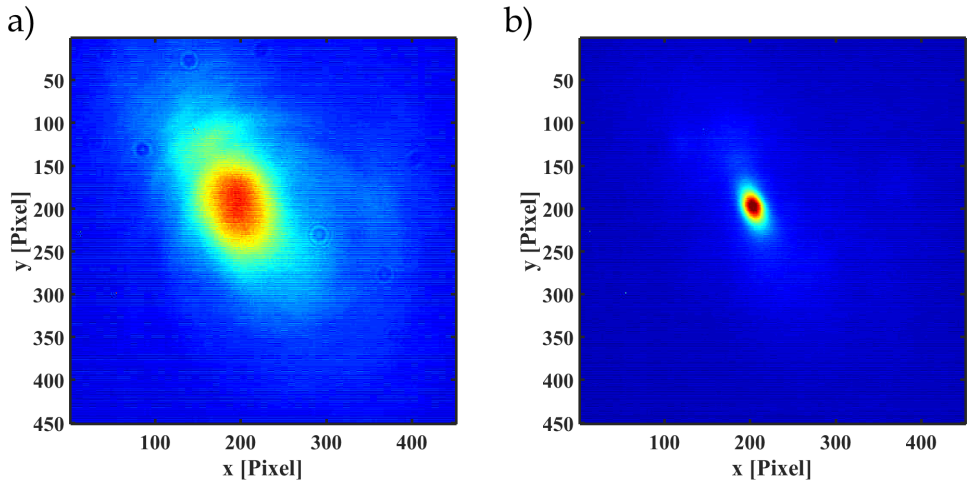

Figure 2.6: Camera images of the IR beam in the position of the THG crystal a) after passing through a 1 m lens, and b) after passing through a 1 m lens and followed by a flat 250 μm thick SHG BBO crystal (each pixel is 5.2 μm).

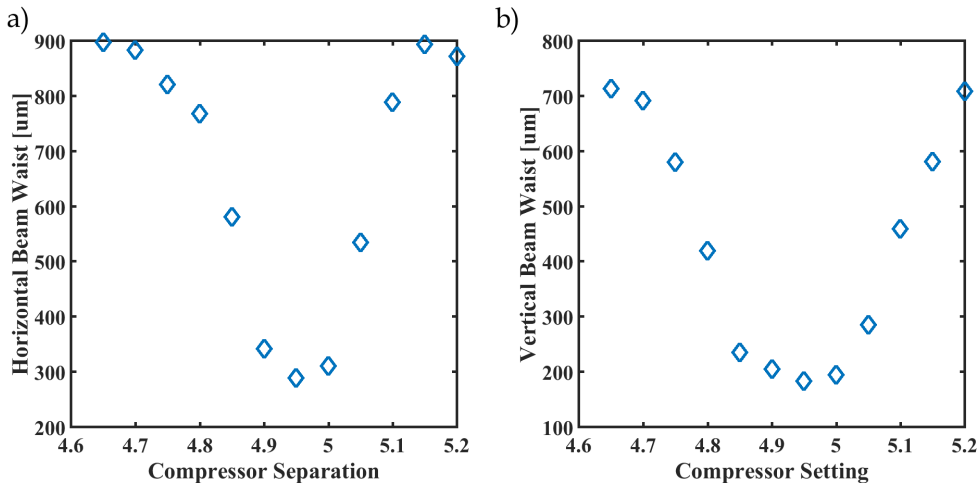

Figure 2.7: Compressor setting of the amplifier versus the beam waist in the, a) horizontal direction, and b) vertical direction (each pixel is 5.2 μm).

The calcite crystal was placed back in the system directly after the SHG crystal and a compressor scan was repeated. The results of this scan can be seen in Fig. 2.8. It can clearly be seen that the beam is shrinking between compressor settings 4.50 and 4.70, but at setting 4.80 one starts to see a hole in the mode that becomes very clear at compressor setting 4.95. From this measurement it is obvious that the calcite crystal was burning at the most intense part of the beam, hence the donut

mode seen in the UV.

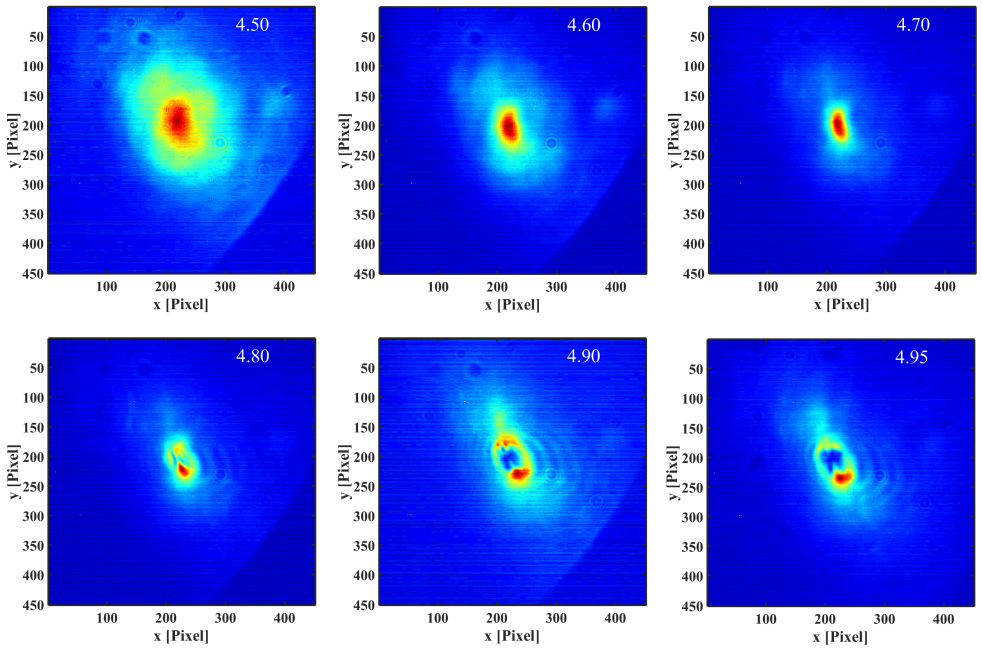

Figure 2.8: Images in the position of the THG crystal of the self focusing of the IR beam for different compressor settings (indicated in the upper right corner) after going through a 1 m lens, a 250 μm thick SHG crystal, and a 1 mm thick calcite crystal (each pixel is 5.2 μm).

2.3.2 Simulation

To better understand this self-focusing seen in the system a simple model was generated. Consider a monochromatic wave propagating in the z-direction, with known field values E(x, y, 0) in the xy-plane. Now assume one wants to know what the field is on some observation plane a distance z away. In other words, what is $E(x, y, z)$, given $E(x', y', 0)$ in Fig. 2.9?

Huygens' Principle says that one can imagine that every point on a wavefront to be a point source for a spherical wave. Each point in the new wavefront is the superposition of all the spherical waves added together from the original wavefront. This principle will enable one to calculate what will happen to an arbitrary wavefront as it propagates. Mathematically one can write this as

$$\Delta E(x, y, z) = -\frac{i}{\lambda}\frac{e^{ikr}}{r}E(x', y', 0)\Delta a' \tag{2.8}$$

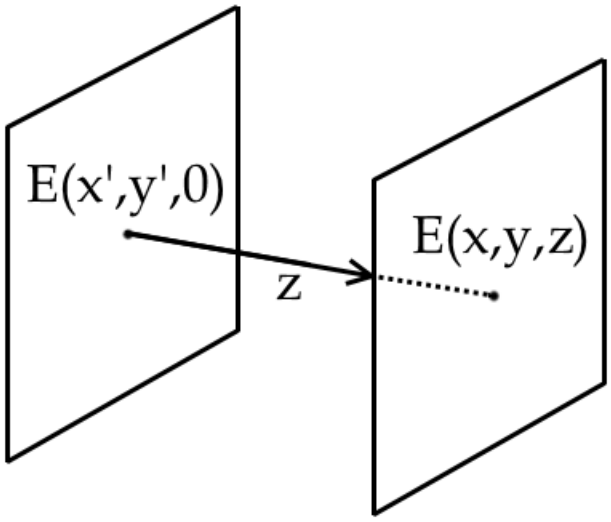

Figure 2.9: Taking a initial two-dimensional electric field distribution, $E(x', y', 0)$, and propagating along z to a new plane, $E(x, y, z)$.

where

$$r = \sqrt{(x - x')^2 + (y - y')^2 + z^2} \tag{2.9}$$

and $k = \frac{2\pi n}{\lambda}$ and Δa is a tiny element of area surrounding the point $(x', y', 0)$ on the source plane, where the field has the value $E(x', y', 0)$. The factor $-i/\lambda$ arises in a more mathematical treatment of Huygens' principle.

For Fresnel diffraction one has

$$kr = k\sqrt{(x - x')^2 + (y - y')^2 + z^2} \tag{2.10}$$

and expanding this expression one gets

$$kr = kz + \frac{k}{2z}\left[(x - x')^2 + (y - y')^2\right] - \frac{k}{8z^3}\left[(x - x')^2 + (y - y')^2\right]^2 + \cdots. \tag{2.11}$$

Assuming one is looking at propagation distances where $z^3 \gg \frac{k}{8}\left[(x - x')^2 + (y - y')^2\right]^2$, then one can just keep the first two terms. One has to sum over all the Huygens wave components in the source plane to calculate the

complete field in the observation plan. Doing this one gets the expression

$$\boxed{E(x,y,z) \approx -\frac{ie^{ikz}}{\lambda z}\int\int E(x',y',0)e^{-ik\left[(x-x')^2+(y-y')^2\right]/2z}dx'dy'} \tag{2.12}$$

Eq. 2.12 is called Fresnel diffraction, and the derivation up to this point is simply summarizing the more detailed discussion outlined in [32]. Fresnel diffraction is used to simulate the self focusing of the wavefront.

For the model the problem is reduced to one dimension by integrating over the y-direction. The initial Gaussian intensity profile that was measured with a camera was used. The max intensity is defined as

$$I_{\text{max}} = \frac{\text{Pulse Energy}}{\text{Pulse Duration} \times \text{Area}}, \tag{2.13}$$

and the square root of this intensity profile is used as the initial electric field profile. The effect of the lens is and the Kerr self-focusing are modeled through the phase. A lens can be simply modeled as a quadratic spatial phase

$$\phi_{\text{Lens}} = \kappa x^2, \tag{2.14}$$

where κ is a constant defined by wavelength of the light and curvature of the lens, and x is the spatial dimension. A generic way to think about the phase acquired by the wavefront as it passes through the lens is that because the lens is curved there is a varying thickness over the lens. The speed of light when passing through a material is reduced by c/n, where n is the index of refraction of the material. The portion of the wavefront that goes through the center of the lens sees the most material and gets delayed the most, whereas the edges get delayed the least. So, there is an overall retardation of the wavefront by the lens that essentially writes the curvature of the lens onto the wavefront. Generically, this is just the "optical path" and no material needs to be implied. Even though spherical lenses are being used the phase is approximated as quadratic.

The Kerr self-focusing can be modeled by first noting that the Kerr effect gives an intensity dependent index of refraction.

$$n(I) = n_0 + n_2 I. \tag{2.15}$$

Looking at the propagation phase $\phi = kz$, where the definition of the wavevector is $k = 2\pi n/\lambda$. So, the phase from the Kerr nonlinearity in the system can be defined

as

$$\phi_{\text{Kerr}} = \frac{2\pi n_2 I}{\lambda}, \tag{2.16}$$

where I is the one dimensional Gaussian intensity profile of the pulse. The overall phase on the pulse is then

$$\phi_{\text{Total}} = \phi_{\text{Lens}} + \phi_{\text{Kerr}}. \tag{2.17}$$

The system is modeled with and without the non-linear Kerr phase in order to see its effect on the system. It can be informative to think of the Kerr nonlinearity as retarding the most intense portion of the wavefront. In the system this will cause a portion of the wavefront to focus before the rest of the wavefront. This can be seen in Fig. 2.10, where the effects of self focusing after passing through the 1 m lens modeled, using $n_2 = 3.35 \times 10^{-16}$ [W/cm^2] value for BK7 glass [33]. These simulations are done matching all of the experimental conditions at the time of the measurements in the previous section (700 μJ pulse energy, 30 fs pulse duration, 1.6 mm beam waist) and it becomes evident that the pulse is intense enough to drive self-focusing in the system. This confirmed that the beams were indeed intense enough to drive self-focusing in the system and that this was very likely the source of the problem.

The system was also modeled taking into account the 1 m lens and the SHG BBO crystal. The calculated wavefront became extremely distorted after the SHG BBO crystal, and the results become hard to interpret. Therefore, for clarity only the results for after the 1 m lens are shown.

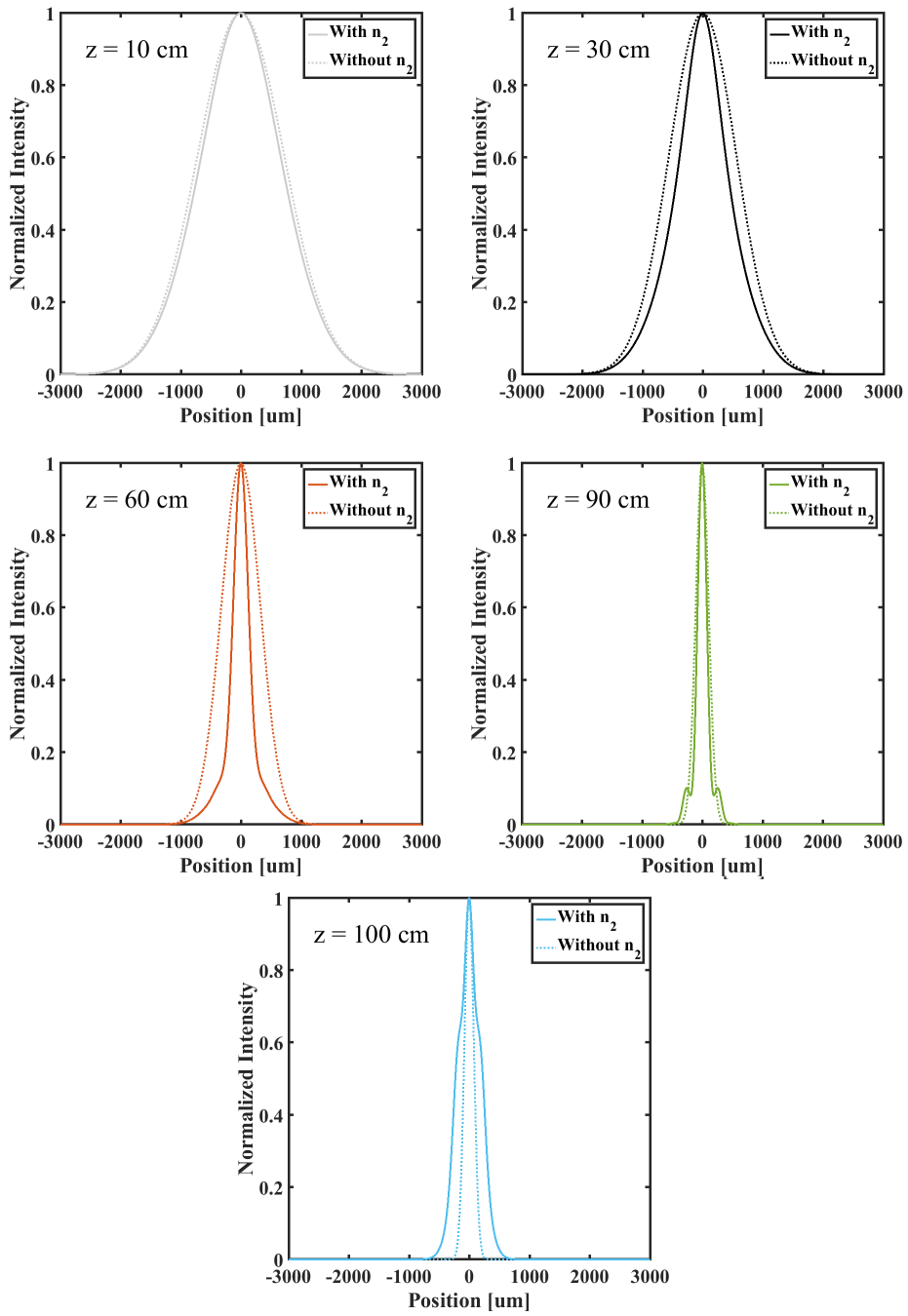

Figure 2.10: Intensity profile for a Gaussian beam with a 1.6 mm waist at different propagation distances, z, passing through a 1 m lens (z=0) with and without taking into account the Kerr nonlinearity of the lens material.

2.3.3 Solution to the Problem

Based on this analysis the THG process had to be redesigned in order to generate a cleaner THG mode. The solution was to move the SHG BBO crystal as far away from the IR focus as possible without loosing too much second harmonic efficiency. The SHG was found to almost saturate without even focusing, so the SHG BBO and the calcite crystal were moved as close possible to one meter lens. The THG crystal had to stay in the same position in order to get $\sim 5\%$ THG generation efficiency. With the one meter lens still in the system the previous analysis shows that there is still self-focusing in the system, but by moving the SHG and the calcite crystals to less intense regions after the lens the subsequent self-focusing in these crystals was mitigated. After these improvements the third harmonic power and mode were greatly improved, and now there was enough UV power and a clean enough mode to generate the fifth harmonic.

2.4 Experimental Apparatus

The first generation of the experimental beamline can be seen in Fig. 2.11. This configuration was used for the data collected in Chapter 3, Chapter 4, and the uracil data presented in Chapter 5. The IR beam from the amplifier is split into two portions which have pulse energies of 1.1 mJ and 100 μJ. The 1.1 mJ of IR is used to create 50 μJ of UV ($\hbar\omega = 4.78$ eV) light through second-harmonic-generation (SHG), followed by a calcite delay compensator, proceeded by third-harmonic-generation (THG) in a BBO crystal as previously stated. An uncoated 1 mm thick CaF_2 window is inserted into the beam at 45° to act as a beamsplitter for the UV. A 5 μJ pulse from the front surface reflection of the CaF_2 window is used as the UV in the experiments. In the remaining IR arm a telescope corrects for the chromatic aberrations of the subsequent 30 cm CaF_2 lens. Approximately 100 nJ of the fifth-harmonic (VUV), ($\lambda = 156$ nm, $\hbar\omega = 7.94$ eV), is generated by focusing the remaining 40 μJ of UV and 100 μJ of residual IR into an argon gas cell utilizing the non-collinear-four-wave-mixing process discussed previously.

In Fig. 2.12 one can see a detailed schematic of the inside of the vacuum system. The VUV is generated in the argon gas cell kept at 300 Torr, then it passes through a 500 μm thick CaF_2 window into an interaction chamber, which is maintained at a pressure of 10^{-7} Torr. The VUV-pulse first passes under the repeller plates of the time-of-flight mass spectrometer (TOFMS). It is then reflected by a dichroic mirror of radius of curvature $R = 268$ mm. The mirror has a high reflectivity coating of $> 90\%$ at 0° for $156 - 160$ nm light and $< 5\%$ reflectivity for 260 nm and 800 nm. This enables the residual UV and IR radiation left over from VUV generation

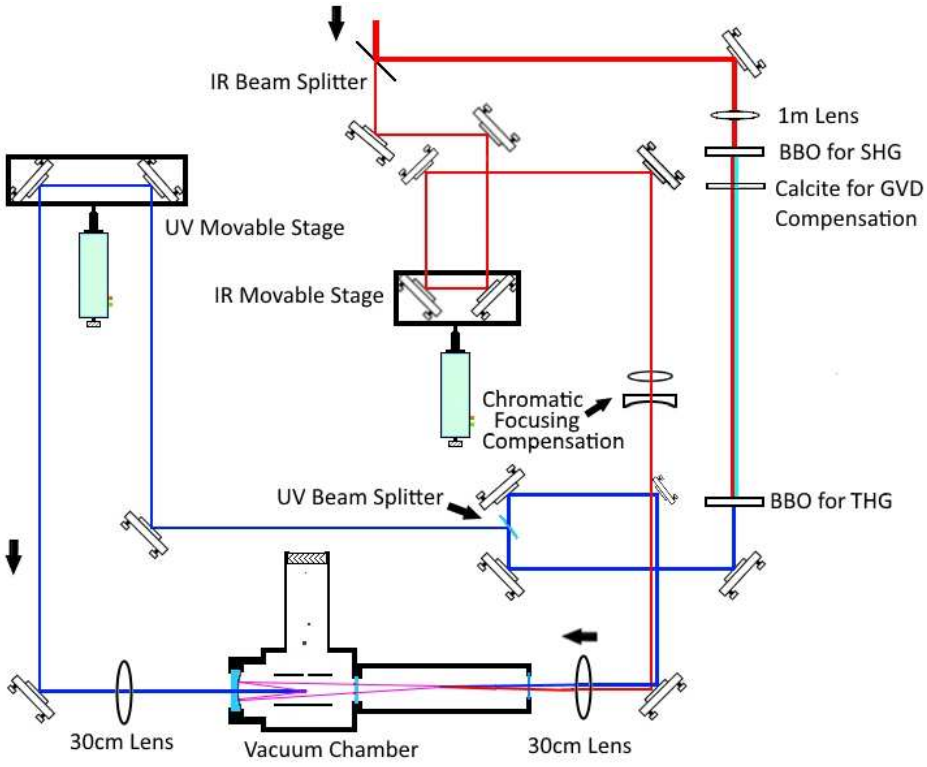

Figure 2.11: Schematic diagram of the experimental apparatus. Red, cyan, blue, and purple lines show the fundamental, second harmonic (generated via second harnomic generation (SHG)), third harmonic (UV), and fifth harmonic (VUV) beams respectively. One movable stage is used to temporally overlap the IR and UV pulses for VUV generation, and a second is used to perform the VUV-UV pump-probe experiment.

to be separated from the VUV. The reflected VUV-pulse is then focused under the TOFMS repeller plates. The $5\ \mu$J of UV reserved for the probe is sent through the dichroic mirror and also focused under the TOFMS repeller plates.

The VUV pulse reflected from the dichroic mirror inside the vacuum chamber has to be steered under the hole in the repeller plates. To do this a custom movable mirror mount for vacuum was designed, whose SolidWorks drawings can be seen in the inset of Fig. 2.12. A KF40 blank with a hole drilled through the center and a o-ring groove set around the hole was used as a custom window holder for the vacuum system. This KF40 window holder was connected to a KF40 bellow. Around the neck of the bellow a collar was constructed with three holes in the side where the ball tip head of a high precision 1/4”-80 Fine Hex Adjuster (Thorlabs)

can sit. An aluminum frame was also constructed with three slots where 1/4”-80 Locking Bushings with Nut (Thorlabs) could be locked in place. This aluminum frame is bolted in place independent of the vacuum chamber. The 1/4”-80 Fine Hex Adjusters are threaded through the 1/4”-80 Locking Bushings, when the vacuum chamber comes under vacuum the bellow contracts and the 1/4”-80 Fine Hex Adjuster ball tip heads come into contact with the holes in the collar. This contraption acts like a Gimbal mount for the dichroic mirror and enables steering of the VUV beam.

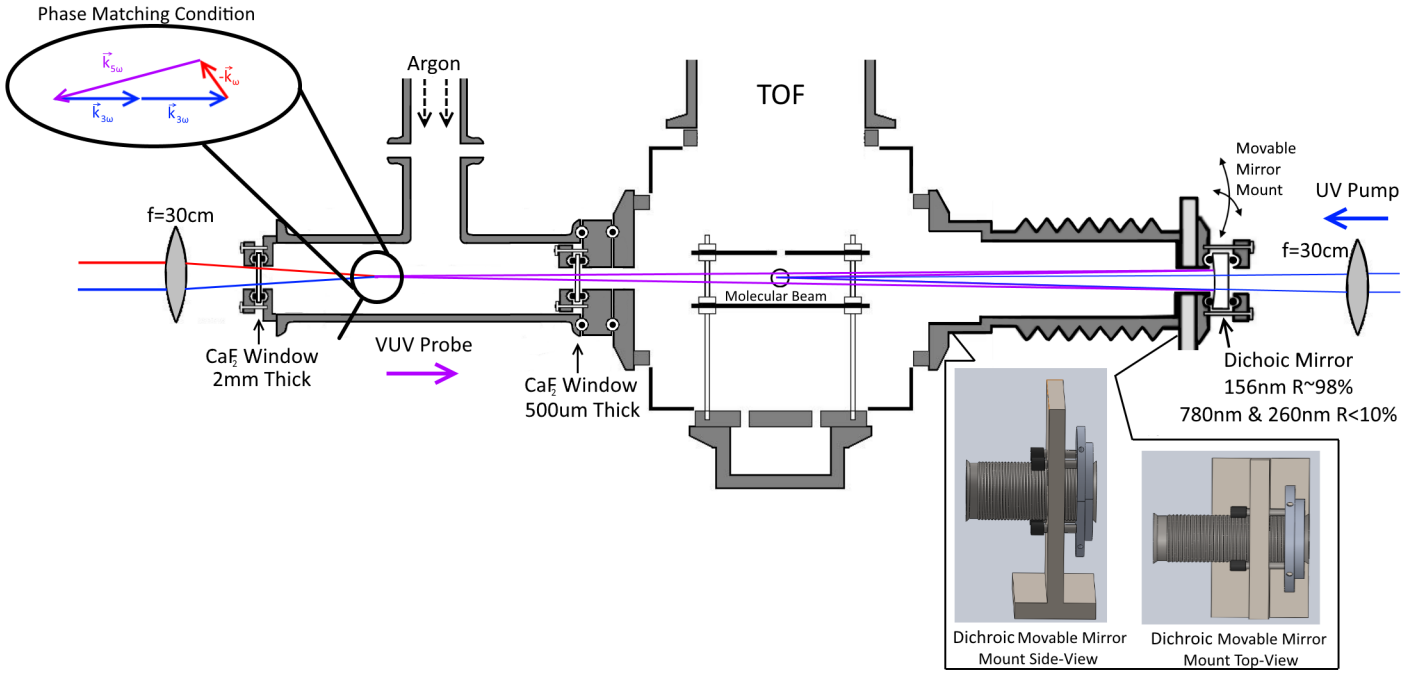

Figure 2.12: Initial vacuum chamber schematic

2.5 Time-of-Flight Mass Spectrometer

A schematic of the time-of-flight (TOF) tube and the detection scheme can be found in Fig. 2.14. The molecular beam is propagating out of the page and is perpendicular to the laser pulses between the repeller plates. Where the laser pulses and the molecular beam intersect, ions are generated. The ions are directed upwards through the use of a high DC voltage on the bottom repeller plate, where the bottom plate is kept at +800 V and the top plate is kept at ground. The top plate has a small hole in it that enables the ions to pass through. The ions then fly along a TOF tube in order to distinguish the different mass species by their different flight times. The ions are then converted into electrons and amplified with a microchannel plate (MCP) stack. The front of the MCP is at -1950 V, the back plate is at -50 V, and an anode, where the signal is read off, of is kept at ground.

In Fig. 2.13 a time-of-flight mass spectrum is shown for strong-field ionization of 1,3-cyclohexadiene (C_6H_8) showing all the mass fragments. After strong-field ionization 1,3-cyclohexadiene fragments into parts and the mass spectrum shows that the apparatus has a mass resolution of 1 AMU.

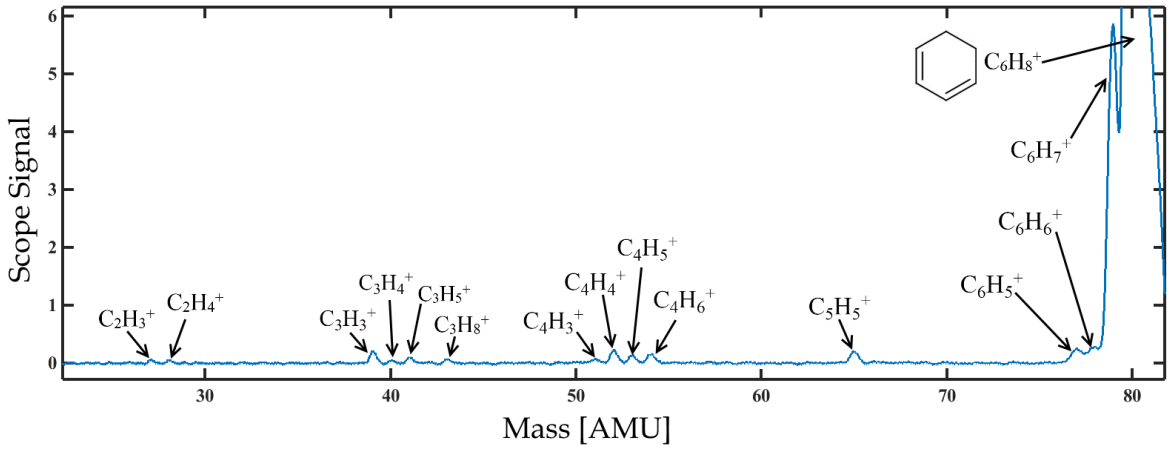

Figure 2.13: Time-of-flight mass spectrum for strong-field ionizion of 1,3-cyclohexadiene showing that the detector has single AMU resolution.

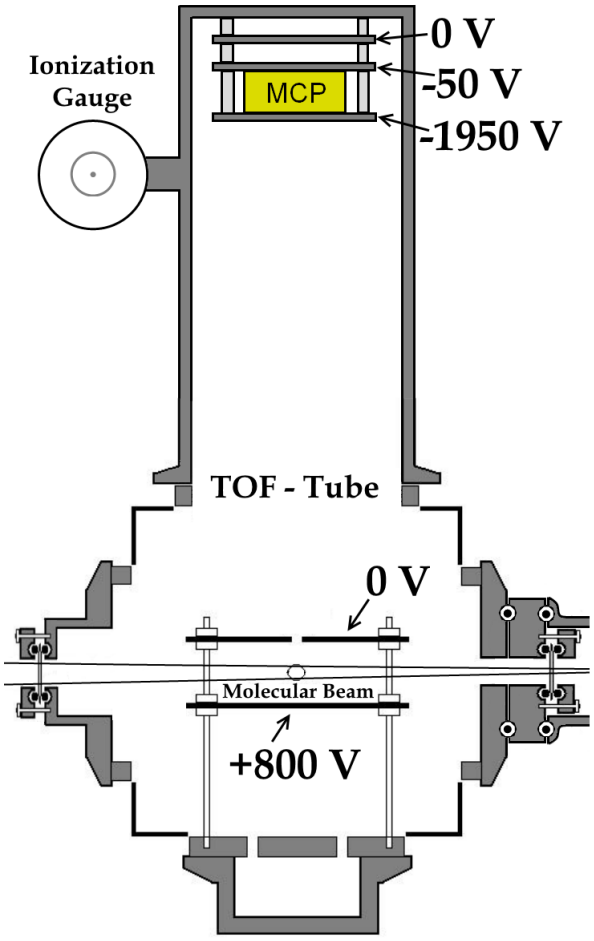

Figure 2.14: Time-of-flight Mass Spectrometer (TOFMS). The bottom repaller plate is kept at +800 V and the top plate is kept at 0 V. The static electric field sends ions through the hole in the top repeller plate and into the TOF tube. The ions are detected and amplified by a MCP stack with the front plate kept at -1950 V, the back plate at -50 V, and the anode kept at 0 V. The amplified signal is read off the anode.

2.6 Solid Sample Molecular Nozzle

The molecular nozzle used for liquid and gas samples is a simple effusive molecular beam nozzle made from a 1/4" OD stainless steel tube with a shim stock cap brazed on top with a 50 μm hole in its center. For gas, the nozzle simply utilizes a regulator on the gas tank and a needle valve. The needle valve has enough control in order to maintain a constant pressure behind the nozzle, hence a steady flow into the chamber.

For liquid samples, LN2 is used to freeze the sample, enabling roughing out of any background atmospheric gas. A valve followed by a gas reservoir behind the molecular nozzle is used to generate a molecular beam. The valve is opened and the sample is slowly warmed until the desire pressure is reached inside the interaction chamber, and then the valve is shut and the reservoir, filled with the pure sample, is used to maintain the molecular beam for an extended period of time.

This nozzle cannot be used for solid samples, because the vapor pressure of a solid sample is too low to build up sufficient pressure in the reservoir. Therefore a new nozzle had to be designed to generate a narrow molecular beam from a solid sample in the interaction chamber with the laser pulses. The solid sample of most interest to this thesis work was uracil. At room temperature, uracil has a negligible vapor pressure and must be heated in order to have enough gas phase molecules in order to run an experiment. Uracil can be heated to $\sim 200^\circ$ C in oder to get sufficient vapor pressure to perform experiments without degrading the sample, which happens at higher temperatures.

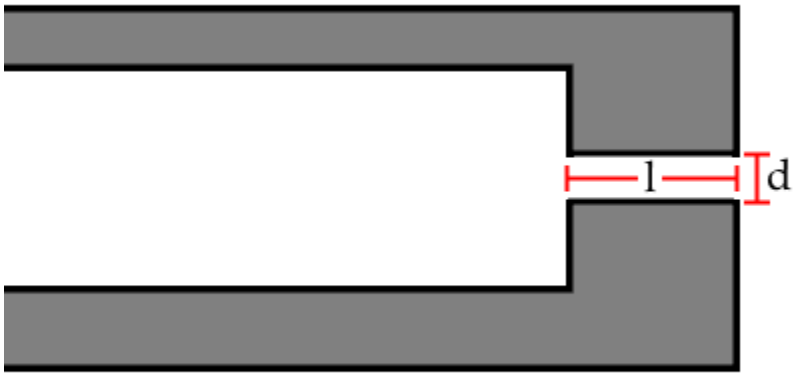

Figure 2.15: Zoom in of the nozzle head. The quantities l and d are defined that are used in determining the angle of the effusive nozzle.

The FWHM, $\theta_{1/2}$, is a general quantity used to characterize a molecular beam profile that gives the expected beam spread for a flat radial density profile. For a tube

$$\theta_{1/2} = 1.68d/l, \tag{2.18}$$

where d is the diameter of the hole and l is the length [34], as indicated in Fig. 2.15. The solid sample nozzle was designed to have an l = 6 mm and d = 0.609 mm in order to give a full angle, $2\theta_{1/2}$, of 19.5°.

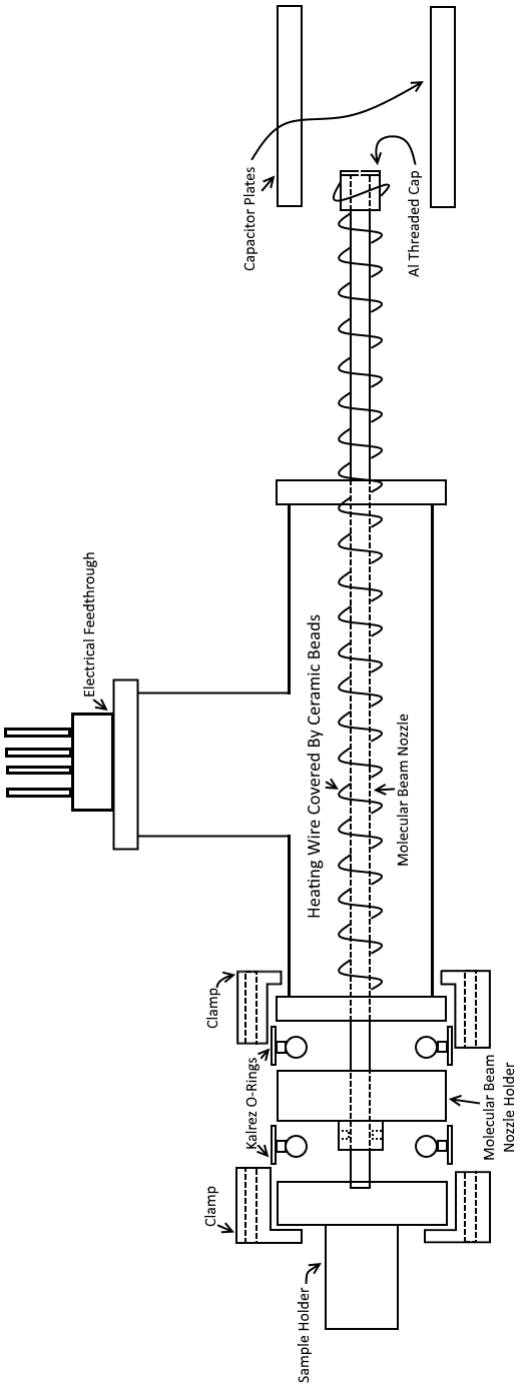

Figure 2.16: Solid sample design.

The full design of the solid sample holder can be seen in Fig. 2.16. The sample holder is a KF40 unbored aluminum stub that was drilled out with a 1" end mill. It is connected to a custom made molecular beam nozzle holder that is made from aluminum and designed to hold two KF40 centering rings on its surface. The vacuum seal of the molecular beam nozzle holder is made by two Kalrez o-rings that can withstand temperatures up to 316° C. In the center of the molecular beam nozzle holder is a threaded hole to hold the molecular beam nozzle, which is a 1/4" aluminum rod that is threaded on the outside at the end. The other side of the molecular beam nozzle holder is connected to a standard KF40 Tee. The sampler holder is held together with two pairs of bulk head clamps held with #10-32 bolts and plate nuts. The aluminum molecular beam nozzle is wrapped in Nickel-Chromium heating wire that is kept from shorting to the aluminum rod by ceramic beads. The heating wire was originally wrapped in Kapton film, but when heated to 200° C the Kapton film outgasses too much and brings the pressure in the interaction chamber above 1×10^{-5} Torr from a base pressure of 1×10^{-7}, without any powdered sample in the holder. This pressure is too high to turn on the MCPs safely without having arcing. This effect is a bake-out type effect from surface contamination and/or trapped volumes of gas, and Ait takes days for the system to pump lower than 1×10^{-5}, at which point the sample is also depleted. The end of the molecular beam nozzle is an aluminum cap that is treaded onto the rod in order to have interchangeable heads to generate different molecular beam angles. Electrical feedthroughs are needed at the spare end of the Tee in oder to supply power to the heating wire and for getting a reading from a thermal couple at the tip of the nozzle. The back of the sample holder is externally wrapped in heating tape and maintained at 190° C, and the molecular nozzle head is kept at 200° C to have a temperature gradient across the nozzle that ensures the nozzle head does not clog.

A problem with this design is that the once the Kalrez o-rings have been heated to 200° C the shape of the o-ring warps. If the joint is left alone it continues to hold vacuum well, but they do not handle being opened and resealed more than a couple of times before they stop being able to hold vacuum. The Kalrez o-rings were used because it was thought they could handle being resealed multiple times. In the end the sample holder with a KF40 to CF adapter was replaced with a CF sample holder. This enables the molecular beam nozzle holder to remain untouched. Because this joint is left untouched it would have been more economical to use metal o-rings instead of Kalrez o-rings.

A simple apparatus that measures solid sample deposits at various distances from the nozzle to determine the angular spread of the nozzle was constructed. The results of these measurements shows that the molecular beam angular spread is actually $\sim 35°$ instead of the expected 19.5°, but is sufficient for the experiment.

2.7 Detecting the Generated VUV

Before performing any experiment a way of detecting and characterizing the generated VUV needed to be developed. A VUV photomultiplier tube (PMT) is expensive and does not discriminate between the incident UV or VUV. The VUV is generated through the use of a UV pulse, therefore there will be residual UV that will follow the VUV (with a difference in angle of 2 mRad) and would trigger the VUV PMT. A VUV PMT would require one to use a VUV monochrometer to separate the UV and the VUV. Scintillating materials, such as sodium salicylate, fluoresce for both the UV and the VUV and the fluoresce signal could be detected with a standard PMT. This would lower the cost, but would still require the use of a VUV monochrometer.

Since an ionization chamber was already available the simplest solution was to find a molecule with an ionization potential significantly higher than that of the photon energy of the UV, but lower than the photon energy of the VUV. The molecule that fit these criteria was α-terpinene, with an ionization potential of 7.57 eV [35]. The ion signal from α-terpinene was used as a measure of the VUV fluence, which allows one to tweak the IR and the UV to maximize the VUV light generated.

2.8 Getting UV-VUV Spatial and Temporal Overlap

A major difficulty for these experiments was getting spatial and temporal overlap of the UV and the VUV pulses in oder to perform pump-probe experiments. Since the VUV cannot be transmitted outside the vacuum chamber, an approximate time-zero could not be acquired for the pulses outside the chamber through DFG in a nonlinear crystal, as standard practice in many ultrafast time-resolved experiments. A method of aligning the UV and VUV beams spatially (x,y) and temporally (t) inside the vacuum chamber had to be developed.

To align the beam in the y-direction, the vertical direction between the repeller plates, the TOFMS was utilized. The exact arrival time of a specific mass peak in the TOFMS is dependent on exactly where the ion was generated between the repeller plates. By ensuring that the parent ion peak from both the UV and the VUV beams arrived at the same time, to within several nanoseconds, one could get $\sim \mu$m overlap between the two pulses in the y-direction.

Aligning the beams in the x-direction, the horizontal direction between the repeller plate, was much more difficult. To do this a special repeller plate had to be designed, shown in Fig. 2.17. It has a series of four 50 μm diameter holes drilled into the plate in a line along the laser propagation direction. The 50 μm hole size fixes the x-position of both beams, and the multiple holes helped increase the ion

signal. A 1 mm hole was also made in the repeller plate, so that once temporal overlap was found the UV and VUV beams could be moved over to a larger hole in order to increase the signal to noise ratio.

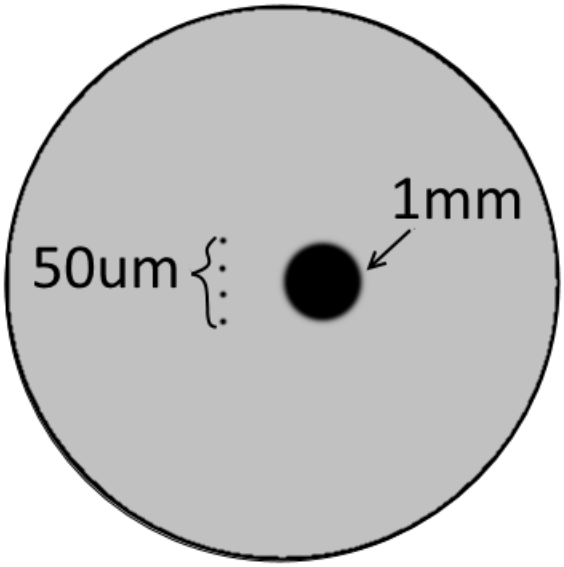

Figure 2.17: Repeller plate design for aligning the UV and the VUV beams in the x-direction, horizontal direction between the repeller plates.

Now the only degree of freedom that remains unfixed is time, t. For temporal overlap it was best to change molecules in the system from α-terpinene to ethylene. Ethylene is an ideal candidate because it has an extremely large absorption cross section of 10^{-16} cm^2, [36], in the VUV and undergoes rapid internal conversion that makes it a good indicator of time-zero. With such a large absorption cross section one easily perform VUV-pump UV-probe measurements on the molecule. The delay of the UV arm was scanned until a cooperative signal appeared from both the VUV and the UV, indicating that temporal overlap between the two pulses had been found.

In Fig. 2.18 a TOFMS is shown where both ethylene and α-terpinene are in the interaction chamber. The α-terpinene signal, 136 AMU, is mostly due to single photon ionization from the VUV. α-terpinene does have an excited state that the

UV can pump to, and a small UV-pump VUV-probe signal is seen in this system, but this pump-probe signal is masked by the single photon ionization. Therefore, α-terpinene it is not a good candidate to find time-zero in (evident from Fig. 2.18). Ethylene, on the other hand, cannot be ionized by a single photon of the VUV, some multiphoton ionization of ethylene from the VUV in the TOFMS is seen. The ethylene signal, 28 AMU, is very strong and clear at time-zero and is in stark contrast to the off time-zero signal, as be seen in Fig. 2.18.

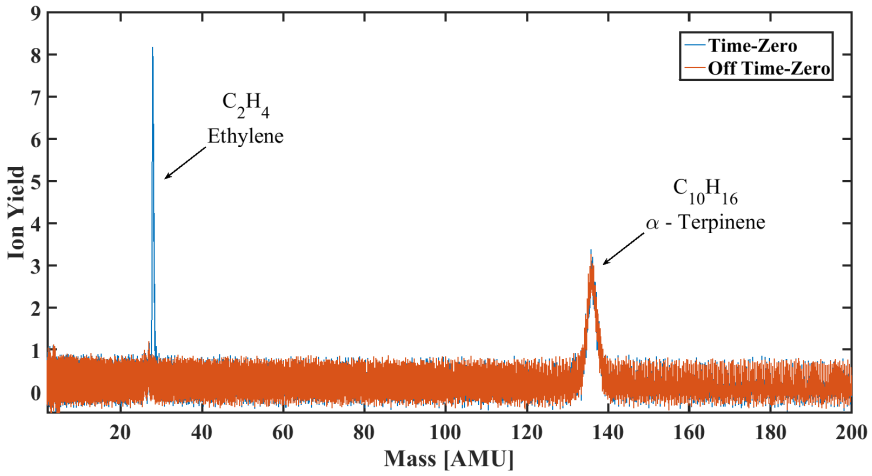

Figure 2.18: Ethylene and α-terpinene TOFMS at time-zero and off time-zero.

After finding spacial and temporal overlap several times the usefulness of the line of four 50 μm holes became less and less. For the 1 mm hole it was found that if the ion yield for each beam separately was maximized by going directly through the center of the hole, that this was good enough to align the beams in the x-directions. For a single photon pump and single photon probe it was found that one could work outside the outside of the tight foci of the beams and use larger beam sizes ($\sim$200 μm). Being out of the foci of the beams lowers their intensities, hence reducing the multiphoton processes. As a result of these observations the repeller plate design was changed for the data taken in Chapter 5. The new repeller plate design can be seen Fig. 2.19. The 5 mm long by 1 mm wide slot allows one to collect ions generated from a larger region and increases the overall signal to noise ratio.

2.9 Time Resolution of the Experiment

As a test and characterization of the apparatus, the VUV-pump UV-probe signal were recorded for ethylene, which has been studied in earlier work and has a very

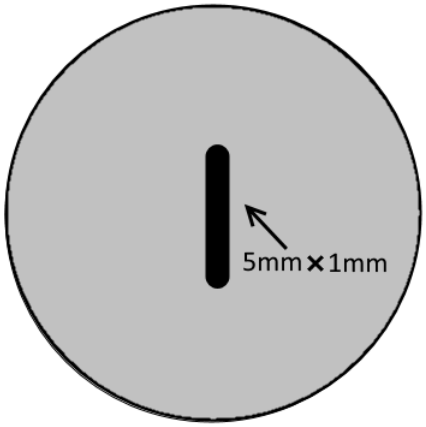

Figure 2.19: Repeller plate design with a 5 mm long by 1 mm wide slot.

rapid decay, $\tau \sim 30fs$, [37, 38, 39]. The results of this pump-probe scan and the subsequent fitting can be seen in Fig. 2.20. For the fitting of the ethylene pump-probe data it is assumed that the UV and VUV pulses are Gaussian in time, then the apparatus' impulse response time, σ, is dictated by the pulse durations. Therefore, σ is essentially the convolution of the pump and probe pulse durations. t_0 corresponds to time-zero (where the UV and VUV pulses are overlapped). A_1 and τ_1 are the amplitude and decay constant for the molecular decay. Θ is the Heaviside step function, and is used to ensure that the molecular dynamics in the model cannot initiate until the excited state is populated. The overall fitting function is

$$f(t) = e^{-\frac{(t-t_0)^2}{2\sigma^2}} \otimes \left[\Theta\left(t-t_0\right) \cdot \left(A_1 e^{-\frac{(t-t_0)}{\tau_1}}\right)\right]. \tag{2.19}$$

In order to determine the error in the decay constant for the ethylene pump-probe data the error of the individual fits compared to systematic errors in the experiment was examined. To check this, the pulse duration of the beams was changed and it was evaluated how the extracted decay constant of ethylene varied.

The perpendicular grating separation of a pulse compressor in the amplifier was used to change the pulse durations in the interaction chamber. Details on how the perpendicular grating separation effects the pulse duration can be found in Appendix A. Experiments on ethylene were reperformed at each grating separation

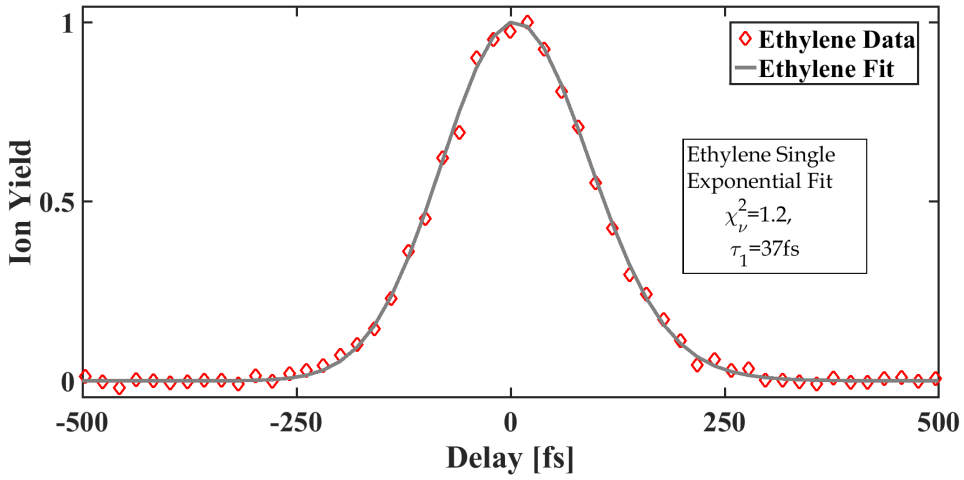

Figure 2.20: VUV-Pump UV-probe data and fit for ethylene's parent ion (C_2H_4^+).

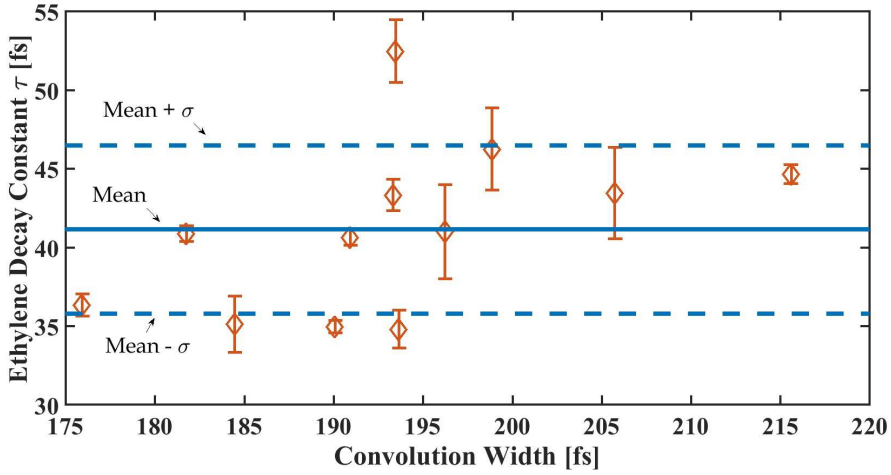

Figure 2.21: Decay constant, τ, for fits to ethylene parent ion signal measured with different VUV and UV pulse durations. The error bars on each point are determined by the χ^2 fits. The solid blue line is the mean of the measurements and the dashed blue lines are one standard deviation, σ, above and below the mean.

position. For each grating position the data was refit and from the fit the FWHM of the convolution of the pump and probe pulse and the decay constant of the molecule were extracted. In order to determine the individual error bars for each decay constant, τ, the value of τ obtained from the fit was fixed and the fit was re-minimized letting al the other parameters evolve freely. The value of τ was slowly varied until

the χ^2 value changed by one, and this value of τ was used as the individual data point error bar, as outlined in [40].

Fig. 2.21 shows the results of this compressor scan. It is evident that the spread in the data points is significantly larger than the individual error bars. The individual error bars from the fit vary from $\approx \pm 1$ to ± 2 fs, whereas the standard deviation in all the data points is ± 5 fs, which can be taken as a more realistic indication of the uncertainty. One should note that the distribution of decay constants about the mean is not completely random, but shows a slight trend with pulse or cross correlation duration. This indicates that the measurement of the decay time for ethylene might be a slight overestimate based on the pulse duration, which is larger than the measured decay time. The measurements are also consistent with previous measurements of ethylene's decay constant of $\sim$ 30 fs [37, 38, 39]. This analysis assumes that there is no chirp to the two pulses and that they are completely symmetric in nature. This is not necessarily true, but because the results attained with this model are comparable to previously measured results it indicates that this assumption is acceptable to use.

The IRF of $\sim$200 fs represents the time resolution for the apparatus for the experiments performed in Chapter 2, Chapter 3, and for the uracil data presented in Chapter 5. For the diiodomethane data, presented in Chapter 5, several improvements to the apparatus were implemented (discussed in Section 2.12: Improvements to the Time Resolution), so that the IRF of the apparatus was reduced by a factor of two. The improvements to the time resolution can be seen in Fig. 2.22, where the extracted FWHM of the IRF from the fit was 102 fs.

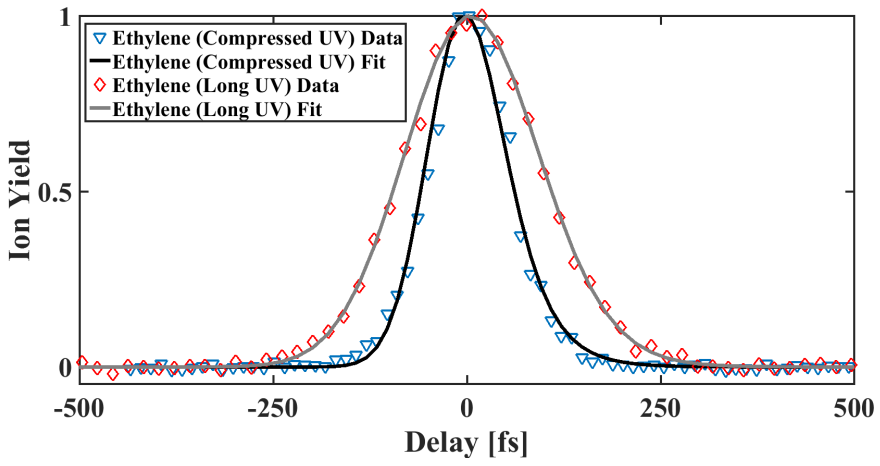

Figure 2.22: VUV-pump UV-probe data and fit for parent ion signal from ionization of ethylene.

2.10 Residual UV in the VUV Generation Problem

As mentioned previously, a dichroic mirror was used to separate the residual UV and IR used in generating the VUV from the VUV used in the experiment. The dichroic mirror has a high reflectivity coating of $> 90\%$ at $0°$ for $156 - 160$ nm light and $< 5\%$ reflectivity for 260 nm and 800 nm. The small amount of UV reflected from the mirror is significant, since 40 μJ of UV is used to generate the VUV. A 5% reflection results in 2 μJ of UV, which is enough to drive multiphoton ionization in its focus.

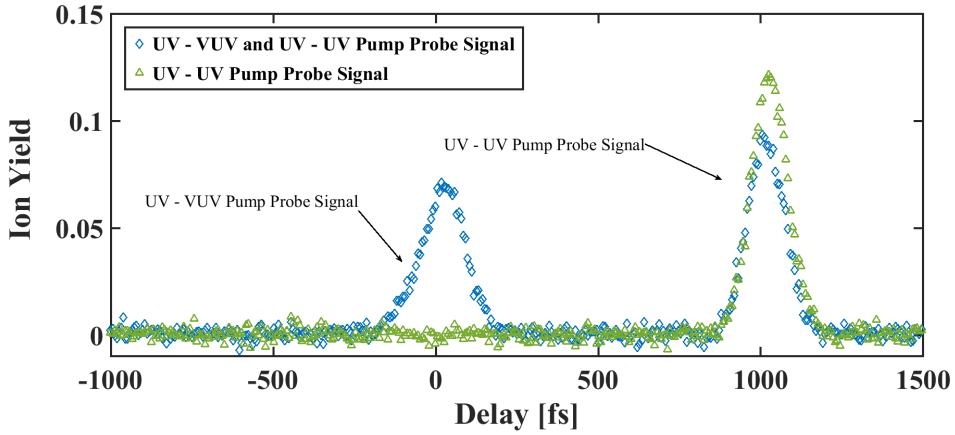

Figure 2.23: $CH_2I_2^+$ UV-pump VUV-probe and UV-pump UV-probe ion yield signal.

In Fig. 2.23 a typical UV-VUV pump-probe scan is shown from CH_2I_2, blue diamonds, that are collected in this apparatus. There are two peaks in this data, one at 0 fs delay and another at +1000 fs delay. The suspicion is that the second peak is from a UV-pump UV-probe combined signal. To verify this the IR pulse needed to generate the VUV is blocked and retake the pump-probe data, this data is the green triangles in Fig. 2.23. It is clear that the peak at 0 fs delay is no longer present and that the peak at +1000 fs delay became larger. This is good evidence that the peak at 0 fs delay is from UV-pump and VUV-probe. The delay between the two signals of 1 ps is consistent with the group velocity difference between the UV and the VUV after passing through the 500 μm thick CaF_2 window that separates the argon gas cell from the interaction region. The increase in the UV-pump UV-probe peak hight in the absence of the IR needed for the VUV generation is believed to be due to the fact that UV photons are not being converted into VUV photons, hence more are available for ionization in the interaction chamber.

2.11 Contamination of the Mirrors in the Vacuum Chamber

While running experiments with the UV and the VUV it was found that the VUV signal would greatly diminish from day-to-day. After examining the optics in the interaction chamber, the dichroic Layertec mirror and the CaF_2 window, they both had material deposits corresponding to where the beam was incident on them. In Fig. 2.24 an image of these deposits can be seen. These deposits could not be removed with standard optics cleaning solutions or ultrasonic cleaning. It was learned that the high photon energy of the VUV can cause the cracking of large organic molecules into its lighter hydrocarbons components that can stick to optics.

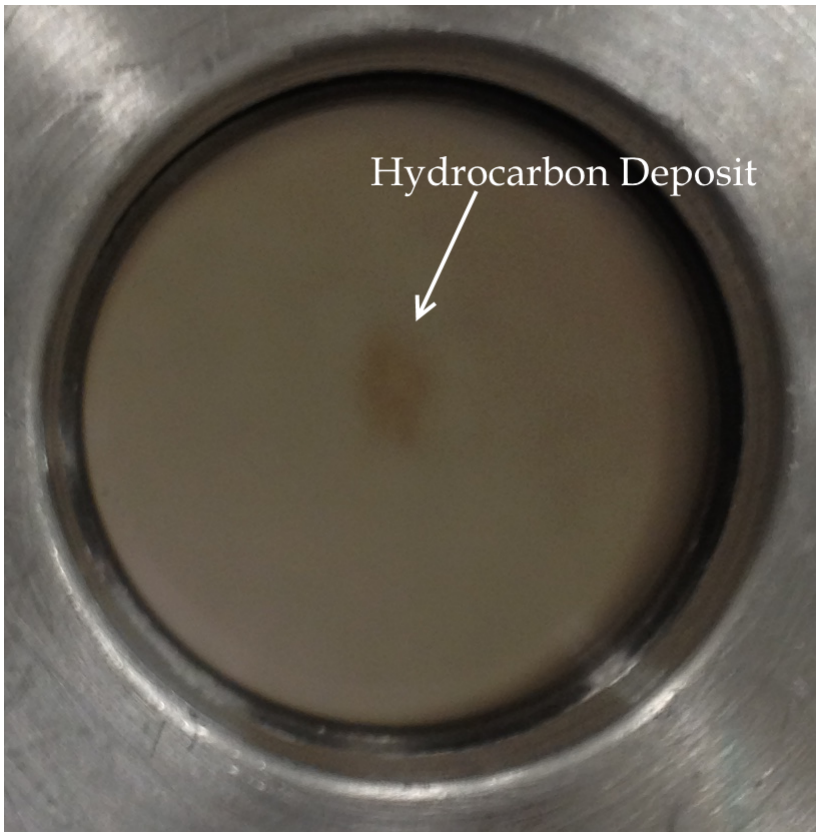

Figure 2.24: Hydrocarbon deposit on the VUV dichroic mirror.

One could not afford to replace the dichroic mirrors on a daily basis, and needed to develop a process for cleaning these hydrocarbon contaminants from the optics. The best method found for cleaning the Layetec dichroic mirros is through UV/ozone cleaning, as outlined in [41]. Atomic oxygen and ozone are produced

when O_2 absorbs UV light less than 245.4 nm and dissociates. Ozone produced at low UV wavelengths, sub 245.5 nm, can then be dissociated by higher UV wavelengths, 250 - 300 nm, to also produce oxygen. Most hydrocarbons have strong absorption bands between 200 and 300 nm, so light in the region can be used to excite and or dissociate these molecules. The excited contaminant molecules, and the free radicals produced by the dissociation of contaminant molecules, react with atomic oxygen to form simpler volatile molecules,such as CO_2, H_2O, and N_2. The combination of UV light and ozone has been shown to clean surfaces 2000 times faster than UV light or ozone alone [41].

First the dichroic mirror was placed in a plasma etcher with oxygen, where the plasma would produce UV radiation and ozone that could be used to clean the optic. The process cleaned the hydrocarbon film, but the method proved too aggressive for the LaF_3 high reflectivity coating. The dichroic mirror was no longer functional after this cleaning, since the coating was effectively removed.

A more gentle means to clean the optics needed to be found. Next, a simple mercury lamp which provides frequencies at 184.9 nm, to produce ozone, and 253.7 nm, to excite the contaminant hydrocarbons was considered. A Mineralight Lamp Short Wave UV-254 nm (Model UVS-54) was used for this cleaning. It takes approximately two days of sitting under the mercury lamp to completely clean the optics and bring them back to their original performance.

In order to reduce the rate of this hydrocarbon deposition on the optics a LN2 cold trap was added to the chamber, schematic shown in Fig. 2.25. A fundamental goal of this apparatus is to study large hydrocarbons, so in essence the experiment was contaminating the chamber every time sample was loaded. To mitigate the amount of hydrocarbons that get near the mirrors the cold trap was added in line with the effusive molecular beam. The target molecules are to pass through the interaction region with the lasers and then hit the cold trap where the molecules are frozen, so they do not ricochet off the chamber walls and get near the mirrors.

Adding this cold trap to the chamber did not substantially change the contamination rate of the mirrors. Putting a residual gas analyzer (RGA) onto the chamber it was realized that there were mass peaks in the chamber that correspond to pump oil. The vacuum system uses an Alcatel - Annecy 5150 CP turbo pump with greased bearings, and a Welch 1397 mechanical roughing pump to back the turbo. These both contribute to vacuum oil, large organic molecules, that can be cracked by the VUV and cause the contamination of the mirrors. Since the ability to develop a completely oilless vacuum system was not possible, the CaF_2 window and the dichroic mirror had to be replaced after every day of running the experiment and clean them with the mercury lamp. The hydrocarbon coating on the optic does not look like what is shown in Fig. 2.24 after one day of exposure to the VUV. After one day of performing experiments with the VUV the VUV reflectivity of the optic

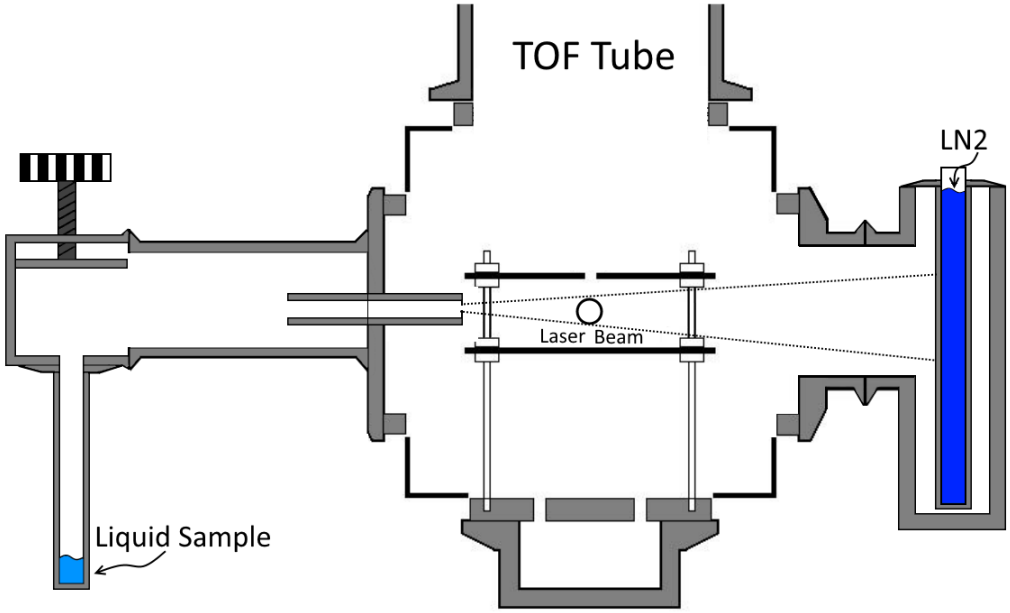

Figure 2.25: Cold trap addition to the vacuum system to mitigate contamination of the optics through cracking of our sample.

drops by approximately 50%, and the optic gets a very thin cloudy coating that can usually only be seen through thin film diffraction from the room lights at a glancing angle. The heavy brown spot in Fig. 2.24 only occurs after months of running, and steering of the VUV beam around the optic to improve performance.

2.12 Improvements to the Time Resolution

The temporal resolution of the apparatus of ∼200 fs was not ideal for studying very fast molecular dynamics. One is forced to rely on high signal to noise ratios in order to extract fast molecular dynamics that are much shorter than the pulse duration, as done for ethylene. Ultimately, one would want the shortest pulses possible in the vacuum chamber.

2.12.1 Minimizing Material in the IR & UV Arms

The first step in minimizing the pulse duration is to track all of the group velocity dispersion (GVD) and third order dispersion (TOD) from every optic in the system, and see their effect on the pulse duration. Once the optical components that were contributing the most to the elongation of the pulse are identified, it is possible to determine how to reconfigure the system in order to get shorter pulses in the interaction chamber.

The relations

$$\text{GVD} = \frac{\lambda^3}{2\pi c^2}\frac{d^2n}{d\lambda^2}z, \tag{2.20}$$

and

$$\text{TOD} = -\frac{\lambda^4}{4\pi^2 c^3}\left(3\frac{d^2n}{d\lambda^2} + \lambda\frac{d^3n}{d\lambda^3}\right)z, \tag{2.21}$$

where n is the index of refraction, λ is the wavelength, c is the speed of light, and z is the material thickness, were utilized [42, 43]. The wavelength dependence of the index of refraction is given by each material's Sellmeier equation.

First, the dispersion in the IR beam is tracked. In Fig. 2.26 a standard amplifier spectrum from the laser system is shown in panel a, and in panel b the transform limited pulse that can be generated from this bandwidth is shown. The transform limited pulse is sometimes referred to as the Fourier transform limited pulse duration, and is the minimum pulse duration that can be acquired from a given bandwidth. From this it is known that the bandwidth can support a 31 fs pulse and this can be used to calculate the pulse duration as the beam passes through various material. The IR beam is transmitted through a 1 mm beamsplitter. Then the IR beam goes through two lens that act as a telescope. The telescope corrects for the chromatic aberrations in the focusing lens, so that the UV-arm and the IR-arm focus to the same position in the argon gas cell. After the beamspiltter and telescope, the calculated the pulse duration is 43 fs. A CaF_2 lens is placed after the telescope focusing the IR into the argon gas cell. The gas cell has a 2 mm CaF_2 entrance window. After going through the lens and window the pulse duration is calculated to be 53 fs.

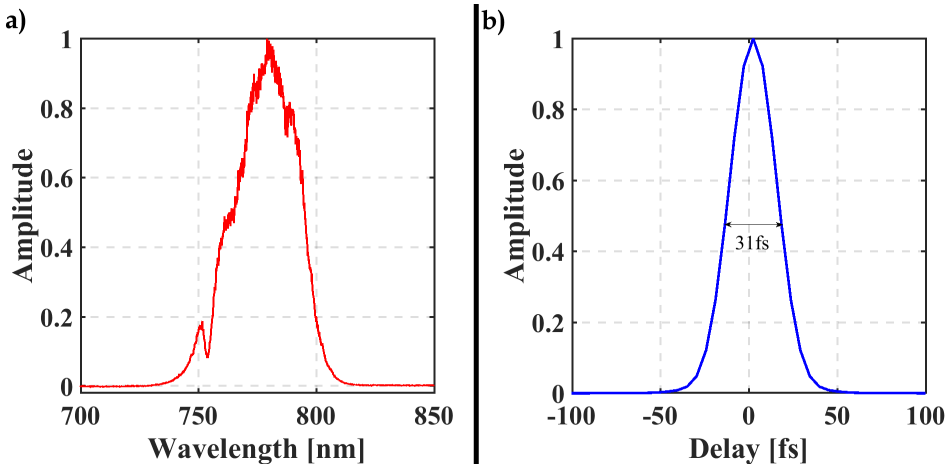

Figure 2.26: a) Measured amplifier spectrum. b) Transform limited pulse based on the measured spectrum.

Material in IR Beam of VUV Generation				
Material	**Thickness [mm]**	**GVD [fs^2]**	**TOD [fs^3]**	**Pulse duration [fs]**
BK7 Beam-splitter	1	46.57	31.52	31.3
BK7 f = 300 mm lens	3	139.71	94.56	34.6
BK7 f = -150 mm lens	3	139.71	94.56	42.5
CaF_2 f = 300 mm lens	3	86.20	48.53	48.5
CaF_2 Window	2	57.47	32.35	52.8
Total	**12**	**469.66**	**301.52**	

Next, the dispersion of the UV arm is tracked. As previously mentioned, in the THG scheme the IR beam is focused into the THG crystal in order to have a high enough intensity to generate a sufficient amount of third harmonic. Therefore, for the UV pulse the UV bandwidth is measured in two positions. One position is directly after the Type II THG crystal and the other is after the beam passes through its focus, and the results of these measurements can be seen in Fig. 2.27.After the UV focus a significant amount of bandwidth is generated. The cause of this broadening will be addressed in the next section, but here the effects of dispersion on both of these bandwidths is calculated.

The UV beam for the pump arm goes through a 3 mm CaF_2 lens and then it has to be transmitted through the 6 mm thick CaF_2 substrate of the dichroic Layertec mirror.

Depending on the bandwidth of the UV pulse one can have dramatically different pulse duration in the interaction chamber. For the UV spectrum measured before the UV focus the transform limited pulse duration is calculated to be 45 fs. After the UV focus the bandwidth can sustain a 20 fs pulse.

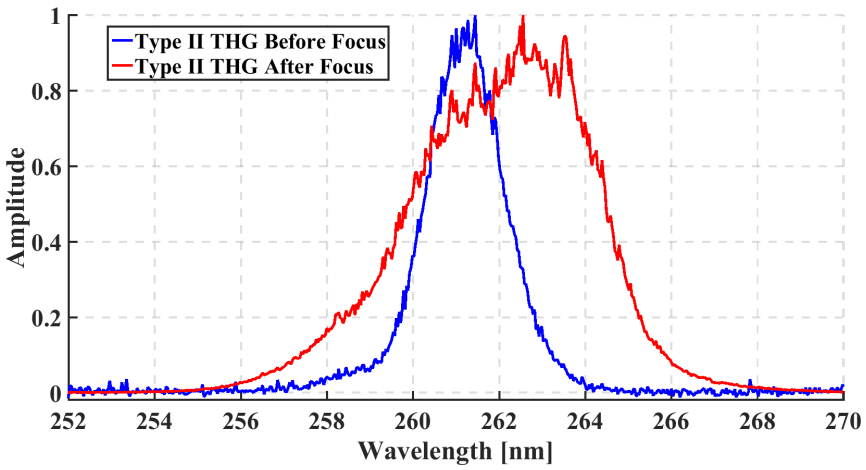

Figure 2.27: Spectrum of the third harmonic before and after the focus in the Type II THG setup

With bandwidth to sustain a 45 fs pulse the UV pulse would be 87 fs in the interaction chamber. If the CaF_2 lens is replaced with a refractive optic the pulse duration in the interaction chamber the UV pulse duration is calculated to be 67 fs.

With bandwidth to sustain a 20 fs pulse the UV pulse would be 168 fs in the interaction chamber. If the CaF_2 lens is replaced with a refractive optic the pulse duration in the interaction chamber is calculated to be 113 fs.

Material in UV-Pump Beam					
Material	**Thickness [mm]**	**GVD [fs^2]**	**TOD [fs^3]**	**Pulse Duration (20 fs)**	**Pulse Duration (45 fs)**
CaF_2 f = 300 mm lens	3	400.98	104.76	59 fs	53 fs
CaF_2 Layertec mirror	6	801.95	209.52	87 fs	168 fs
Total	**9**	**1202.93**	**314.28**		

The VUV pulse duration is assumed to be $\sim$50 fs at its generation, because the IR pulse used for its generation is calculated to be 53 fs in the argon gas cell. Even if one had the VUV bandwidth to sustain a 30 fs pulse the 500 μm CaF_2 window would stretch the pulse out to 40 fs in the interaction chamber.

From this analysis it is evident that UV is the main contributing factor to the poor resolution, and if one changed from focusing with a curved mirror instead of a lens one would make significant gains to the pulse duration. Based on this analysis the apparatus was updated, as shown in Fig. 2.28, in order to try and improve the pulse duration.

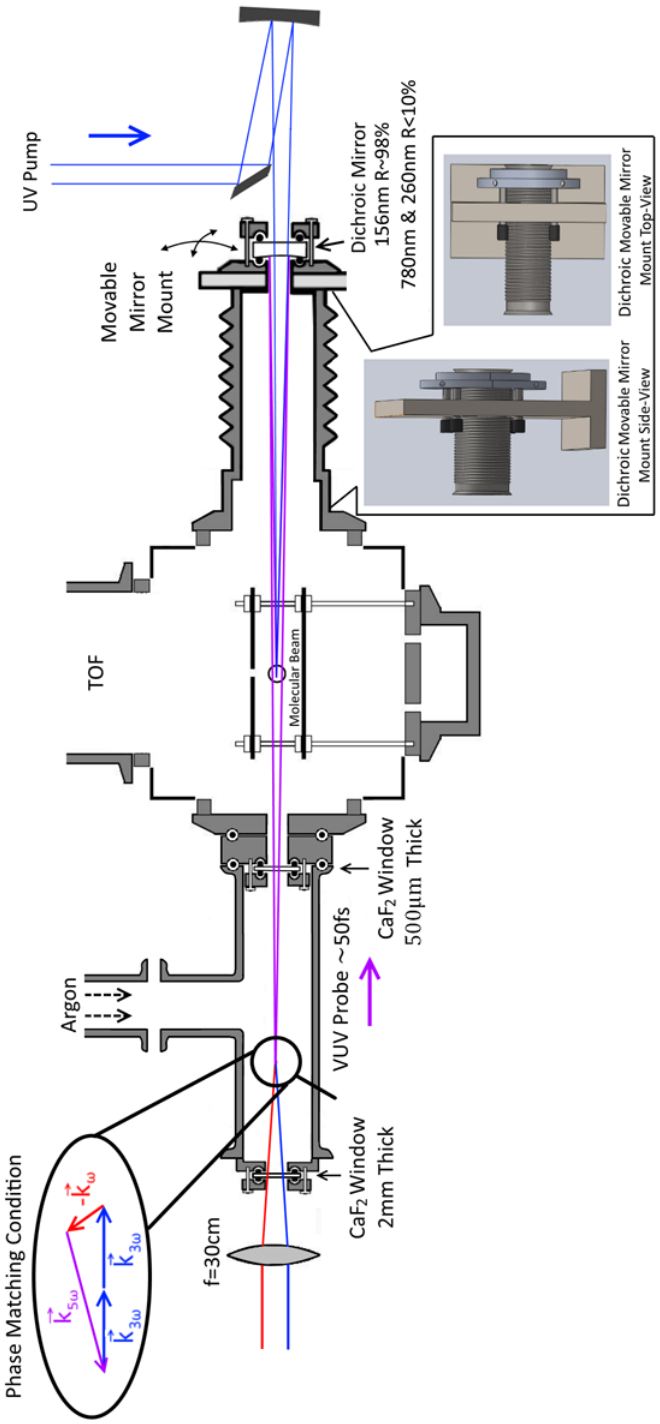

Figure 2.28: Updated time resolution vacuum chamber schematic

2.12.2 Revisiting the THG Setup

The calculations of the GVD and the TOD in the previous sections tells one that by changing the UV focusing optic one should see a significant change in the UV pulse duration. The analysis also shows that the dispersion associated with the bandwidth of the UV after the focus in the THG setup is too large to get a sub 110 fs UV pulse in the chamber without having a way of compressing the UV.

A proper characterization of the pulse with self-diffraction frequency resolved optical gating (SD-FROG), [44], is required to better understand what is causing this extra bandwidth in the UV pulse. The result of this SD-FROG can be seen in Fig. 2.29. The UV pulse has a very obvious chirp to it, its bandwidth is much larger than one would expect from our initial IR pulse, and its general shape is poor.

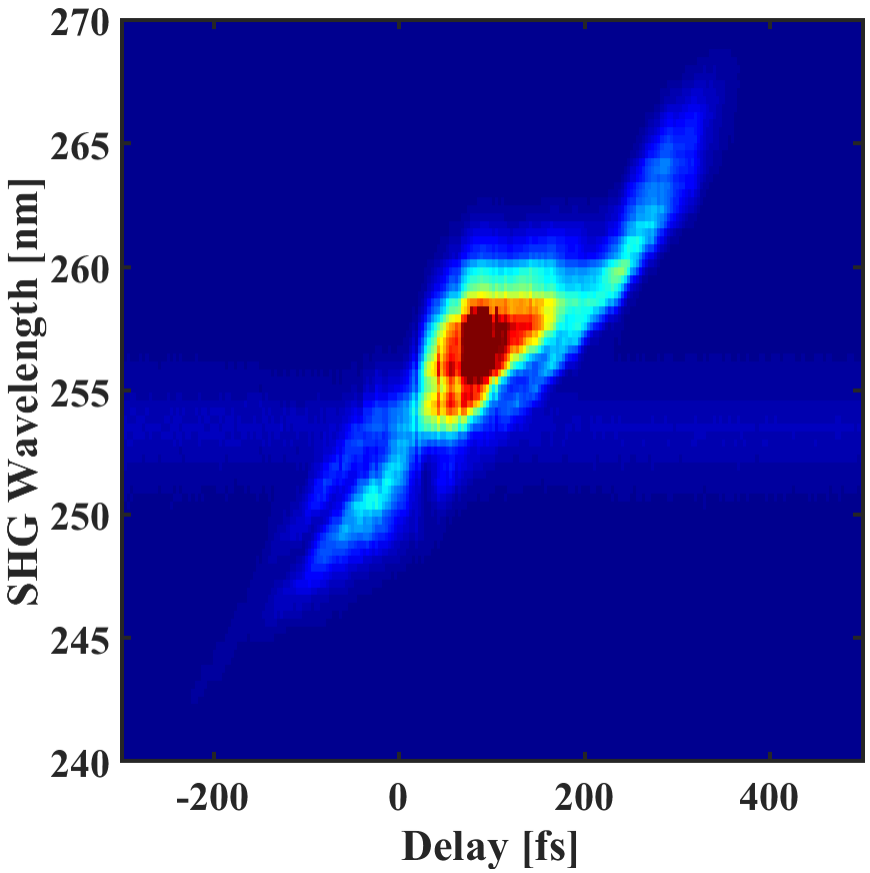

Figure 2.29: SD-FROG of the third harmonic after the UV focus with Type II THG.

The hypothesis is that when the UV passes through its focus it undergoes self-

phase modulation leading to the generation of extra bandwidth, that is ultimately leading to the long pulse durations.

2.12.3 Flowing Helium Over the Focus

The first idea on how to mitigate the self-phase modulation of the UV pulse in the focus was to flow helium over the focus after the UV generation, as depicted in Fig. 2.30. The idea is that Helium has such a high ionization potential that it would prevent any ionization in the focus and mitigate the self-phase modulation.

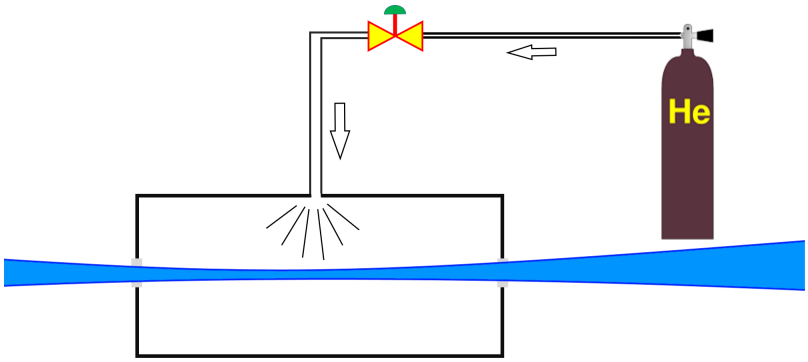

Figure 2.30: Schematic for flowing helium over the UV focus

Performing an SD-FROG on the pulse while flowing helium over the focus did not yield any significant improvements to the pulse duration. Also, the helium flow added significant turbulence to the beam and made it an infeasible solution to the problem.

2.12.4 Rethinking the THG: Type I versus Type II

Using a 1 m lens to increase the intensity of the beams in order to generate enough third harmonic for the experiments has proven problematic on multiple occasions. Here it is checked to see if one can generate enough third harmonic without focusing. To model this system SNLO, a free software developed by Dr. Arlee Smith [45], was used. For this simulation 1 mJ of 780 nm and 120 μJ of 390 nm light was assumed. The both pulses are assumed to have durations of 50 fs and beam diameters of 6 mm. The appropriate crystal angles for maximizing the THG with these wavelength is calculated by SNLO. Assuming a crystal thickness of 100 μm one can then simulate this system in SNLO.

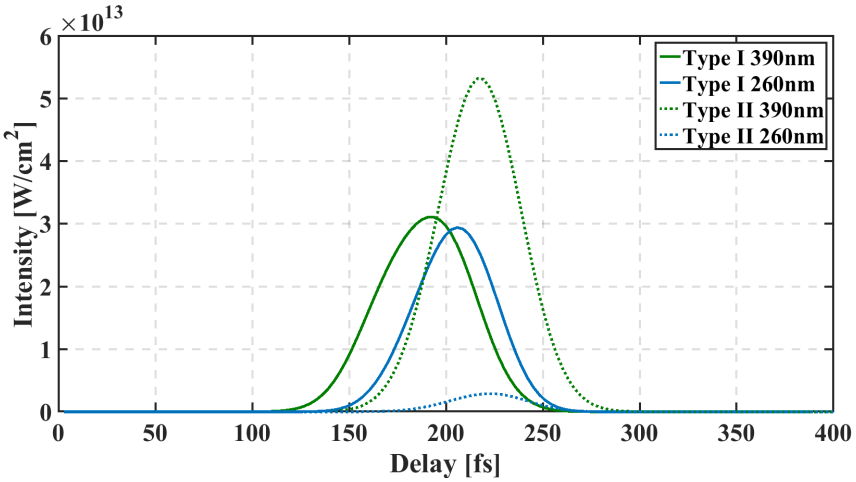

Figure 2.31: Calculation performed in SNLO of Type I and Type II THG using the experimental input conditions without focusing the initial IR beam.

The results of these simulations can be found in Fig. 2.31. Type I THG is much more efficient than the Type II THG, and one does not need to do any focusing during the generation process to get the amount of third harmonic needed for the experiments.

The new beamline developed for the implementation of Type I THG can be seen in Fig. 2.32. A waveplate that acts as a half-waveplate at 780 nm and a full-waveplate at 390 nm is required to rotate the polarizations of the fundamental and the second harmonic, so that Type I harmonic generation can be done in the THG crystal. A new THG crystal also had to added that was cut for Type I THG, and the 1 m lens was removed from the system.

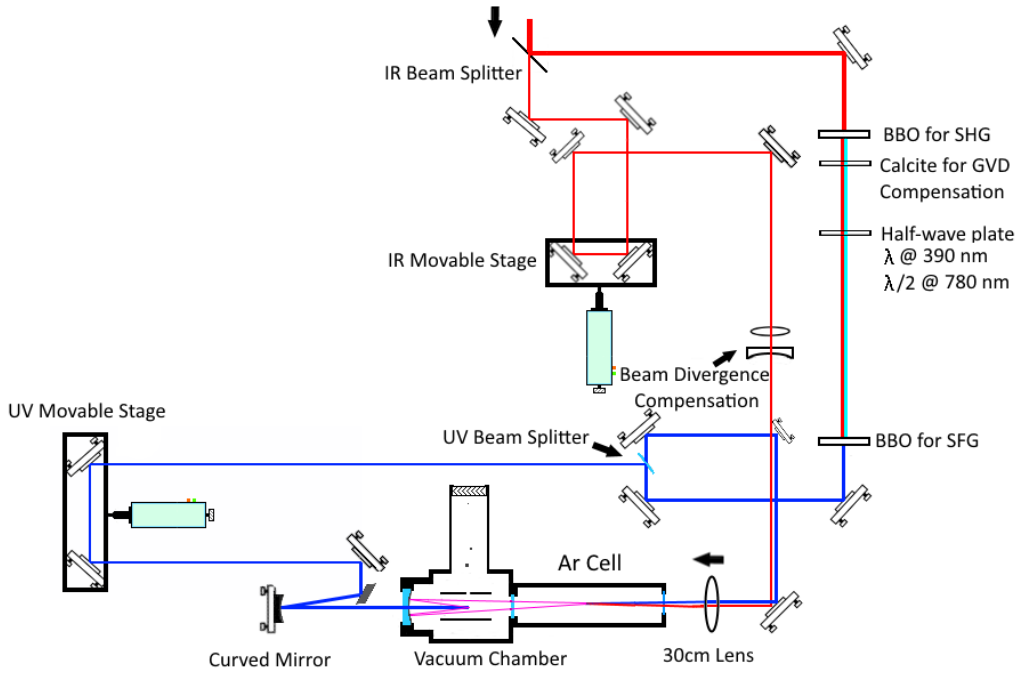

Figure 2.32: Schematic diagram of the experimental apparatus. Red, cyan, blue, and purple lines show the fundamental, second harmonic (generated via second harmonic generation (SHG)), third harmonic (UV), and fifth harmonic (VUV) beams respectively. The THG setup is changed to perform Type I THG without the use of a focusing element.

The THG setup is able to produce comparable third harmonic without focusing to what was attained through focusing with Type II THG. Also, not having the focusing lens cleaned up the mode that was previously still being distorted by self focusing. The spectrum and the transform limited pulse from the Type I THG without the focusing lens can be seen in Fig. 2.33 and Fig. 2.34, respectively.

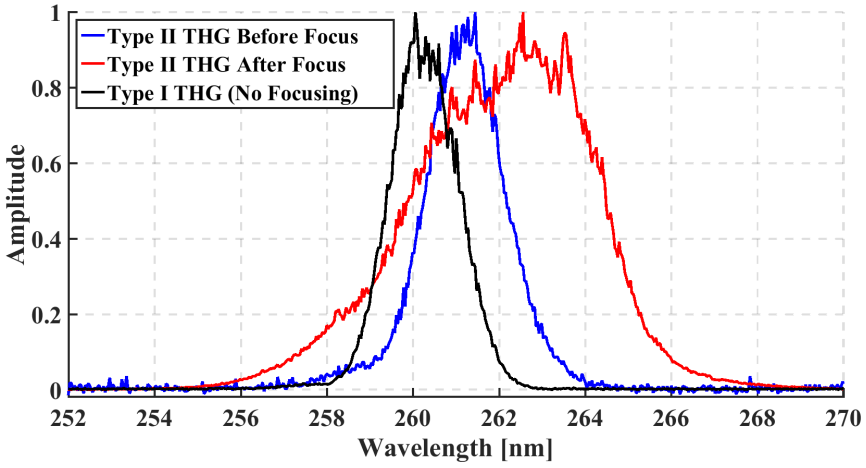

Figure 2.33: UV spectrum before and after the UV focus with Type II THG and the UV spectrum with Type I THG without and focusing.

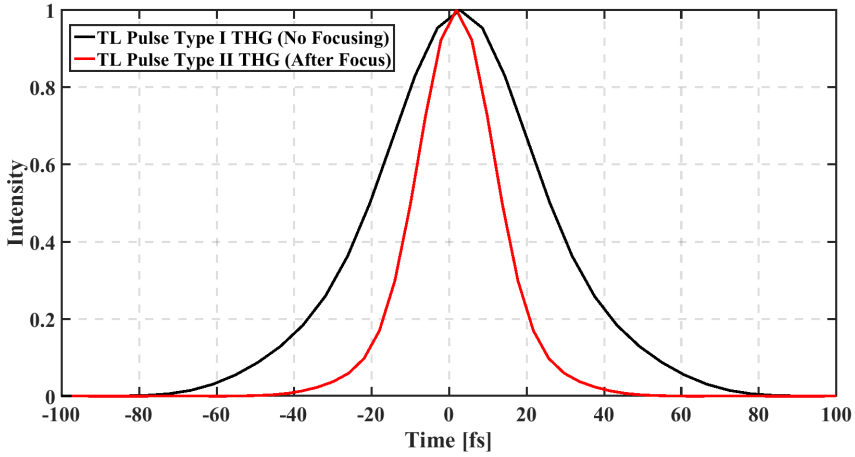

Figure 2.34: Transform limited pulse duration calculated from the UV spectrum after the focus for Type II THG and for Type I THG without any focusing elements.

The UV spectrum is no longer undergoing self-phase modulation and the transform limited pulse is $\sim$45 fs. An SD-FROG for this Type I THG can be seen in

Fig. 2.35. There is still a chirp to the UV pulse, but it is much cleaner than the SD-FROG from the Type-II THG in Fig. 2.29.

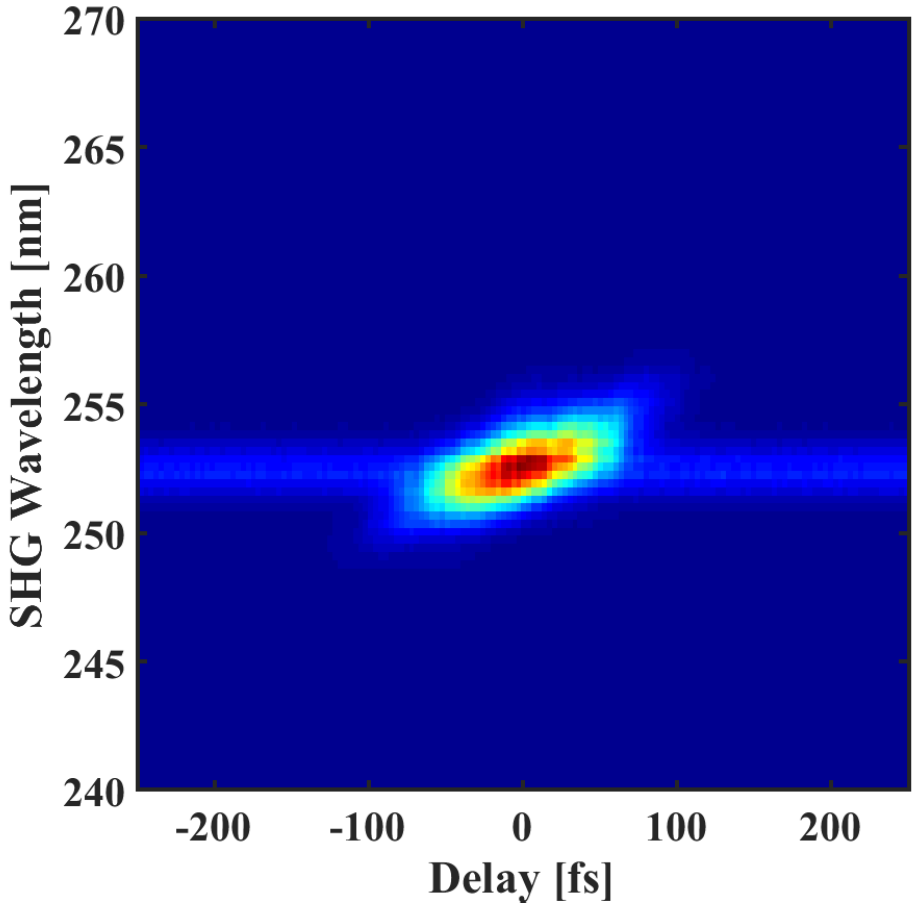

Figure 2.35: SD-FROG for the UV pulse after the Type I THG setup without any focusing elements.

One can also measure the pulse duration in the ethylene data, seen in Fig. 2.36, alongside the previous pulse duration measurements (this figure was previously shown in Fig. 2.22 but it is reshown here for ease of access). It is evident that the pulse duration has been reduced by a factor of two with these upgrades.

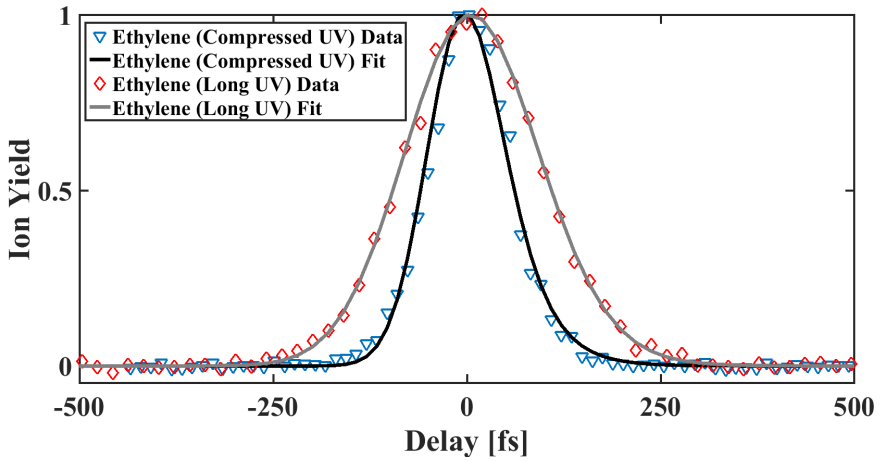

Figure 2.36: VUV-Pump UV-probe data and fit for ethylene's parent ion.

Chapter 3

Ultrafast Internal Conversion Dynamics of Highly Excited Pyrrole Studied with VUV-Pump UV-Probe Spectroscopy

3.1 Introduction and Motivation

Pyrrole (C_4H_5N), has been of intense experimental [46, 47, 48, 49, 50, 51, 52, 53] and theoretical interest [54, 55, 56, 57, 58, 59, 60] because it is considered an important building block for understanding the ultrafast dynamics of larger pyrrole-containing biomolecules, such as hemoglobin, vitamin B_{12}, chlorophyll, and tryptophan. Pyrrole exhibits rich photo-induced dynamics when excited with UV radiation, and its internal conversion and dissociation dynamics have been studied extensively both experimentally and theoretically.

Experimental work on the relaxation dynamics of photoexcited pyrrole has focused on pumping the first absorption band, with time-resolved studies probing the fate of molecules excited with pump wavelengths between 200 and 260 nm [47, 48, 49, 50, 51, 52]. These experiments, which made use of ionization as a probe, established that the molecule undergoes rapid internal conversion and dissociation on timescales of ~ 100 fs or less. Experiments that made use of velocity map imaging to measure the momentum of hydrogen ions generated by the probe pulse [48] found both fast and slow H^+, indicating dissociation on both the excited and ground state surfaces. The relative yields indicated that dissociation on the excited state dominated over internal conversion to the ground state followed by dissociation.

Several theoretical studies have examined the excited state dynamics in pyrrole. Three pathways involving conical intersections between S_1 and S_0 have been identified which are involved in nonadiabatic decay to the ground state or dissociation [54, 55, 56, 57, 58, 59, 60]. In particular, dissociation along the N-H bond has been found to be important in many studies. Recent theoretical work by Barbatti $et\ al$ [55] using the trajectory surface hopping approach with excitation energies between 193 nm and 248 nm indicated that while excitation to the first absorption band (wavelength of 248 nm) led to N-H bond stretching and fission, excitation with higher energy to the second absorption band (wavelength of 193 nm) led to slower decay (timescales of about 200 fs) with more complicated dynamics.

In this chapter, excitation of pyrrole is considered with a VUV pulse, corresponding to an excitation energy of about 8 eV. This corresponds to a higher excitation energy than all previous experiments and is motivated by the question of how the initial excitation influences the relaxation dynamics. Of particular interest in this study is whether the decay of the excited state is primarily due to dissociation on an excited state surface, or internal conversion to the ground state. Relaxation dynamics of radical cations (uracil, 1,3-cyclohexadiene, and hexatriene) using trajectory surface hopping was previously studied [61], and it was found that relaxation to the ground ionic state was rapid ($<$100 fs), taking place before dissociation. The density of states in these cations is similar to the density of states in highly excited pyrrole, and thus while excitation at lower energy resulted primarily in dissociation, one would expect more competition between internal conversion and dissociation at higher energies.

The original idea for developing the VUV light source was to use it as a probe of neutral state dynamics, and not as a pump to initiate Rydberg state dynamics. When performing UV-pump VUV-probe spectroscopy one should be aware of the relative strengths of the UV and VUV absorption cross sections for your system of interest. If the UV and the VUV absorption cross sections are comparable dynamics will be launched on both sides of time-zero. In other words, when the VUV proceeds the UV, negative time delays in a UV-pump VUV-probe experiment, dynamics initiated by the VUV will be probed and vice versa when the pulse order is reversed for positive times. This leads to a complicated pump-probe signal that requires careful treatment to disentangle the UV and VUV initiated dynamics. For the case of pyrrole, it was experimentally observed that the VUV absorption cross section is significantly larger than the UV absorption cross, enabling us to carryout this work. So, for the experiments performed in this chapter the excited state dynamics are probed with the UV pulse having a $\sim$5 eV photon energy, which, for pyrrole, allows for ionization from any excited state of the molecule without background signal from the ground state (IP = 8.2 eV [62, 63, 64, 65, 66, 67, 68, 69, 70, 71, 72, 73])

3.2 Computational Methods

In order to interpret the experimental results, our collaborators Pratip Chakraborty and Spiridoula Matsika, performed electronic structure calculations of the neutral and ionic states of pyrrole. The ground state of pyrrole was optimized using B3LYP/6-31+G(d). The excited state energies and oscillator strengths were calculated using equation of motion coupled cluster for excited states (EOM-EE-CCSD) and the aug-cc-pVTZ basis set. Ionic states were obtained using the equation of motion coupled cluster for ionization potentials (EOM-IP-CCSD) method and the same basis set. The QChem software package was used for these calculations [74]. The N-H bond was stretched from its equilibrium position in steps of 0.2 Angstroms, and the excited and ionic states along this coordinate were calculated. The excited states were characterized using natural transition orbitals (NTOs) obtained from the EOM-EE-CCSD method. Molden was used for visualization of the orbitals [75].

Fig. 3.1 shows the orbitals and the calculated potential energy surfaces along the N-H coordinate. The orbitals are natural transition orbitals obtained from diagonalizing the transition density [76]. The orbitals are the eigenfunctions of the matrix and represent particle-hole pairs, while the numbers shown in the figure are the eigenvalues. The importance of a particular particle-hole excitation to the overall transition is reflected in the associated eigenvalue. When a state has more than one pair it means that it cannot be described by a single hole-particle representation in the NTO picture. States 4^1B_1 and 4^1A_1 are the high-lying "bright" states that are accessible with the VUV-pump pulse. Looking at their orbitals on the right-hand-side of the plot it is evident that we are driving a $\pi \rightarrow \pi^*$ transition. Orbitals describing states 1^1B_2 and 1^1A_2 are on the left-hand side of the plot and they show that these are $\pi \rightarrow \sigma^*$ states which are not stabilized along the N-H coordinate and they can lead to dissociation.

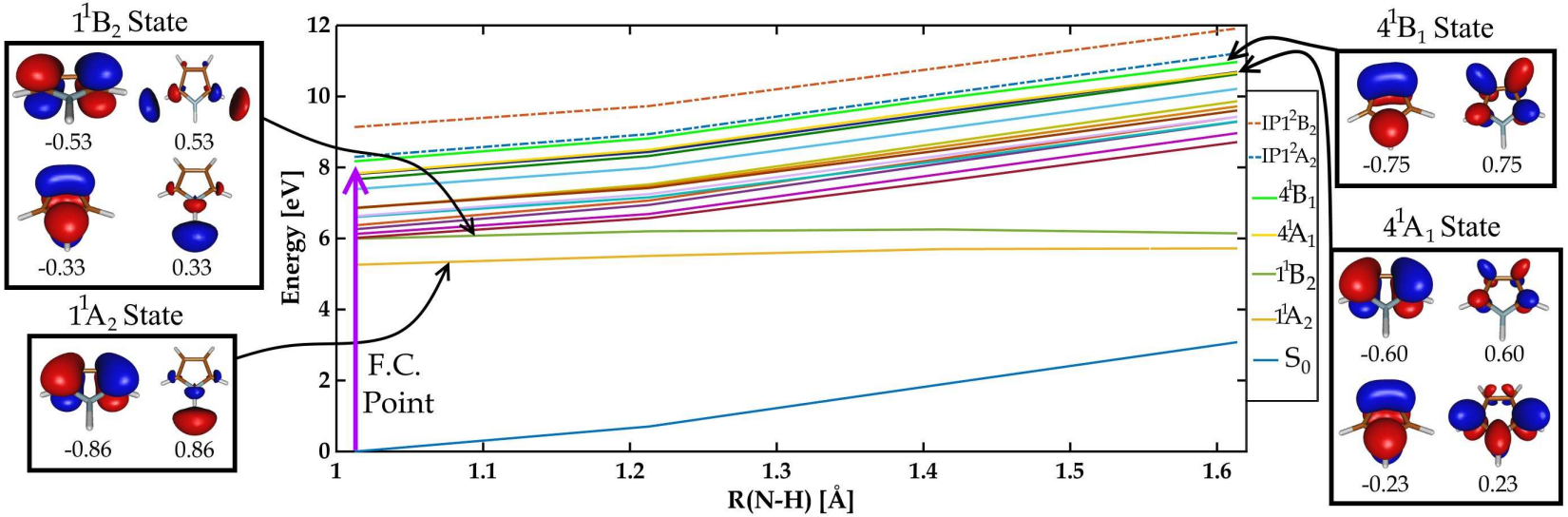

Figure 3.1: Natural transition orbitals (left and right sides) and energies as a function of N-H distance (center) with their associated eigenvalue. The dominant particle-hole pair of orbitals for states 4^1B_1 and 4^1A_1, which are the "bright" states accessible by the VUV pulse from the ground state, are shown on the right. The singly occupied orbitals for states 1^1B_2 and 1^1A_2, which are the low lying dissociative states along the N-H bond, are shown on the left. The purple arrow indicates the Frank Condon (F.C.) point. The ionic states are shown with dashed lines while the neutral states are shown with solid lines.

The density of states that the VUV pulse is exciting to is very high, so one would expect very fast radiationless decay from the absorbing state to 1^1B_2 or 1^1A_2. By inspecting the configurations and orbitals describing the 1^1B_2 and 1^1A_2 states and the low lying ionic states we see that ionization is allowed based on Koopmans' theorem (generally described in Section 3.2.2 Koopmans Correlation). In other words, the two lowest ionic states are described by the same valence orbitals involved in the excited states, and can be accessed by removing the π^* electron. Thus, these excited states can be easily ionized with our probe. In addition to the Koopmans' correlations, the figure makes it clear that for the range of N-H distances considered here, we are energetically able to ionize the molecule from any of the excited states, given their energies relative to the probe photon energy. Thus, the fact that the parent ion signal decays to zero at long time delays indicates that the molecule either relaxes back to the ground state or dissociates.

We note that for larger N-H bond lengths, reference [58] shows the ionization potential from S_1 increasing beyond our probe photon energy. Thus, our measurements cannot exclude the possibility of dissociation on S_1 despite the lack of fragment ion signal. This point is addressed further in the chapter.

3.2.1 Koopmans Correlation

States are said to be Koopmans correlated when the ionic states are described by the same valence orbitals that are involved in the excited states. An attempt to visualize this Koopmans correlation is made in Fig. 3.2, where the electron configuration in a molecular orbital picture is depicted for the ground state, S_0, the first excited state, S_1, the first ionic state, D_0, and the second ionic state, D_1, for a generic molecular system. HOMO is the highest occupied molecular orbital, HOMO - 1 is the second highest occupied molecular orbital, HOMO - 2 is the third highest occupied molecular orbital, and LUMO is the lowest unoccupied molecular orbital. When the molecule transitions from S_0 to S_1 an electron is excited from the HOMO to the LUMO. Now, consider ionizing the system and removing an electron. The weakest bound electron, the electron in the LUMO, would be the likeliest candidate to be removed from the system, and this would leave the system with the electron configuration for D_0. Therefore, one would say that ionization from S_1 is correlated to D_0 and not to D_1, because that would require the removing of a more deeply bound electron and the reordering of the remaining electrons.

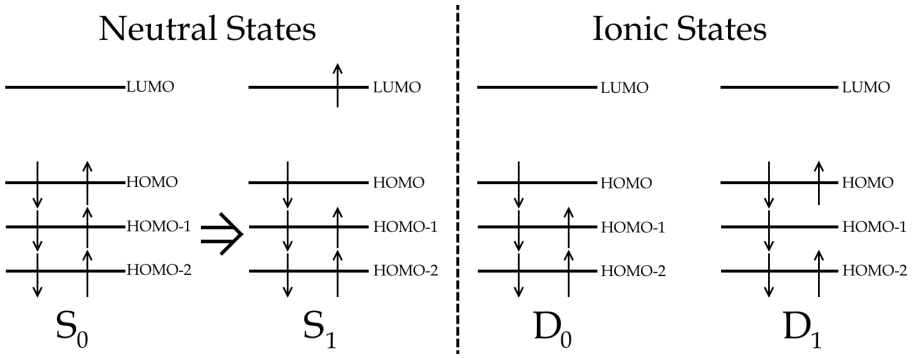

Figure 3.2: Electron configuration in a molecular orbital picture for the ground state, S_0, the first excited state, S_1, the first ionic state, D_0, and the second ionic state, D_1, for a generic molecular system.

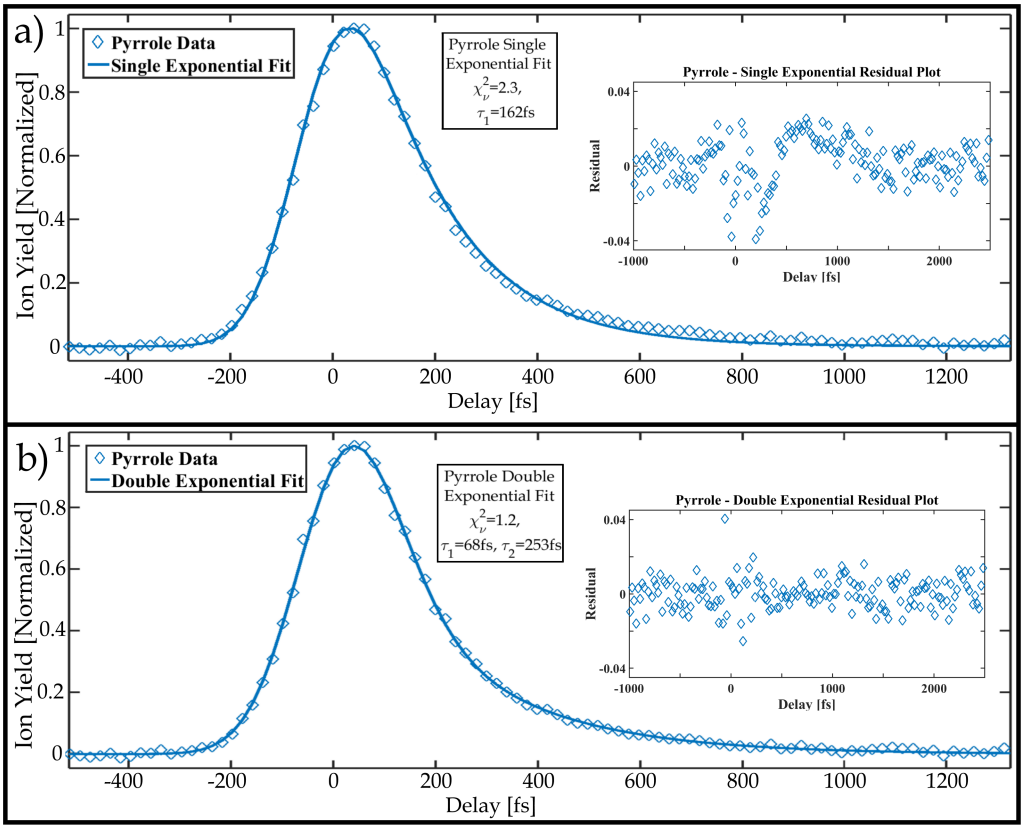

Figure 3.3: The blue diamond data points show VUV-pump UV-probe measurements performed on pyrrole (C_4H_5N) respectively. a) A pyrrole decay constant, $\tau = 162$ fs, is extracted from a mono-exponential fit with a $\chi^2 = 2.3$. The residual plot for this mono-exponential fit to the pyrrole data is shown in the inset. b) Two exponential decay constants, $\tau_1 = 68$ fs and $\tau_2 = 253$ fs, are extracted from a dual-exponential fit with a $\chi^2 = 1.2$. The residuals, shown in the inset plot, are randomly distributed, indicating that this fit is more consistent with the measurements.

3.3 Results and Analysis

The parent ion yield for pyrrole, $C_4H_5N^+$, as a function of VUV-pump UV-probe delay is shown as blue diamonds in Fig. 3.3. At negative delays the UV-probe pulse comes before the VUV-pump pulse, while for positive delays the VUV pulse comes first. For the simplest fit a mono-exponential decay is assumed to describe the molecular dynamics. In order to account for the finite duration of our pump and probe pulses (which have a Gaussian temporal profile), a Gaussian convolved with

a decaying exponential is used as the fitting function.

Looking at the fit in panel a of Fig. 3.3, it is obvious that the mono-exponential pyrrole fit does not describe our data well after 400 fs. The residual plot, Fig. 3.3 panel a inset, for the pyrrole pump-probe data fit to a mono-exponential clearly has structure, and the fit has a $\chi^2_\nu = 2.3$. χ^2_ν is the reduced-χ^2 of the fit and is defined as the χ^2 of the fit divided by the degrees of freedom of the fit. The χ^2_ν value of 2.3 indicates that the fit does not accurately reflect the measurement.

Panel b of Fig. 3.3 shows that a dual exponential function fits the data well with a χ^2_ν value of 1.2. The decay constants are 68 fs and 253 fs instead of the 162 fs obtained from the mono-exponential fit. Fig. 3.3 panel b inset is the residual plot for the dual-exponential fit. The residual is randomly distributed, indicating that we have a good fit to our data and that a double exponential decay provides a reasonable description of our measurement.

3.4 Kinetic Models

The clear dual exponential nature of the pyrrole data encourages one to try and construct simple kinetic models in order to develop a physical interpretation. Several kinetic models were constructed, shown in Fig. 3.4, to describe this system. In these models, k is the decay constant between two states and correspond to $1/\tau$ values in the text.

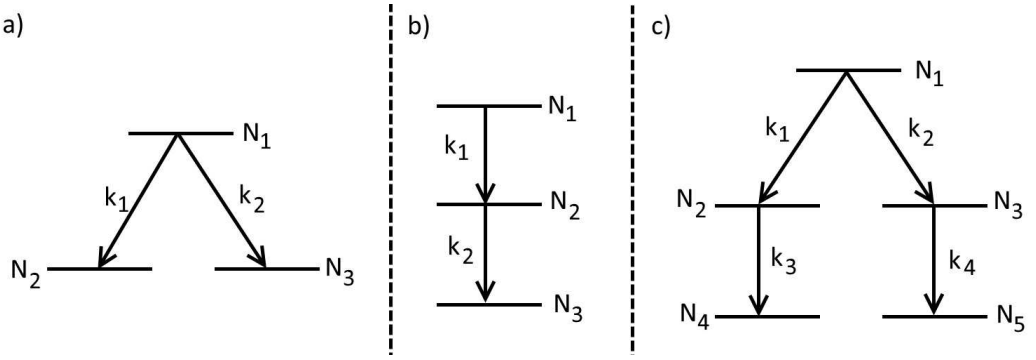

Figure 3.4: Different Decay Schemes

In Fig. 3.4 a) the simplest scheme is shown has two different decay channels from the same state. The population in N_1 can be ionized by the probe to produce the parent ion. The total ionization yield is proportional to the population in N_1, which is

$$N_1 = N_1(0)e^{-(k_1+k_2)t}. \tag{3.1}$$

In this model $N_1(0)$ is the initial population in N_1 (derivations are presented in the following section). This model yields a single exponential, hence it cannot explain the double exponential nature of our pyrrole data.

We then consider Fig. 3.4 b). Here is an effective three level model for the dynamics, where decay from the initial excited state to an intermediate state gives one timescale, while decay of this intermediate state to the ground state gives the second. Both the initial excited state and intermediate state can be ionized by the probe pulse to produce the parent ion. In this simple picture, the total ionization yield is proportional to the sum of the populations, N, in the intermediate and initial states, N_1 and N_2, with

$$N = N_1(0)\left[1 + \frac{k_1}{k_2 - k_1}\right] e^{-k_1 t} - \frac{k_1}{k_2 - k_1} N_1(0) e^{-k_2 t}. \tag{3.2}$$

This model would seem to explain the fit to a double exponential with two distinct decay constants. But, when one constrain the fit of the data to Eq. 3.2, and the amplitudes are constrained by k_1 and k_2, the fit cannot capture the dynamics.

Finally, Fig. 3.4 c) is considered where one has two parallel decays (5 level system). The initial excited state, N_1, is said to decay via two channels, N_2 and N_3. From N_2 the system decays into N_4 and from N_3 the system decays into N_5. Again, it is assumed that the total ionization yield is proportional to the sum of the populations, N, in the intermediate and initial states N_1, N_2, and N_3. In this model, the combined signal, N, is

$$\begin{aligned} N = \left[N_1(0) + N_1(0)\frac{k_1}{k_3 - k_1 - k_2} + N_1(0)\frac{k_2}{k_4 - k_1 - k_2}\right] e^{-(k_1+k_2)t} \\ - N_1(0)\frac{k_1}{k_3 - k_1 - k_2} e^{-k_3 t} - N_1(0)\frac{k_2}{k_4 - k_1 - k_2} e^{-k_4 t}. \end{aligned} \tag{3.3}$$

This model, even with the constrained amplitudes, fits our data very well. This model gives values τ_1 = 293 fs, τ_2 = 84 fs, τ_3 = 290 fs, and τ_4 = 70 fs with a χ^2_ν of 1.26.

While this model fits our data well, the real dynamics are undoubtedly much more complicated. These kinetic models show that the double exponential nature we see in the pyrrole data cannot be accurately described by the simple pictures seen in Fig. 3.4 a) and b). This is not surprising, considering the complexity of pyrrole's relaxation dynamics with many states involved.

3.4.1 Derivation of Sequential Kinetic Model

The sequential kinetic model shown in panel b of Fig. 3.4 is attained by deriving the populations as a function of time in states N_1 and N_2. First, the population in N_1 is solved

$$\frac{dN_1(t)}{dt} = -N_1 k_1, \tag{3.4}$$

which becomes

$$N_1(t) = N_1(0)e^{-k_1 t}. \tag{3.5}$$

With the solution to the population as a function of time in N_1 one can solve for the population as a function of time in N_2 starting with

$$\frac{dN_2(t)}{dt} = k_1 N_1(t) - k_2 N_2(t). \tag{3.6}$$

Plug in the solution for N_1 and the expression

$$\frac{dN_2(t)}{dt} = k_1 N_1(0)e^{-k_1 t} - k_2 N_2(t) \tag{3.7}$$

is obtained. Multiplying through by $e^{k_2 t}$ and rearranging the equation one gets

$$e^{k_2 t}\left[\frac{dN_2(t)}{dt}\right] + k_2 e^{k_2 t} N_2(t) = k_1 N_1(0)e^{-k_1 t}e^{k_2 t}. \tag{3.8}$$

Using the fact that

$$\frac{d\left[e^{k_2 t}N_2(t)\right]}{dt} = e^{k_2 t}\left[\frac{dN_2(t)}{dt}\right] + k_2 e^{k_2 t} N_2(t) \tag{3.9}$$

and simplify the left hand side of Eq. 3.8 so that one gets

$$\frac{d\left[e^{k_2 t}N_2(t)\right]}{dt} = k_1 N_1(0)e^{(k_2-k_1)t}. \tag{3.10}$$

Integrating Eq. 3.10 yields

$$e^{k_2 t}N_2(t) = \frac{k_1}{k_2 - k_1}N_1(0)e^{(k_2-k_1)t} + C. \tag{3.11}$$

Using the initial condition that at $t = 0$ the population $N_2 = 0$, gives $C = -\frac{k_1 N_1(0)}{k_2 - k_1}$. Plugging this back into Eq. 3.11 one can write the population of N_2 as a function

of time as

$$N_2(t) = \frac{k_1}{k_2 - k_1} N_1(0) \left[e^{-k_1 t} - e^{-k_2 t} \right] \tag{3.12}$$

The total population that can be ionized by the probe is $N_{Total} = N_1 + N_2$, and can be written as

$$\boxed{N_{Total}(t) = N_1(0) \left[1 + \frac{k_1}{k_2 - k_1} \right] e^{-k_1 t} - \frac{k_1}{k_2 - k_1} N_1(0) e^{-k_2 t}.} \tag{3.13}$$

3.4.2 Derivation of the Parallel Decay Kinetic Model

The parallel decay model in panel c Fig. 3.4 can be derived using the same procedure outlined for the sequential decay model. First, one solves for N_1 and the expression

$$N_1(t) = N_1(0) e^{-(k_1 + k_2)t} \tag{3.14}$$

is obtained. Then, using this solution one solves for the population in N_2

$$N_2(t) = \frac{N_1(0) k_1}{k_3 - k_1 - k_2} e^{-(k_1 + k_2)t} - \frac{N_1(0) k_1}{k_3 - k_1 - k_2} e^{-k_3 t}, \tag{3.15}$$

and the population in N_3

$$N_3(t) = \frac{N_1(0) k_2}{k_4 - k_1 - k_2} e^{-(k_1 + k_2)t} - \frac{N_1(0) k_2}{k_4 - k_1 - k_2} e^{-k_4 t}. \tag{3.16}$$

From this one can calculate the total population that can be ionized by the probe as

$$\boxed{\begin{aligned} N_{Total}(t) = & \left[N_1(0) + \frac{N_1(0) k_1}{k_3 - k_1 - k_2} + \frac{N_1(0) k_2}{k_4 - k_1 - k_2} \right] e^{-(k_1 + k_2)t} \\ & - \frac{N_1(0) k_1}{k_3 - k_1 - k_2} e^{-k_3 t} - \frac{N_1(0) k_2}{k_4 - k_1 - k_2} e^{-k_4 t}. \end{aligned}} \tag{3.17}$$

3.5 Discussion

Even though the two stage kinetic model does not fit the experiment well, the dual-exponential fit implies a two stage process indicating two time-scales for internal conversion, or internal conversion followed by dissociation. In order to determine whether the decay of the parent ion involves dissociation, the fragment ion yield is monitored. The most relevant fragment ion is $C_4H_4N^+$, as dissociation along

the N-H coordinate is the most likely to occur [47, 48, 49]. The calculation of the energy levels along the N-H stretching coordinate indicate that the 4.8 eV probe photon energy should be enough to ionize the molecule as it is dissociating along the N-H coordinate. In addition, the calculations of the molecular orbitals for the neutral and cation along the dissociation coordinate indicate that ionization along the dissociation coordinate is not forbidden by Koopmans correlations. However, in the TOFMS there is no distinct $C_4H_4N^+$ peak, suggesting that there is no dissociation. In order to allow for the possibility of a small amount of $C_4H_4N^+$ being formed but overwhelmed by the $C_4H_5N^+$ signal in the TOFMS, the lower mass end of the $C_4H_5N^+$ peak is binned with a large enough window so we could capture the $C_4H_4N^+$ peak, if it were there. Fig.[3.5] shows that any $C_4H_4N^+$ fragment which is formed has the same decay dynamics as the parent ion ($C_4H_5N^+$), indicating the fragment ion is formed after ionization rather than in the neutral. If the molecule were evolving on a dissociative potential after rapid internal conversion, one would expect to see a delayed peak in the fragment dissociation yield. (A simple model for why we would expect to see a delay in the fragment relative to the parent ion peak will be discussed in Section 3.6: Model for Relative Delay Between the Parent and Fragment Ion Yield from a Dissociative Potential).

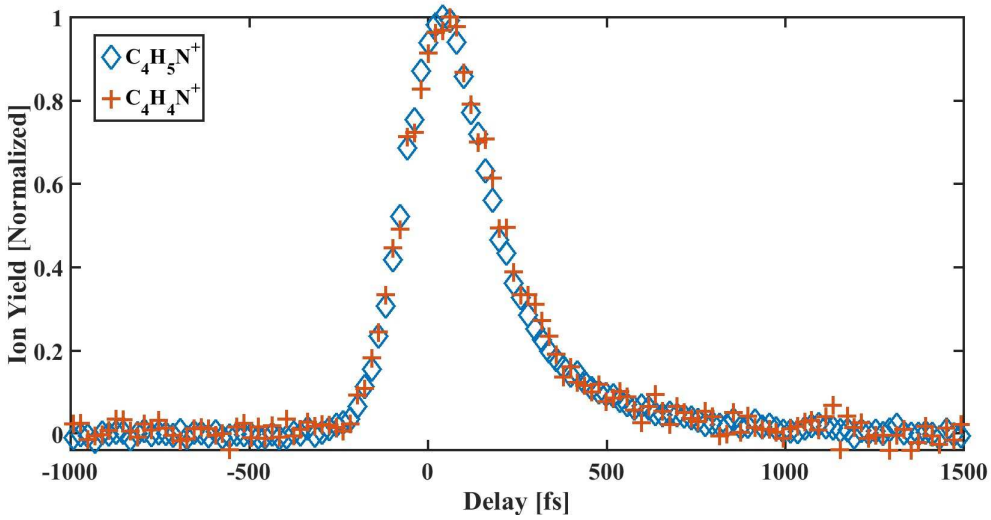

Figure 3.5: Pyrrole parent ion $C_4H_5N^+$ and $C_4H_4N^+$ fragment ion yields as a function of pump-probe delay.

While the calculation of the energy levels along the N-H stretching coordinate suggest that the 4.8 eV of photon energy should be enough to ionize the $C_4H_4N^+$ fragment as it is dissociating, as an extra precaution we performed pump-probe

measurements for higher UV pulse energies, such that one could ionize any neutral fragments formed with an ionization potential higher than the UV photon energy via two photon absorption. These measurements yielded the same results, giving further evidence that there is negligible dissociation compared with internal conversion to the ground state.

The fact that the pyrrole measurements cannot be fitted to a single exponential decay implies that there is not a single rate limiting step in the case of pyrrole. Given that the relaxation of pyrrole to the ground state starting with an internal energy of 8 eV involves many more states than the relaxation after 5 eV excitation, it is not surprising that there is more than one timescale involved.

3.6 Model for Relative Delay Between the Parent and Fragment Ion Yield from a Dissociative Potential

Here a simple model is presented to support the argument that dissociation on an excited potential energy surface after internal conversion would produce a delayed peak in the fragment signal.

In this simple model there are five states. A pump pulse excites a fraction of the population in N_0 to N_1, which represents a non-dissociative electronic state. While the population is in N_1 it can decay into state N_2 (a dissociative state) with some decay rate. A probe pulse can now transfer population from N_2 to N_3 and population from N_2 to N_4. The population that ends up in N_3 represents the parent ion in this model, and the population that ends up in N_4 represents the fragment ion. A schematic of this simple level system can be seen in Fig. 3.6.

The system of differential equations used to describe this system are

$$\begin{aligned}
\frac{dN_0}{dt} &= -N_0(0)e^{-(t/\tau_{pump})^2} \\
\frac{dN_1}{dt} &= +N_0(0)e^{-(t/\tau_{pump})^2} - kN_1 - N_1 e^{-(t-\Delta t)^2/\tau_{probe}^2} \\
\frac{dN_2}{dt} &= kN_1 - N_2 e^{-(t-\Delta t)^2/\tau_{probe}^2} \\
\frac{dN_3}{dt} &= N_1 e^{-(t-\Delta t)^2/\tau_{probe}^2} \\
\frac{dN_4}{dt} &= N_2 e^{-(t-\Delta t)^2/\tau_{probe}^2}.
\end{aligned} \tag{3.18}$$

With this model one can crudely simulate our pump-probe experiment. Taking τ_{pump} and τ_{Probe} to be 100fs and checking to see if a delay in the parent and the fragment ion yields can be seen. In Fig. 3.7 we used a decay rate, k in Eq. 3.18,

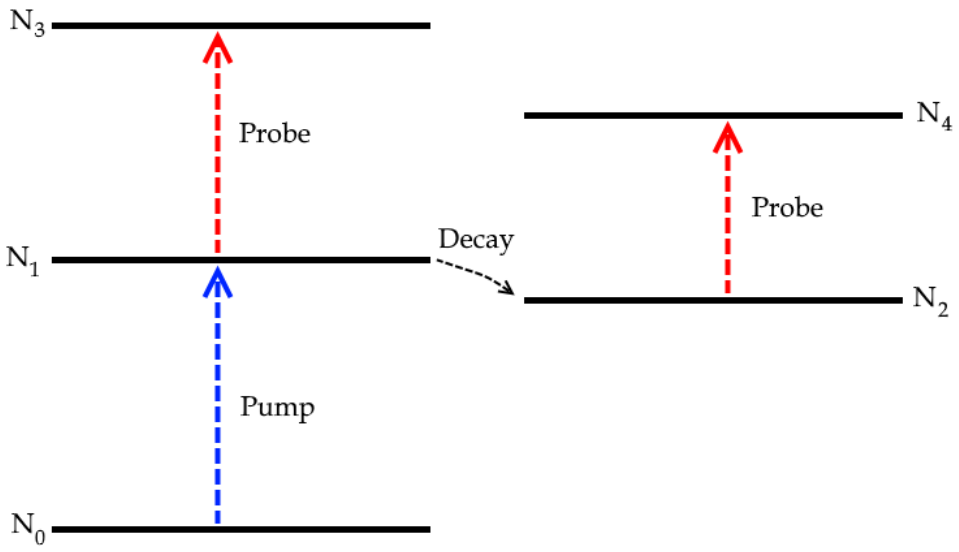

Figure 3.6: Schematic of a simple rate equation model of dissociation dynamics.

from N_1 to N_2 of 1/100 fs, and it is clear that there is a delay in the peaks of the parent and the fragment ion yields.

In Fig. 3.8, this decay constant was increased from N_1 to N_2 to 1/20 fs and there still is a discernible delay between the parent and the fragment ions even with this very fast decay.

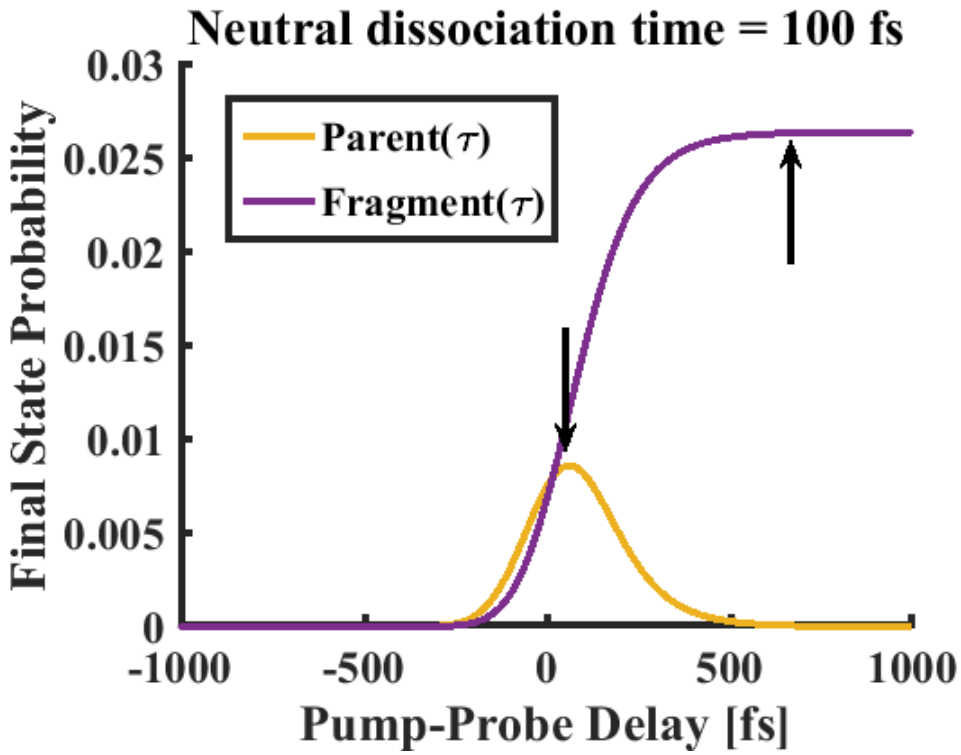

Figure 3.7: A simple rate equation model of the dissociation a decay constant k of 1/100 fs and a pump and probe pulse with 100 fs pulse durations. The arrows indicate the maximum peak position for the parent and the fragment ions.

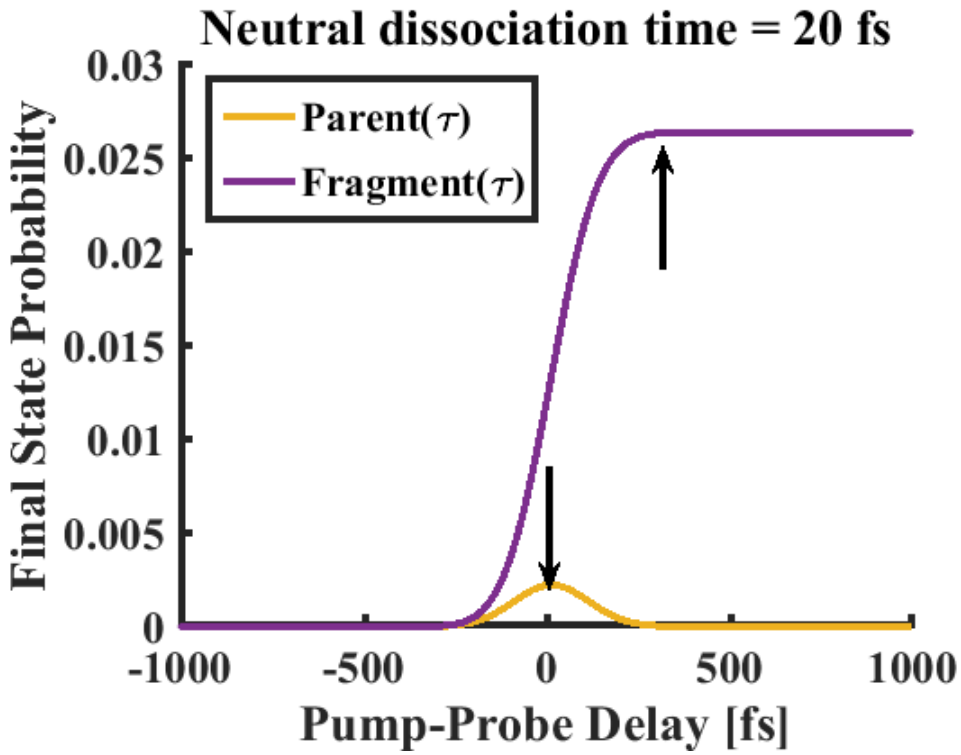

Figure 3.8: A simple rate equation model of the dissociation a decay constant k of 1/20 fs and a pump and probe pulse with 100 fs pulse durations. The arrows indicate the maximum peak position for the parent and the fragment ions.

3.7 Conclusion

We make use of a newly developed VUV-pump UV-probe apparatus to study the ultrafast relaxation of highly excited pyrrole. Electronic structure calculations help interpret the measurements, which show a two step decay process with time constants of 68 fs and 253 fs. While earlier measurements that pumped the first absorption band at around 5 eV found a mix of dissociation and internal conversion, we find that the decay of the excited state and our ionization signal is driven largely by rapid internal conversion to the ground state.

Chapter 4

Vibrationally Assisted Below-Threshold Ionization

4.1 Introduction and Motivation

The conversion of electronic potential energy into nuclear kinetic energy is one of the most ubiquitous features of photoexcited molecular dynamics. As a wave packet moves down an excited potential energy surface following photoabsorption, electronic potential energy is converted into nuclear kinetic energy. In a diatomic molecule, kinetic and potential energy are exchanged every half period for motion in a bound state. This exchange can be observed in many time resolved spectroscopies [77, 78]. However, in larger polyatomic systems with many degrees of vibrational freedom, the conversion of nuclear kinetic energy into electronic potential energy is much harder to observe because the nuclear kinetic energy is distributed over many modes.

The UV pump (260 nm, 4.77 eV) VUV probe (156 nm, 7.94 eV) time resolved photoionization apparatus allows one to study this conversion of vibrational kinetic energy into electronic energy via vibrationally assisted below threshold ionization. I consider the ionization of 1,3-cyclohexadiene (CHD, C_6H_8), whose ionization potential value is slightly above the photon energy of 7.94 eV. The excited state dynamics of CHD has been the subject of intense study, [79, 80, 81, 82, 83], and its neutral excited state dynamics are well understood. Initial excitation to the first bright state (S_1) is followed by rapid internal conversion to the ground states, with some fraction of the molecules isomerizing to form 1,3,5-hexatriene (HT). It is well established that there are no local minima on the excited state, and after about 200 fs there is no longer any probability of finding the molecule in an excited state. Thus,

with an ionization potential (IP) of 8.21 eV[1], it is a prime candidate to explore vibrationally assisted below threshold ionization. After excitation and internal conversion, there is about 5 eV of energy in the vibrationally hot ground state. If some of this energy can be converted into electronic potential energy, then this would allow for below threshold ionization.

I contrast the measurements in CHD with similar measurements for cis,cis-1,3-cyclooctadiene (cis,cis-COD, C_8H_12), which has similar relaxation dynamics to CHD, but a higher IP of 8.58 eV.

4.2 Experimental Apparatus

As outlined in Chapter 2, a Ti:Sapphire laser (1.2 mJ, 1 kHz, 30 fs, 780 nm) is used to generate ultrafast UV and VUV pulses. The cross-correlation time measured in ethylene for the UV and VUV in these experiments is 200 fs. In conjunction with a time-of-flight mass spectrometer (TOFMS), these pulses are used to perform pump-probe ion yield measurements on CHD and cis,cis-COD. Gas-phase CHD and cis,cis-COD molecules are injected into the vacuum chamber as a room temperature effusive molecular beam.

4.3 Computational Methods

Conical intersections (CIs) between S_0 and S_1 were calculated by the collaborators Pratip Chakraborty and Spiridoula Matsika for cis,cis-COD using the State Averaged Complete Active Space Self Consistent Field (SA-CASSCF) method and the cc-pVDZ basis set. An active space of 4 electrons in 4 orbitals (4,4) was used and 2 states were averaged (SA2-CASSCF). Linear interpolations in internal coordinates at the SA4-CASSCF level were used to connect cis,cis-COD to the two CIs found, and the CIs to the products. The conical intersection for CHD is taken from previous work [83]. Linear interpolations between CHD and the CI and HT and the CI were computed using CASSCF(6,6) with the cc-pVDZ basis set and averaging 3 states. The computational packages Gaussian [84] and COLUMBUS [85] were used for the CASSCF calculations.

Franck-Condon (FC) factors are defined as $\left|\langle\psi_{v_{\text{final}}}|\psi_{v_{\text{initial}}}\rangle\right|^2$, where $\psi_{v_{\text{initial}}}$ and $\psi_{v_{\text{final}}}$ are the initial and final vibrational states. The FC factors for the molecular systems are important for our interpretation of the experimental results, as will be

[1]The IPs used are all calculated at the EOM-IP-CCSD/6-311+G(d) level using Q-Chem. The calculated and experimentally measured values are listed in Table 4.1. We do not have measured IPs for all reactants, so we use the calculated values for consistency.

discussed later in the Chapter. For the FC factor calculations, S_0 and the D_0 were optimized at the B3LYP/6-31G(d) and UB3LYP/6-31G(d) levels, respectively, for both molecules. Frequency calculations were performed at the same level of theory in order to obtain the normal modes. FC factors between S_0 and D_0 for all the molecules were calculated using ezSpectrum 3.0 code [86]. ezSpectrum 3.0 can calculate the FC factors between the initial and target vibrational state wavefunctions using two approximations: parallel normal modes approximation and Duschinsky rotations of the normal modes as full-dimensional integrals. They have used the latter method to do the calculations. The S_0 and D_0 minima for a molecule were used as initial and target electronic states, respectively. As we were interested to see ionization from the hot vibrational levels of S_0 to the lowest lying vibrational levels of D_0, our collaborators kept the energy threshold for S_0 at 4.20 eV, while that for D_0 was kept at 0.60 eV. The maximum vibrational excitations in the initial state and the target state were taken as 5 and 2 respectively in order to keep the calculations tractable. The spectrum intensity threshold was set at 10^{-7}. The optimizations and frequency calculations were performed using Q-Chem software [74], and MacMolPlt [87] was used to visualize the molecules and normal modes. IPs for all systems were calculated at the EOM-IP-CCSD/6-311+G(d) level using Q-Chem.

4.4 Experimental Results

UV pump VUV probe experiments were performed on CHD, and the results for fragment $C_6H_7^+$ can be seen in Fig. 4.1. In the UV pump VUV probe measurements conducted, the most prominent signal is from the parent ion ($C_6H_8^+$). However, since the parent ion can be formed by two photon absorption from the pump pulse, there is substantial background in the pump-probe signal. Therefore, the attention was focused on the $C_6H_7^+$ fragment, which is background free, but can still be formed by single photon absorption from each of the pump and probe pulses. The appearance energies (AEs) of the fragments in CHD are taken from the electron-impact measurements in [88]. The total energy available from absorption of both UV and VUV pulses is 12.7 eV, so energetically it is possible to form the parent ion, $C_6H_8^+$, as well as $C_6H_7^+$ (AE = 10.82 eV).

Figure 4.1 shows the $C_6H_7^+$ yield as a function of pump probe delay. The attention was focused on the difference in ion yield between positive and negative delays. At negative time delays the VUV pulse precedes the UV pulse, and vise versa for positive time delays. The pump-probe data shows a cooperative UV pump VUV probe signal in $C_6H_7^+$ at time zero. After time-zero, when the UV pulse has been incident on the molecule and it has undergone internal conversion down to the ground state (where the ionization potential of both isomers is above the photon en-

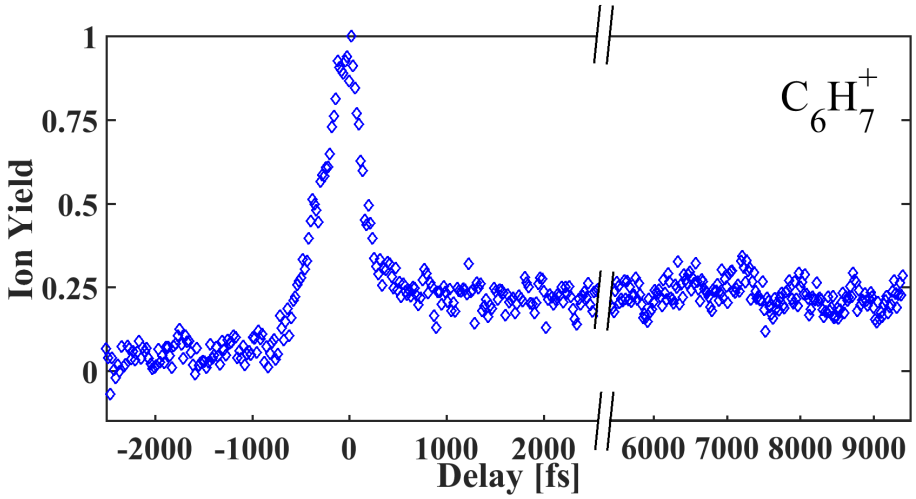

Figure 4.1: CHD pump probe data for $C_6H_7^+$ fragment.

ergy of the probe) one still measures a yield was still measured which is about 20% of the yield in ionizing from the excited state (for which the probe is well above the ionization potential) near zero time delay.

For comparison, UV pump VUV probe experiments were also performed on a similar molecule, cis,cis-COD. The AEs of cis,cis-COD are not available, but binning over all possible fragments in the TOFMS a pump-probe signal is seen for the parent, $C_8H_{12}^+$, and the fragments $C_7H_9^+$, $C_6H_8^+$, and $C_5H_7^+$. In contrast to CHD, none of the resulting products from the UV pump VUV probe scan show any sign of a ledge (below threshold ionization) after time-zero. The results of the pump probe measurements can be seen in Fig. 4.2, where the fragment $C_6H_8^+$ has the most prominent signal.

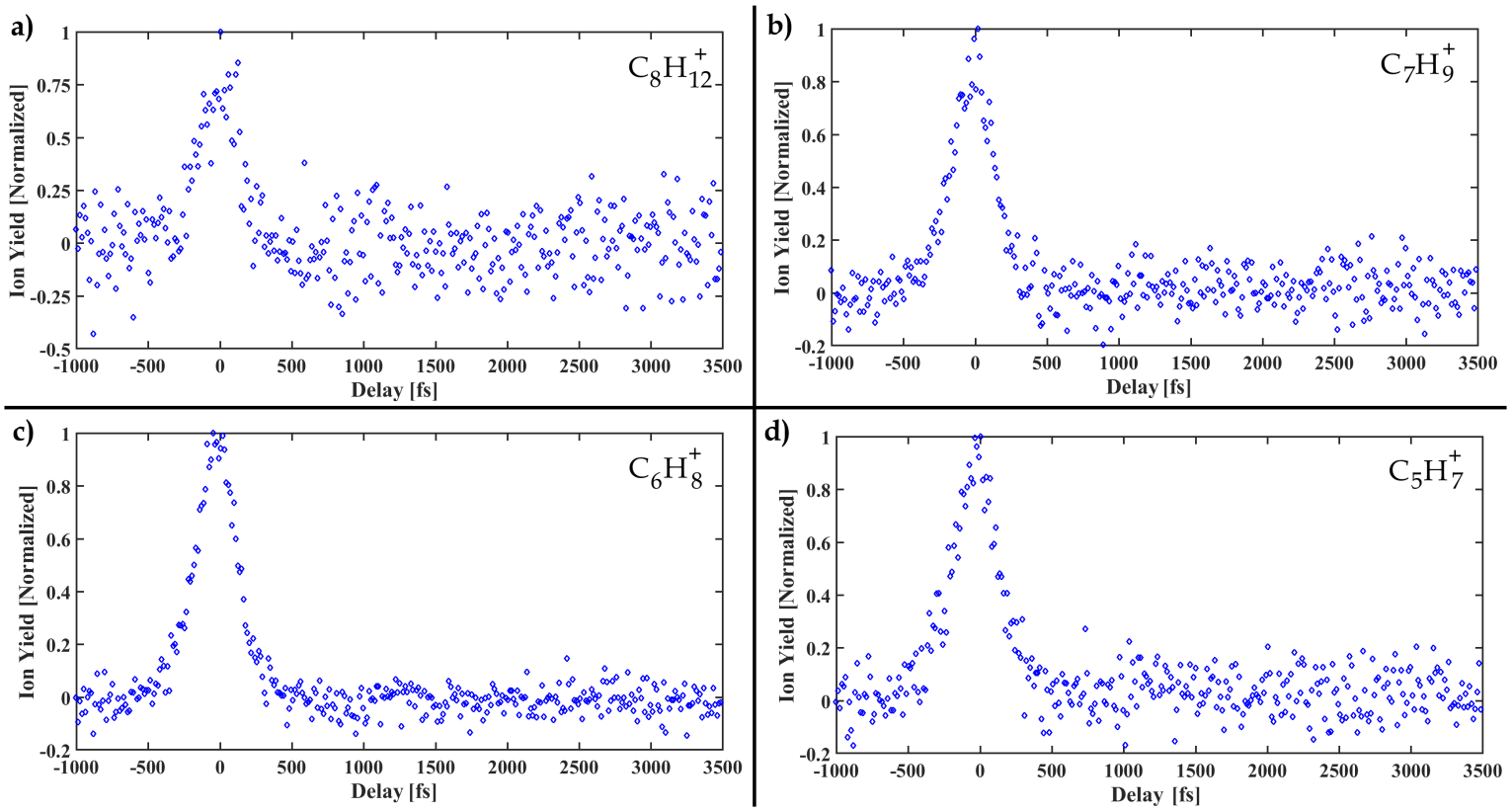

Figure 4.2: cis,cis-COD pump probe data for a) $C_8H_{12}^+$ parent, b) $C_7H_9^+$ fragment, c) $C_6H_8^+$ fragment, and d) $C_5H_7^+$ fragment ions.

4.5 Calculations

In order to interpret the persistence of a nonzero ionization yield for CHD at long positive time delays, the excited state dynamics have to be considered in more detail and a number of calculations have to be performed. As noted above, CHD is a well studied molecule, and its relaxation dynamics after UV pumping have been considered in detail [79, 80, 81, 82, 83]. The UV pump pulse launches a wave packet on the bright S_1 state (see Figure 4.7), which quickly changes character diabatically because of an avoided crossing with the dark S_2 state.

From the S_1 state, two CIs have been identified between S_1 and S_0, with one being symmetric and the other asymmetric. According to the reference [82], the asymmetric CI dominates the relaxation dynamics. Fig. 4.3 a) shows a diagram of the CI between the S_1 and S_0 states in CHD. Once on S_0 again, the molecule can go back to the original equilibrium neutral geometry in the ground state, CHD configuration, or isomerize into 1,3,5 hexatriene (HT). The branching ratio for forming ground state CHD versus HT has been measured to be 7:3, [80] (represented in the figure as the quantum yield ϕ).

The excited state dynamics for cis,cis-COD after being pumped in the UV have also been studied. UV pump IR probe femtosecond measurements have been performed on COD by Fuss et. al. in [89], and nanosecond UV laser irradiation of cis,cis-COD was performed in [90]. Our collaborators performed electronic structure calculations on cis,cis-COD and identified two possible CIs that can lead to internal conversion back into its ground state, isomerization into cis-bicyclo[4,2,0]oct-7ene (BCO), or isomerization cis,trans-1,3-cyclooctadiene (cis,trans-COD). cis,cis-COD and cis,trans-COD have several conformers. They used the lowest energy conformer in each case, which has a population of 70% and 99%, for cis,cis-COD and cis,trans-COD, respectively. In Fig. 4.3 b) and c) they identify the reaction pathways for the different CIs, the geometry of the molecule at the CIs, and the relative quantum yields to the different photochemical products, ϕ, [89]. For cis,cis-COD, as in CHD, there are similar neutral state dynamics that lead to ultrafast internal conversion and isomerization after excitation with the UV pump.

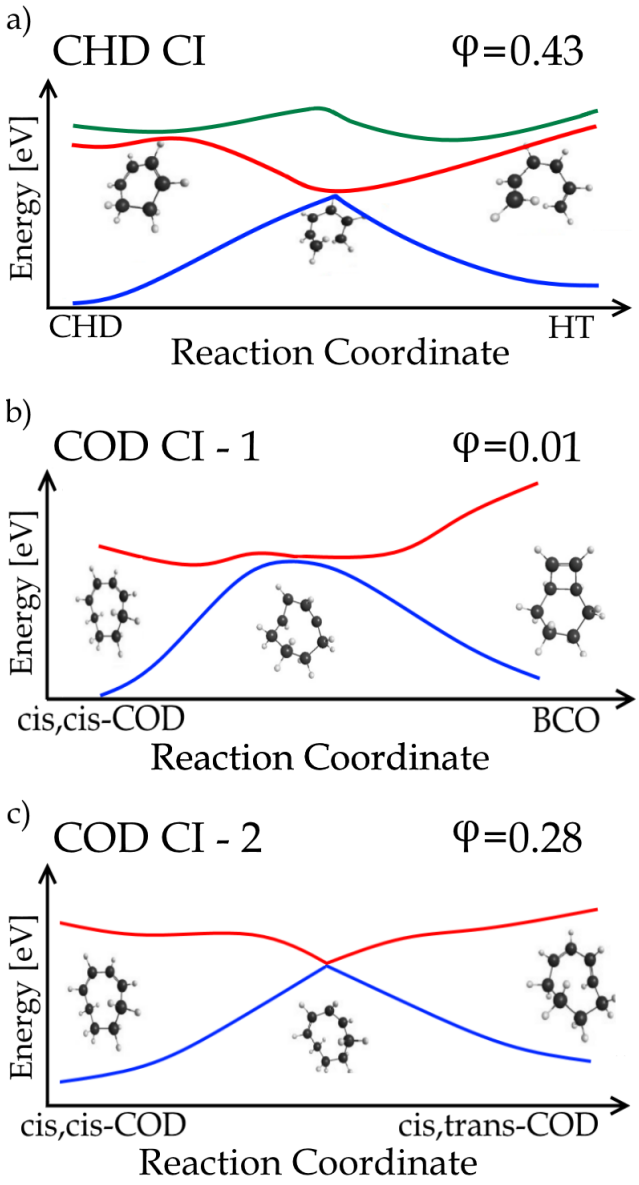

Figure 4.3: Potential energy surfaces (PES) and relevant CIs for a) CHD that can lead to isomerization into HT, b) cis,cis-COD that can lead to isomerization to BCO, and c) cis,cis-COD that can lead to isomerization to cis,trans-COD. Where ϕ indicates the quantum yield of the photochemical products [80, 89]. Blue [bottom curve] $\Rightarrow S_0$, Red [middle curve in a) and top curve in b) and c)] $\Rightarrow S_1$, and Green [top curve in a)] $\Rightarrow S_2$.

In Table 4.1, the calculated vertical IPs are listed , calculated adiabatic IPs, and the average of measured values for the IPs of all the relevant products. In Fig. 4.4, a cartoon of a potential energy surface depicting the difference between vertical and the adiabatic ionization potentials is shown. The vertical IP is measured as the energy required to transition from the minimum of the ground state, S_0, to the first ionic state, D_0. The adiabatic IP is the energy difference between the minimum of S_0 to the minimum of D_0.

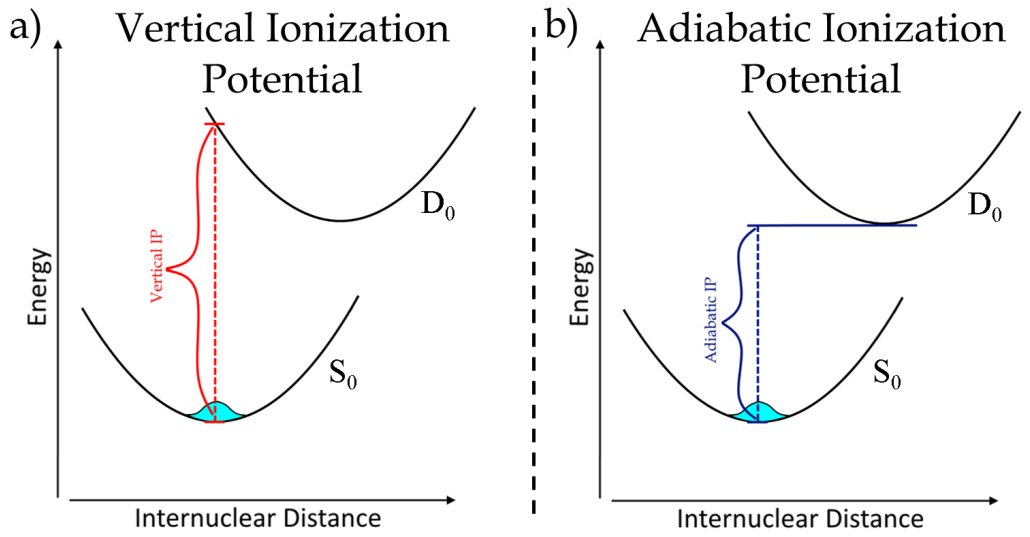

Figure 4.4: Cartoon of a potential energy surface a) depicting the vertical ionization potential and b) depicting the adiabatic ionization potential.

From Table 4.1 one can see that the calculated vertical transition IPs are within 0.1 eV of the measured values. All of the vertical IPs of the possible products are at least 0.26 eV or more above the probe photon energy. This indicates that the signal in CHD at long times is not simply due to formation of an isomer with an ionization potential lower than the probe photon energy.

Finally, in order to understand how ground state vibrations can lead to below threshold ionization, the FC factors are looked at between excited vibrational levels in the ground state, S_0, and lower lying vibrations in the ground state of the cation, D_0. The aim is to identify high lying vibrational levels in S_0 that have a good FC overlap with low lying vibrational levels in D_0, that can be ionized with 7.94 eV of photon energy.

Fig. 4.5 shows the calculated FC factors squared for CHD, HT, cis-cis COD, cis,trans-COD, and BCO. The calculated adiabatic IPs are used in each case. The x-axis is the energy difference between the vibrational levels in S_0 and D_0. The y-

Molecule	Calculated Vertical IP [eV]	Calculated Adiabatic IP [eV]	Measured IP [eV]
1,3-cyclohexadiene (CHD)	8.21	8.04	8.26 [88, 91, 92, 93, 94, 95, 96]
1,3,5-hexatriene (HT)	8.37	8.12	8.31 [88, 97, 98, 99]
cis,cis-1,3-cyclooctadiene (cis,cis-COD)	8.58	8.26	8.68 [94]
cis,trans-1,3-cyclooctadiene (cis,trans-COD)	8.42	7.98	N.A.
cis-bicyclo[4,2,0] oct-7ene (BCO)	9.13	8.87	N.A.

Table 4.1: Calculated vertical IPs, adiabatic IPs, and the average measured ionization potentials for CHD and cis,cis-COD and their relevant isomers

axis is the FC factors squared for the different vibrational levels. The VUV photon energy is indicated by a red [vertical] line in all the subplots in Fig. 4.5.

Fig. 4.5 a) shows the FC factors between vibrational levels in the ground state, S_0, and the first ionic state, D_0, for CHD. Note that a significant fraction of the vibrational levels in the hot S_0 can be ionized to D_0 with the probe pulse - those to the left of the red line. This is also true for HT, but in contrast, note that a smaller fraction of vibrational levels can be ionized for cis,cis-COD, cis,trans-COD, and BCO. The magnitudes of the FC factors are also much smaller in cis,cis-COD, cis,trans-COD, and BCO.

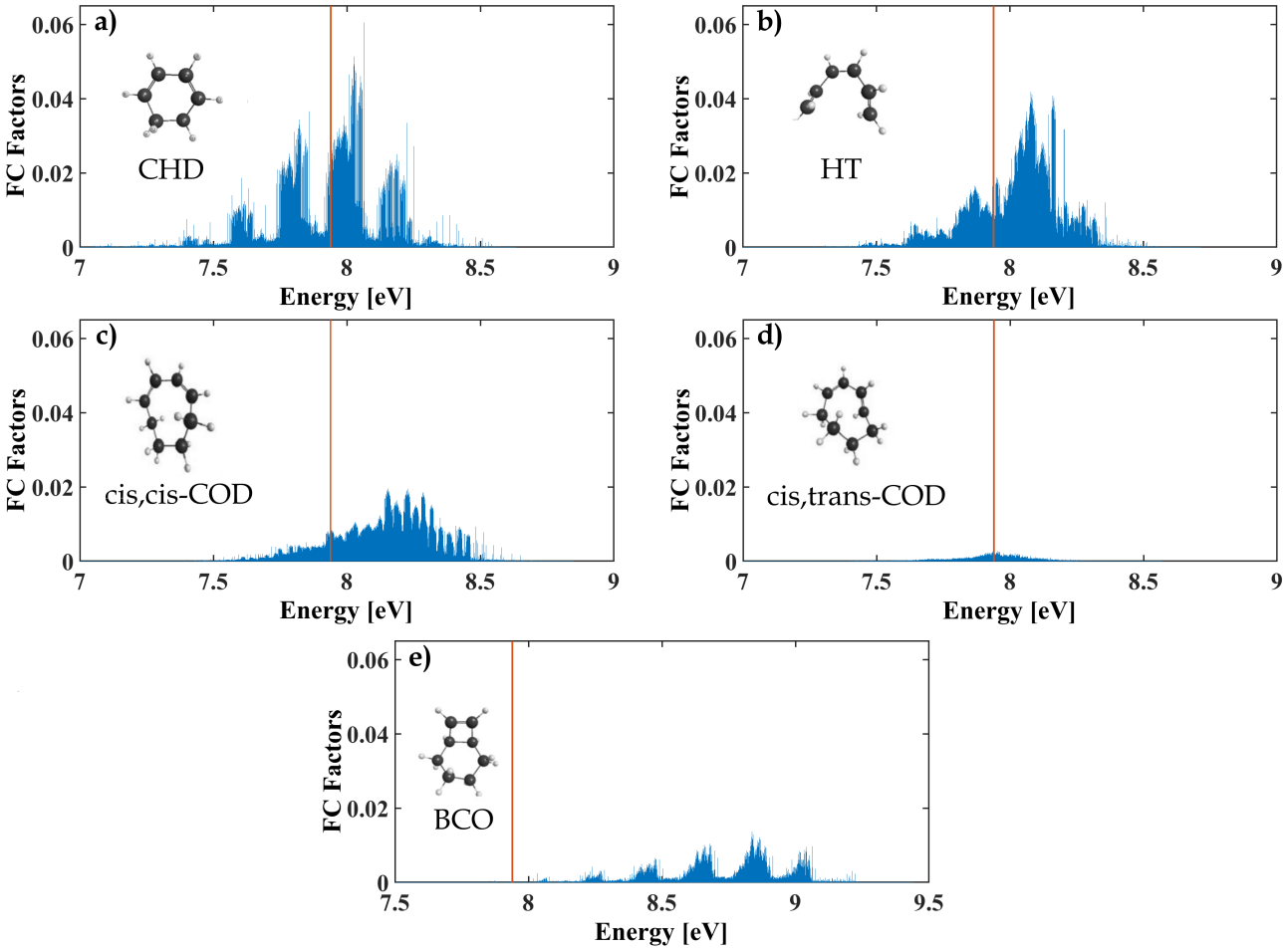

Figure 4.5: Franck-Condon factors squared ($|FCF|^2$) for vibrational levels in a) CHD, b) HT, c) cis,cis-COD, d) cis,trans-COD, and d) BCO between their ground states, S_0, and first ionic states, D_0. The red [vertical] line in each of the subplots indicates the probe photon energy.

4.5.1 CHD Relaxation Geometries

Fig. 4.6 shows the CHD geometries at the S_0 minimum, the asymmetric CI, symmetric CI, and after isomerization into HT. The carbons are labeled one through six in the S_0 geometry.

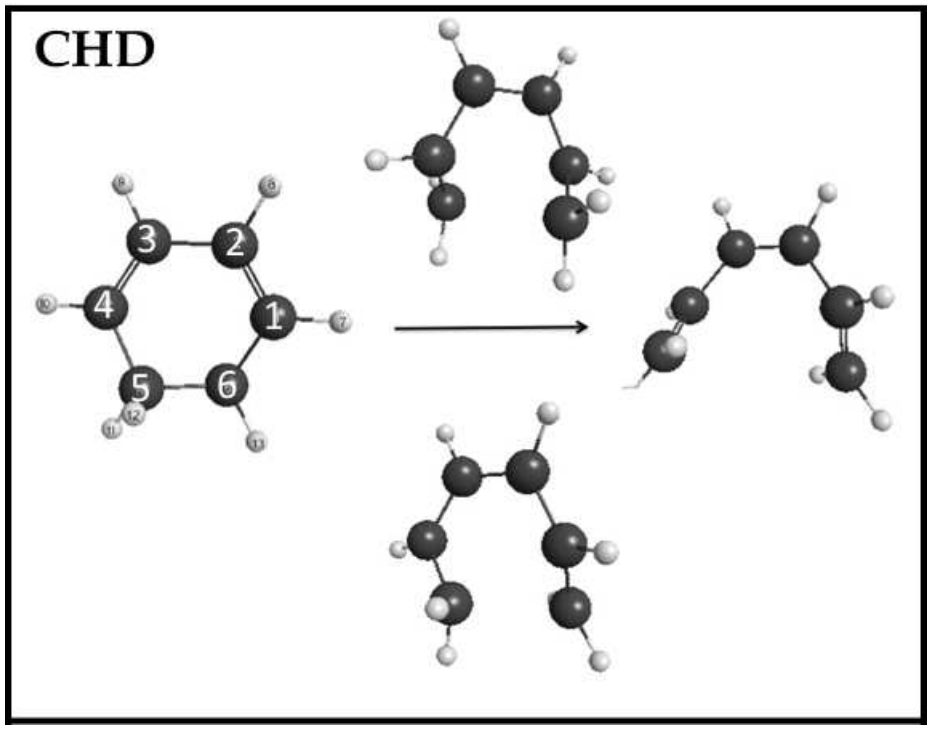

Figure 4.6: CHD geometry at the S_0 minimum (left), the asymmetric CI (top), symmetric CI (bottom), and after isomerization into HT (right)

As the molecule goes through the symmetric and asymmetric CIs the position of the carbons is documented in Table 4.2. The RMS displacement of the carbons going through the asymmetric stretch is 0.68 Å, and the RMS displacement of the carbons going through the symmetric stretch is 1.20 Å. If the molecule isomerizes into HT the RMS displacement of the carbons is 1.85 Å.

Table 4.3 shows the calculated bond lengths for S_0 and D_0. They show that going from S_0 to D_0 the single bonds compress and the double bonds expand.

	1-2 [Å]	2-3' [Å]	3-4' [Å]	4-5' [Å]	1-6' [Å]	react(5-6) [Å]	RMS D [Å]
CHD	1.35	1.46	1.35	1.51	1.51	1.53	–
Asymmetric CI	1.43	1.41	1.38	1.448	1.44	2.19	–
Symmetric CI	1.44	1.38	1.44	1.49	1.49	2.72	–
HT	1.47	1.35	1.47	1.34	1.34	3.35	–
Difference on bonds lengths from CHD							
Asymmetric CI	0.08	-0.05	0.03	-0.06	-0.07	0.66	0.68
Symmetric CI	0.09	-0.08	0.09	-0.02	-0.02	1.19	1.20
HT	0.12	-0.11	0.12	-0.17	-0.17	1.83	1.85

Table 4.2: Calculated C-C bond movement for CHD

	1-2 [Å]	**2-3' [Å]**	**3-4' [Å]**	**4-5' [Å]**	**1-6' [Å]**	**react(5-6) [Å]**
CHD D_0	1.39	1.42	1.39	1.48	1.48	1.54
CHD S_0	1.35	1.46	1.35	1.51	1.51	1.53
$\mathbf{D_0 - S_0}$	0.04	-0.05	0.04	-0.03	-0.03	0.01

Table 4.3: Calculated bond lengths for S_0 and D_0

4.5.2 Vibrational Modes of CHD

Table 4.4 lists the vibrational modes in CHD. The geometry optimization and frequency calculations were done with B3LYP/6-31G(d). Mode 27, in bold in Table 4.4, is the mode associated with the coordinate where high lying vibrational levels in S_0 having a good FC overlap with low lying vibrational levels in D_0, and can lead to ionization with a 7.94 eV probe. (More discussion in the next section).

Vibrational Mode Number	**Frequency [cm^{-1}]**	**Vibrational Mode Number**	**Frequency [cm^{-1}]**
1	191	19	1214
2	302	20	1281
3	481	21	1370
4	520	22	1379
5	573	23	1419
6	675	24	1456
7	766	25	1500
8	782	26	1511
9	859	**27**	**1660**
10	940	28	1725
11	971	29	2981
12	973	30	2992
13	990	31	3076
14	1013	32	3076
15	1054	33	3166
16	1078	34	3173
17	1183	35	3188
18	1201	36	3197

Table 4.4: Vibrational Modes of CHD

4.6 Discussion

The fact that the bulk of the FC factors lie to the right of the red line in Fig. 4.5 for cis,cis-COD, cis,trans-COD, and BCO, in addition to the fact that they are much smaller than for CHD or HT is consistent with the measurements of hot ground state ionization for CHD, but no hot ground state ionization for COD.

The FC factors in Fig. 4.5 a) have a regular structure with a period of $\sim$0.2 eV, corresponding to the frequency of C-C stretching. This suggests that if C-C stretching motion is activated during internal conversion, then it can lead to the vibrationally assisted below threshold ionization. One considers whether the passage of the molecule through the relevant CI during internal conversion could excite this motion. Figure 5 shows the normal mode which is mainly responsible for the vibrational progression seen in the FC factors for CHD identified by our collaborators. This mode involves the symmetric stretching of both double bonds in the molecule. The figure also shows the derivative coupling vector at the conical intersection between S_1 and S_0. The motion indicated by this vector is also mainly along the stretching motion of the C-C bonds, and it will be activated as the wavepacket passes through the CI. The similarity between the coupling vector and the normal mode indicates that much of the electronic energy converted to vibrational energy after passing through the CI will be excitation along the normal mode shown. Another indication of the vibrational excitation along the C-C modes is given by calculating the RMS deviation of the six C-C bonds in CHD between the FC region and the CI.

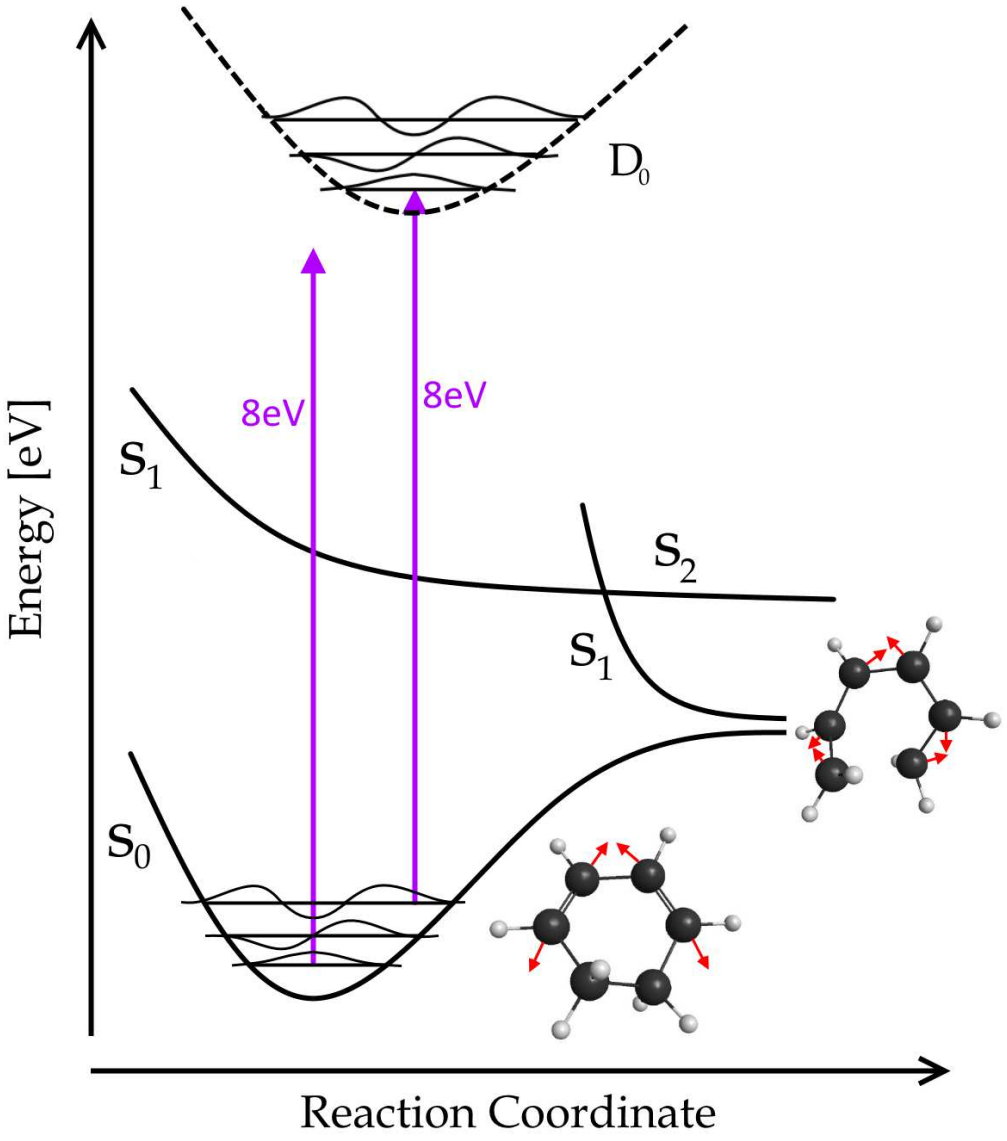

Figure 4.7: In S_0 and D_0, vibrational levels and wavefunctions are sketched to illustrate the Franck-Condon principle that can lead to below threshold ionization. CHD energy level cartoon illustrating the FC overlap argument for vibrationally assisted ionization. At the conical intersection between S_0 and S_1 is a picture of the molecule with the motion of the carbons along the derivative coupling vector indicated. Next to S_0, is a picture indicating the normal mode motion associated with the coordinate for which the high lying vibrational levels in S_0 have good FC overlap with low lying vibrational levels in D_0.

In Section 4.5.1: CHD Relaxation Geometries, are the calculated C-C bond lengths at the S_0 minimum , the symmetric CI, the asymmetric CI, and HT geometries. The RMS displacement of the carbons at the asymmetric CI from their initial S_0 minimum geometry is 0.7 Å, indicating that there is indeed substantial C-C stretching activated during passage through the CI. The bond lengths for S_0 and the D_0 are also calculated. Going from S_0 to D_0, the double bond expand while the single bonds compress, and this is reflected in the progression seen in the FC factors associated with vibrational mode 27, shown in Fig. 4.7, at 1660 cm^{-1} (0.2 eV, see Section 4.5.2: Vibrational Modes of CHD) .

In cis,cis-COD, cis,trans-COD, and BCO the FC factors at 7.94 eV are just too small to see significant below threshold ionization.

Before concluding, another possibility that is considered in order to interpret the results is excitation of vibrationally hot CHD into a neutral Rydberg state by the probe, from which the molecule can autoionize as a result of the excess vibrational energy. The absorption spectrum of CHD can be found in [100, 101, 102], and there is a strong absorption band at 7.94 eV. The question then is whether absorption to such a high excited neutral state can lead to autoionization. In order to address this question the character of the states was examined that lead to the strong absorption at 7.94 eV, and the probability of ionization for states 0.1 - 0.3 eV below threshold was considered. In [103] it is indicated that autoionization of anthracene and naphthalene with 1-2 eV of vibrational energy only takes place for energies up to 0.1 eV below the ionization threshold. Furthermore, the character of the state which dominates the absorption at 7.94 eV is that of a valence state ($8^1A(V_3)$). This would require internal conversion prior to autoionization, and the internal conversion would lead to lower electronic states, which are even less likely to autoionize. Therefore, it is argued that the ionization yield that is measured for positive pump-probe delays is dominated by vibrationally assisted ionization rather than Rydberg excitation followed by autoionization.

4.7 Conclusion

Below threshold ionization of 1,3-cyclohexadiene is observed, which is interpreted in terms of vibrationally assisted ionization, where vibrational energy is converted to electronic energy. This is facilitated by the excitation of C-C stretching vibrations, which are activated during internal conversion from the photo-excited state down to the ground state.

Chapter 5

Strong and Weak Field Ionization in Pump-Probe Spectroscopy

5.1 Introduction

In recent years, there has been significant debate about the relative merits of strong-field ionization (SFI), which involves multi-photon absorption, versus weak-field ionization (WFI), where a single photon is absorbed, as probes of excited state dynamics in molecules.

As mentioned in Chapter 1, SFI has the advantage of enabling one to use wavelengths with relatively low photon energies, which tend to be easier to generate, have less material dispersion to compensate for, and are readily transmitted by most standard window material. In SFI, one can increase the intensity of the laser pulse in order to drive higher order multiphoton processes, therefore one does not have to worry about effectively "running out" of photon energy as a wave packet undergoes internal conversion. However, calculations of an N electron molecule in a strong field are computationally expensive and difficult to carry out for multiple molecular geometries.

Within the SFI regime there are two subclassifications of ionization. The first of these two subclassifications is multiphoton ionization. In multiphoton ionization one can use the same general picture used in WFI, where the electromagnetic field is quantized. Instead of absorbing a single photon to ionize the system, multiple photons can be absorbed. As in WFI, the energy difference between what is required to ionize the system and the energy that is absorbed from the field is carried away by the electron in the form of translational kinetic energy. The second of these two subclassifications is tunnel ionization. In tunnel ionization the external field is assumed to be classical, and that the field is intense enough to tilt the binding po-

tential of the system. If the tunneling frequency of the electron wave function is much larger than the frequency of the external field, then the electron has the ability to tunnel out and subsequently ionize the system.

On the left-hand side of Fig. 5.1 is a cartoon showing SFI in the tunneling regime. The figure tries to show that in the SFI regime the ionization is not necessarily of the valence electron. As derived in [104], the tunnel ionization rate goes exponentially with the ionization potential of the system. Therefore, if the ionization potential for different electronic states are only slightly different then there can be significant contributions to the ionization from multiple states. Hence, multiple electrons are circled in gray to indicate that more than one electron can contribute to the ionization.

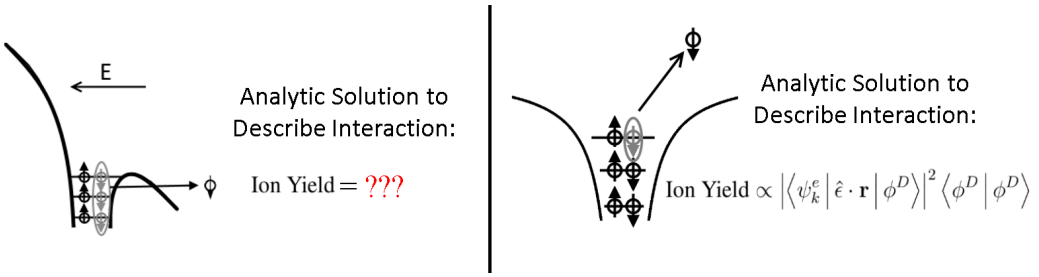

Figure 5.1: A cartoon depicting SFI on the left-hand side and WFI on the right-hand side.

The right-hand side of Fig. 5.1 is a cartoon depicting WFI, where there is clearly no significant stark shifting of the system. The advantage of WFI as a probe of molecular dynamics is that one can write an solution to describe the interaction using perturbation theory that accurately captures the ionization dynamics, and can be calculated with reasonable computational time. As mentioned in Chapter 1 and shown in Fig. 5.1, the total ion yield for each molecular geometry in the WFI perturbative regime produced by a dynamics calculation can be expressed in terms of a Dyson orbital as:

$$\text{Ion Yield} \propto \left|\left\langle \psi_k^e \right| \hat{\epsilon} \cdot \mathbf{r} \left| \phi^D \right\rangle\right|^2 \left\langle \phi^D \right| \left. \phi^D \right\rangle, \tag{5.1}$$

where $\hat{\epsilon}$ is the polarization direction of the light, $\mathbf{r}$ the position operator, ψ_k^e the free (continuum) electron wave function with momentum k, and $\left\langle \phi^D \right| \left. \phi^D \right\rangle$ is the Dyson norm. The figure also shows the in the WFI regime, with energies just above the ionization potential, one ionizes a valence electron, indicated with the gray circle. However, the generation and implementation of the appropriate wavelengths (photon energies) can be challenging, material dispersion become significantly worse as one moves towards the VUV, VUV pulses must be generated and propagated in

vacuum, and there are few materials that can be used to transmit these wavelengths. The fixed energy of the probe can cause one to effectively "run out" of photon energy and not allow one to follow the full dynamics from excited states back down to the ground state. Also, molecules can have strong Rydberg absorption bands that have larger oscillator strengths than the lower lying transitions one wants to study, thus making the analysis more difficult.

The goal of the work presented in this Chapter is to do a detailed comparison of SFI and WFI on the same molecule with the same detection techniques. Two different kinds of excited state dynamics are considered, internal conversion and dissociation, in two different molecules, and the measurements are compared directly with high level dynamics calculations in order to assess the relative strengths and weaknesses of the two approaches. Earlier work found significant differences between multi-photon ionization with a 1.55 eV probe and single photon ionization with a 14 eV probe [105]. The goal of this previous work was to determine which regime was more sensitive to molecular dynamics, whereas here the goal is to demonstrate which approach can be best compared quantitatively with calculations of the excited state dynamics.

A comparison of WFI and SFI is carried out by following dissociation in diiodomethane, CH_2I_2, and internal conversion in uracil. The excited state dynamics of both diiodomethane and uracil have been the subject of intense theoretical and experimental studies [107, 108, 109, 110, 111, 112, 113, 114, 115, 116, 117, 118, 119, 120, 106, 121, 122, 123, 124, 125, 126, 127]. Fig. 5.2 shows one dimensional representations (cartoons) of the relevant potential energy surfaces for both molecules. In CH_2I_2 (panel a of Fig. 5.2), earlier studies concluded that after being pumped with UV light at 260 nm, the molecule undergoes direct dissociation [122], producing CH_2I and I fragments. For uracil (panel b of Fig. 5.2), excitation with a pump pulse centered at 260 nm promotes the molecule to the first bright excited state, S_2, which is predominantly of $\pi\pi^*$ character near the ground state minimum (Franck Condon point). From S_2, the molecule can undergo radiationless decay via two seams of conical intersections S_2/S_1 and S_1/S_0. It is generally accepted that there is population trapping on S_1, while the extent of trapping on S_2 depends on the barrier on that surface. While intersystem crossing has been found to play a role in the relaxation dynamics of uracil [120], triplet states are not shown in the cartoon for the sake of simplicity.

5.2 Experimental Setup

These measurements are conducted with the use of a time-of-flight mass spectrometer (TOFMS). UV (260 nm, 4.8 eV) and VUV pulses (156 nm, 7.95 eV) are used

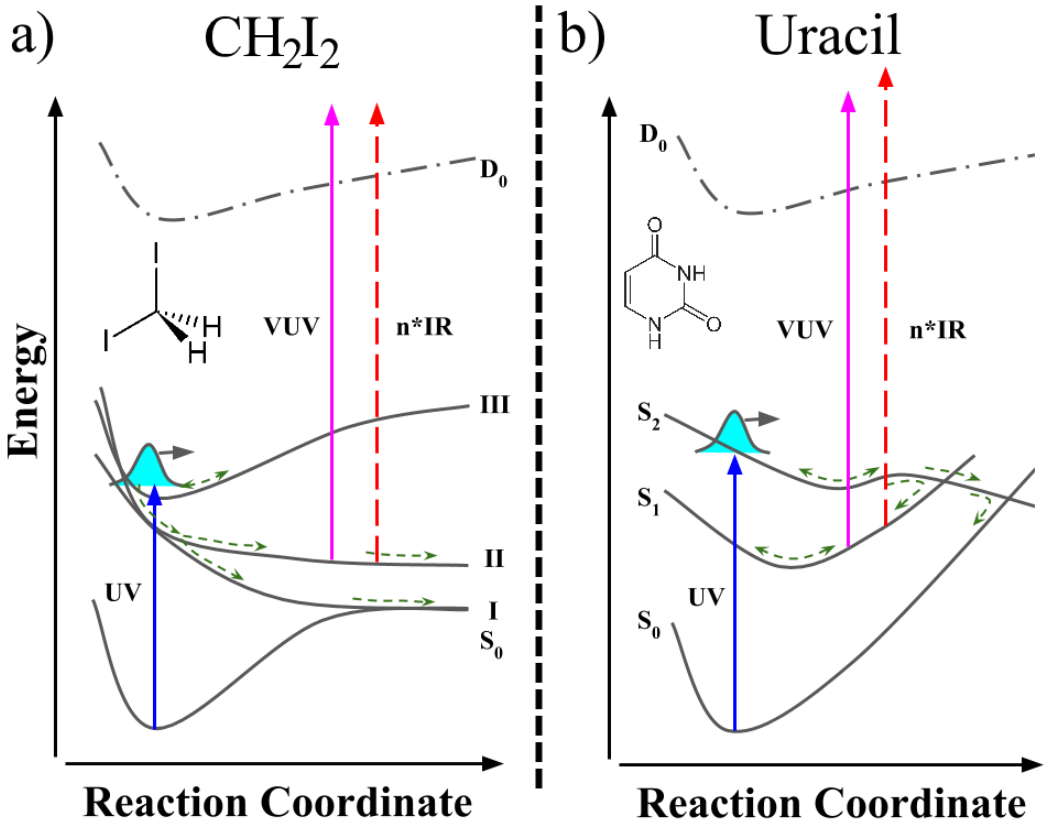

Figure 5.2: Cartoons showing the excited state dynamics in a) CH_2I_2 after UV absorption [106], and b) uracil after UV absorption [107]. The different ionization probes for WFI (solid magenta line) and SFI (dashed red line) are also indicated.

to perform pump-probe ion yield measurements. The details of the apparatus can be found in Chapter 2.

The IRF of the apparatus for the CH_2I_2 data is $\sim$ 100 fs, and for the uracil measurements the IRF is $\sim$ 200 fs. This is due to the fact that the uracil data was taken before the time resolution of the apparatus was improved (see Chapter 2). Since uracil's dynamics are on much longer timescales than the IRF of the system it was deemed sufficient for this study. Gas-phase diiodomethane and uracil are injected into the system as an effusive molecular beam at 25°C and 200°C, respectively.

5.3 Experimental Results

For WFI UV-VUV pump-probe measurements performed on diiodomethane, CH_2I_2, transient ion yields for the parent ion, $CH_2I_2^+$, and the fragment ion, CH_2I^+, are observed. The total energy available following the absorption of one photon from each of the pump and probe pulses is 12.75 eV. The observation of the parent and this fragment ion are consistent with previous measurements [128, 129, 130, 131], where the appearance energies (AE) of $CH_2I_2^+$ and CH_2I^+ are about 9.46 and 10.49 eV respectively.

The total ion yield pump-probe signal for both SFI and WFI of CH_2I_2 can be seen in Fig. 5.3 a) plotted on the same graph. Negative time delays are shaded gray, because attention should be focused on positive time delays where the UV-pump precedes the VUV-probe. The SFI data for CH_2I_2 was taken by Dominik Geissler for his Master's Thesis work [132]. Both methods reveal a very fast $\sim$50 fs decay, but the SFI measurements show a longer component to the decay ($\sim$ 400 fs). Since the excited state dynamics in both experiments are identical, the differences in the measured signals must be due to differences in the interaction between the molecules and the probe pulse - i.e. the difference in the measurements comes from the different sensitivities that WFI and SFI have to the excited state dynamics. It is believed that this longer decay in the SFI CH_2I_2 pump-probe signal is due to a multiphoton resonance which enhances the ion yield as the molecule dissociates [105, 21, 22, 23, 24, 19, 20, 25]. As the wavepacket dissociates on the neutral excited state, the molecular structure can be such that n-photons ($n < IP/h\nu$) from the strong field probe can come into resonance with an intermediate state, between the excited state and the continuum, increasing the ionization rate. This interpretation is consistent with earlier measurements of multi-photon resonances in SFI of halogenated methane molecules [20]. Since one doesn't know *a priori* (i.e. without carrying out detailed electronic structure calculations for different molecular geometries) whether resonances will modify the ion signal versus structure/configuration for SFI, one cannot know whether the SFI signal versus time is directly connected to changes in molecular geometry, or distorted by the intermediate dynamic resonances that occur.

In the uracil UV-VUV WFI pump-probe experiments, the parent ion was measured, $C_4H_4N_2O_2^+$, and the fragment ion measured with mass 69 in atomic mass units (AMU) in the TOFMS. These observations are consistent with photon impact AE (9.15 $\pm$ 0.03 eV for the parent ion and 10.95 $\pm$ 0.05 eV for the fragment ion, $C_3H_3NO^+$ (mass 69 AMU) [133]). The appearance energies of other fragments are all greater than 12.75 eV.

The total ion pump-probe signal for WFI UV-VUV pump-probe experiments and SFI UV-IR pump-probe experiments on uracil can be seen in Fig. 5.3 b). The

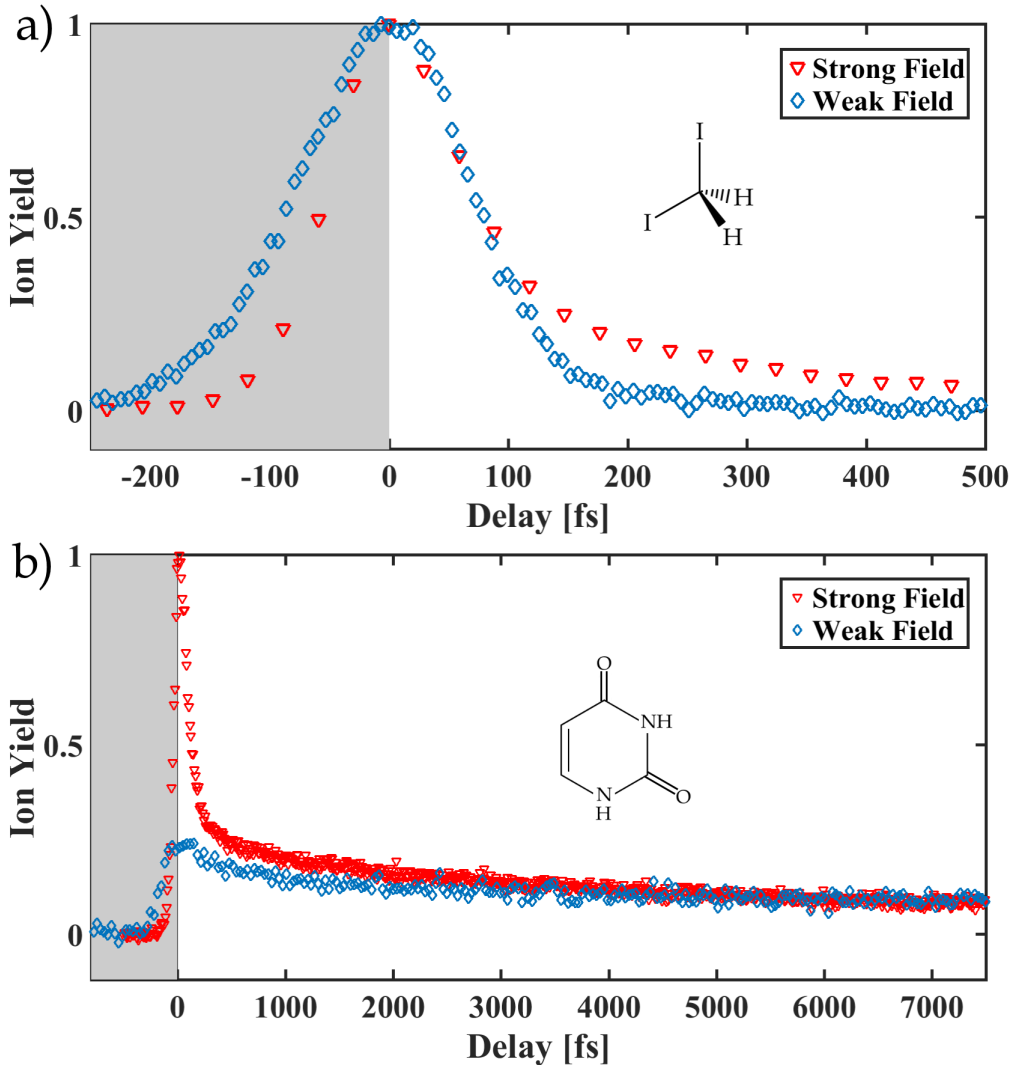

Figure 5.3: a) Weak-field UV-VUV and strong-field UV-IR total ion yield pump-probe measurement on diiodomethane. b) Weak-field UV-VUV and strong-field UV-IR total ion yield pump-probe measurement on uracil.

SFI experiments presented here were carried out by Marija Kotur as part of her PhD thesis work [134]. For SFI, it was found that the exact structure of the pump-probe signal can vary with the intensity of the probe, which highlights one of the major difficulties working with the SFI as a probing mechanism (see Section 5.3.5: Error Bar Determination for Uracil Strong-Field Ionization Measurements).

Analyzing the WFI and SFI results on uracil and performing χ^2 fitting it became

clear that the pump-probe signals consist of two decay timescales, one short and one long (details of this fitting can be seen in Section 5.3.1: CH_2I_2 and Uracil Fitting Results). The SFI and WFI signals have similar long decay timescales, but they differ significantly for the shorter time-scales. The SFI yield has a sharp peak at zero time delay, which is not seen in the WFI scan. As in the case of CH_2I_2, given the same dynamics excited by the pump-pulse, the difference in signal must derive from differences in the sensitivity of the two probes. The sharp peak near zero delay in the SFI data could be due to multiple effects: an enhancement in the multi-photon ionization yield due to the overlap of the pump and probe pulses, a distortion of the potential energy surfaces by the strong field of the probe pulse, or to the greater sensitivity of the SFI yield to wave packet motion away from the FC region. In any case, it is clear that SFI exaggerates, or distorts the motion of the wave packet near the FC region.

Figure 5.3 illustrates one of the difficulties in only looking at decay constants to compare an experiment to theory. The SFI measurements can not be fitted to a single exponential decay in either of the two cases considered here. Comparing one decay time from a multi-parameter fit with several decay components to theory can be very misleading. The fit parameters can be coupled and the relative importance of a given decay time depends on the details of the fitting procedure. For example, if the fit amplitudes for different timescales differ greatly, it is hard to appreciate how much each plays a role. The difficulty of just looking at time-constants without their corresponding amplitudes is apparent from looking at Fig. 5.3 panel b). For the WFI uracil data the relative amplitudes of the short and long decays are similar, whereas for SFI the relative amplitude to the short decay is much larger than the long decay. Comparing the time constants of the SFI and WFI uracil data does not justly convey their stark differences at short timescales. Also, for the SFI uracil data, at a first glance, the most important feature appears to be the rapid decay away from timezero, but it turns out that it is actually not.

As a result, it is argued here that the best test of quantitative agreement between a particular theory and experiment is to plot the experiment and theory together on the same graph.

5.3.1 CH_2I_2 and Uracil Fitting Results

Instead of looking at the total ion yield it can also be informative to look at the pump-probe signal of the different fragments produced and to fit the results.

First, the fitting functions for the data must be defined. For all the data collected it is assumed that the UV and VUV pulses are Gaussian in time, then the apparatus' impulse response time, σ, is dictated by the pulse durations. Therefore, σ is essentially the convolution of the pump and probe pulse durations. t_0 corre-

sponds to time-zero (where the UV and VUV pulses are overlapped). A_n and τ_n are the amplitude and decay constant for the molecular decay, where n indicates the number of exponentials used in the fit. The minimum n is used that gives $\chi^2_\nu \sim 1$ ($\chi^2_\nu = \chi^2/\nu$ is the reduced χ^2 of the system, were ν is the degrees of freedom of the measurement). Θ is the Heaviside step function, and is used to ensure that the molecular dynamics cannot initiate until the excited state is populated.

The fitting function for the WFI CH_2I_2 data and for the SFI CH_2I_2 parent ion data is

$$f(t) = e^{-\frac{(t-t_0)^2}{2\sigma^2}} \otimes \left[\Theta\left(t-t_0\right) \cdot \left(A_1 e^{-\frac{(t-t_0)}{\tau_1}}\right)\right], \tag{5.2}$$

and the fitting function for the WFI CH_2I_2 fragments ion data is

$$f(t) = e^{-\frac{(t-t_0)^2}{2\sigma^2}} \otimes \left[\Theta\left(t-t_0\right) \cdot \left(A_1 e^{-\frac{(t-t_0)}{\tau_1}} + A_2 e^{-\frac{(t-t_0)}{\tau_2}}\right)\right]. \tag{5.3}$$

The WFI UV-VUV CH_2I_2 pump-probe scans for the parent and the fragment ions together with fits can be seen in Fig. 5.4 a). The SFI results and fitting of CH_2I_2 can be seen in Fig. 5.4 b).

The results of the fitting of the parent ion for both SFI and WFI give consistent decay constants, but some discrepancy between the yields for the two methods appears in the fragment ion data. Both methods reveal a very fast $\sim$ 50 fs decay, but the SFI data also show a longer component to the decay with $\tau = 380$ fs.

The fitting function for the uracil data was slightly more complicated. As mentioned in the Chapter 2, the dichroic mirror which combines the UV-pump pulse and VUV-probe pulse does not act as a perfect filter for the residual UV used to generate the VUV, and a 5% of this UV is reflected and generates a UV-pump UV-probe background signal in the uracil data. This UV-pump UV-probe background was discussed in Chapter 2, but because of the long timescales involved in uracil the 1 ps delay, due to the group velocity dispersion of the CaF_2 window, between the UV-pump VUV-probe signal and the UV-pump VUV-probe signal is still well within the decay dynamics of uracil.

UV-pump UV-probe background scans are taken with the IR to generate the VUV blocked. This UV-pump UV-probe alone signal has to be subtracted from the UV-pump VUV-probe scans that have the residual UV-pump UV-probe signal in them. As shown in Chapter 2, if there is no VUV generation there are more UV photons available in the interaction chamber, and UV-pump UV-probe signal increases. This makes a straight subtraction of the two signals more difficult.

In Fig. 5.5 the green diamonds represent the raw uracil parent ion yield signal that is recorded. It is evident that there are two peaks. The first peak, at 0 fs, is the UV-pump VUV-probe signal, and the second peak, at $\sim$ 1000 fs, is the UV-pump

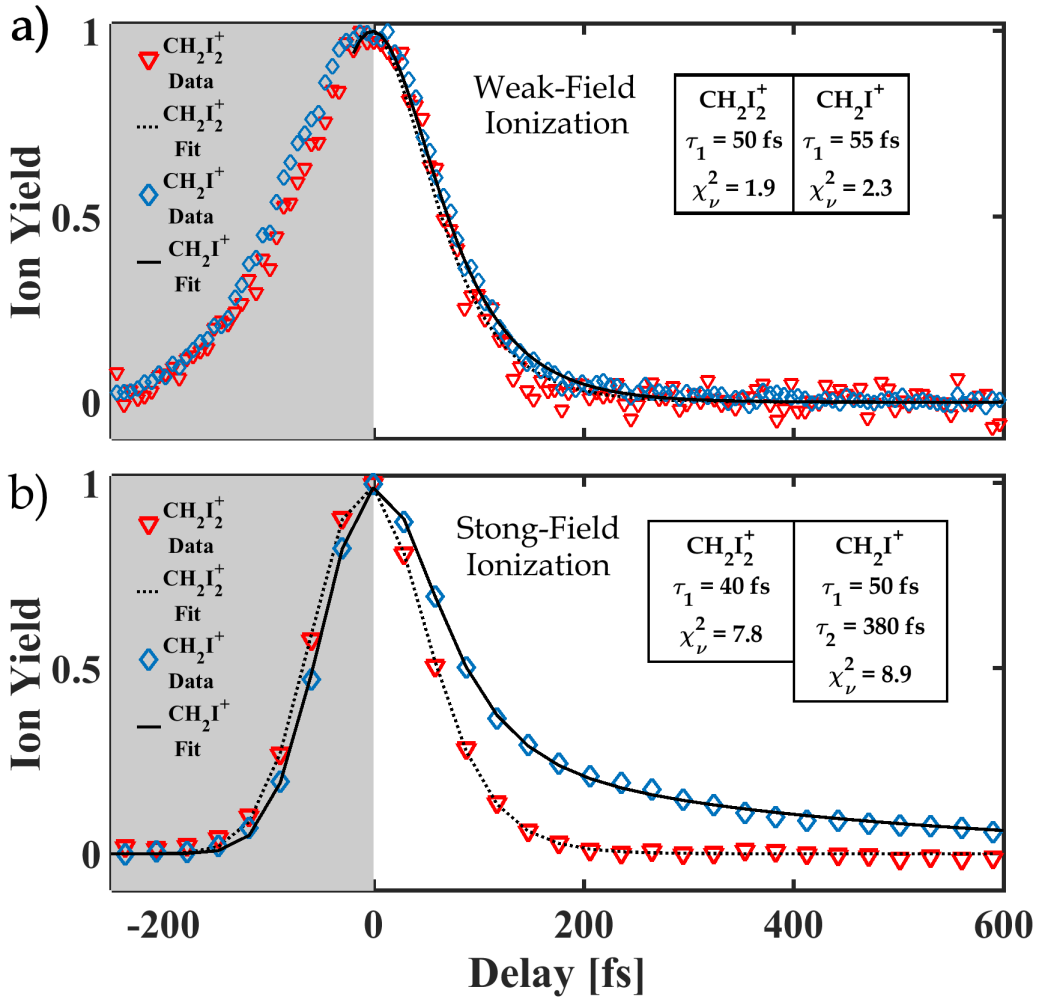

Figure 5.4: a) Weak-field UV-VUV pump-probe measurement and fitting on diiodomethane. b) Strong-field UV-IR pump-probe measurement and fitting on diiodomethane.

UV-probe signal. The background pump-probe scans performed with only the UV in the chamber in order to characterize the background signal can be seen in the inset of Fig. 5.5.

Since the UV-pump UV-probe signal cannot simply be subtracted from the data, the UV-pump UV-probe dynamics are incorporated into the fit. The overall fitting

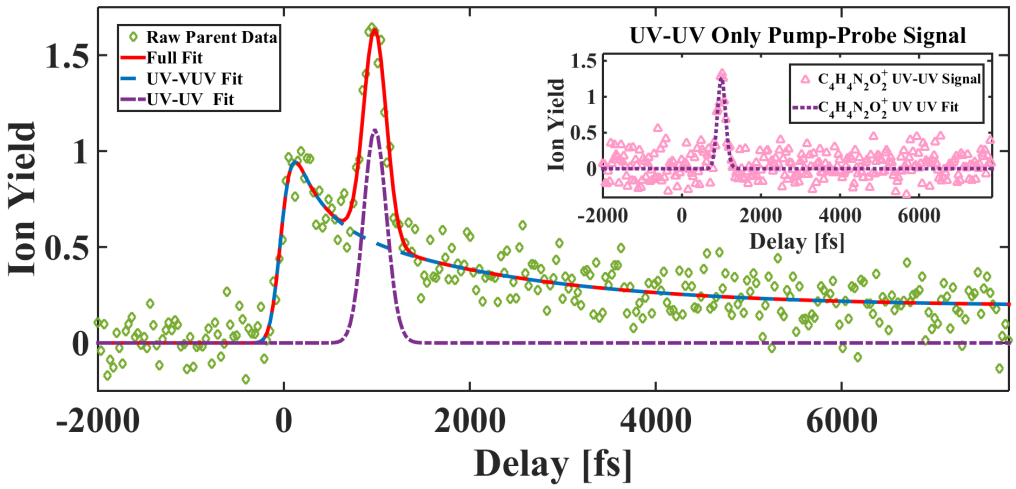

Figure 5.5: The green diamonds are the raw data collected for the parent ion that contain both the UV-pump VUV-probe and UV-pump UV-probe signals. The red solid curve is the full fit given by Eq. 1. The dashed cyan curve is the UV-pump VUV-probe fit component. The purple dashed-dotted curve is the UV-pump UV-probe fit component. The inset plot is contains UV-pump UV-probe data taken without any VUV present. The light blue diamonds are the UV-pump UV-probe data and the dashed-dotted purple line is the fit to the UV-pump UV- probe data.

function for the WFI uracil data is

$$f(t) = e^{-\frac{(t-t_0)^2}{2\sigma^2}} \otimes \left[\Theta\left(t-t_0\right) \cdot \left(A_1 e^{-\frac{(t-t_0)}{\tau_1}} + A_2 e^{-\frac{(t-t_0)}{\tau_2}} + A_3\right)\right] + e^{-\frac{\left(t-t_0'\right)^2}{2\sigma'^2}} \otimes \left[\Theta\left(t-t_0'\right) \cdot \left(A' \cdot e^{-\frac{\left(t-t_0'\right)}{\tau'}}\right)\right]. \tag{5.4}$$

This fitting function has two main components: the first component is the UV-pump VUV-probe signal, and the second is the UV-pump UV-probe signal. The convolution of the UV-pump and VUV-probe pulse durations is again σ, and t_0 corresponds to time-zero (where the UV and VUV pulses are overlapped). t_0' represents the time-zero for the two UV pulses, and σ' is the time resolution of the UV-pump UV-probe signal in the apparatus. A' and τ' is the amplitude and decay constant for the UV-pump UV-probe molecular decay. Θ is again the Heaviside step function.

From these background scans, Fig. 5.5 inset, it is possible to extract t_0', σ', and τ' to use in Eq. 1, which are then fixed when doing the fitting of the combined UV-pump VUV-probe and UV-pump UV-probe scan. The purple dashed-dotted curve in the main plot of Fig. 5.5 is the fit to the UV-pump UV-probe component, and

is the same as the purple dashed-dotted line in the inset (except for the amplitude factor A').

In Fig. 5.5, the red curve is the complete fit, shown in Eq. 1, with both the UV-pump VUV-probe and UV-pump UV-probe components. The cyan dashed curve is the UV-pump VUV-probe fit. Characterizing the UV-pump UV-probe background signal independently of the VUV signal enables fitting to the UV-pump UV-probe data, and then it is possible to subtract the UV-pump UV-pump contribution from the raw data and generate the plots in Fig. 5.3 and Fig. 5.8.

The UV-VUV fit also consists of two exponential decays and a constant. A_1 and τ_1 characterize the amplitude and decay constant for the first decay. A_2 and τ_2 are the amplitude and decay constant of the second decay. The constant, A_3, represents the population that has a decay constant on the order of nanoseconds, so on these timescales it manifests itself as a constant.

In the WFI data there is a ledge in both the parent and the fragment ion data. By a ledge it's meant that the ion yield from before time-zero is lower than the ion yield at long time delays (if the molecule were relaxing back to its ground state one would expect these levels to be equal on either side of time-zero). So, this ledge is encapsulated in the fit as A_3.

A question that arises is, "What is the physical significance of this ledge?". The Dyson Norms [26, 107] tell us that the population trapped in S_1 should mostly lead to D_1, which would then form the fragment ion. Therefore, the ledge seen in the parent ion signal is not from population trapping in S_1.

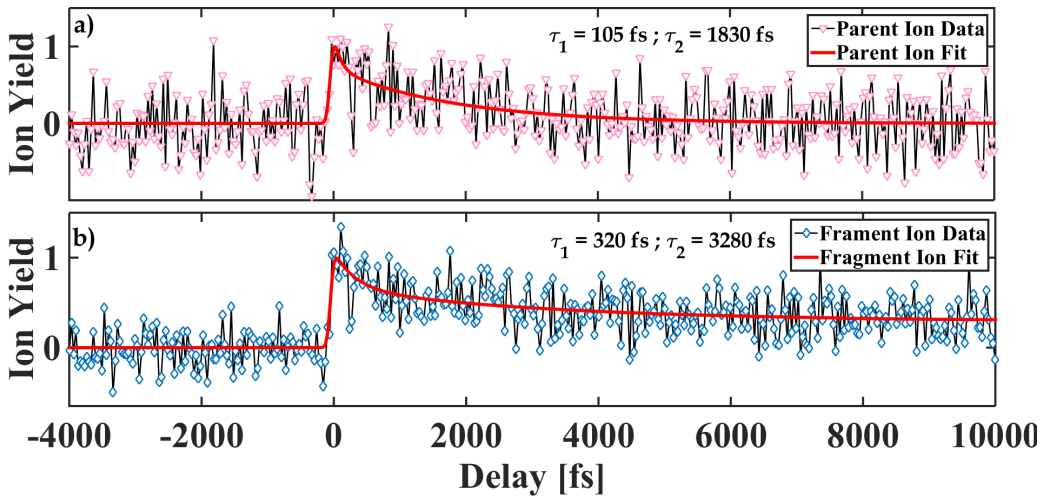

Figure 5.6: Parent ion yield in uracil with no multi-photon UV background signal.

One hypothesis for the ledge in the parent ion signal is that it is due to a multiphoton ionization background from the UV-pump. In order to get a better signal

to noise ratio for the uracil data the UV intensity was increased, but this leads to a multiphoton UV absorption and a background parent ion signal in the TOFMS. The pump-probe signal sits on top of this multiphton ionization background signal. According to our collaborators' calculations, the VUV pulse alone can pump to a Rydberg state of uracil, this Rydberg state is called S_N. A cartoon of uracil's potential energy surface can be seen in Fig. 5.7 depicting the initiation of different dynamics. Panel a shows that the absorption of two UV photons can cause multiphoton ionization to from S_0 to D_0, panel b shows the UV launched dynamics on S_2 from S_0 that one wants to study here, and panel c shows the VUV launched dynamics on a Rydberg state, S_N, from S_0. If the VUV pulse comes before the UV pulse, that is generating this multiphoton ionization background, this can lead to some depletion of the ground state, and subsequently cause less multiphoton signal from the ground state. In Fig. 5.6 the data was retaken with no multiphoton UV signal visible in the TOFMS, and the ledge seen in the parent ion signal disappeared, but the ledge in the fragment ion persisted with time constants consistent with what had previously been extracted. This is what one would expect if the ledge in the fragment ion signal was from trapping on the potential energy surface, and if the ledge in the parent ion signal was from a multiphoton ionization background.

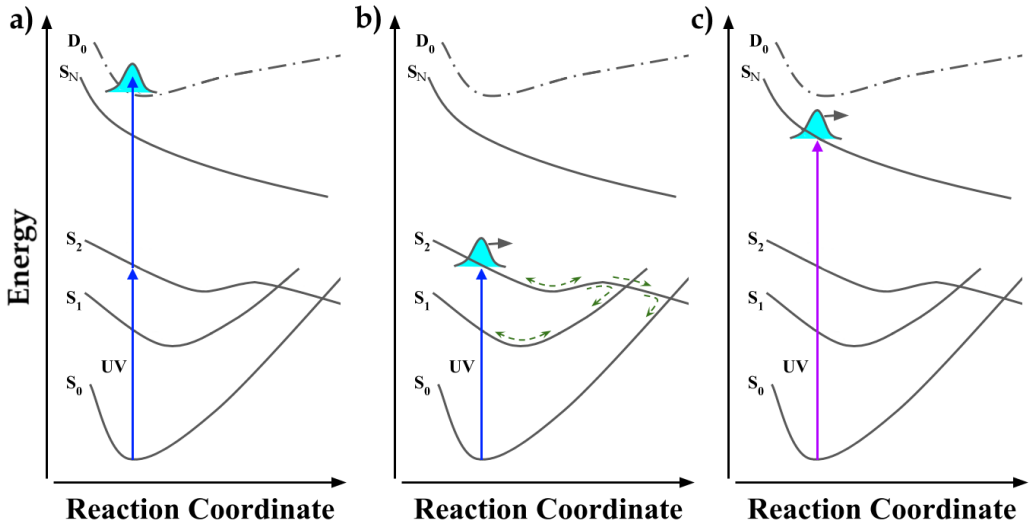

Figure 5.7: Cartoon of uracil's potential energy surface depicting a) UV multiphoton ionization to D_0 from S_0, b) UV excitation to S_2 from S_0, and c) VUV excitation to a Rydberg state S_N from S_0.

The parent and fragment ion yields along with fits for WFI UV-pump VUV-probe experiments on uracil can be seen in Fig. 5.8 a). The SFI UV-pump IR-probe experiments and fitting can be seen in Fig. 5.8 b).

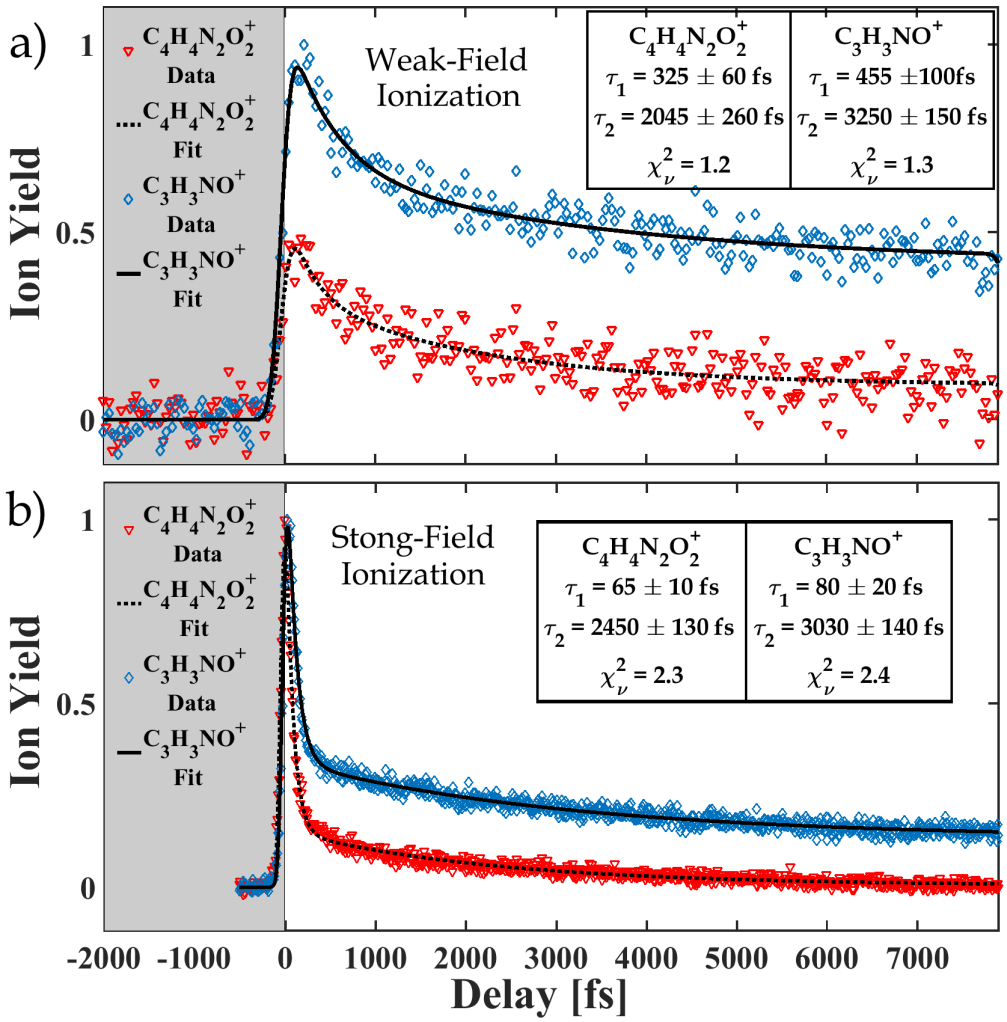

Figure 5.8: a) Weak-field UV-VUV pump-probe experiment on uracil. b) Strong-field UV-IR pump-probe experiment on uracil

In uracil, error bars for a fit parameter in the WFI scans are determined by the range over which χ^2 changes by 1 from its minimum value. The SFI results for uracil are sensitive to systematic effects (such as the laser intensity of the strong field probe), and these systematic effects appear to be the main source of error in the fitting for these experiments. To account for these in the calculation of uncertainties in the SFI uracil data, four different data sets with varying probe intensity were analyzed. Each data set was individually fitted. The results of this fitting can be seen in Fig. 5.9 for both the parent and the fragment ion decay constants. The mean, μ, and the mean plus and minus the standard deviation, σ, are also plotted. Unlike

in the weak-field experiments, the error extracted from the individual data sets from $\Delta\chi^2 = 1$ is much smaller than the variation in the decay constants from data set to data set. This indicates that the dominant source of error in these experiments is systematic.

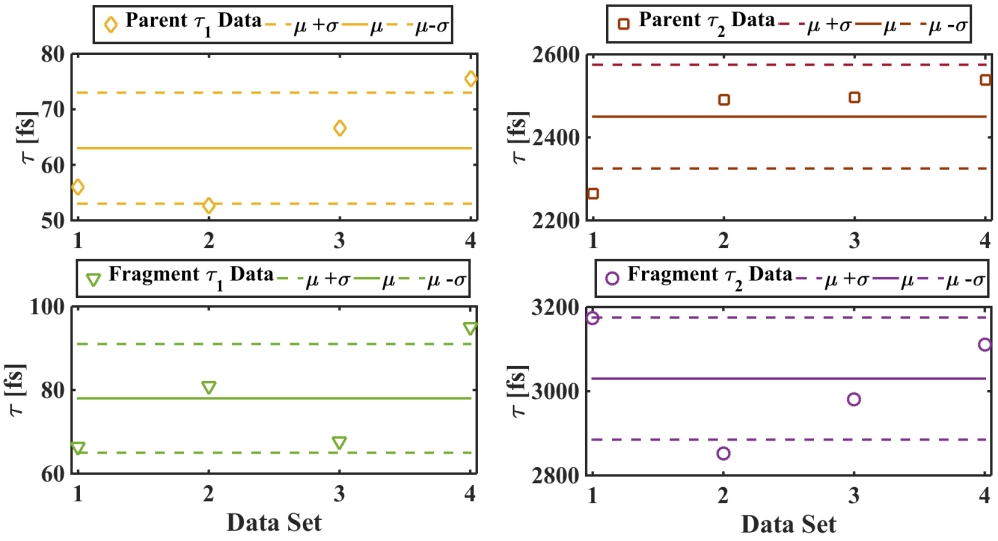

Figure 5.9: Uracil decay constants extracted from strong field ionization experiments with varying probe intensities in order to determine the systematic errors in the experiment, so error bars can be set on the decay constants.

For the parent ion, $C_4H_4N_2O_2^+$, the shorter decay, $\tau_1 = 325 \pm 50$ fs, is consistent with either a rapid motion away from the Frank-Condon region, or a portion of the wavepacket making a rapid non-adiabatic transition to S_1 or S_0. The longer decay constant, $\tau_2 = 2045 \pm 260$ fs, suggests that a portion of the wavepacket is trapped in a minimum for several picoseconds. For the fragment ion, $C_3H_3NO^+$, time constants of $\tau_1 = 455 \pm 100$ fs and $\tau_2 = 3250 \pm 150$ fs were extracted. The SFI results and fitting can be seen in Fig. 5.8 b). For the parent ion $\tau_1 = 65 \pm 10$ fs and $\tau_2 = 2450 \pm 130$ fs. For the fragment ion $\tau_1 = 80 \pm 20$ fs and $\tau_2 = 3030 \pm 140$ fs. Within the error bars the long decay constants for both the parent and the fragment are consistent for both SFI and WFI, but this is clearly not the case for the shorter decay constants.

The two probe techniques used here are probing the same dynamics in the same molecule. Any differences between the detected signals from the two probe techniques has to come from differences in the probing mechanism itself. Since the long timescale dynamics measured with the SFI and WFI probes are consistent it can be concluded that these dynamics are coming from neutral state dynamics

within uracil. These long timescales could be indicative of some trapping of the wave packet on the S_2 minimum, but these measurements are not definitive. The differences between the short time constants indicate that the SFI probe is driving nonlinearities in the system that are distorting the neutral excited state dynamics being measured.

5.4 Theoretical Results and Discussion

The differences between WFI and SFI as a probe of excited state dynamics are highlighted by comparing theory and experiment. The calculations for CH_2I_2 were carried out by our collaborators Philipp Marquetand and Tamás Rozgonyi, and the calculations for uracil were conducted by our collaborators Pratip Chakraborty and Spiridoula Matsika. For both molecules, they carried out trajectory surface hopping calculations of the dynamics, using the SHARC [135, 136, 137] and NEWTON-X [138, 139] packages. The ionization yield as a function of delay was based upon the excited state populations as a function of time, with Dyson norms calculated in addition for the case of CH_2I_2. Details of the CH_2I_2 calculation can be found in Appendix B.1: CH_2I_2 Calculation Details.

For CH_2I_2 the calculations were done with SHARC based on MS-CASPT2 (multi-state complete active space perturbation theory second order) level of theory [140] and coupled with Dyson norm calculations [141] in order to carry out a thorough comparison to the experimental results. The convolution of the calculations with the IRF of the apparatus, acquired from the ethylene VUV-UV pump-probe scans, is required to accurately compare the experimental results to the theory. The results of this analysis can be seen in Fig. 5.11 a).

The timescales involved in the CH_2I_2 molecular dynamics are shorter than the IRF of our apparatus, and it must be verified that the experiment can distinguish between different molecular dynamics timescales. To do this a comparison of the experimental measurements with calculations is performed, where the dynamics are stretched or contracted by factors of 1.5 and 2 prior to the convolution. The stretched and contracted calculations together with the data can be seen in Fig. 5.10. It is clear from the figure that the measurements agree well with the original calculation data, while disagreeing with the stretched or contracted data. This indicates that the measurement contains more information than just an upper bound on the dynamics or timescale.

For uracil, CASPT2 analytic gradients are not available and numerical gradients would be computationally prohibitive. Therefore, dynamics are carried out on potentials calculated at the complete active space self consistent field (CASSCF) and multireference configuration interaction with single excitations (MRCIS) levels of

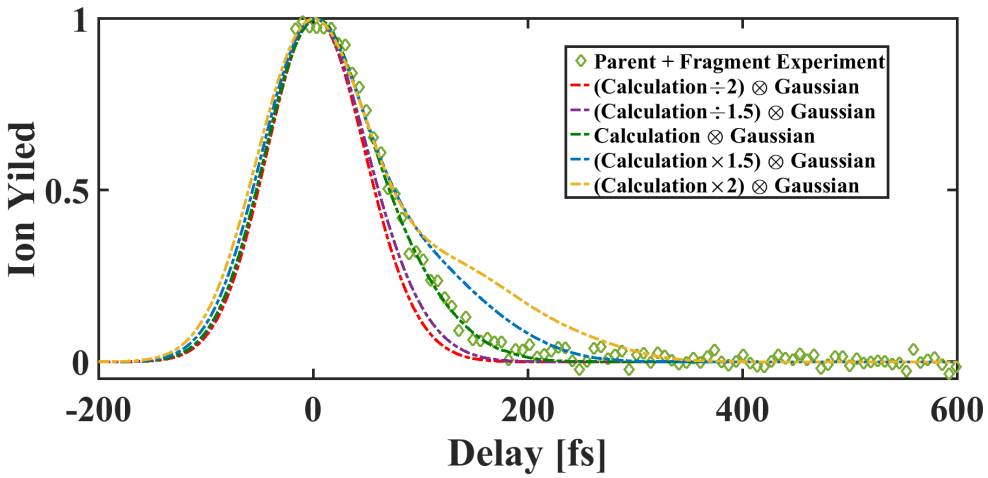

Figure 5.10: Scaling the CASPT2 dynamics and Dyson norm calculation on diiodomethane and convolving with a 100 fs FWHM Gaussian to check the comparison between theory and experiment.

theory using the Columbus 7.0 and NewtonX packages [142, 143, 144]. CASSCF dynamics calculations are performed to track the dynamics for 1 ps, and MRCIS dynamics calculations, due to the greater computational complexity, are carried out for only 500 fs. MRCIS is a higher level of theory than CASSCF, and is used to check the validity of the CASSCF calculations. To compare these results to the UV-pump VUV-probe signal the total ion yield is used, assuming that the total excited state populations (S_1 and S_2) are ionized, and taking the S_1 and S_2 populations as the total ion signal. To verify that this assumption is valid, earlier work from our group and collaborators that studied the variation in the Dyson norms for ionization of uracil from S_1 and S_2 was reexamined [107]. These results indicated that there were no dramatic differences in the Dyson norms on these states in moving between the S_2 minimum, the S_1 minimum, and the S_1/S_2 CI geometries. Since only these two states are involved in the dynamics, and there is not much variation in the Dyson norms from these two states, therefore the Dyson norms are not calculated at each point in the trajectories.

Again, the results of the computation were convolved with the IRF of the system for an accurate comparison to the experiment. The results of this analysis can be seen in Fig. 5.11 b). The agreement between the experimental WFI data and the MRCIS and CASSCF calculations is quite good (details of the uracil calculations can be found in Appendix B.2: Uracil Calculation Details).

The agreement between the WFI experimental data and the calculations highlights a key difference between SFI and WFI. SFI and WFI may provide a similar

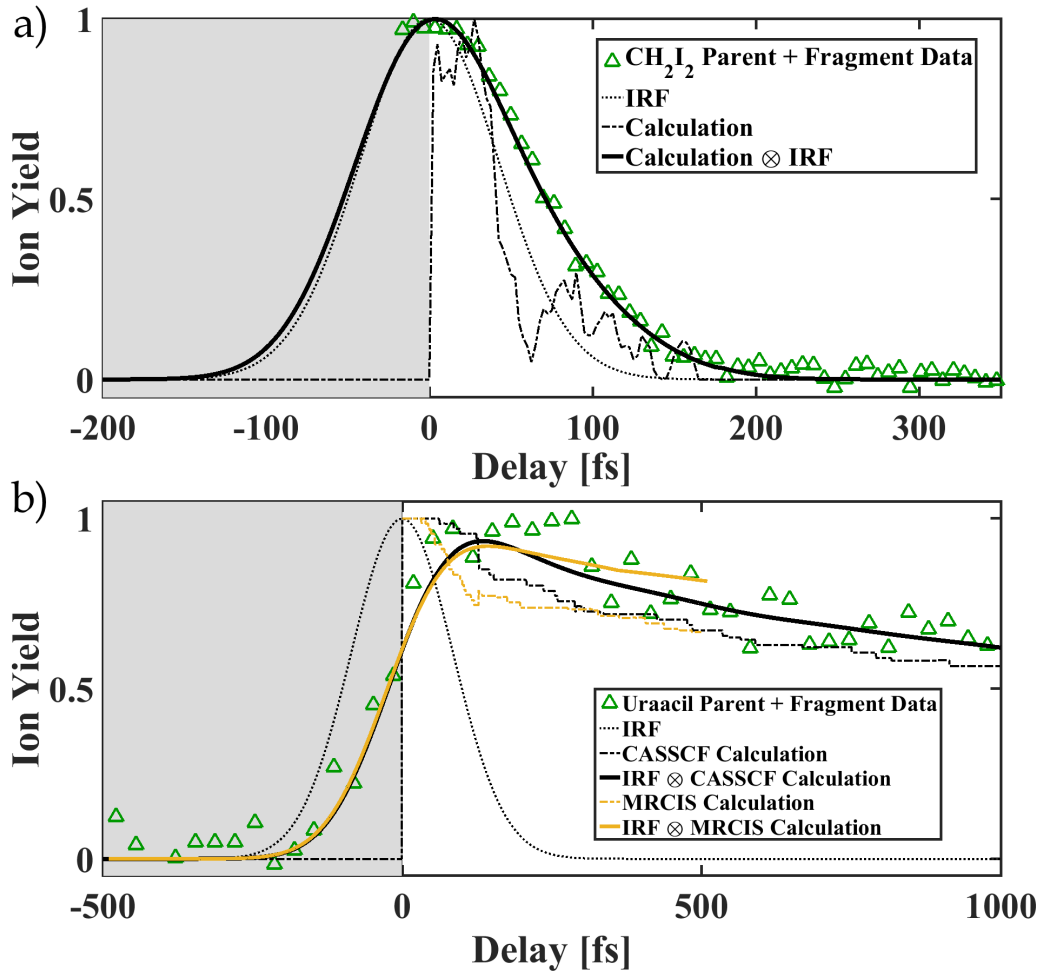

Figure 5.11: a) CH_2I_2 WFI UV-VUV pump-probe total ion yield data (green triangle), CASPT2 dynamics with Dyson norms calculation on CH_2I_2 (dotted-dashed line), IRF of the apparatus (dotted line), and convolution of the calculation and the IRF of the system (solid line). b) Uracil WFI UV-VUV pump-probe total ion yield data (upward facing green triangle), CASSCF calculation for uracil (black dotted-dashed line), impulse response function (IRF) of the apparatus (black dotted line), convolution of the CASSCF calculation and the IRF of the system (solid black line), MRCIS calculation for uracil (gold dotted-dashed line), and convolution of the MRCIS calculation and the IRF of the system (solid gold line).

qualitative picture of the relaxation dynamics, but only WFI can be used for a real quantitative comparison with calculations.

By qualitative agreement, it is meant that the decay curves look similar (i.e.

exponential or multiexponential behavior), yield timescales of the same order of magnitude, and show similar trends (i.e. the ionization yield for Uracil has a long tail for both SFI and WFI whereas the WFI and SFI ion yields for CH_2I_2 do not). However, in order to test the validity of a calculation or discriminate between two different theories, quantitative agreement is required. It is argued here that best test of quantitative agreement is to plot experimental and theoretical results together on the same graph. A direct comparison between SFI measurements and calculations of the excited state dynamics is impossible without explicit calculations of the SFI dynamics, which are computationally expensive and unfeasible for the timescales involved in the excited state dynamics probed here. The qualitative agreement between WFI and SFI measurements of the excited state dynamics illustrates the fact that both ion yields contain similar information on the excited state dynamics. The quantitative agreement between the WFI measurements and calculations, however, allows one to interpret and understand the dynamics at a level of detail not possible with SFI.

5.5 Molecular Movies

5.5.1 Uracil

The good agreement between the calculations and the experiment leads one to trust the dynamics calculations with a higher degree of confidence than before. Our collaborators Pratip Chakraborty and Spiridoula Matsika were able to provide us with the calculation details presented in this section. In Fig. 5.12 is a representation of the uracil molecule with all of the atoms labeled to corresponding to how they will be referred to in the calculation.

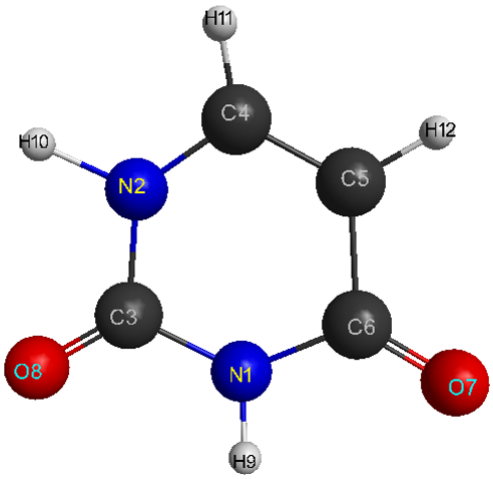

Figure 5.12: Uracil molecule with the atoms labeled corresponding to the calculation.

In Fig. 5.13 the individual trajectories from the uracil calculations performed are shown depicting the C6=O7 bond length, the dihedral angle H11-N2-C5-C4, and the dihedral angle H12-C4-C6-C5 versus time. For these trajectories it is evident that the wave packet is delocalized in the system and that there is not obvious path on the PES that the wave packet consistently samples.

Trying to pull more out of the dynamics the average C6=O7 bond lengths versus time are plotted in the bottom panel of Fig. 5.14. One has to be careful plotting the average distance for trajectories, because if multiple distinct pathways are accessed the average may be meaningless. The average value for the C6=O7 bond distance originally starts near the S_0 minimum value for the C6=O7 bond distance, moves through the S_2 minimum value for the C6=O7 bond distance, and settles at the S_1 minimum value for the C6=O7 bond distance. These results are consistent with previous calculations [108], where the wave packet is launched on the S_2 potential

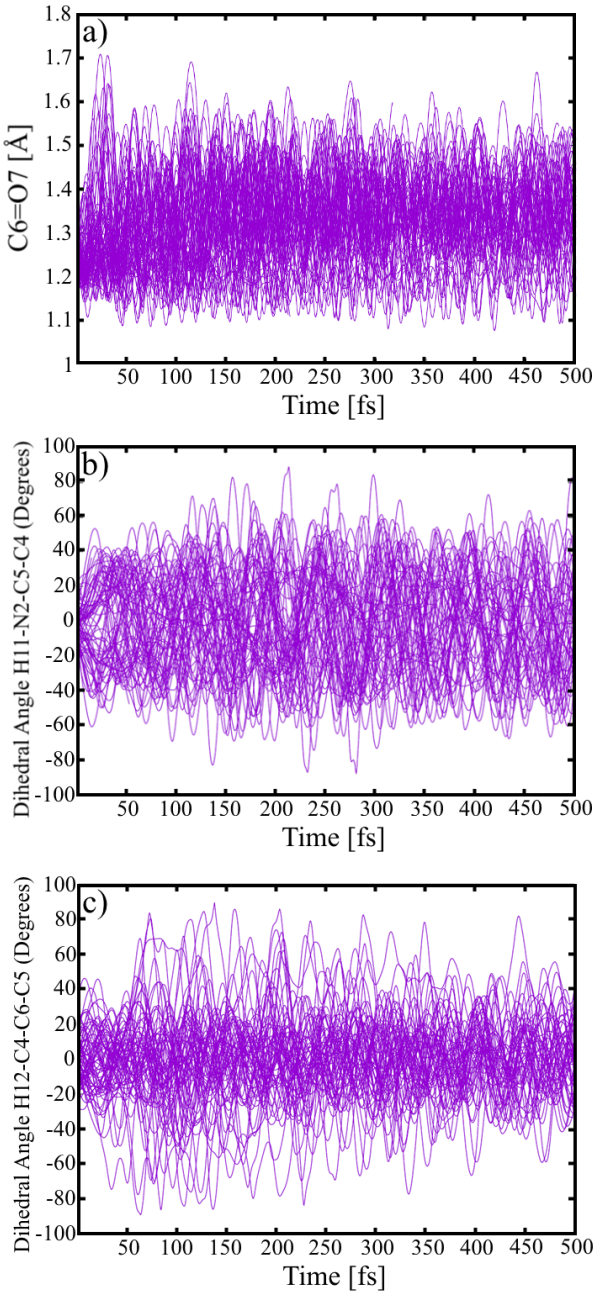

Figure 5.13: Uracil calculation trajectories versus time for the a) C6=O7 bond length, b) Dihedral angle H11-N2-C5-C4, and c) Dihedral angle H12-C4-C6-C5.

from S_0 at the S_0 minimum geometry position. The wave packet evolves through the S_2 minimum and can pass through a CI and evolve to the minimum of S_1, or through another CI and back to the S_0 minimum.

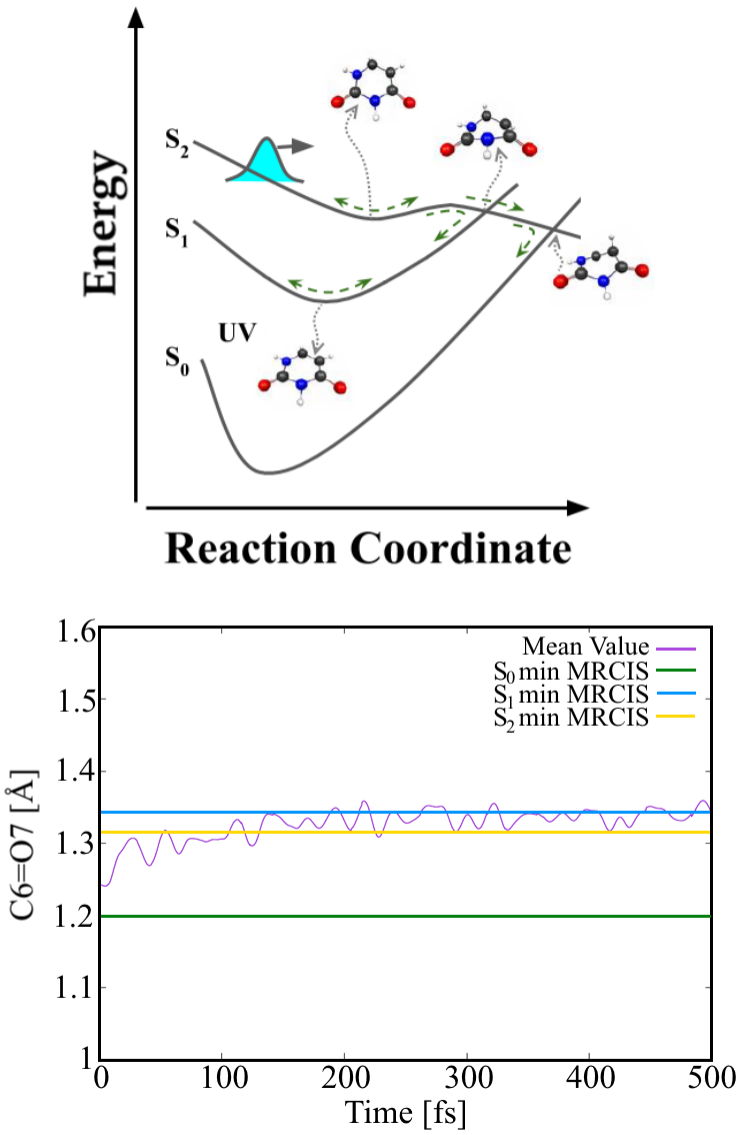

Figure 5.14: Top: Uracil geometries calculated and presented in [108] at key locations in the potential energy surface. Bottom: Mean value of the C6=O7 distance for all of the trajectories versus time. The C6=O7 bond lengths for the S_0, S_1, and S_2 minimum geometries calculated at the MRCIS level of theory are also shown.

From the calculations one can look at a single trajectory and construct a "molecular movie" of the dynamics, Fig. 5.15. The trajectories in this system did not have a localized nature, so the movie is instructive to look at but does not capture all the dynamics. For this trajectory hopping from S_2 to S_1 occurred at 82 fs and hopping from S_1 to S_0 occurred at 106 fs, and the molecular geometry at the CIs can be observed.

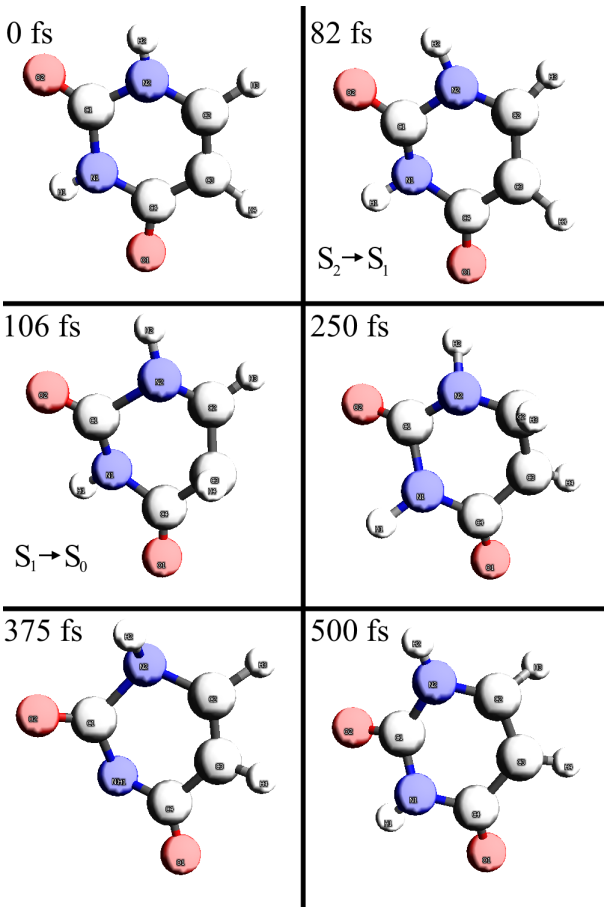

Figure 5.15: Uracil "molecular movie" showing the molecular geometry versus time generated from a single calculation trajectory. For this trajectory hopping from S_2 to S_1 occurred at 82 fs and hopping from S_1 to S_0 occurred at 106 fs.

5.5.2 CH_2I_2

Fig. 5.16 shows a generalized picture of the CH_2I_2. The calculations show that there is a dissociation of the iodine, labeled I2 in Fig. 5.16, and a rotation of the CH_2 around the remaining iodine, I1. In Chapter 6 CH_2I_2 is revisited, along with the molecule CH_2BrI, using time-resolved photoelectron spectroscopy and a more detailed description of the molecular dynamics and a better "molecular movie" of the dynamics is given.

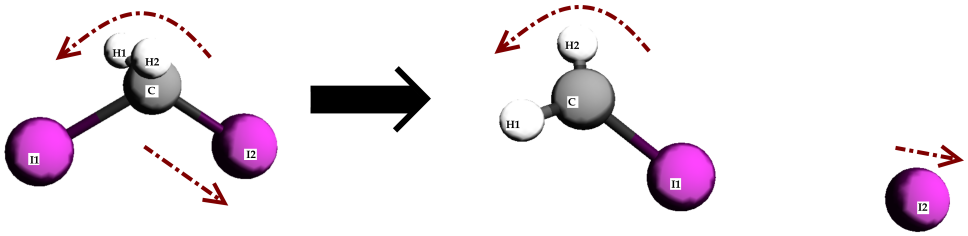

Figure 5.16: CH_2I_2 geometries calculated.

Chapter 6

CH_2I_2 and CH_2BrI Photoelectron Spectroscopy

6.1 Introduction

In this Chapter we study the neutral state dynamics of diiodomethane, CH_2I_2, and bromoiodomethane, CH_2BrI, after being pumped with UV-light at 267 nm, using time-resolved photoelectron spectroscopy (TRPES). CH_2I_2 and CH_2BrI have previously been the subject of intense theoretical and experimental studies [106, 121, 122, 123, 124, 125, 126, 127, 145, 146, 147, 148].

A cartoon of CH_2I_2's potential energy surface can be seen in Fig. 6.1 a). A wave packet is initially launched on a superposition of electronic states which are bound along the C-I coordinate, these states are represented by III. The wave packet undergoes rapid internal conversion from III to states II and I, which are a superposition of electronic states that are dissociative along the C-I coordinate. For CH_2BrI, the electronic structure is very similar to CH_2I_2. CH_2BrI also has a superposition of electronic states that are bound state along the C-I coordinate, but these states are at slightly higher energies than in CH_2I_2, and our probe does not have enough photon energy to access them. Therefore, in CH_2BrI the wavepacket is initially launch directly to a superposition of electronic states that are dissociative along the C-I coordinate, represented by I and II in Fig. 6.1 b).

6.2 Experimental Apparatus

These experiments were performed at the National Research Council of Canada, in collaboration with the femtolabs research groups there. An amplified Coherent Legend Elite Duo (7.0 mJ, 1 kHz, 35 fs, 800 nm) laser system is utilized. The

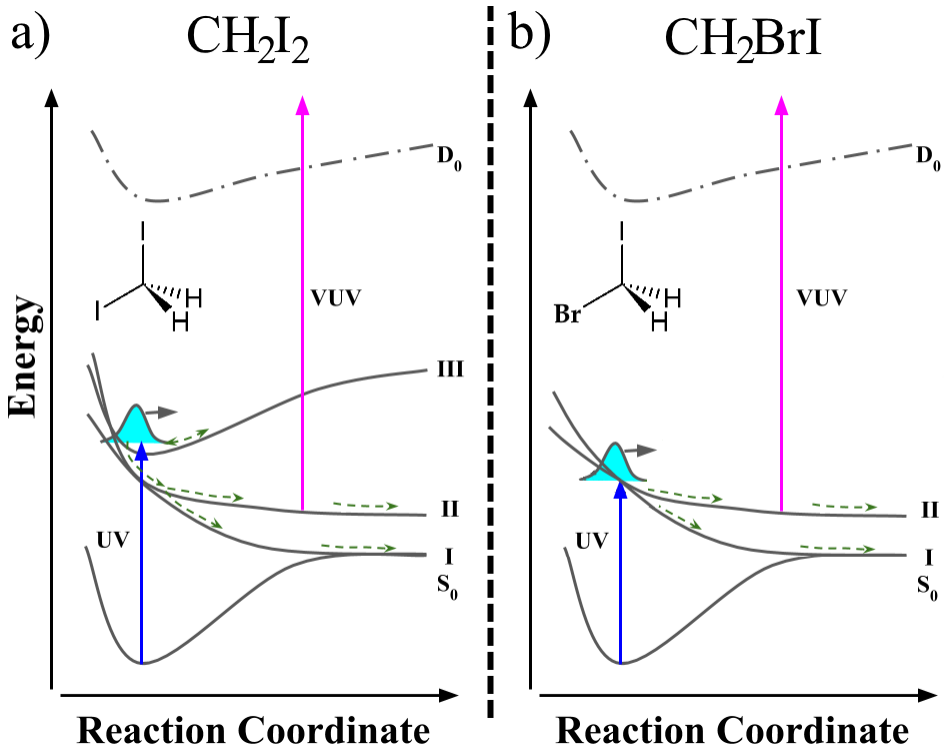

Figure 6.1: A cartoon of the PES for a) CH_2I_2 and b) CH_2BrI.

details of the UV (267 nm, 4.6 eV) and VUV (161 nm, 7.7 eV) generation can be found in [149]. I will summarize the apparatus they developed for doing TRPES with a UV-pump and a VUV-probe, but I was not involved it the development of the apparatus.

Fig. 6.2 is a schematic of their experimental apparatus. 3.25 mJ from the amplifier is used in these experiments. The transmitted portion of the beam from a 70:30 beamsplitter is used as the IR arm in the non-collinear four-wave mixing needed to generate the fifth harmonic of the laser system. The reflected portion of the beam is incident on another 70:30 beam splitter. The reflected portion is used to generate the UV for the VUV generation, and the transmitted portion is used to generate the UV for the pump in the experiments. The details of the THG for both UV arms can be seen in the inset of Fig. 6.2, the incident fundamental frequency is doubled through Type I harmonic generation in a BBO crystal, then the beam passes through a calcite compensation plate to compensate for the group velocity mismatch of the fundamental and second harmonics in the SHG and THG crystals, then the polarization of the fundamental frequency is rotated in a zero-order waveplate so that it matches the polarization of the second harmonic, and finally the second harmonic

and the fundamental frequency are incident in another BBO crystal cut for Type 1 THG. The fundamental frequency and the third harmonic reserved for the fifth harmonic generation are focused into a gas cell kept at 32 Torr of argon through a 500 μm thick CaF_2 Brewster window with a 2 m radius of curvature (ROC) mirror and a 1.5 m ROC mirror, respectively. Utilizing the same non-collinear four-wave mixing scheme outline in Chapter 2, developed in [29, 30], the fifth harmonic of the laser system is generated and used as the VUV probe in these experiments. A glass tube is inserted around the VUV generation region in order to protect the optics from unwanted byproducts generated in the UV and IR foci. The VUV generated inside the argon gas cell is incident on several dichroic mirrors that reflect $> 90\%$ for the VUV and $< 10\%$ for the UV and the IR in order to dispose of the residual UV and the IR, and to act as a beam combiner with the UV-pump. The VUV is focused with a curved aluminum mirror with a 2 m ROC.

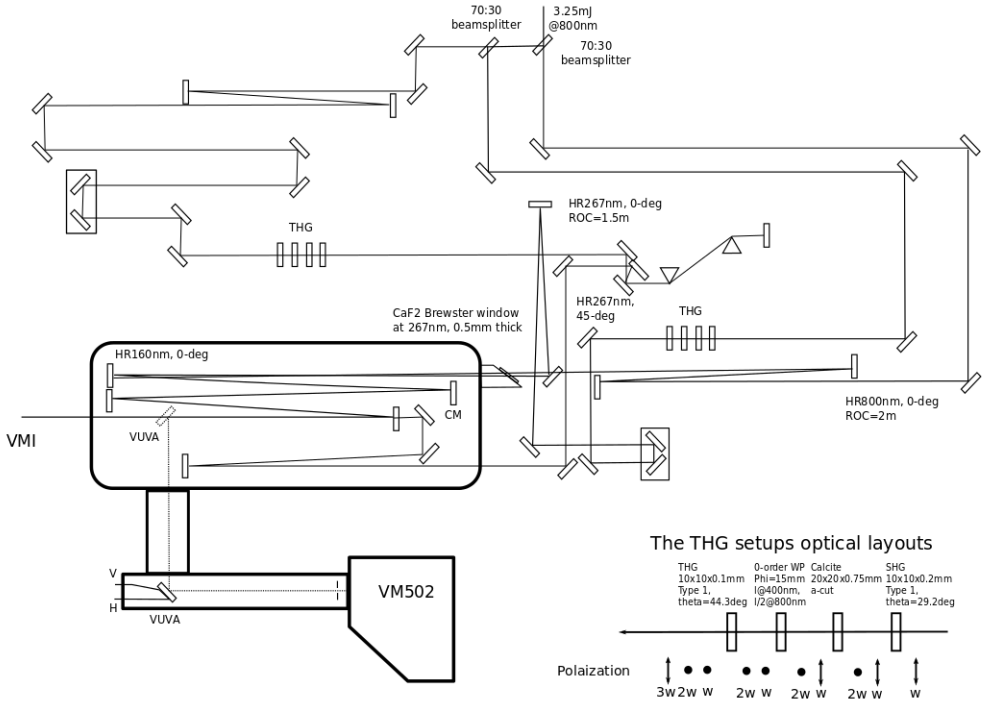

Figure 6.2: NRC VUV Generation [149] (Figure was made by Ruaridh Forbes)

The UV-pump is generated with the same THG technique used for the UV needed for the VUV generation described above. The UV-pump arm contains a prism compressor to compensate for the GVD and minimize the UV pulse duration in the interaction chamber. In the argon gas cell the UV-pump is focused with a 1.4 m ROC aluminum curved mirror.

In order to achieve spatial overlap of the UV and the VUV probe a pickoff mirror can be inserted after the VUV/UV beam combiner, where the UV and the VUV can be steered through a pinhole, placed at their foci, into a VUV spectrometer. The VUV is steered through the pinhole with a movable mirror after the pickoff mirror, and once the VUV is well coupled into the spectrometer the UV can be coupled by steering the beam with a mirror outside the argon gas cell. By having the VUV and the UV both well coupled into the spectrometer through the same pinhole in their focus gives us rough spatial overlap between the UV and the VUV beams. The UV and the VUV are transmitted into the interaction chamber (VMI Spectrometer) through a 500μm CaF_2window. The temporal overlap of the UV-pump and the VUV-probe is measured in Xenon through non-resonant 1 + 1' photon ionization, yielding a cross correlation of 75 fs, which we will use as the impulse response function (IRF) of our apparatus.

The VMI spectrometer system where the TRPES experiments are performed is also described in [149], but I will summarize the system here. The system consists of a source chamber for the molecular beam, and an interaction chamber where the light-matter interactions are performed. The sample gases, $\sim 2\%$ of the target molecule seeded in He through the use of a bubbler, were introduced into the spectrometer by means of a pulsed molecular beam. The beam was produced by a 1 kHz Even-Lavie pulse valve [150], which was heated to 60°C throughout the experiments in order to prevent clustering. The molecular beam is expanded through a 250 μm conical nozzle into a source chamber kept at $\sim 1 \times 10^{-6}$ Torr. The beam is then skimmed, to yield a beam with an estimated diameter of around 1 mm, before entering an interaction chamber along the VMI spectrometer axis, typically held at a base pressure $\sim 1 \times 10^{-8}$ Torr, and intersected, at 90°, by the co-propagating pump and probe laser pulses. Long baffle arms are attached to the interaction chamber along the laser propagation direction in order to absorb any electrons generated from stray light from the UV and VUV (both of which have photon energies above the work functions of the aluminum and stainless-steel of the chamber). Photoelectrons produced from the pump probe laser interaction were focused using VMI lenses configured to map the $\sqrt{E}_{\text{Kinetic}}$ of the charged particles generated by the laser to a position on the detector. The detector consists of a microchannel plate (MCP) stack (amplifies the incident charged particles by $\sim 1 \times 10^6$), a phosphor screen (fluorescence signal that preserves the spacial information of the electron hits on the MCP), and a camera outside the vacuum chamber to collect the fluorescence signal from the phosphor. The intensities of the pump and the probe beams were attenuated by changing the angle of the waveplate in the THG setup in the respective arm. The intensities were set to minimize multiphoton ionization from either the pump or probe beams alone.

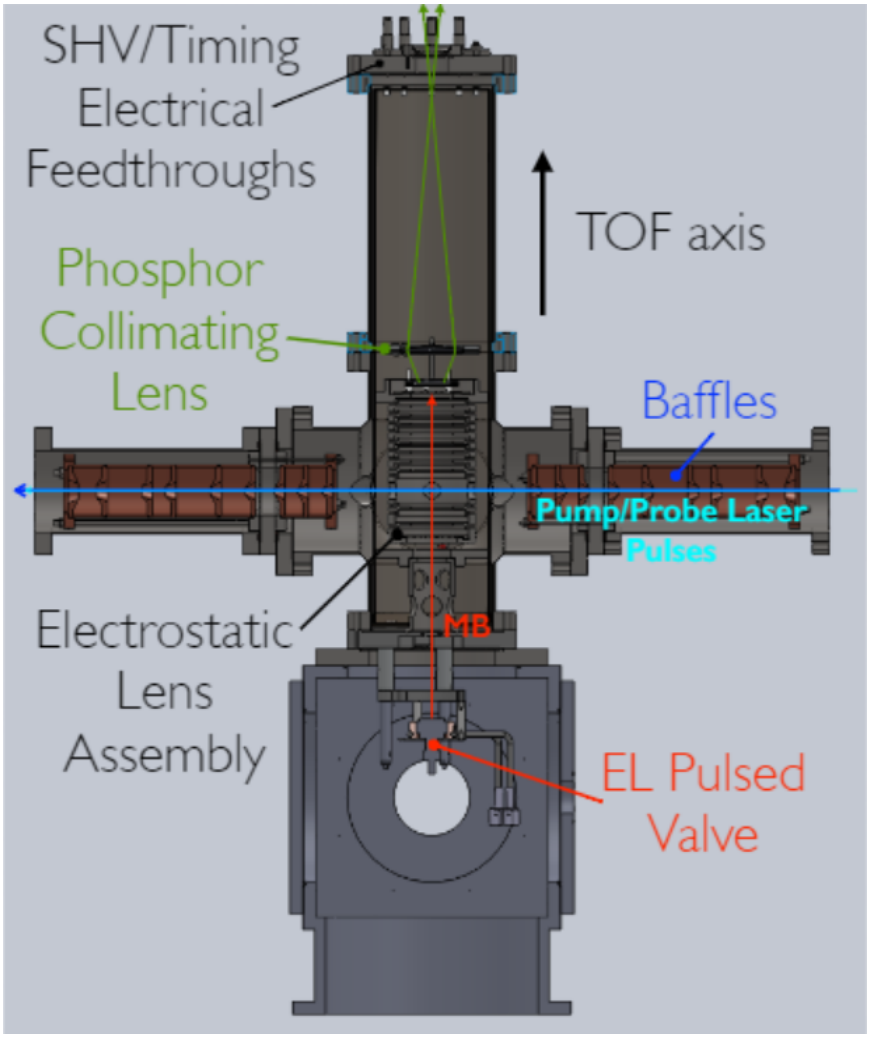

Figure 6.3: National Research Council of Canada's TRPES Apparatus (Figure made by Iain Wilkinson)

6.3 Calculations

The calculations presented in this chapter are performed by our collaborators Philipp Marquetand and Tamás Rozgonyi utilizing the same procedure outlined in Appendix B.1: CH_2I_2 Calculation Details. Instead of calculating the dynamics for a 260 nm (4.8 eV) pump here they are calculated for a 267 nm (4.6 eV) pump.

Fig. 6.4 a) and Fig. 6.5 a) are the calculated PES for CH_2I_2 along the relevant C-I coordinate. In this particular adiabatic representation the diagonalized Hamiltonian is the sum of the Molecular-Coulomb Hamiltonian [151, 152] and the Spin-Orbit Coupling matrices.

Comparing Fig. 6.4 a) and 6.5 a) to Fig. 6.1 a) and b), respectively, one can see the individual states that contribute to the superposition of electronic states that constitute I (red), II (blue), and III (cyan) in the PES cartoon. Only the relevant electronic states to our photon energies are shown. The ionization potential of CH_2I_2 is 9.46 eV and the ionization potential of CH_2BrI is 9.70 eV [153, 154, 155, 156]. The calculated cationic states (yellow), above the dashed line in the figure, are needed to accurately capture the ionization step and determine the kinetic energy (KE) of the ionized electron. In Fig. 6.4 b) and 6.5 b) the populations as a function of time are shown for the ground state, state 1(black), the states that constitute I, states 2-8 (red), the states that constitute II, states 9-12 (blue), and the states that constitute III, states 13-15 (cyan). For CH_2I_2 these calculations show that the wave packet is initially launched completely onto the set of bound states III and after about 30 fs a significant population can be found in dissociative states II and I. This calculation shows that rapid internal conversion from the bound states III to the dissociative states I and II occurs before the molecule dissociates. An interesting feature of the CH_2I_2 calculation is that approximately 25% of the population stays in the bound states III after 100 fs. For CH_2BrI it is clear that the bound states III are energetically unavailable to our pump, and that the wave packet is launched onto both the dissociative states I and II. There is initially rapid internal conversion between states I and II before the population in I and II becomes steady around 50%.

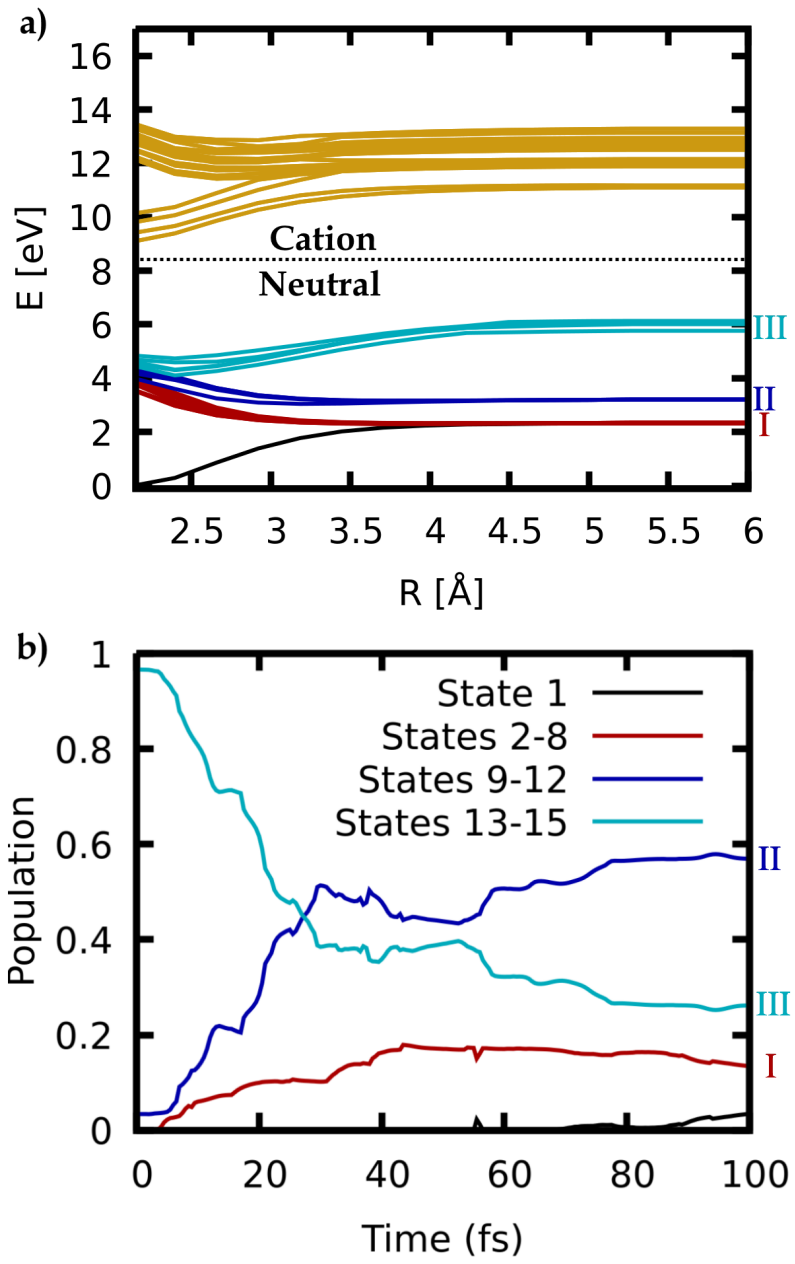

Figure 6.4: a) CH_2I_2 calculated potential energy surface along the relevant C-I coordinate. The states are color coded to correlate to the ground state (black), states I (red) , II (blue), III (cyan), and the cationic states (yellow) labeled in PES cartoon. b) The calculated populations in the ground state, I, II, and III as a function of time.

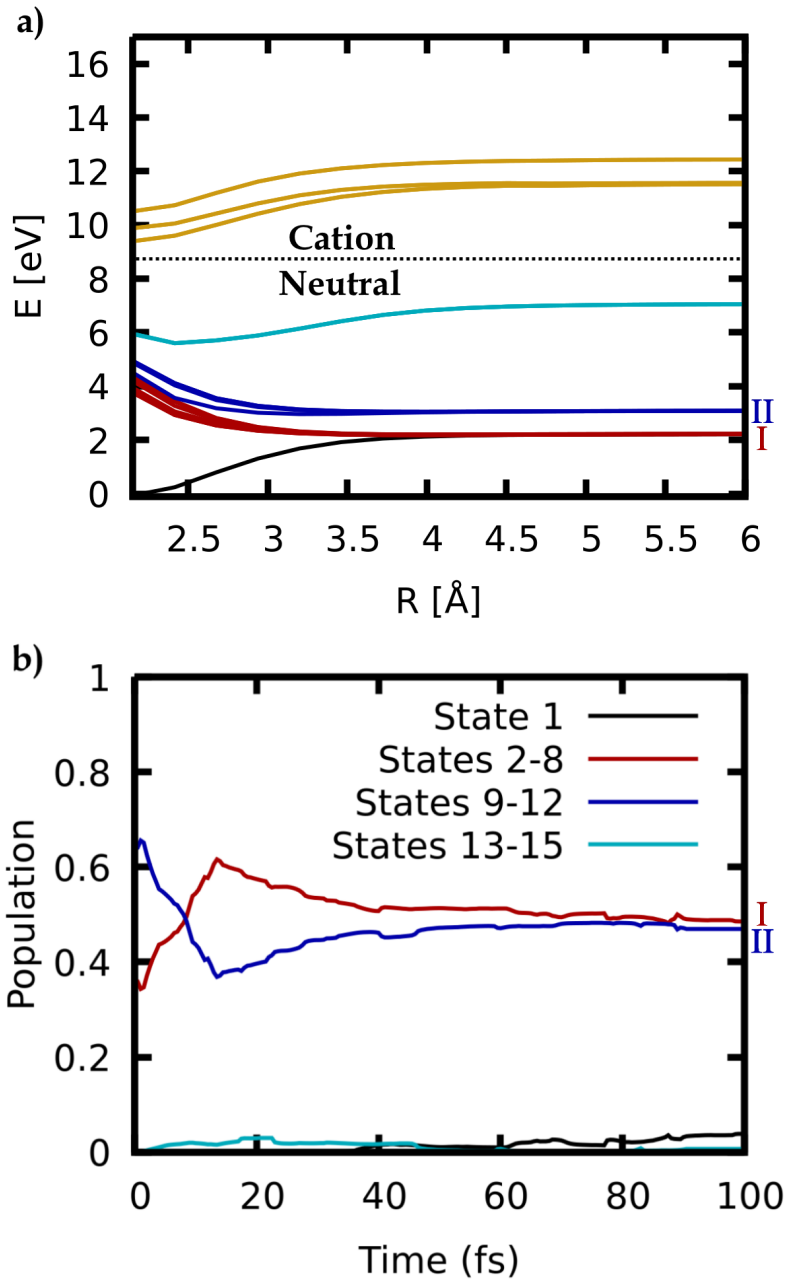

Figure 6.5: a) CH_2BrI calculated potential energy surface along the relevant C-I coordinate. The states are color coded to correlate to the ground state (black), states I (red) , II (blue), III (cyan), and the cationic states (yellow) labeled in PES cartoon. b) The calculated populations in the ground state, I, II, and III as a function of time.

In the calculation wave packets are stochastically launched on the excited state potentials within the bandwidth of the pump laser. An ensemble of trajectories are launched and the results from all these trajectories can be seen in Fig. 6.6, where the the y-axis is the ionization potential of the molecule as the wave packet evolves on the potential energy surface. Since the photon energy of our probe is 7.7 eV we will only see the dynamics below this energy. In order to visualize this calculation in terms of KE of the electrons the photon energy has to be subtracted by the ionization potential (this will be done later in this chapter in order to accurately compare the calculation with the experimental results). After $\sim$100 fs many of the trajectories crash. Hence, the few trajectories that remain for longer times are over weighted in this figure, therefore the calculation should be trusted only for the first 100 fs.

Also, trajectories tend to crash when the wave packet leaves the active space of the calculation, so the long lived trajectories are biased to those that remained within the active space of the calculation. In other words, the crashing of a trajectory is not random, but rather an inability to model the dynamics fully with the resources available for the calculation [157].

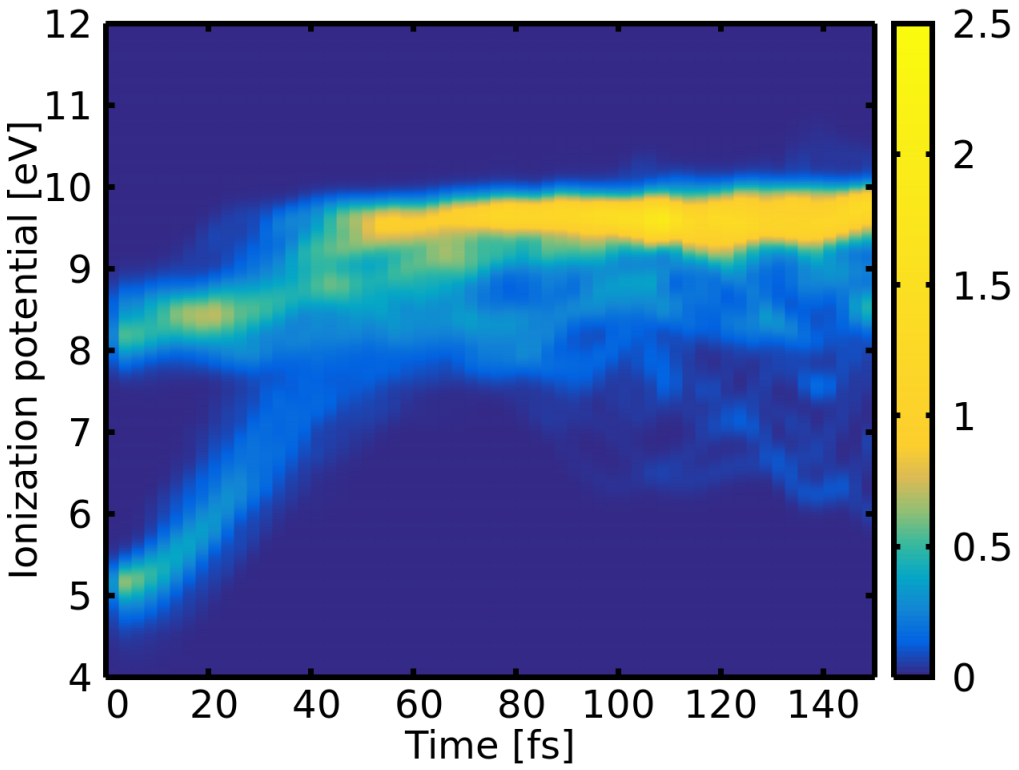

Figure 6.6: Philipp Marquetand's CH_2I_2 calculations done with SHARC based on CASPT2 level of theory.

In the calculation Dyson norms were calculated and used in order to determine the relative yields to the cationic states from the neutral excited states. The questions arises, ”How accurate are the Dyson norms?”, and ”How important are they in this system?”.

In order to answer these questions we look at the calculation with and without using Dyson norms. Fig. 6.7 shows the results of this analysis. In Fig. 6.7 a), we plot the calculated ionization potential for an ensemble of trajectories with the Dyson norms all set to one, and this can be directly compares to Fig. 6.7 d) where the same ensemble of trajectories is used with the calculated Dyson norms.

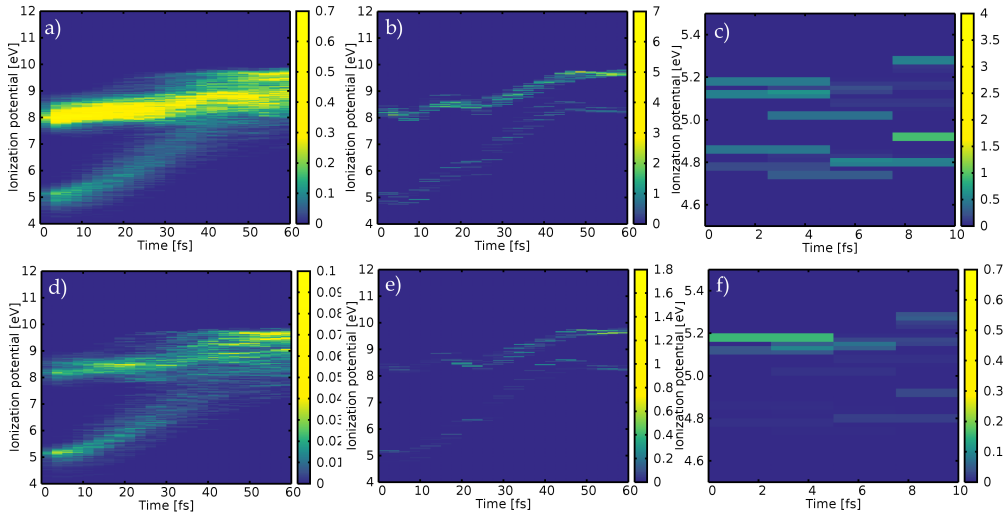

Figure 6.7: Calculated Photoelectron spectra with: a) the Dyson norms all set to one for an ensemble of trajectories, b) the Dyson norms all set to one for a single trajectories, c) the Dyson norms all set to one for a single trajectories zoomed in around time-zero, d) calculated Dyson norms for an ensemble of trajectories, e) calculated Dyson norms for a single trajectories, and f) calculated Dyson norms for a single trajectories zoomed in around time-zero

Single trajectory are also observed with all the Dyson norms set to one and using the calculated Dyson norms, Fig. 6.7 b) and e), receptively. Zooming in on the first 10 fs and focusing our attention on the 4.5 to 5.5 eV energy range, Fig. 6.7 c) and f). It is evident, especially from Fig. 6.7 c) and f), that the Dyson norms favor ionization from some states and suppress ionization from other, as we would expect. But, the overall character of the decay is preserved when comparing the calculation with and without applying the calculated Dyson norms. When it is said that the overall character of the decay is preserved, it is meant that there are band at certain energies that remain regardless of the Dyson norms. For these systems the

Dyson norms appear to give a small, albeit important, adjustment to the dynamics calculations, and they do not dramatically alter the overall dynamics.

6.4 Data Analysis

6.4.1 Background Subtraction

There are multiple sources of background electrons in this experiment that have to be eliminated or subtracted from the data. The photon energies of the UV and the VUV are both above the work function of the aluminum and the stainless steel, of which the vacuum chamber is constructed. This means that any stray or scattered light from the pulses will create electrons. To mitigate the effect of these stray electrons, long baffle arms were installed in order to absorb any of the electrons generated from beam scatter. Though these baffle arms are very effective the subtraction stray electrons that get through the baffles still needs to be performed. The electrons that are generated from any background gas in the chamber is also a concern.

In order to subtract both the electrons due to the scattering of light and from any background gas in the chamber the capability of the pulsed molecular nozzle was utilized. For every pump probe delay, measurements are made with the optical pulses overlapped with the molecular pulse, and with the molecular beam pulse delayed such that the optical pulses only interact with background gas. With these two measurements a subtraction of any background signals from residual gas in the chamber and/or scattered electrons can be done.

There is also the worry about electrons that are generated from ionization from the pump alone and from the probe alone, call this single-color signal. Therefore, signal is collected from the pump and probe beams alone after every scan in order to eliminate any single-color signal from the data.

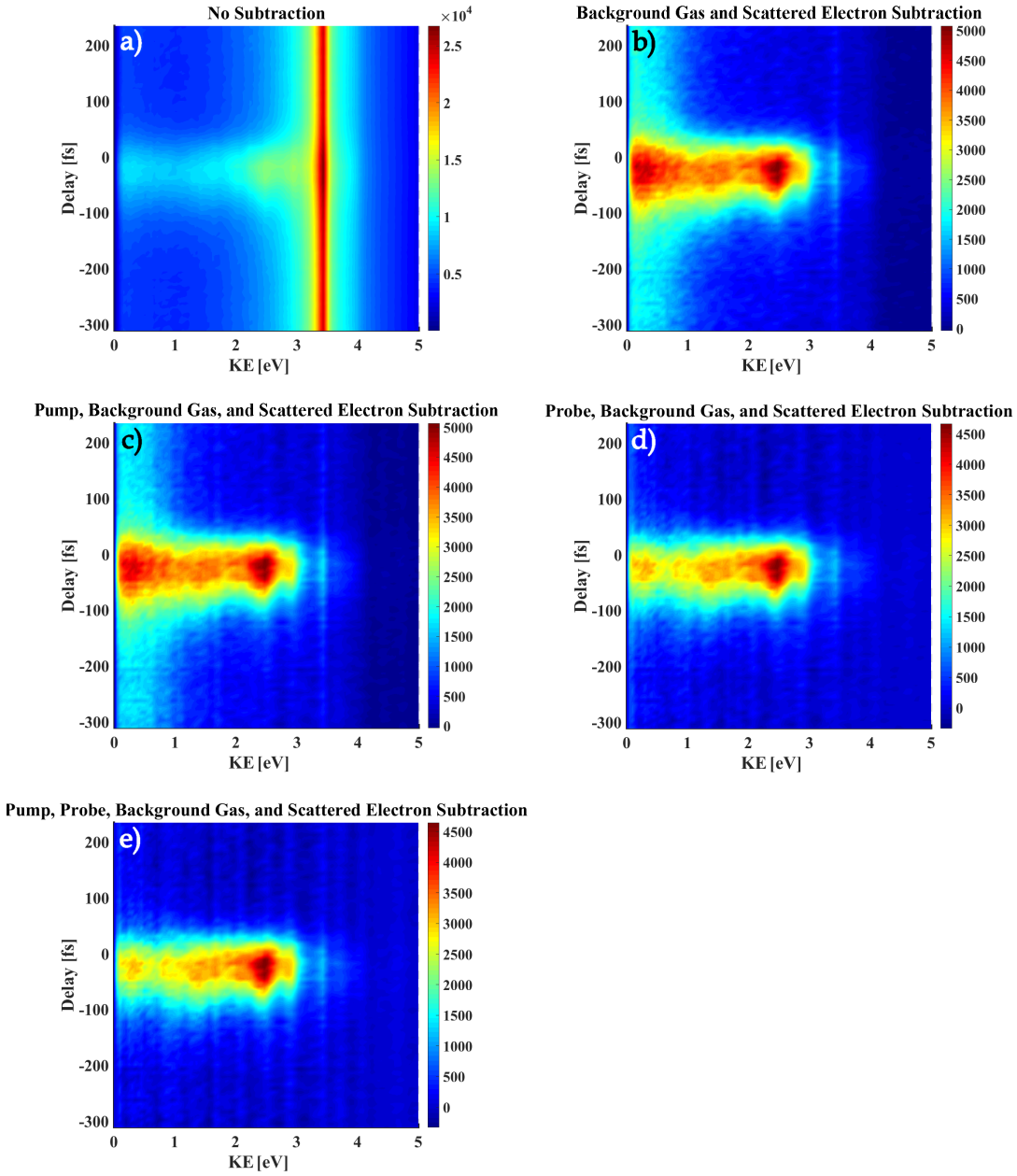

Figure 6.8: CH_2I_2 TRPES a) from raw images with no background subtraction, b) from images with subtraction of the background gas and scattered electrons from stray light from the UV and the VUV pulses, c) from images with subtraction of the pump pulse alone signal, background gas, scattered electrons, d) from images with subtraction of the probe pulse alone signal, background gas, scattered electrons, e) from images with subtraction of the pump pulse alone signal, probe pulse alone signal, background gas, scattered electrons

In Fig. 6.8, the extracted TRPES is plotted from images with various levels of background subtraction. The shocking feature of the image with no subtraction, Fig. 6.8 a), is the strong peak at $\sim$ 3.5 eV. This is simply the edge of the MCP. The VMI was set to image with 3 eV hitting the edge of the detector. Pump-probe scans were performed with the VMI voltages set so that the maximum kinetic energy of the electrons collected was 10 eV, it was found that no electrons are seen with more than 3 eV of energy. So, in order to maximize our resolution the max kinetic energy detected was set to 3 eV. Once the edge of the MCP is subtracted from the images, along with the background gas and scattered electrons, the image is significantly cleaner, Fig. 6.8 b). Then the single-color signals from the pump and the probe alone can be examined and their subtraction effects on the overall signal can be determined. The additional subtraction of the pump, Fig. 6.8 c) shows little to no change when compared to 6.8 b), indicating there is little to no single-color signal from the pump alone. In Fig. 6.8 d), the probe alone signal is subtracted on top of the background gas and scattered electron signal. It is evident that this subtraction eliminates the low energy strip in the signal that is evident in b) and c). The final background subtracted TRPES, with subtraction of the background gas and scattered electrons, the pump generated electrons, and the probe generated, can be seen in Fig. 6.8 e).

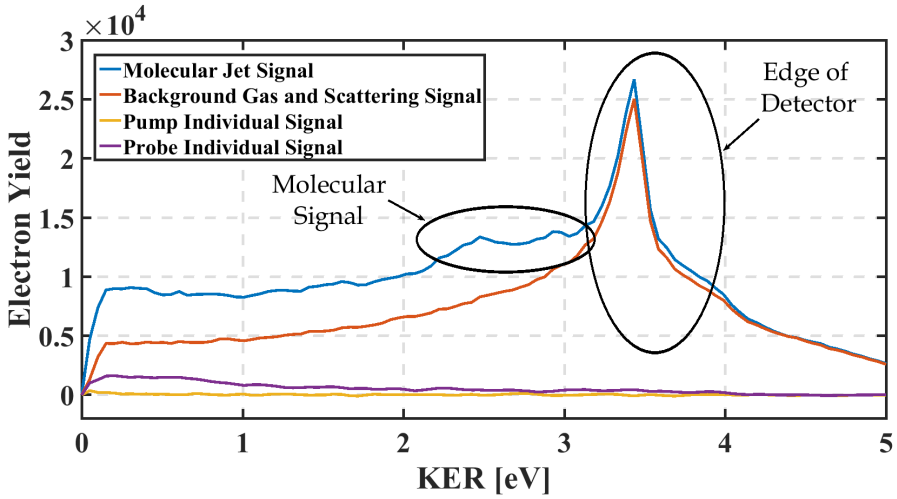

Figure 6.9: CH_2I_2 TRPES lineouts at time-zero for images used in the background analysis.

In oder to visualize the contributions from the different background sources better the photoelectron spectra lineouts at time-zero are examined. In Fig. 6.9, the individual background components are looked at that will be subtracted from the

molecular jet signal. It is clear from these lineouts that the most significant background is from the background gas and the scattered electrons. In the figure the sharp peak that comes from the edge of the MCP is circled, and the peak in the molecular jet signal that is clearly from the molecular dynamics. From Fig. 6.9 it is clear that there is a background from the probe alone signal, but the pump alone signal appears to contribute little to no background signal. The sum of the background gas and scattered electrons signal, individual pump signal, and the individual probe signal is the total background signal.

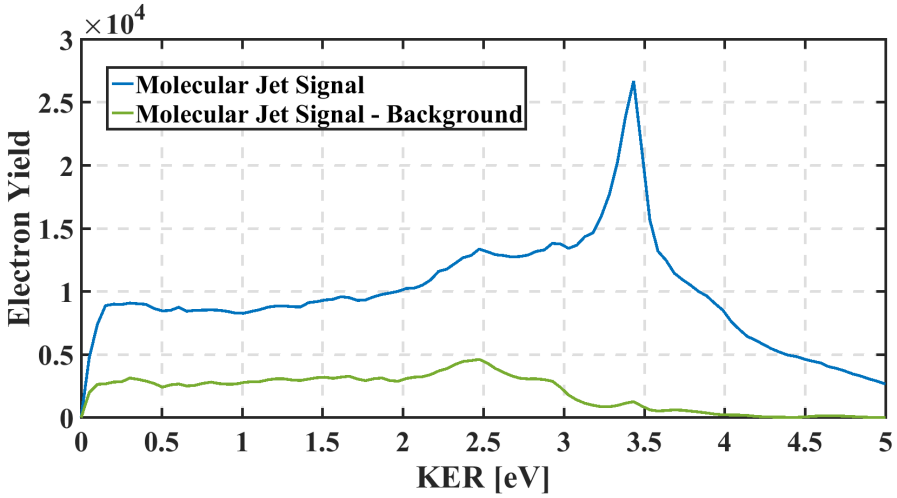

Figure 6.10: CH_2I_2 TRPES data with and without background subtraction.

In Fig. 6.10, the molecular jet signal lineout at time-zero is shown with and without the subtraction of the total background. After this background subtraction one can be confident that the signal is coming from an interaction of the target molecule with both the pump and the probe.

6.4.2 Determining the Impulse Response Function of the System and Fixing an Accurate Time-Zero

Non-resonant 1 + 1' photon ionization of xenon is used to determine the IRF and time-zero of the experiment. The TRPES of xenon can be seen in Fig. 6.11. It is evident that there is a slight asymmetry to the data (a slight diagonal tilt with respect to delay) that indicates to us that there is a slight chirp to our pulse.

In Fig. 6.11, the y-axes' zero time is only roughly determined, so in order to set zero time to be the time when the pump and probe pulses are maximally overlapped, time-zero, with a much higher degree of accuracy the xenon data is fit to a Gaussian

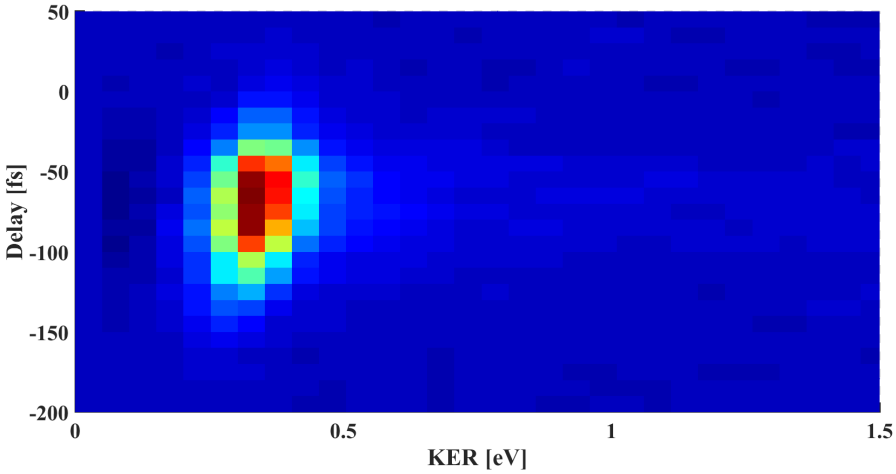

Figure 6.11: Xenon TRPES Data.

to determine the center. Integrating over the kinetic energy (KE) axes in Fig. 6.11 around the xenon peak is done in order to easily fit the data. The result of this integration of the data and the subsequent fitting can be seen in Fig. 6.12.

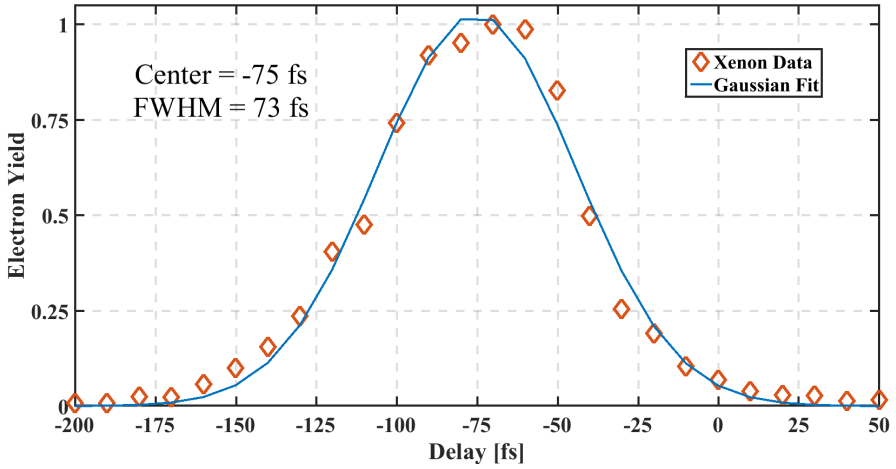

Figure 6.12: Gaussian fit to the energy integrated xenon TRPES data.

From this data the FWHM of the IRF was determined to be $\sim$75 fs, and that the center for this particular data set, time-zero, was at -75 fs. Before and after every experiment time-zero is checked in xenon to make sure that time-zero has not shifted due to a slipping of the delay stage. When the xenon data is taken after completing the experiment on our target molecule data there is still residual

target molecule left in the chamber, so we can see the xenon timing and the target molecule timing with the same measurement. In Fig. 6.13, the xenon data along with the residual CH_2I_2 TRPES are shown on the same graph.

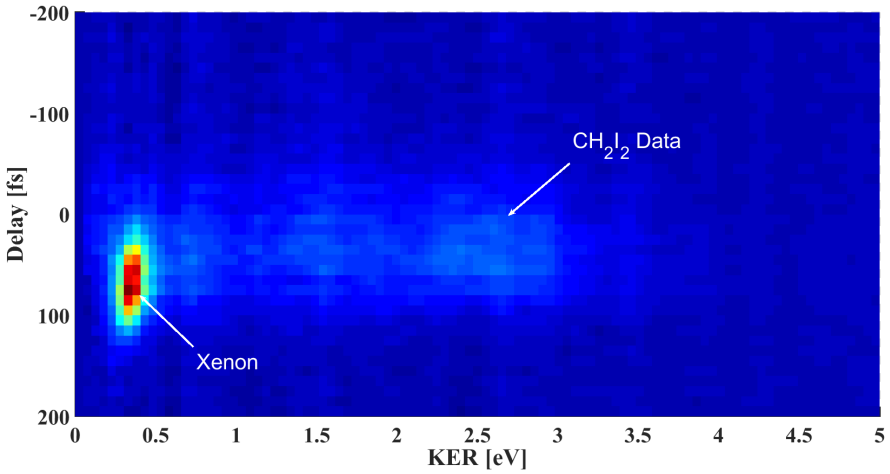

Figure 6.13: TRPES of xenon with a residual CH_2I_2 molecular signal visible.

From Fig. 6.13 it is clear that the CH_2I_2 peak is shifted towards negative delays relative to the xenon peak. This indicates that the CH_2I_2 dynamics have a strong Rydberg component coming from a VUV-pump dynamics, and that these dynamics are pulling the peak towards negative times. The question that arises from this analysis is, "Are we actually seeing any UV-pump VUV-probe dynamics?". The fear is that the oscillator strength of the VUV transition is so much larger than that of the UV transition, and that the Rydberg dynamics are dominating the signal. This question is addressed in Section 6.4.4: Showing Clear Evidence for UV Molecular Dynamics. In this section a simple model is constructed with both UV-pump VUV-probe and VUV-pump UV-probe dynamics and just VUV-pump UV-probe dynamics, and we show that our signal is consistent with measuring UV-pump VUV-probe dynamics.

6.4.3 TOFMS For CH_2I_2 and CH_2BrI

In previous chapters ions have been exclusively measured in order to visualize molecular dynamics. For ions the measurements are performed be measuring time-of-flight mass spectrum, calibrating the mass peaks, and following the mass peaks dynamics versus time. Binning a specific mass peak ables one to discriminate the target molecule signal from any background sources in the system. In the experiments discussed in this chapter TRPES are considered, and therefore electrons are

measured. With electrons one has to be careful and make sure that there is no contamination from other molecules, or the formation of clusters, in the system. One cannot distinguish electrons from different molecules in the molecular jet, so we have to make sure that our molecular jet only contains our target molecule.

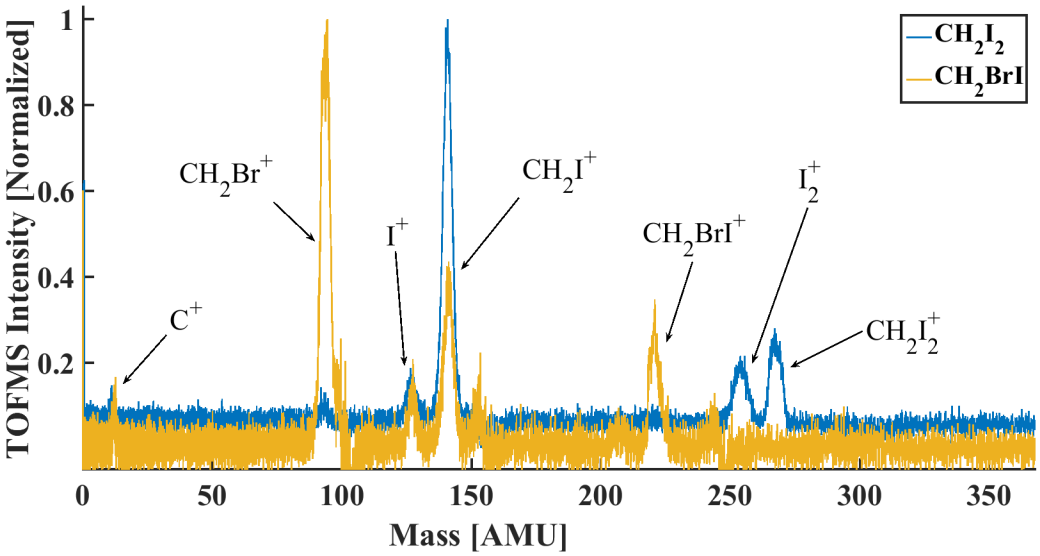

Figure 6.14: TOFMS for CH_2I_2 and CH_2BrI

To check this we perform multiphoton ionization with the UV and record the time-of-flight mass spectra (TOFMS) for the ions, shown in Fig. 6.14. The two data sets were taken with CH_2I_2 only (blue) and CH_2BrI only (yellow) in the molecular jet. The pulsed nozzle and the bubbler are also thoroughly cleaned when the target molecule to be studied is changed. It is evident from the TOFMS that there is some contamination in the sample from I_2 in the CH_2I_2 data that we should be mindful of, and there is no evidence of clustering in either sample (the mass spectrum goes out to 1000 AMUs, but the trace is cut to make it easier to read). This lends confidence to the idea that the signal observed is coming from unclustered CH_2I_2 and CH_2BrI molecules. But not observing evidence of clusters in TOFMS does not rule out their existence in the molecular beam, because clusters can be unstable and fragment into the components that are observed in the TOFMS before it reaches the detector.

6.5 Results and Discussion

The TRPES experimental and calculated results for CH_2I_2 can be seen in Fig. 6.15. The calculated results have been convolved with the IRF of the system to compare

them with the experiment. From [158] the VUV absorption cross section is estimated to be four times that of the UV absorption cross section. This means that around time-zero the signal is a combination of both UV and VUV excited dynamics. Because of this, the signal level at longer times is multiplied by 2.5 to help show the UV dynamics signal that are being suppressed by the stronger VUV dynamics. It is also good to note that the signal from the VUV-pump and UV-probe dynamics should be identical to the signal from UV-pump and VUV-probe dynamics at exactly time-zero. For movements of the wave packet away from time-zero there will be differences in the two sides dynamics that are complicated to disentangle at short times due to the time-resolution of the measurements.

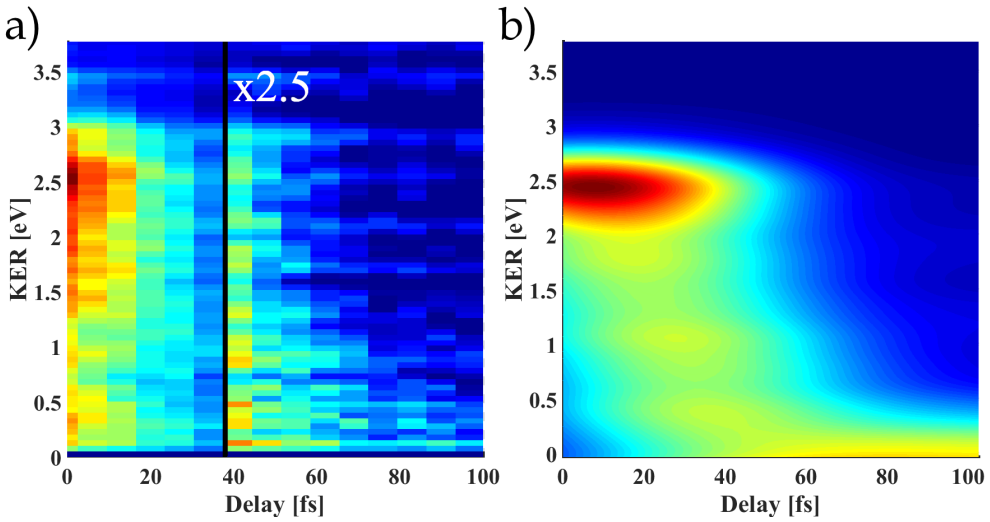

Figure 6.15: CH_2I_2 time-resolved photoelectron spectra a) experimental b) calculated

There is good agreement between the experimental and calculated TRPES in Fig. 6.15. There is an initial peak at 2.5 eV, corresponding to ionization to D_0 with $h\nu - IP$ at the Franck Condon point. Then the peak decays rapidly and shifts to lower energy as the wave packet rides down the PES.

The TRPES experimental and calculated results for CH_2BrI can be seen in Fig. 6.16. The calculation and the experiment show two peaks at time-zero separated by $\sim$ 0.9 eV. These two peaks are due to two different cationic states that can reached by the VUV after the molecule is pumped with the UV. The calculation and the experiment both show a rapid decay of the two peaks in $\sim$80 fs, and show evidence at longer delays of a very slight lower energy tail.

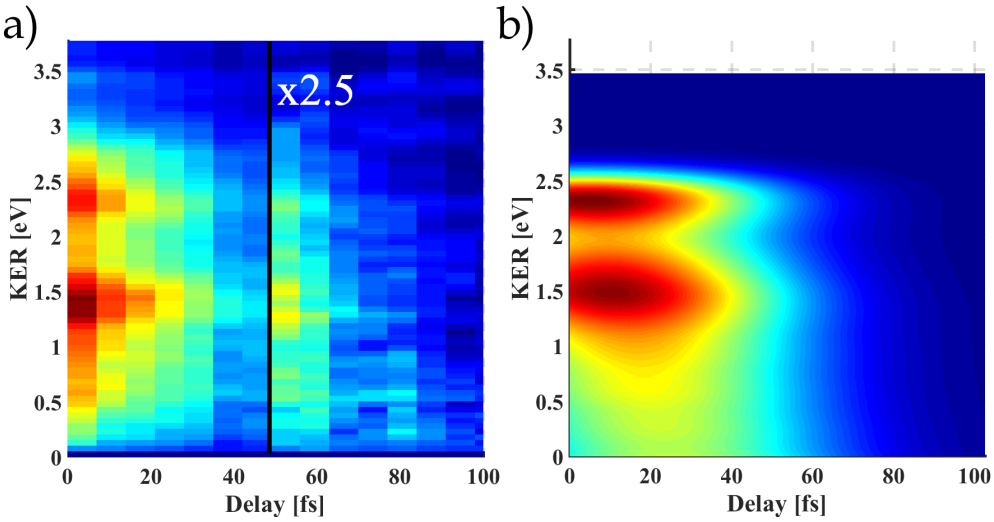

Figure 6.16: CH_2BrI time-resolved photoelectron spectra a) experimental b) calculated

The level of agreement between the calculation and the data here is really quite remarkable, where the calculation and the experiments are in such good agreement without any adjustable parameters. Being able to plot the calculation and the experimental data side-by-side and do a detailed comparison of the features with this data is invaluable. Instead of trying to fit the calculations and the experimental data to decay constants, that do not always do justice to the rich dynamics that are really being undertaken in these systems, it is more transparent to have the calculation and the data plotted together. This agreement gives one the confidence to interpret the theory in detail, providing a complete picture of the dynamics. If one didn't have such good agreement, then there would be little confidence in interpreting the theory.

6.5.1 Showing Clear Evidence for UV Molecular Dynamics

In order to verify that the experiment is capturing UV-pump VUV-probe dynamics the experiment is modeled. The IRF of the apparatus measured to be 75 fs from the xenon TRPES data, as previously mentioned in detail. The overall molecular decay is modeled with a sum of two exponential decays, with the VUV decay having four times the amplitude of the UV dynamics. The factor of four difference in the amplitudes of the UV and the VUV decays is determined by analyzing optical density measurements and calculations presented in [158]. The molecular dynamics

signal is then convolved with the IRF of the apparatus. The UV dynamics are then removed from the molecular dynamics signal and the convolution with the IRF is done again. The results can be seen in Fig. 6.17. Alongside the model is the experimental CH_2I_2 TRPES data integrated from 0 - 0.5 eV. This energy region was chosen because this is the energy region where there appears to be long lived positive timescale dynamics. The experimental data is used to determine the time constants for the decays used. It is clear that with only VUV dynamics there should be no signal past 80 fs. Clearly seeing a signal at 80 fs in the experimental data indicates that we are indeed resolving UV-pump VUV-probe dynamics.

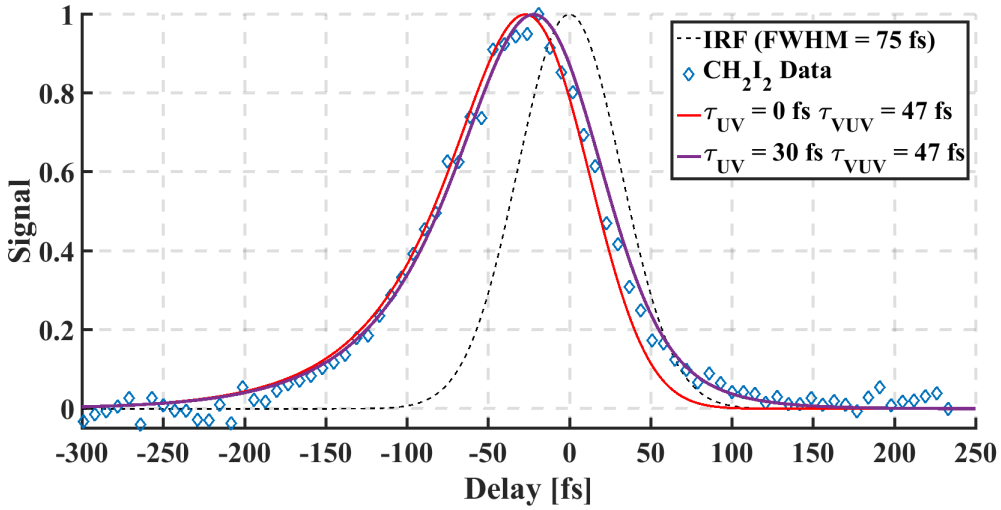

Figure 6.17: The convolution of the IRF and the molecular dynamics signal with (purple) and without (red) UV dynamics plotted alongside the experimental CH_2I_2 data (integrated TRPES data from 0 - 0.5 eV) and the IRF of the system.

Fig. 6.18 shows the individual components used in this simple model of the molecular dynamics signal.

As another check, the integration of the CH_2I_2 TRPES data was binned into energy regions of 0.5 eV. The results of this binning can be seen in Fig. 6.19. It is clear that as one bins to higher energies the tail in the signal towards the UV-pump VUV-probe side of the dynamics begins to disappear. This is consistent with Philipp Marquetand's calculations that say one should only see a lower energy tail.

Compare the signal at lower and higher energy binning to convolutions with and without the UV molecular dynamics can be seen in Fig. 6.20. From this analysis it is clear that at higher energies the dynamics cannot be distinguished from the VUV dynamics. If the data really contained information on the UV driven dynamics, then

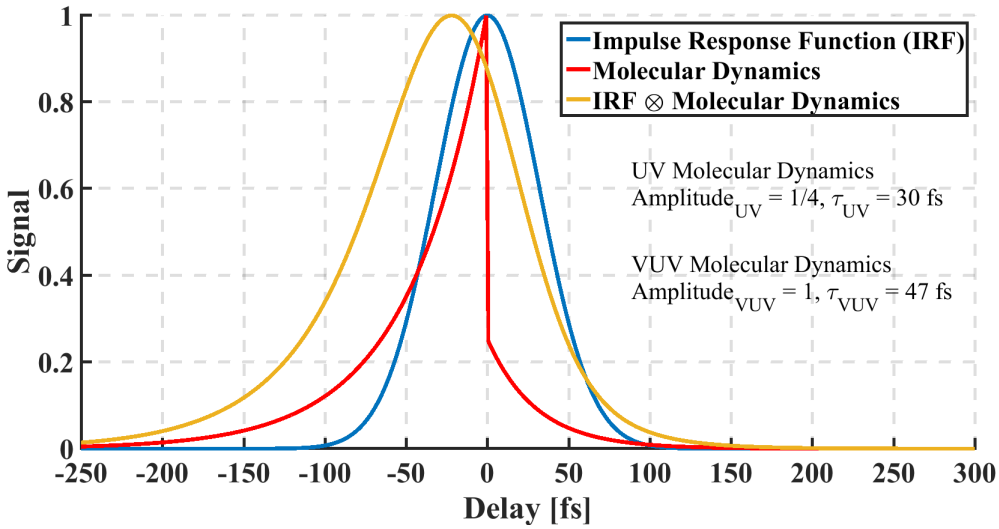

Figure 6.18: The modeling of the molecular dynamics of CH_2I_2. The UV dynamics has an amplitude of 1/4 and a decay constant of 30 fs, and the VUV dynamics has an amplitude of 1 and a decay constant of 47 fs. We convolve this with the measured IRF to model the experiment.

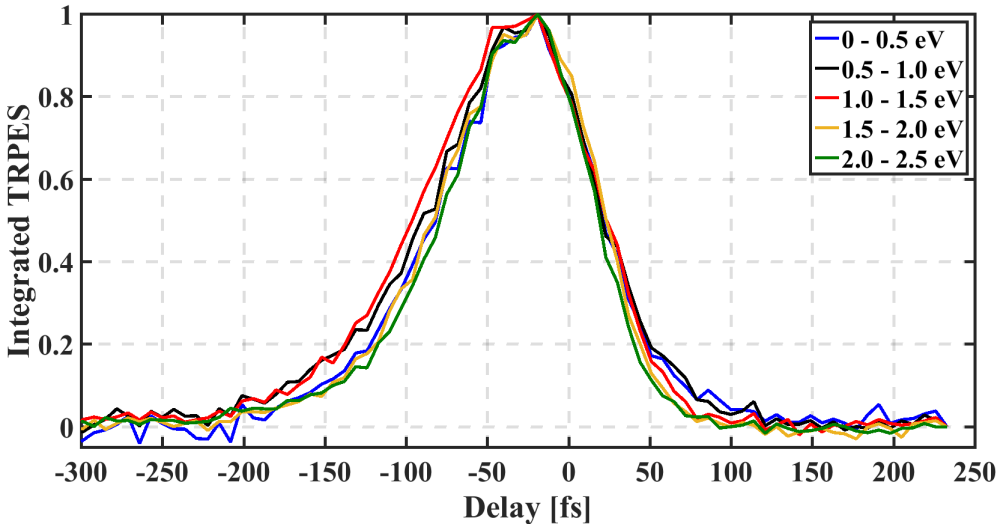

Figure 6.19: CH_2I_2 TRPES integrated over different energy regions.

one would expect an energy dependence in the decay at positive times based on calculations carried out by Philipp Marquetand. Since there is an energy dependence

in the decay for positive times that matches these calculations it is evident that UV driven dynamics are being observed in these measurements.

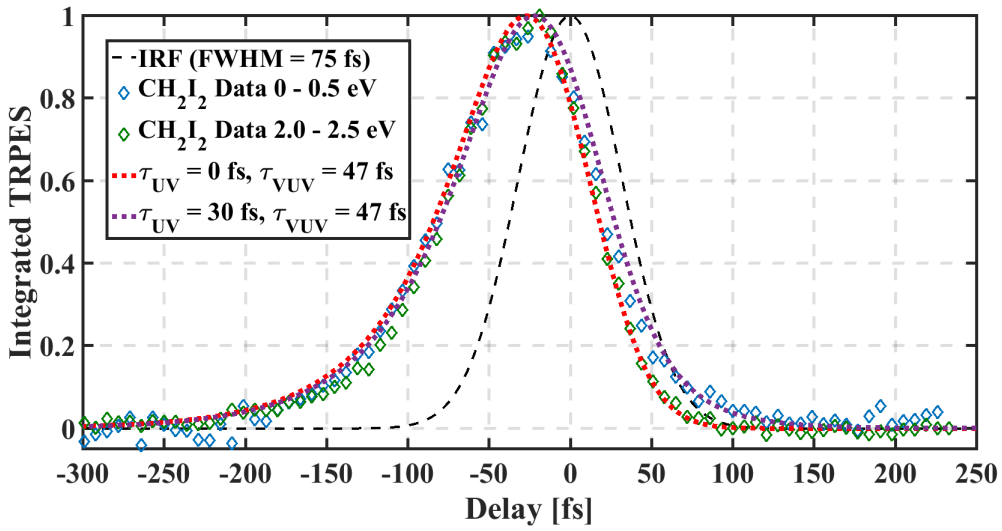

Figure 6.20: CH_2I_2 TRPES data integrated over the low energy region (0 - 0.5 eV) and the high energy region (2 -2.5 eV), alongside the IRF of the system, simulated signal with just VUV dynamics (dotted red line), and simulated signal with VUV and UV dynamics (dotted purple line).

6.6 Molecular Movies

With confidence in the calculation, the calculation can be examined in more detail to gain more insight into the molecular dynamics that cannot be realized from the experiment. In Fig. 6.21 the C-I bond distances for the iodines, I_1 and I_2, are shown versus time for the different trajectories. This figure illustrates the variable lifetimes of different trajectories and that several trajectories crash before 100 fs.

In Fig. 6.21 there are three main grouping that can be seen from the trajectories. The first is that some of the trajectories have an upward slope to the bond length with an oscillatory behavior. The upward slope indicates that the iodine is dissociating, and the oscillation is indicative of a rotation of the carbon around the non-dissociated iodine. The second grouping is just an oscillation around the initial bond length. This indicates that the iodine is not dissociating in these trajectories and that the carbon is simply oscillating with respect to the iodine. The third grouping are trajectories that don't appear to have much movement in the C-I distance. Since the molecule is symmetric and has two iodines the first two grouping can be put together. In the trajectories where I_1 dissociates, I_2 remains bound to the carbon. In trajectories where I_2 dissociates, I_1 remains bound to the carbon. Therefore, the dynamics are the same that produce the two groupings. The third grouping is a unique case where it is believed that the molecule does not dissociate along the C-I coordinate, but rather the wave packet explores another coordinate (the calculation is currently being checked to look into this hypothesis).

The bond distances and angles between all the atoms in the molecule are tracked versus time, not just the C-I bond distance, in these dynamics calculations, and from this information a "molecular movie" can be constructed for each trajectory.

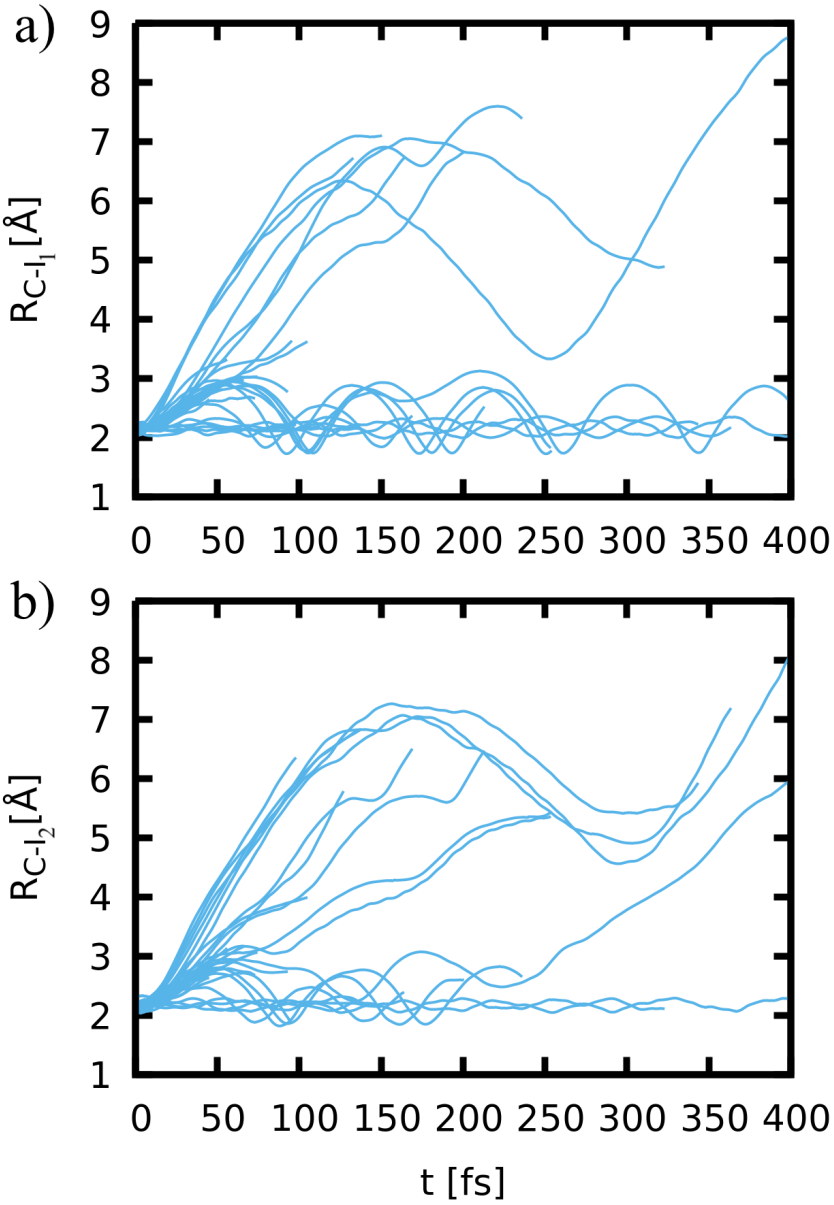

Figure 6.21: Calculation results for CH_2I_2 that show a) the C-I_1 bond distance versus time for all trajectories, and b) the C-I_2 bond distance versus time for all trajectories.

Snapshots were taken from a single trajectory that seemed to capture the general dynamics of this system to generate "molecular movie" seen in Fig. 6.22 for CH_2I_2 in 15 fs intervals. The overall motion undertaken by the molecule are indicated in the first panel at 0 fs. The two main motions of the molecule are a dissociation of an iodine and the rotation of the CH_2 around the remaining iodine.

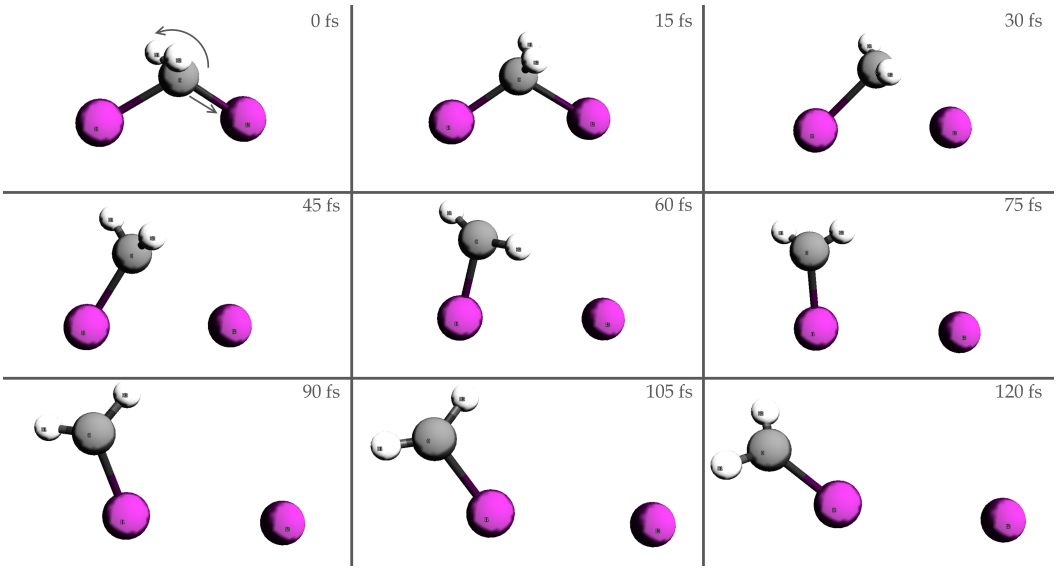

Figure 6.22: CH_2I_2 molecular movie generated from calculations. Snapshots of the movie in 15 fs steps are shown. At 0 fs we indicate the general motion undertaken by the molecule. There is a rotation of the CH_2 around the iodine and dissociation (leaving) of the other iodine from the system.

In Fig. 6.23 the C-I bond and the C-Br bond distances are shown versus time for the different trajectories. In CH_2BrI the trajectories are much longer lived. There are two main groupings of trajectories. One where the C-I distance has an upward slope and an oscillatory nature, and one where the C-I distance simply oscillates. The upward slope and the oscillation indicates that the iodine is dissociating and that the carbon is then left to oscillate around the remaining bromine. The trajectories where the C-I distance only oscillates are correlated with trajectories where the bromine dissociates. It is also interesting to note that the trajectories that show bromine dissociation tend to all crash around 150 fs, whereas the trajectories that show iodine dissociation all live for 400 fs. This can indicate a problem with the active space of the calculation and that is cannot completely capture the bromine dissociation dynamics.

As was the case for CH_2I_2, the bond distances and angles between all the atoms in the molecule are tracked versus time in these dynamics calculations.

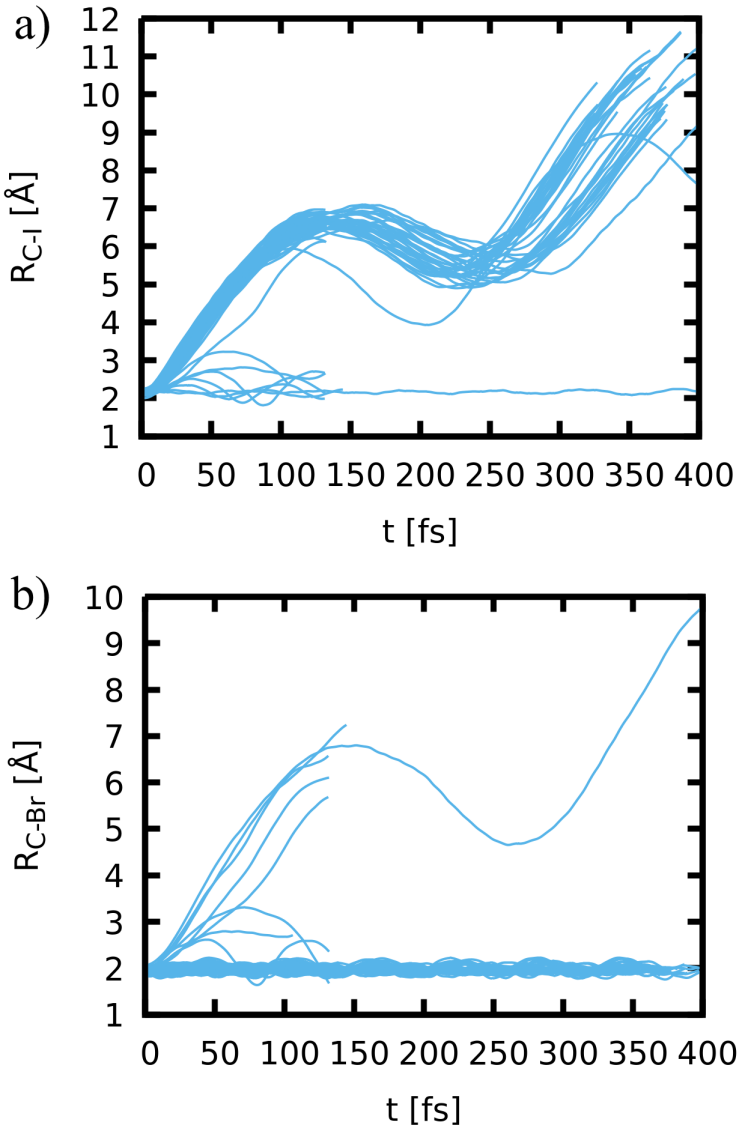

Figure 6.23: CH_2BrI trajectories.

Again, snapshots were taken from a single trajectory that seemed to capture the general dynamics of this system to generate "molecular movie" seen in Fig. 6.24 for CH_2BrI in 15 fs intervals. The overall motion undertaken by CH_2BrI is very similar to those for CH_2I_2 and are indicated in the first panel at 0 fs. The two main motions of the molecule are a dissociation of an iodine and the rotation of the CH_2 around the bromine.

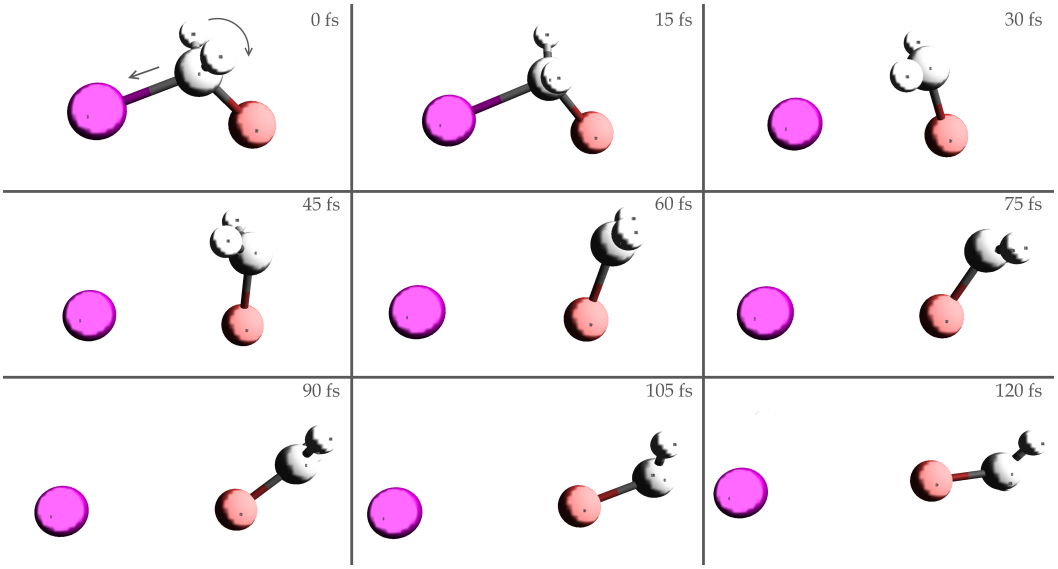

Figure 6.24: CH_2BrI molecular movie generated from calculations. Snapshots of the movie in 15 fs steps are shown. At 0 fs we indicate the general motion undertaken by the molecule. There is a rotation of the CH_2 around the bromine and dissociation (leaving) of the iodine from the system.

With these "molecular movies" we have accomplished our original goal of pursuing and experimental technique that can give us a detailed calculable observable that can be used to give us enough confidence in our calculations that one can trust the "molecular movies" that are generated from them.

6.7 Conclusion

UV-pump and weak-field ionization VUV-probe time-resoled photoelecton spectroscopy was performed on CH_2I_2 and CH_2BrI, where the kinetic energy release of the emitted electron was collected versus the delay between the pump and the probe pulses. These experiments there then directly compared to detailed dynamics calculations, and it was found that there was a high degree of agreement between the two. The strong agreement between the calculations and the experimental data enables one to really trust the "molecular movie" generated from the dynamics calculations.

Chapter 7

Conclusion

This thesis covered the use of ionization as a probe of molecular dynamics. A WFI pump probe time-resolved ionization spectrometer that utilized UV (260 nm) and VUV (156 nm) light was developed to study molecular dynamics. The high lying neutral excited state dynamics of pyrrole were examined. Previous studies had pumped pyrrole to low lying excited states and witnessed dissociation of a hydrogen atom as the dominant decay channel, whereas it was found when pumping pyrrole to a high lying excited state that internal conversion appeared to be the dominant relaxation channel of the system. Because of the high density of states of highly excited pyrrole this study was related to the relaxation dynamics of radical cations, where rapid internal conversion to the ground ionic state tends to occurred before dissociation. The conversion of vibrational kinetic energy into electronic potential energy was examined in large organic molecules with many degrees of freedom. In 1,3-cyclohexadine below threshold ionization was observed. It was interpreted in terms of vibrationally assisted ionization facilitated by the excitation of C-C stretching vibrations, which were activated during internal conversion from the photo-excited state down to the ground state. WFI and SFI are directly compared are probes of molecular dynamics. It was found that SFI and WFI may provide a similar qualitative picture of the relaxation dynamics, but only WFI can be used for a real quantitative comparison with calculations. Using a WFI time-resolved photoelectron spectrometer at the Nation Research Council of Canada a detailed comparison was performed of the photoelectron spectra with calculation for diiodomethane and bromoiodomethane. After verifying the calculations with these experiments, "molecular movies" were constructed based off of the calculations.

In this thesis it is argued that the only way to truly make a "molecular movie" is through calculation, and the goal of experiment should be to measure an observable that can be readily calculated in order to verify calculations. It was shown that a high degree of agreement between experiment and theory can indeed be obtained

through the use of WFI time resolved photoelectron and photoion spectroscopy. For future experiments, a TimepixCam, with nanosecond individual pixel resolution, could be integrated with VMI detection of both electrons and ions to serve as more thorough verification of calculations.

Bibliography

[1] J. C. Williamson, J. Cao, H. Ihee, H. Frey, and A. H. Zewail, "Clocking transient chemical changes by ultrafast electron diffraction," *Nature*, vol. 386, no. 6621, p. 159, 1997.

[2] M. Dantus, S. B. Kim, J. C. Williamson, and A. H. Zewail, "Ultrafast electron diffraction. 5. experimental time resolution and applications," *The Journal of Physical Chemistry*, vol. 98, no. 11, pp. 2782–2796, 1994.

[3] P. Reckenthaeler, M. Centurion, W. Fuß, S. A. Trushin, F. Krausz, and E. E. Fill, "Time-resolved electron diffraction from selectively aligned molecules," *Physical Review Letters*, vol. 102, no. 21, p. 213001, 2009.

[4] S. Weathersby, G. Brown, M. Centurion, T. Chase, R. Coffee, J. Corbett, J. Eichner, J. Frisch, A. Fry, M. Gühr, *et al.*, "Mega-electron-volt ultrafast electron diffraction at slac national accelerator laboratory," *Review of Scientific Instruments*, vol. 86, no. 7, p. 073702, 2015.

[5] J. Yang, M. Guehr, X. Shen, R. Li, T. Vecchione, R. Coffee, J. Corbett, A. Fry, N. Hartmann, C. Hast, K. Hegazy, K. Jobe, I. Makasyuk, J. Robinson, M. S. Robinson, S. Vetter, S. Weathersby, C. Yoneda, X. Wang, and M. Centurion, "Diffractive imaging of coherent nuclear motion in isolated molecules," *Physical Review Letters*, vol. 117, p. 153002, Oct 2016.

[6] J. Cao and K. R. Wilson, "Ultrafast x-ray diffraction theory," *The Journal of Physical Chemistry A*, vol. 102, no. 47, pp. 9523–9530, 1998.

[7] K. Gaffney and H. Chapman, "Imaging atomic structure and dynamics with ultrafast x-ray scattering," *Science*, vol. 316, no. 5830, pp. 1444–1448, 2007.

[8] F. Schotte, M. Lim, T. A. Jackson, A. V. Smirnov, J. Soman, J. S. Olson, G. N. Phillips, M. Wulff, and P. A. Anfinrud, "Watching a protein as it functions with 150-ps time-resolved x-ray crystallography," *Science*, vol. 300, no. 5627, pp. 1944–1947, 2003.

[9] M. P. Minitti, J. M. Budarz, A. Kirrander, J. S. Robinson, D. Ratner, T. J. Lane, D. Zhu, J. M. Glownia, M. Kozina, H. T. Lemke, M. Sikorski, Y. Feng, S. Nelson, K. Saita, B. Stankus, T. Northey, J. B. Hastings, and P. M. Weber, "Imaging molecular motion: Femtosecond x-ray scattering of an electrocyclic chemical reaction," *Phys. Rev. Lett.*, vol. 114, p. 255501, Jun 2015.

[10] R. Berera, R. van Grondelle, and J. T. Kennis, "Ultrafast transient absorption spectroscopy: principles and application to photosynthetic systems," *Photosynthesis Research*, vol. 101, no. 2-3, pp. 105–118, 2009.

[11] C. Ruckebusch, M. Sliwa, P. d. Pernot, A. De Juan, and R. Tauler, "Comprehensive data analysis of femtosecond transient absorption spectra: A review," *Journal of Photochemistry and Photobiology C: Photochemistry Reviews*, vol. 13, no. 1, pp. 1–27, 2012.

[12] C. Wan, T. Fiebig, S. O. Kelley, C. R. Treadway, J. K. Barton, and A. H. Zewail, "Femtosecond dynamics of dna-mediated electron transfer," *Proceedings of the National Academy of Sciences*, vol. 96, no. 11, pp. 6014–6019, 1999.

[13] J.-M. L. Pecourt, J. Peon, and B. Kohler, "Ultrafast internal conversion of electronically excited rna and dna nucleosides in water," *Journal of the American Chemical Society*, vol. 122, no. 38, pp. 9348–9349, 2000.

[14] W. J. Schreier, T. E. Schrader, F. O. Koller, P. Gilch, C. E. Crespo-Hernández, V. N. Swaminathan, T. Carell, W. Zinth, and B. Kohler, "Thymine dimerization in dna is an ultrafast photoreaction," *Science*, vol. 315, no. 5812, pp. 625–629, 2007.

[15] A. Stolow and J. G. Underwood, "Time-resolved photoelectron spectroscopy of non-adiabatic dynamics in polyatomic molecules," *arXiv preprint arXiv:1507.02204*, 2015.

[16] A. Stolow, A. E. Bragg, and D. M. Neumark, "Femtosecond time-resolved photoelectron spectroscopy," *Chemical ROeviews*, vol. 104, no. 4, pp. 1719–1758, 2004.

[17] V. Blanchet, M. Z. Zgierski, T. Seideman, and A. Stolow, "Discerning vibronic molecular dynamics using time-resolved photoelectron spectroscopy," *Nature*, vol. 401, no. 6748, p. 52, 1999.

[18] S. Ullrich, T. Schultz, M. Z. Zgierski, and A. Stolow, "Electronic relaxation dynamics in dna and rna bases studied by time-resolved photoelectron spectroscopy," *Physical Chemistry Chemical Physics*, vol. 6, no. 10, pp. 2796–2801, 2004.

[19] P. Sándor, V. Tagliamonti, A. Zhao, T. Rozgonyi, M. Ruckenbauer, P. Marquetand, and T. Weinacht, "Strong field molecular ionization in the impulsive limit: Freezing vibrations with short pulses," *Physical review letters*, vol. 116, no. 6, p. 063002, 2016.

[20] V. Tagliamonti, P. Sándor, A. Zhao, T. Rozgonyi, P. Marquetand, and T. Weinacht, "Nonadiabatic dynamics and multiphoton resonances in strong-field molecular ionization with few-cycle laser pulses," *Physical Review A*, vol. 93, no. 5, p. 051401, 2016.

[21] I. Wilkinson, A. E. Boguslavskiy, J. Mikosch, J. B. Bertrand, H. J. Wörner, D. M. Villeneuve, M. Spanner, S. Patchkovskii, and A. Stolow, "Excited state dynamics in so2. i. bound state relaxation studied by time-resolved photoelectron-photoion coincidence spectroscopy," *The Journal of chemical physics*, vol. 140, no. 20, p. 204301, 2014.

[22] C. Okabe, T. Nakabayashi, Y. Inokuchi, N. Nishi, and H. Sekiya, "Ultrafast excited-state dynamics in photochromic n-salicylideneaniline studied by femtosecond time-resolved rempi spectroscopy," *The Journal of chemical physics*, vol. 121, no. 19, pp. 9436–9442, 2004.

[23] S. Trushin, W. Fuss, and W. Schmid, "Conical intersections, pseudorotation and coherent oscillations in ultrafast photodissociation of group-6 metal hexacarbonyls," *Chemical Physics*, vol. 259, no. 2, pp. 313–330, 2000.

[24] S. Trushin, W. Fuss, W. Schmid, and K. Kompa, "Femtosecond dynamics and vibrational coherence in gas-phase ultraviolet photodecomposition of cr (co) 6," *The Journal of Physical Chemistry A*, vol. 102, no. 23, pp. 4129–4137, 1998.

[25] V. Tagliamonti, B. Kaufman, A. Zhao, T. Rozgonyi, P. Marquetand, and T. Weinacht, "Time-resolved measurement of internal conversion dynamics in strong-field molecular ionization," *Physical Review A*, vol. 96, no. 2, p. 021401, 2017.

[26] M. Spanner, S. Patchkovskii, C. Zhou, S. Matsika, M. Kotur, and T. C. Weinacht, "Dyson norms in xuv and strong-field ionization of polyatomics: Cytosine and uracil," *Physical Review A*, vol. 86, no. 5, p. 053406, 2012.

[27] C. Melania Oana and A. I. Krylov, "Dyson orbitals for ionization from the ground and electronically excited states within equation-of-motion coupled-cluster formalism: Theory, implementation, and examples," *The Journal of Chemical Physics*, vol. 127, no. 23, p. 234106, 2007.

[28] R. W. Boyd, *Nonlinear optics*. Elsevier, 2003.

[29] M. Beutler, M. Ghotbi, F. Noack, and I. Hertel, "Generation of sub-50-fs vacuum ultraviolet pulses by four-wave mixing in argon," *Optics letters*, vol. 35, no. 9, pp. 1491–1493, 2010.

[30] M. Ghotbi, M. Beutler, and F. Noack, "Generation of 2.5 μj vacuum ultraviolet pulses with sub-50 fs duration by noncollinear four-wave mixing in argon," *Optics letters*, vol. 35, no. 20, pp. 3492–3494, 2010.

[31] A. Börzsönyi, Z. Heiner, M. Kalashnikov, A. Kovács, and K. Osvay, "Dispersion measurement of inert gases and gas mixtures at 800 nm," *Applied optics*, vol. 47, no. 27, pp. 4856–4863, 2008.

[32] P. Milonni and J. H. Eberly, *Laser Physics.–J.* Wiley & Sons, Hoboken, 2010.

[33] X. Lu, Q. Liu, Z. Liu, S. Sun, P. Ding, B. Ding, and B. Hu, "Measurement of nonlinear refractive index coefficient using emission spectrum of filament induced by gigawatt-femtosecond pulse in bk7 glass," *Applied optics*, vol. 51, no. 12, pp. 2045–2050, 2012.

[34] F. Rugamas, D. Roundy, G. Mikaelian, G. Vitug, M. Rudner, J. Shih, D. Smith, J. Segura, and M. Khakoo, "Angular profiles of molecular beams from effusive tube sources: I. experiment," *Measurement Science and Technology*, vol. 11, no. 12, p. 1750, 2000.

[35] X. Wang, S. Tong, M. Ge, W. Wang, and D. Wang, "Photoelectron spectroscopy of terpenoids and prediction of their rate constants in atmospheric oxidation reactions," *Chinese science bulletin*, vol. 55, no. 35, pp. 4018–4025, 2010.

[36] K. Kosma, S. A. Trushin, W. Fuß, and W. E. Schmid, "Ultrafast dynamics and coherent oscillations in ethylene and ethylene-d 4 excited at 162 nm," *The Journal of Physical Chemistry A*, vol. 112, no. 33, pp. 7514–7529, 2008.

[37] P. Farmanara, O. Steinkellner, M. Wick, M. Wittmann, G. Korn, V. Stert, and W. Radloff, "Ultrafast internal conversion and photodissociation of

molecules excited by femtosecond 155 nm laser pulses," *The Journal of chemical physics*, vol. 111, no. 14, pp. 6264–6270, 1999.

[38] T. Allison, *Femtosecond molecular dynamics studied with vacuum ultraviolet pulse pairs*. PhD thesis, UC Berkeley: Physics, 2010.

[39] H. Tao, T. Allison, T. Wright, A. Stooke, C. Khurmi, J. Van Tilborg, Y. Liu, R. Falcone, A. Belkacem, and T. Martinez, "Ultrafast internal conversion in ethylene. i. the excited state lifetime," *The Journal of chemical physics*, vol. 134, no. 24, p. 244306, 2011.

[40] P. Bevington and D. K. Robinson, *Data reduction and error analysis for the physical sciences*. McGraw-Hill, New York, 2003.

[41] J. R. Vig, "Uv/ozone cleaning of surfaces," *Journal of Vacuum Science & Technology A: Vacuum, Surfaces, and Films*, vol. 3, no. 3, pp. 1027–1034, 1985.

[42] J.-C. Diels and W. Rudolph, *Ultrashort laser pulse phenomena*. Elsevier, 2006.

[43] Z. Chang, *Fundamentals of attosecond optics*. CRC Press, 2016.

[44] R. Trebino, *Frequency-resolved optical gating: the measurement of ultrashort laser pulses*. Springer Science & Business Media, 2012.

[45] A. V. Smith, *Crystal nonlinear optics: with SNLO examples*. AS-Photonics, 2015.

[46] D. Blank, S. North, and Y. Lee, "The ultraviolet photodissociation dynamics of pyrrole," *Chemical physics*, vol. 187, no. 1-2, pp. 35–47, 1994.

[47] J. Wei, J. Riedel, A. Kuczmann, F. Renth, and F. Temps, "Photodissociation dynamics of pyrrole: Evidence for mode specific dynamics from conical intersections," *Faraday discussions*, vol. 127, pp. 267–282, 2004.

[48] J. Wei, A. Kuczmann, J. Riedel, F. Renth, and F. Temps, "Photofragment velocity map imaging of h atom elimination in the first excited state of pyrrole," *Physical Chemistry Chemical Physics*, vol. 5, no. 2, pp. 315–320, 2003.

[49] A. van den Brom, M. Kapelios, T. Kitsopoulos, N. Nahler, B. Cronin, and M. Ashfold, "Photodissociation and photoionization of pyrrole following the multiphoton excitation at 243 and 364.7 nm," *Physical Chemistry Chemical Physics*, vol. 7, no. 5, pp. 892–899, 2005.

[50] G. Roberts, C. Williams, H. Yu, A. Chatterley, J. Young, S. Ullrich, and V. Stavros, "Probing ultrafast dynamics in photoexcited pyrrole: timescales for 1 $\pi\sigma^*$ mediated h-atom elimination," *Faraday discussions*, vol. 163, pp. 95–116, 2013.

[51] R. Montero, V. Ovejas, M. Fernández-Fernández, Á. Conde, and A. Longarte, "Revisiting the relaxation dynamics of isolated pyrrole," *The Journal of chemical physics*, vol. 141, no. 1, p. 014303, 2014.

[52] V. Vallet, Z. Lan, S. Mahapatra, A. Sobolewski, and W. Domcke, "Photochemistry of pyrrole: Time-dependent quantum wave-packet description of the dynamics at the $\pi 1\sigma^*$-s0 conical intersections," *The Journal of chemical physics*, vol. 123, no. 14, p. 144307, 2005.

[53] G. Roberts, C. Williams, H. Yu, A. Chatterley, J. Young, S. Ullrich, and V. Stavros, "Probing ultrafast dynamics in photoexcited pyrrole: timescales for 1 $\pi\sigma^*$ mediated h-atom elimination," *Faraday discussions*, vol. 163, pp. 95–116, 2013.

[54] A. Sobolewski, W. Domcke, C. Dedonder-Lardeux, and C. Jouvet, "Excited-state hydrogen detachment and hydrogen transfer driven by repulsive 1 $\pi\sigma^*$ states: a new paradigm for nonradiative decay in aromatic biomolecules," *Physical Chemistry Chemical Physics*, vol. 4, no. 7, pp. 1093–1100, 2002.

[55] M. Barbatti, J. Pittner, M. Pederzoli, U. Werner, R. Mitrić, V. Bonačić-Koutecký, and H. Lischka, "Non-adiabatic dynamics of pyrrole: Dependence of deactivation mechanisms on the excitation energy," *Chemical Physics*, vol. 375, no. 1, pp. 26–34, 2010.

[56] K. Saita, M. Nix, and D. Shalashilin, "Simulation of ultrafast photodynamics of pyrrole with a multiconfigurational ehrenfest method," *Physical Chemistry Chemical Physics*, vol. 15, no. 38, pp. 16227–16235, 2013.

[57] G. Wu, S. Neville, O. Schalk, T. Sekikawa, M. Ashfold, G. Worth, and A. Stolow, "Excited state non-adiabatic dynamics of pyrrole: A time-resolved photoelectron spectroscopy and quantum dynamics study," *The Journal of chemical physics*, vol. 142, no. 7, p. 074302, 2015.

[58] M. Barbatti and K. Sen, "Effects of different initial condition samplings on photodynamics and spectrum of pyrrole," *International Journal of Quantum Chemistry*, vol. 116, no. 10, pp. 762–771, 2016.

[59] M. Vazdar, M. Eckert-Maksić, M. Barbatti, and H. Lischka, "Excited-state non-adiabatic dynamics simulations of pyrrole," *Molecular Physics*, vol. 107, no. 8-12, pp. 845–854, 2009.

[60] M. Sapunar, A. Ponzi, S. Chaiwongwattana, M. Mališ, A. Prlj, P. Decleva, and N. Došlić, "Timescales of n–h bond dissociation in pyrrole: a nonadiabatic dynamics study," *Physical Chemistry Chemical Physics*, vol. 17, no. 29, pp. 19012–19020, 2015.

[61] M. Assmann, T. Weinacht, and S. Matsika, "Surface hopping investigation of the relaxation dynamics in radical cations," *The Journal of chemical physics*, vol. 144, no. 3, p. 034301, 2016.

[62] L. Klasinc, A. Sabljić, G. Kluge, J. Rieger, and M. Scholz, "Chemistry of excited states. part 13. assignment of lowest π-ionizations in photoelectron spectra of thiophen, furan, and pyrrole," *Journal of the Chemical Society, Perkin Transactions 2*, no. 5, pp. 539–543, 1982.

[63] V. Galasso, L. Klasinc, A. Sabljić, N. Trinajstić, G. C. Pappalardo, and W. Steglich, "Conformation and photoelectron spectra of 2-(2-furyl) pyrrole and 2-(2-thienyl) pyrrole," *Journal of the Chemical Society, Perkin Transactions 2*, no. 1, pp. 127–131, 1981.

[64] G. D. Willett and T. Baer, "Thermochemistry and dissociation dynamics of state-selected c4h4x ions. 3. c4h5n+," *Journal of the American Chemical Society*, vol. 102, no. 22, pp. 6774–6779, 1980.

[65] J. M. Tedder and P. H. Vidaud, "Charge-exchange mass spectra of thiophene, pyrrole and furan," *Journal of the Chemical Society, Faraday Transactions 2: Molecular and Chemical Physics*, vol. 76, pp. 1516–1522, 1980.

[66] C. Cooper, A. Williamson, J. C. Miller, and R. Compton, "Resonantly enhanced multiphoton ionization of pyrrole, n-methyl pyrrole, and furan," *The Journal of Chemical Physics*, vol. 73, no. 4, pp. 1527–1537, 1980.

[67] A. D. Williamson, R. Compton, and J. Eland, "Accurate photoionization thresholds by multiphoton ionization: Pyrrole," *The Journal of Chemical Physics*, vol. 70, no. 1, pp. 590–591, 1979.

[68] E. Van Veen, "Triplet π to π^* transitions in thiophene, furan and pyrrole by low-energy electron-impact spectroscopy," *Chemical Physics Letters*, vol. 41, no. 3, pp. 535–539, 1976.

[69] O. Thorstad and K. Undeim, "Mass spectrometry of onium compounds," *Chemischer Informationsdienst*, vol. 6, no. 9, pp. no–no, 1975.

[70] P. Linda, G. Marino, and S. Pignataro, "A comparison of sensitivities to substituent effects of five-membered heteroaromatic rings in gas phase ionization," *Journal of the Chemical Society B: Physical Organic*, pp. 1585–1587, 1971.

[71] P. Derrick, L. Åsbrink, O. Edqvist, B.-Ö. Jonsson, and E. Lindholm, "Rydberg series in small molecules: Xii. photoelectron spectroscopy and electronic structure of pyrrole," *International Journal of Mass Spectrometry and Ion Physics*, vol. 6, no. 3-4, pp. 191–202, 1971.

[72] V. Potapov and Y. Oa, "Photoionization and electron structure of pyrrole and its methyl derivatives," *DOKLADY AKADEMII NAUK SSSR*, vol. 192, no. 1, p. 131, 1970.

[73] K. Watanabe, T. Nakayama, and J. Mottl, "Ionization potentials of some molecules," *Journal of Quantitative Spectroscopy and Radiative Transfer*, vol. 2, no. 4, pp. 369–382, 1962.

[74] Y. Shao, Z. Gan, E. Epifanovsky, A. Gilbert, M. Wormit, J. Kussmann, A. Lange, A. Behn, J. Deng, X. Feng, *et al.*, "Advances in molecular quantum chemistry contained in the q-chem 4 program package," *Molecular Physics*, vol. 113, no. 2, pp. 184–215, 2015.

[75] G. Schaftenaar and J. Noordik, "Molden: A pre- and post-processing program for molecular and electronic structures," *J. Comput.-Aided Mol. Design*, vol. 14, p. 123, 2000.

[76] R. Martin, "Natural transition orbitals," *The Journal of chemical physics*, vol. 118, no. 11, pp. 4775–4777, 2003.

[77] M. Dantus, R. Bowman, and A. Zewail, "Femtosecond laser observations of molecular vibration and rotation," *Nature*, vol. 343, no. 6260, p. 737, 1990.

[78] T. Baumert, M. Grosser, R. Thalweiser, and G. Gerber, "Femtosecond time-resolved molecular multiphoton ionization: The na 2 system," *Physical Review Letters*, vol. 67, no. 27, p. 3753, 1991.

[79] W. Fuß, W. Schmid, and S. Trushin, "Time-resolved dissociative intense-laser field ionization for probing dynamics: Femtosecond photochemical ring opening of 1, 3-cyclohexadiene," *The Journal of Chemical Physics*, vol. 112, no. 19, pp. 8347–8362, 2000.

[80] S. Adachi, M. Sato, and T. Suzuki, "Direct observation of ground-state product formation in a 1, 3-cyclohexadiene ring-opening reaction," *The journal of physical chemistry letters*, vol. 6, no. 3, pp. 343–346, 2015.

[81] S. Deb and P. M. Weber, "The ultrafast pathway of photon-induced electrocyclic ring-opening reactions: the case of 1, 3-cyclohexadiene," *Annual review of physical chemistry*, vol. 62, pp. 19–39, 2011.

[82] M. Garavelli, C. Page, P. Celani, M. Olivucci, W. Schmid, S. Trushin, and W. Fuss, "Reaction path of a sub-200 fs photochemical electrocyclic reaction," *The Journal of Physical Chemistry A*, vol. 105, no. 18, pp. 4458–4469, 2001.

[83] M. Kotur, T. Weinacht, B. J. Pearson, and S. Matsika, "Closed-loop learning control of isomerization using shaped ultrafast laser pulses in the deep ultraviolet," *The Journal of chemical physics*, vol. 130, no. 13, p. 134311, 2009.

[84] R. A. Gaussian09, "1, mj frisch, gw trucks, hb schlegel, ge scuseria, ma robb, jr cheeseman, g. scalmani, v. barone, b. mennucci, ga petersson et al., gaussian," *Inc., Wallingford CT*, 2009.

[85] H. Lischka, T. Müller, P. G. Szalay, I. Shavitt, R. M. Pitzer, and R. Shepard, "Columbus—a program system for advanced multireference theory calculations," *Wiley Interdisciplinary Reviews: Computational Molecular Science*, vol. 1, no. 2, pp. 191–199, 2011.

[86] V. Mozhayskiy and A. Krylov, "ezspectrum, see http://iopenshell. usc. edu/downloads," *Google Scholar*.

[87] B. M. Bode and M. S. Gordon, "Macmolplt: a graphical user interface for gamess," *Journal of Molecular Graphics and Modelling*, vol. 16, no. 3, pp. 133–138, 1998.

[88] J. L. Franklin and S. R. Carroll, "Effect of molecular structure on ionic decomposition. ii. electron-impact study of 1, 3-and 1, 4-cyclohexadiene and 1, 3, 5-hexatriene," *Journal of the American Chemical Society*, vol. 91, no. 24, pp. 6564–6569, 1969.

[89] W. Fuß, S. Panja, W. E. Schmid, and S. A. Trushin, "Competing ultrafast cis-trans isomerization and ring closure of cyclohepta-1, 3-diene and cycloocta-1, 3-diene," *Molecular Physics*, vol. 104, no. 5-7, pp. 1133–1143, 2006.

[90] K. Komori-Orisaku, Y. Hirose, and I. Iwakura, "Pulsed nd: Yag laser-induced photoreaction of cis, cis-1, 3-cyclooctadiene at 266 nm: selective cyclization to cis-bicyclo [4.2. 0] oct-7-ene," *Photochemical & Photobiological Sciences*, 2017.

[91] K. Kimura, *Handbook of HeI photoelectron spectra of fundamental organic molecules*. Japan Scientific Societies Press; Halsted Press, 1981.

[92] G. Bieri, F. Burger, E. Heilbronner, and J. P. Maier, "Valence ionization energies of hydrocarbons," *Helvetica Chimica Acta*, vol. 60, no. 7, pp. 2213–2233, 1977.

[93] D. Demeo and M. El-Sayed, "Ionization potential and structure of olefins," *The Journal of Chemical Physics*, vol. 52, no. 5, pp. 2622–2629, 1970.

[94] P. Bischof and E. Heilbronner, "Photoelektron-spektren von cycloalkenen und cycloalkadienen. vorläufige mitteilung," *Helvetica Chimica Acta*, vol. 53, no. 7, pp. 1677–1682, 1970.

[95] S. Worley, T. Webb, D. H. Gibson, and T.-S. Ong, "On the electronic structures of cyclobutadiene and trimethylenemethane," *Journal of Organometallic Chemistry*, vol. 168, no. 1, pp. C16–C20, 1979.

[96] E. Heilbronner, T. Hoshi, J. Rosenberg, and K. Hafner, "Alkyl-induced, natural hypsochromic shifts of 2a]-2x and 2b]-2x transitions of azulene and naphthalene radical cations," *NOUVEAU JOURNAL DE CHIMIE-NEW JOURNAL OF CHEMISTRY*, vol. 1, no. 2, pp. 105–112, 1977.

[97] M. Allan, J. Dannacher, and J. Maier, "Radiative and fragmentation decay of the cations of trans-and cis-1, 3, 5-hexatriene and of all trans-1, 3, 5-heptatriene in the a(π- 1) states, studied by emission and photoelectron–photoion coincidence spectroscopy," *The Journal of Chemical Physics*, vol. 73, no. 7, pp. 3114–3122, 1980.

[98] G. Bieri, F. Burger, E. Heilbronner, and J. P. Maier, "Valence ionization energies of hydrocarbons," *Helvetica Chimica Acta*, vol. 60, no. 7, pp. 2213–2233, 1977.

[99] R. Gavin Jr and S. A. Rice, "Spectroscopic properties of polyenes. ii. the vacuum ultraviolet spectra of cis-and trans-1, 3, 5-hexatriene," *The Journal of Chemical Physics*, vol. 60, no. 8, pp. 3231–3237, 1974.

[100] R. P. Frueholz, W. M. Flicker, O. A. Mosher, and A. Kuppermann, "Electronic spectroscopy of 1, 3-cyclopentadiene, 1, 3-cyclohexadiene and 1, 3-cycloheptadiene by electron impact," *The Journal of Chemical Physics*, vol. 70, no. 4, pp. 2003–2013, 1979.

[101] R. McDiarmid, A. Sabljić, and J. Doering, "Valence transitions in 1, 3-cyclopentadiene, 1, 3-cyclohexadiene, and 1, 3-cycloheptadiene," *The Journal of chemical physics*, vol. 83, no. 5, pp. 2147–2152, 1985.

[102] M. Merchán, L. Serrano-Andrés, L. S. Slater, B. O. Roos, R. McDiarmid, and X. Xing, "Electronic spectra of 1, 4-cyclohexadiene and 1, 3-cyclohexadiene: a combined experimental and theoretical investigation," *The Journal of Physical Chemistry A*, vol. 103, no. 28, pp. 5468–5476, 1999.

[103] P. M. Johnson and T. J. Sears, "Photo-assisted intersystem crossing: The predominant triplet formation mechanism in some isolated polycyclic aromatic molecules excited with pulsed lasers," *The Journal of chemical physics*, vol. 143, no. 4, p. 044305, 2015.

[104] L. Keldysh *et al.*, "Ionization in the field of a strong electromagnetic wave," *Sov. Phys. JETP*, vol. 20, no. 5, pp. 1307–1314, 1965.

[105] M. Koch, T. J. Wolf, and M. Gühr, "Understanding the modulation mechanism in resonance-enhanced multiphoton probing of molecular dynamics," *Physical Review A*, vol. 91, no. 3, p. 031403, 2015.

[106] B. W. Toulson, J. P. Alaniz, J. G. Hill, and C. Murray, "Near-uv photodissociation dynamics of ch 2 i 2," *Physical Chemistry Chemical Physics*, vol. 18, no. 16, pp. 11091–11103, 2016.

[107] S. Matsika, M. Spanner, M. Kotur, and T. C. Weinacht, "Ultrafast relaxation dynamics of uracil probed via strong field dissociative ionization," *The Journal of Physical Chemistry A*, vol. 117, no. 48, pp. 12796–12801, 2013.

[108] M. Kotur, T. C. Weinacht, C. Zhou, and S. Matsika, "Following ultrafast radiationless relaxation dynamics with strong field dissociative ionization: a comparison between adenine, uracil, and cytosine," *IEEE Journal of Selected Topics in Quantum Electronics*, vol. 18, no. 1, pp. 187–194, 2012.

[109] S. Ullrich, T. Schultz, M. Z. Zgierski, and A. Stolow, "Electronic relaxation dynamics in dna and rna bases studied by time-resolved photoelectron spectroscopy," *Physical Chemistry Chemical Physics*, vol. 6, no. 10, pp. 2796–2801, 2004.

[110] C. Canuel, M. Mons, F. Piuzzi, B. Tardivel, I. Dimicoli, and M. Elhanine, "Excited states dynamics of dna and rna bases: Characterization of a stepwise deactivation pathway in the gas phase," *The Journal of chemical physics*, vol. 122, no. 7, p. 074316, 2005.

[111] H. Kang, K. T. Lee, B. Jung, Y. J. Ko, and S. K. Kim, "Intrinsic lifetimes of the excited state of dna and rna bases," *Journal of the American Chemical Society*, vol. 124, no. 44, pp. 12958–12959, 2002.

[112] T. Gustavsson, Á. Bányász, E. Lazzarotto, D. Markovitsi, G. Scalmani, M. J. Frisch, V. Barone, and R. Improta, "Singlet excited-state behavior of uracil and thymine in aqueous solution: a combined experimental and computational study of 11 uracil derivatives," *Journal of the American Chemical Society*, vol. 128, no. 2, pp. 607–619, 2006.

[113] T. Gustavsson, N. Sarkar, E. Lazzarotto, D. Markovitsi, and R. Improta, "Singlet excited state dynamics of uracil and thymine derivatives: A femtosecond fluorescence upconversion study in acetonitrile," *Chemical physics letters*, vol. 429, no. 4, pp. 551–557, 2006.

[114] M. Barbatti, A. J. Aquino, J. J. Szymczak, D. Nachtigallová, P. Hobza, and H. Lischka, "Relaxation mechanisms of uv-photoexcited dna and rna nucleobases," *Proceedings of the National Academy of Sciences*, vol. 107, no. 50, pp. 21453–21458, 2010.

[115] H. R. Hudock, B. G. Levine, A. L. Thompson, H. Satzger, D. Townsend, N. Gador, S. Ullrich, A. Stolow, and T. J. Martinez, "Ab initio molecular dynamics and time-resolved photoelectron spectroscopy of electronically excited uracil and thymine," *The Journal of Physical Chemistry A*, vol. 111, no. 34, pp. 8500–8508, 2007.

[116] M. K. Shukla and J. Leszczynski, "Radiation induced molecular phenomena in nucleic acids: a brief introduction," in *Radiation Induced Molecular Phenomena in Nucleic Acids*, pp. 265–299, Springer, 2008.

[117] Z. Lan, E. Fabiano, and W. Thiel, "Photoinduced nonadiabatic dynamics of pyrimidine nucleobases: on-the-fly surface-hopping study with semiempirical methods," *The Journal of Physical Chemistry B*, vol. 113, no. 11, pp. 3548–3555, 2009.

[118] D. Nachtigallová, A. J. Aquino, J. J. Szymczak, M. Barbatti, P. Hobza, and H. Lischka, "Nonadiabatic dynamics of uracil: population split among dif-

ferent decay mechanisms," *The Journal of Physical Chemistry A*, vol. 115, no. 21, pp. 5247–5255, 2011.

[119] B. P. Fingerhut, K. E. Dorfman, and S. Mukamel, "Monitoring nonadiabatic dynamics of the rna base uracil by uv pump–ir probe spectroscopy," *The journal of physical chemistry letters*, vol. 4, no. 11, pp. 1933–1942, 2013.

[120] M. Richter, S. Mai, P. Marquetand, and L. González, "Ultrafast intersystem crossing dynamics in uracil unravelled by ab initio molecular dynamics," *Physical Chemistry Chemical Physics*, vol. 16, no. 44, pp. 24423–24436, 2014.

[121] A. Mandal, P. J. Singh, A. Shastri, and B. Jagatap, "Electronic state spectroscopy of diiodomethane (ch2i2): Experimental and computational studies in the 30 000–95 000 cm- 1 region," *The Journal of chemical physics*, vol. 140, no. 19, p. 194312, 2014.

[122] Y.-J. Liu, L. De Vico, R. Lindh, and W.-H. Fang, "Spin-orbit ab initio investigation of the ultraviolet photolysis of diiodomethane," *ChemPhysChem*, vol. 8, no. 6, pp. 890–898, 2007.

[123] M. Odelius, M. Kadi, J. Davidsson, and A. N. Tarnovsky, "Photodissociation of diiodomethane in acetonitrile solution and fragment recombination into iso-diiodomethane studied with ab initio molecular dynamics simulations," *The Journal of chemical physics*, vol. 121, no. 5, pp. 2208–2214, 2004.

[124] X. Zheng and D. L. Phillips, "Solvation effects on the iodoform ultraviolet direct photodissociation reaction: opening the photoisomerization channel," *Chemical Physics Letters*, vol. 324, no. 1, pp. 175–182, 2000.

[125] J. Zhang, E. J. Heller, D. Huber, D. G. Imre, and D. Tannor, "Ch2i2 photodissociation: Dynamical modeling," *The Journal of chemical physics*, vol. 89, no. 6, pp. 3602–3611, 1988.

[126] S. Roszak, W. Koski, J. Kaufman, and K. Balasubramanian, "Structures and electron attachment properties of halomethanes (cx n y m, x= h, f; y= cl, br, i; n= 0, 4; m= 4 n)," *SAR and QSAR in Environmental Research*, vol. 11, no. 5-6, pp. 383–396, 2001.

[127] M. Kawasaki, S. Lee, and R. Bersohn, "Photodissociation of molecular beams of methylene iodide and iodoform," *The Journal of Chemical Physics*, vol. 63, no. 2, pp. 809–814, 1975.

[128] J. L. Holmes, F. Lossing, and R. McFarlane, "Stabilization energy and positional effects in halogen-substituted alkyl ions," *International journal of mass spectrometry and ion processes*, vol. 86, pp. 209–215, 1988.

[129] B. P. Tsal, T. Baer, A. S. Werner, and S. F. Lin, "Photoelectron-photoion coincidence study of the ionization and fragment appearance potentials of bromo-and iodomethanes," *The Journal of Physical Chemistry*, vol. 79, no. 6, pp. 570–574, 1975.

[130] W. von Niessen, L. Åsbrink, and G. Bieri, "30.4 nm he (ii) photoelectron spectra of organic molecules part vi. halogeno-compounds (c, h, x; x= cl, br, i)," *Journal of Electron Spectroscopy and Related Phenomena*, vol. 26, no. 2, pp. 173–201, 1982.

[131] A. Potts, H. Lempka, D. Streets, and W. Price, "Photoelectron spectra of the halides of elements in groups iii, iv, v and vi," *Philosophical Transactions for the Royal Society of London. Series A, Mathematical and Physical Sciences*, pp. 59–76, 1970.

[132] D. P. M. Geissler, *Concerted Elimination of Cl2 from CCl4 and of I2 from CH2I2 Driven by Intense Ultrafast Laser Pulses*. PhD thesis, Stony Brook University, 2007.

[133] H.-W. Jochims, M. Schwell, H. Baumgärtel, and S. Leach, "Photoion mass spectrometry of adenine, thymine and uracil in the 6–22ev photon energy range," *Chemical Physics*, vol. 314, no. 1, pp. 263–282, 2005.

[134] M. Kotur, *Strong-field Dissociative Ionization as a Probe of Molecular Dynamics and Structure*. PhD thesis, The Graduate School, Stony Brook University: Stony Brook, NY., 2012.

[135] S. Mai, M. Richter, M. Heindl, M. F. S. J. Menger, A. Atkins, M. Ruckenbauer, F. Plasser, M. Oppel, P. Marquetand, and L. González, "Sharc2.0: Surface hopping including arbitrary couplings — program package for non-adiabatic dynamics." sharc-md.org, 2018.

[136] M. Richter, P. Marquetand, J. González-Vázquez, I. Sola, and L. González, "SHARC: ab initio molecular dynamics with surface hopping in the adiabatic representation including arbitrary couplings," *J. Chem. Theory Comput.*, vol. 7, no. 5, pp. 1253–1258, 2011.

[137] S. Mai, P. Marquetand, and L. González, "A general method to describe intersystem crossing dynamics in trajectory surface hopping," *International Journal of Quantum Chemistry*, vol. 115, no. 18, pp. 1215–1231, 2015.

[138] M. Barbatti, M. Ruckenbauer, F. Plasser, J. Pittner, G. Granucci, M. Persico, and H. Lischka, "Newton-x: a surface-hopping program for nonadiabatic molecular dynamics," *Wiley Interdisciplinary Reviews: Computational Molecular Science*, vol. 4, no. 1, pp. 26–33, 2014.

[139] M. Barbatti, G. Granucci, M. Ruckenbauer, F. Plasser, R. Crespo-Otero, J. Pittner, M. Persico, and H. Lischka, "Newton-x: A package for newtonian dynamics close to the crossing seam, version 2." www.newtonx.org, 2016.

[140] S. Mai, P. Marquetand, and L. González, "Intersystem crossing pathways in the noncanonical nucleobase 2-thiouracil: a time-dependent picture," *The journal of physical chemistry letters*, vol. 7, no. 11, pp. 1978–1983, 2016.

[141] M. Ruckenbauer, S. Mai, P. Marquetand, and L. González, "Revealing deactivation pathways hidden in time-resolved photoelectron spectra," *Scientific reports*, vol. 6, p. 35522, 2016.

[142] H. Lischka, T. Müller, P. G. Szalay, I. Shavitt, R. M. Pitzer, and R. Shepard, "Columbus—a program system for advanced multireference theory calculations," *Wiley Interdisciplinary Reviews: Computational Molecular Science*, vol. 1, no. 2, pp. 191–199, 2011.

[143] H. Lischka, R. Shepard, R. M. Pitzer, I. Shavitt, M. Dallos, T. Müller, P. G. Szalay, M. Seth, G. S. Kedziora, S. Yabushita, *et al.*, "High-level multireference methods in the quantum-chemistry program system columbus: Analytic mr-cisd and mr-aqcc gradients and mr-aqcc-lrt for excited states, guga spin–orbit ci and parallel ci density," *Physical Chemistry Chemical Physics*, vol. 3, no. 5, pp. 664–673, 2001.

[144] H. Lischka, R. Shepard, I. Shavitt, R. Pitzer, M. Dallos, T. Müller, P. Szalay, F. Brown, R. Ahlrichs, H. Böhm, *et al.*, "Columbus, an ab initio electronic structure program," 2012.

[145] L. Butler, E. Hintsa, S. F. Shane, and Y.-T. Lee, "The electronic state-selective photodissociation of ch2bri at 248, 210, and 193 nm," *The Journal of chemical physics*, vol. 86, no. 4, pp. 2051–2074, 1987.

[146] W. M. Kwok, C. Ma, D. Phillips, A. W. Parker, M. Towrie, P. Matousek, and D. L. Phillips, "Picosecond time-resolved resonance raman observation

of iso-ch2br–i following a-band photodissociation of ch2bri in the solution phase," *Chemical physics letters*, vol. 341, no. 3-4, pp. 292–298, 2001.

[147] A. N. Tarnovsky, M. Wall, M. Gustafsson, N. Lascoux, V. Sundström, and E. Åkesson, "Ultrafast study of the photodissociation of bromoiodomethane in acetonitrile upon 266 nm excitation," *The Journal of Physical Chemistry A*, vol. 106, no. 25, pp. 5999–6005, 2002.

[148] K.-C. Tang, J. Peng, K. G. Spears, and R. J. Sension, "Communications: Photoinitiated bond dissociation of bromoiodomethane in solution: Comparison of one-photon and two-photon excitations and the formation of iso-ch 2 br–i and iso-ch 2 i–br," 2010.

[149] R. Forbes, V. Makhija, K. Veyrinas, A. Stolow, J. W. Lee, M. Burt, M. Brouard, C. Vallance, I. Wilkinson, R. Lausten, *et al.*, "Time-resolved multi-mass ion imaging: Femtosecond uv-vuv pump-probe spectroscopy with the pimms camera," *The Journal of Chemical Physics*, vol. 147, no. 1, p. 013911, 2017.

[150] U. Even, "The even-lavie valve as a source for high intensity supersonic beam," *EPJ Techniques and Instrumentation*, vol. 2, no. 1, p. 17, 2015.

[151] S. Mai, P. Marquetand, M. Richter, J. González-Vázquez, and L. González, "Singlet and triplet excited-state dynamics study of the keto and enol tautomers of cytosine," *ChemPhysChem*, vol. 14, no. 13, pp. 2920–2931, 2013.

[152] S. Mai, P. Marquetand, and L. González, "A general method to describe intersystem crossing dynamics in trajectory surface hopping," *International Journal of Quantum Chemistry*, vol. 115, no. 18, pp. 1215–1231, 2015.

[153] B. P. Tsal, T. Baer, A. S. Werner, and S. F. Lin, "Photoelectron-photoion coincidence study of the ionization and fragment appearance potentials of bromo-and iodomethanes," *The Journal of Physical Chemistry*, vol. 79, no. 6, pp. 570–574, 1975.

[154] W. von Niessen, L. Åsbrink, and G. Bieri, "30.4 nm he (ii) photoelectron spectra of organic molecules part vi. halogeno-compounds (c, h, x; x= cl, br, i)," *Journal of Electron Spectroscopy and Related Phenomena*, vol. 26, no. 2, pp. 173–201, 1982.

[155] A. Potts, H. Lempka, D. Streets, and W. C. Price, "A discussion on photoelectron spectroscopy-photoelectron spectra of halides of elements in groups

iii, iv, v and vi," *Phil. Trans. R. Soc. Lond. A*, vol. 268, no. 1184, pp. 59–76, 1970.

[156] A. Lago, J. P. Kercher, A. Bödi, B. Sztáray, B. Miller, D. Wurzelmann, and T. Baer, "Dissociative photoionization and thermochemistry of dihalomethane compounds studied by threshold photoelectron photoion coincidence spectroscopy," *The Journal of Physical Chemistry A*, vol. 109, no. 9, pp. 1802–1809, 2005.

[157] T. Allison, H. Tao, W. Glover, T. Wright, A. Stooke, C. Khurmi, J. Van Tilborg, Y. Liu, R. Falcone, T. Martínez, *et al.*, "Ultrafast internal conversion in ethylene. ii. mechanisms and pathways for quenching and hydrogen elimination," *The Journal of chemical physics*, vol. 136, no. 12, p. 124317, 2012.

[158] A. Mandal, P. J. Singh, A. Shastri, and B. Jagatap, "Electronic state spectroscopy of diiodomethane (ch2i2): Experimental and computational studies in the 30 000–95 000 cm- 1 region," *The Journal of Chemical Physics*, vol. 140, no. 19, p. 194312, 2014.

[159] "Ultrafast lecture notes."

[160] A. Weiner, *Ultrafast optics*, vol. 72. John Wiley & Sons, 2011.

[161] F. Aquilante, J. Autschbach, R. K. Carlson, L. F. Chibotaru, M. G. Delcey, L. De Vico, N. Ferré, L. M. Frutos, L. Gagliardi, M. Garavelli, *et al.*, "Molcas 8: New capabilities for multiconfigurational quantum chemical calculations across the periodic table," *Journal of computational chemistry*, vol. 37, no. 5, pp. 506–541, 2016.

[162] J. P. Zobel, J. J. Nogueira, and L. González, "The ipea dilemma in caspt2," *Chemical science*, vol. 8, no. 2, pp. 1482–1499, 2017.

[163] N. Forsberg and P.-Å. Malmqvist, "Multiconfiguration perturbation theory with imaginary level shift," *Chemical Physics Letters*, vol. 274, no. 1-3, pp. 196–204, 1997.

[164] M. Reiher, "Wiley interdiscip," *Rev. Comput. Mol. Sci*, vol. 2, pp. 139–149, 2012.

[165] P. Å. Malmqvist, B. O. Roos, and B. Schimmelpfennig, "The restricted active space (ras) state interaction approach with spin–orbit coupling," *Chemical physics letters*, vol. 357, no. 3-4, pp. 230–240, 2002.

[166] B. Schimmelpfennig, "Amfi–an atomic mean field integral program," *Stockholm University*, 1996.

[167] G. Granucci, M. Persico, and A. Toniolo, "Direct semiclassical simulation of photochemical processes with semiempirical wave functions," *The Journal of Chemical Physics*, vol. 114, no. 24, pp. 10608–10615, 2001.

[168] G. Granucci and M. Persico, "Critical appraisal of the fewest switches algorithm for surface hopping," *The Journal of chemical physics*, vol. 126, no. 13, p. 134114, 2007.

[169] M. Barbatti, G. Granucci, M. Persico, M. Ruckenbauer, M. Vazdar, M. Eckert-Maksić, and H. Lischka, "The on-the-fly surface-hopping program system newton-x: Application to ab initio simulation of the nonadiabatic photodynamics of benchmark systems," *Journal of Photochemistry and Photobiology A: Chemistry*, vol. 190, no. 2-3, pp. 228–240, 2007.

[170] M. Ruckenbauer, S. Mai, P. Marquetand, and L. González, "Revealing deactivation pathways hidden in time-resolved photoelectron spectra," *Scientific reports*, vol. 6, p. 35522, 2016.

[171] F. Plasser, M. Ruckenbauer, S. Mai, M. Oppel, P. Marquetand, and L. González, "Efficient and flexible computation of many-electron wave function overlaps," *Journal of chemical theory and computation*, vol. 12, no. 3, pp. 1207–1219, 2016.

[172] C. Zhu, A. W. Jasper, and D. G. Truhlar, "Non-born-oppenheimer liouville-von neumann dynamics. evolution of a subsystem controlled by linear and population-driven decay of mixing with decoherent and coherent switching," *Journal of chemical theory and computation*, vol. 1, no. 4, pp. 527–540, 2005.

[173] J. Towns, T. Cockerill, M. Dahan, I. Foster, K. Gaither, A. Grimshaw, V. Hazlewood, S. Lathrop, D. Lifka, G. D. Peterson, *et al.*, "Xsede: accelerating scientific discovery," *Computing in Science & Engineering*, vol. 16, no. 5, pp. 62–74, 2014.

[174] J. H. Moore, C. C. Davis, M. A. Coplan, and S. C. Greer, *Building scientific apparatus*. Cambridge University Press, 2009.

Appendix A

Calculation of Second, Third, Fourth, and Fifth Order Phase for the Compressor and the Stretcher

A.1 In Depth Calculation of Phase

Here I show details of a calculation for the dispersion of pulses through gratings [159, 160, 42, 43]. The most common configuration is a pair of parallel gratings.

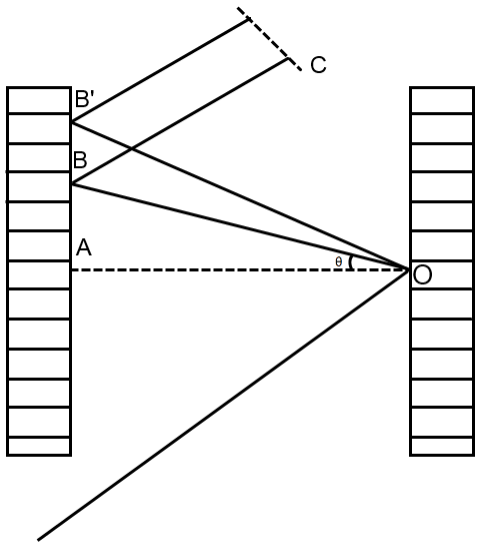

Figure A.1: Parallel grating configuration.

The pulse is incident on the first grating at point O, as seen in Fig. A.1 . The grating equation

$$sin\gamma - sin\theta = m\frac{\lambda}{d} = m\lambda N, \tag{A.1}$$

where m is the diffracted order and d is the grating spacing which can also be expressed as grating frequency $N = \frac{1}{d}$, with units of grooves/mm. In other words $\vec{k}_{diffracted} = \vec{k}_{incident} - \vec{k}_{grating}$. Note that the output is parallel to the input for any λ.

Now consider the red and blue components of a broadband pulse (I'll also only consider the first diffracted order, $m = 1$). From the grating equation, the blue will follow OB' whereas the red will follow OB (they are both normal to the plane C). Thus one expects different path lengths and hence dispersion to occur.

Note that there will be a "spatial chirp" in plane C (i.e. the red and the blue frequencies are spatially separated). The solution is to put a mirror in plane C (or a roof prism to change the beam height), and send the beam back through the grating pair. After the double pass the pulse will not have any spatial chirp, but pick up twice the temporal dispersion.

The problem is to find the path length difference using geometry, as shown in Fig.A.2.

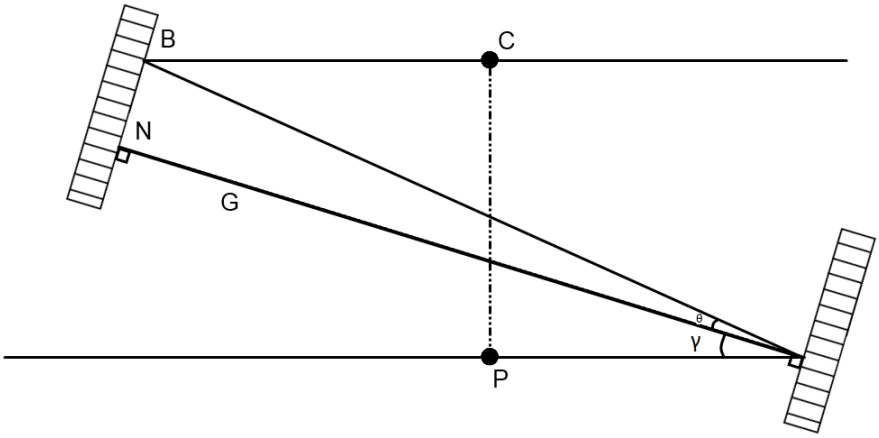

Figure A.2: Configuration of the compressor.

The distance $\overline{PABC}$ is desired (P and C are chosen arbitrarily, only after changes in the distance with ω is desired, so C and P can be chosen for convenience).

From Fig. A.2

$$\overline{PABC} = b + bcos(\gamma + \theta) \tag{A.2}$$

and $b = \frac{G}{cos\theta}$. So

$$\overline{PABC} = \frac{G}{cos\theta}[1 + cos(\gamma + \theta)] \equiv P, \tag{A.3}$$

where P is defined. The total phase shift of $\overline{PABC}$ is

$$\phi = \frac{\omega}{c}\overline{PABC} + C(\omega) = \frac{\omega}{c}P + C(\omega), \tag{A.4}$$

where $C(\omega)$is the phase shift on the gratings. We are interested in relative phases, so one can count from the most convenient point N, where the normal intersects with the grating. There is a relative phase shift of 2π at each groove of a grating, therefore

$$C(\omega) = 2\pi N \times \overline{BN} \tag{A.5}$$

where $N \times \overline{BN}$ is the number of grooves between B and N. From Fig. A.2 it can be seen that $\overline{BN} = Gtan\theta$. The expression for $C(\omega)$ becomes

$$C(\omega) = 2\pi NGtan(\theta(\omega)) \tag{A.6}$$

There is also a phase shift acquired upon reflection, but this is frequency independent.

A.2 Calculation of First Order Phase

One can now calculate the group delay

$$\frac{d\phi}{d\omega} = \frac{d}{d\omega}\left[\frac{\omega P}{c} + C(\omega)\right] = \frac{P}{c} + \left[\frac{\omega}{c}\frac{dp}{d\omega} + \frac{dC(\omega)}{d\omega}\right]. \tag{A.7}$$

Consider first the term in brackets

$$\frac{dC(\omega)}{d\omega} = 2\pi NG\frac{d(tan\theta)}{d\theta}\frac{d\theta}{d\omega} \tag{A.8}$$

$$\frac{d}{d\omega}tan\theta(\omega) = \frac{1}{cos^2\theta}\frac{d\theta}{d\omega} \tag{A.9}$$

$$\frac{dP}{d\omega} = \frac{dP}{d\theta}\frac{d\theta}{d\omega} \tag{A.10}$$

$$\frac{dP}{d\theta} = \frac{d}{d\theta}\left[\frac{G}{cos\theta}(1 + cos(\gamma + \theta))\right] \tag{A.11}$$

$$\frac{dP}{d\theta} = G\frac{d}{d\theta}\left[\frac{1}{cos\theta}(1 + cos\gamma cos\theta - sin\gamma sin\theta)\right] \tag{A.12}$$

$$\frac{dP}{d\theta} = G\frac{d}{d\theta}\left[\frac{1}{cos\theta} + cos\gamma - sin\gamma tan\theta)\right] \tag{A.13}$$

$$\frac{dP}{d\theta} = G\left[\frac{sin\theta}{cos^2\theta} - \frac{sin\gamma}{cos^2\theta}\right] \tag{A.14}$$

$$\frac{dP}{d\theta} = -G\frac{\lambda N}{cos^2\theta} \tag{A.15}$$

Finally solving for the whole term in brackets

$$\frac{\omega}{c}\frac{dp}{d\omega} + \frac{dC(\omega)}{d\omega} = \left[\frac{2\pi}{\lambda}\left(-G\frac{\lambda N}{cos^2\theta}\right) + \frac{2\pi NG}{cos^2\theta}\right]\frac{d\theta}{d\omega} = 0. \tag{A.16}$$

Therefore the first order phase is simply:

$$\frac{d\phi}{d\omega} = \frac{P}{c}. \tag{A.17}$$

A.3 Calculation of Second Order Phase

The group delay dispersion (GDD) is

$$\phi'' = \frac{d^2\phi}{d\omega^2} = \frac{1}{c}\frac{dp}{d\omega} = \frac{1}{c}\frac{dp}{d\theta}\frac{d\theta}{d\omega}. \tag{A.18}$$

$\frac{d\theta}{d\omega}$ needs to be derived. Taking the grating equation

$$sin\gamma - sin\theta = \lambda N = \frac{2\pi cN}{\omega} \tag{A.19}$$

where $\lambda = 2\pi c/\omega$, and performing the derivative one gets

$$\frac{d}{d\omega}(sin\gamma - sin\theta) = -cos\theta\frac{d\theta}{d\omega} = \frac{-2\pi cN}{\omega^2}. \tag{A.20}$$

Therefore,

$$\frac{d\theta}{d\omega} = \frac{2\pi cN}{\omega^2 cos\theta} \tag{A.21}$$

For one pass through the grating pair one gets

$$\phi''_{1pass} = \frac{1}{c}\left(\frac{-G\lambda N}{cos^2\theta}\right)\left(\frac{2\pi cN}{\omega^2 cos\theta}\right) = -\frac{2\pi G\lambda N^2}{cos^2\theta\omega^2} = -\frac{GN^2\lambda^3}{2\pi c^2 cos^3\theta}. \tag{A.22}$$

The second order phase can be expressed in terms of incidence angle, γ, the distance between the gratings measured perpendicularly from the grating surface, G, and the lines/mm of the grating N as

$$\phi'' = -\frac{G\lambda}{\pi c^2}\frac{(\lambda * N)^2}{(1-(sin\gamma - \lambda N)^2)^{3/2}}. \tag{A.23}$$

The most important thing about this equation is that the group delay dispersion is always negative for a parallel grating pair. Thus the grating pair can be used to compensate for the positive dispersion that stretches pulses as they propagate through normally dispersive medium.

A.4 Calculation of Higher Order Phase

From ultrafast notes:

$$\phi^{(3)} = \frac{-3\lambda}{2\pi c} * \phi''\left(1 + \lambda N\frac{(\lambda N - sin\gamma)}{(1-(\lambda N - sin\gamma)^2)}\right) \tag{A.24}$$

$$\phi^{(4)} = -\frac{(2\phi^{(3)})^2}{3\phi^{(2)}} + \left[\frac{\lambda^2 N}{2\pi c\left[1-(\lambda N - sin\gamma)^2\right]}\right]^2 \phi^{(2)} \tag{A.25}$$

As a simple check of this derivation, and in order to calculate the fifth order phase, I used Mathematica to redo these derivatives based off the second order phase.

$$\phi^{(3)} = \frac{(12GcN^2\pi^2(\omega + \omega cos2\gamma + 4cN\pi sin\gamma))}{(\omega(2cN\pi + \omega - \omega sin\gamma)^2(-2cN\pi + \omega + \omega sin\gamma)^2\sqrt{1-\left(-\frac{2cN\pi}{\omega} + sin\gamma\right)^2})} \tag{A.26}$$

I have verified that the two expressions give the same numerical results. Expression for the fourth phase is

$$\begin{aligned}\phi^{(4)} = & \frac{480Gc^3N^4\pi^4(-((2cN\pi)/\omega)+sin\gamma)^2}{\omega^7(1-(-((2cN\pi)/\omega)+sin\gamma)^2)^{7/2}} \\ & - \frac{96Gc^3N^4\pi^4}{\omega^7(1-(-((2cN\pi)\omega)+sin\gamma)^2)^{5/2}} \\ & + \frac{384Gc^2N^3\pi^3(-((2cN\pi)/\omega)+sin\gamma)}{\omega^6(1-(-((2cN\pi)/\omega)+Sin\gamma)^2)^{5/2}} \\ & - \frac{96GcN^2\pi^2}{\omega^5(1-(-((2cN\pi)/\omega)+sin\gamma)^2)^{3/2}}.\end{aligned} \tag{A.27}$$

The for the fifth order phase is

$$\begin{aligned}\phi^{(5)} = & \frac{-6720Gc^4N^5\pi^5(-((2cN\pi)/\omega)+sin\gamma)^3}{\omega^9(1-(-((2cN\pi)/\omega)+sin\gamma)^2)^{9/2}} \\ & - \frac{2880Gc^4N^5\pi^5(-((2cN\pi)/\omega)+sin\gamma)}{\omega^9(1-(-((2cN\pi)/\omega)+sin\gamma)^2)^{7/2}} \\ & + \frac{7200Gc^3N^4\pi^4(-((2cN\pi)/\omega)+sin\gamma)^2}{\omega^8(1-(-((2cN\pi)/\omega)+sin\gamma)^2)^{7/2}} \\ & + \frac{1440Gc^3N^4\pi^4}{\omega^8(1-(-((2cN\pi)/\omega)+sin\gamma)^2)^{5/2}} \\ & - \frac{2880Gc^2N^3\pi^3(-((2cN\pi)/\omega)+sin\gamma)}{\omega^7(1-(-((2cN\pi)/\omega)+sin\gamma)^2)^{5/2}} \\ & + \frac{480GcN^2\pi^2}{\omega^6(1-(-((2cN\pi)/\omega)+sin\gamma)^2)^{3/2}}.\end{aligned} \tag{A.28}$$

A.5 Stretcher Geometry

The stretcher works by imaging the first grating behind the second grating; making the distance between the first and second grating effectively negative. Since the first, second, third, fourth, and fifth order phase are linearly dependent of the grating separation this makes the stretcher give the same numerical value for all the phases, but inverts the sign. The only new thing that needs to be calculated is the distance between the two gratings perpendicular to the grating surface, which we shall call G_s. The quantity l_{eff} for our system is simply $l_{eff} = l - 4f$ since our system is folded in on itself $f_1 = f_2$. To get G_s we simply can say from the diagram that $G_s = l_{eff} cos\theta$ [43].

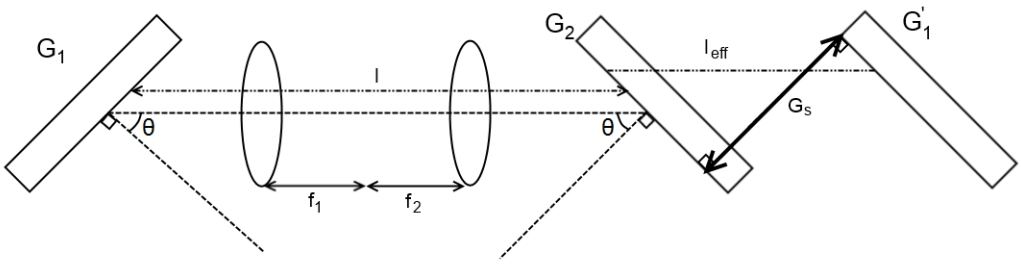

Figure A.3: Schematic of Our Stretcher Configuration

Appendix B

Calculations

B.1 Appendix I: CH_2I_2 Calculation Details

In order to carry out the excited-stated dynamics simulations for CH_2I_2, our collaborators Philipp Marquetand and Tamás Rozgonyi used SHARC (Surface Hopping including ARbitrary Couplings) [135, 136, 137] interfaced with Molcas 8.0 [161]. The electronic structure calculations of the neutral molecule were performed with MS-CASPT2(12,8)/ano-rcc-vdzp (multi-state complete active space perturbation theory second order) based on SA(5/4)-CASSCF(12,8) (complete active space self-consistent field with 12 electrons in 8 orbitals and state-averaging including either 5 singlet or 4 triplet states) calculations. The IPEA shift was set to zero, as this was found to improve the results in combination with the small double-ζ basis set [162]. However, to avoid intruder states and ensure a stable propagation in the dynamics simulations, an imaginary shift of 0.3 Hartree was added [163]. In order to account for scalar-relativistic effects, the second-order Douglas-Kroll-Hess (DKH) Hamiltonian [164] was employed while spin-orbit couplings (SOCs) were computed with the RASSI [165] and AMFI [166] formalisms. The dynamics were run employing the velocity-Verlet algorithm with a time step of 0.5 fs for the nuclear dynamics and a time step of 0.02 fs for the propagation of the electronic wavefunction, using the "local diabatization" formalism [167]. Energy conservation during a surface hop was ensured by scaling of the full velocity vectors, since the non-adiabatic coupling vectors are not available for this level of theory. Our collaborators employed an energy-based decoherence correction with a parameter of 0.1 Hartree [168]. The initial geometries and velocities for the trajectories were sampled from a Wigner distribution of the harmonic ground state potential. In this way, 1000 geometries were produced and a single-point calculation at the MS-CASPT2(12,8) level of theory was performed at each of these to obtain the state

energies and oscillator strengths. The initial excited states were selected stochastically [169] restricting the excitation energy window between 4.775 - 4.825 eV. The ionization probability along the trajectories was obtained in an approximate manner from Dyson norm calculations [170] using their WFOverlap code [171] in a post-processing step. The necessary wavefunctions of the neutral and ionized molecule were obtained at steps of 2.5 fs along the pre-computed trajectories from MS-CASPT2(12,8)/ano-rcc-vdzp or MS-CASPT2(11,8)/ano-rcc-vdzp calculations including altogether 5 singlets, 9 doublets, 4 triplets and 4 quartets as well as all possible SOCs.

B.2 Appendix II: Uracil Calculation Details

The ground state of the biologically relevant tautomer of uracil was optimized at DFT level by our collaborators Pratip Chakraborty and Spiridoula Matsika using the B3LYP functional and 6-31G(d) basis set using Gaussian09 package. The frequencies and normal modes were calculated at the same level of theory. A sampling was performed using a harmonic oscillator Wigner distribution in Newton-X[138, 139] program to generate 500 initial conditions (nuclear coordinates and velocities) based on the optimized geometry and the normal modes from the previous calculation. The S_1 (nπ^*) and S_2 ($\pi\pi^*$) excited states of uracil for the 500 geometries were calculated at both the Complete Active Space Self Consistent Field (CASSCF) and Multi-Reference Configuration Interaction with Singles (MRCIS) levels using cc-pVDZ basis set with an active space of 12 electrons in 9 orbitals. Three states were averaged at the CASSCF level. The vertical excitation energies and oscillator strengths were used to calculate the absorption cross sections to simulate the first absorption band of uracil in both CASSCF and MRCIS methods. The temperature was considered to be 298 K. A Lorentzian line shape and a phenomenological broadening (δ) value of 0.1 eV were employed. Fig. B.1 shows the theoretical absorption spectra of uracil at both the CASSCF and MRCIS level.

They performed nonadiabatic excited state dynamics simulations using trajectory surface hopping in Newton-X on CASSCF(12,9)/cc-pVDZ and MRCIS/CASSCF(12,9)/cc-pVDZ potential energy surfaces calculated using the Columbus 7.0 package[142, 143, 144]. The experimentally measured first absorption peak for uracil in the gas-phase is at 5.08 eV[120]. The first absorption peak is at $\sim$6.60 eV and $\sim$5.90 eV for CASSCF and MRCIS levels, respectively. The pump-pulse generated in the experiment is at 4.77 eV which is 0.31 eV lower than the experimental maximum. So, 0.31 eV is subtracted from the peak of the theoretical spectra at both levels of theory to estimate the center of the pump pulse. The excitation windows were considered to be 6.29 $\pm$ 0.15 eV and 5.59 $\pm$ 0.15

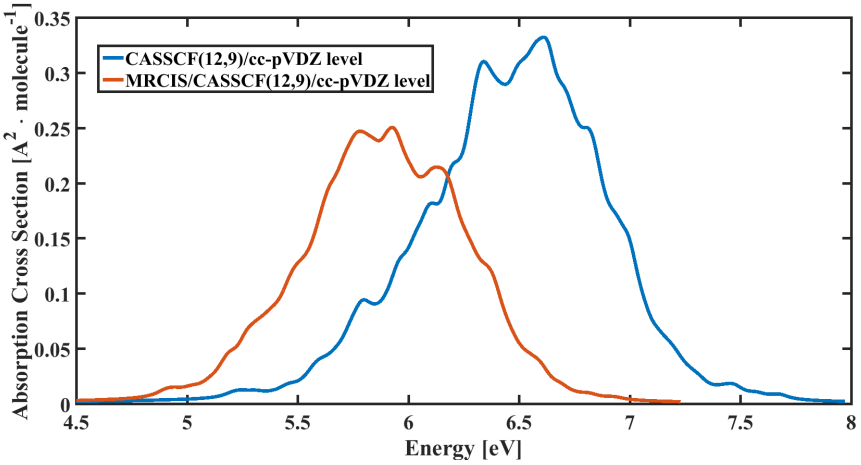

Figure B.1: Theoretical absorption spectra of uracil simulated at the CASSCF(12,9)/cc-pVDZ level and MRCIS/CASSCF(12,9)/cc-pVDZ level.

eV at CASSCF and MRCIS level, respectively, selecting 71 and 73 initial conditions for the aforementioned levels of theory, to be propagated starting from the S_2 state as it is the first bright state in uracil. The fewest switches surface hopping (FSSH) algorithm was used to take into account non-adiabatic events between S_2, S_1 and S_0 states. The FSSH algorithm was corrected for decoherence effects using the approach of 'non-linear decay of mixing' by Zhu et al.[172] and Granucci et al.[168] keeping the parameter, α = 0.1 Hartree. The velocity verlet algorithm was used to integrate Newton's equations of motion with a time step of 0.5 fs and the semi-classical Schrödinger equation was integrated using 5th order Butcher's algorithm with time step of 0.025 fs. The simulations were performed for 1000 fs at the CASSCF level and 500 fs at the MRCIS level using XSEDE's computational resources[173].

B.3 Appendix III: Franck Condon Factors

Our collaborators Pratip Chakraborty and Spiridoula Matsika calculated the Frank Condon (FC) factors of the ground and the excited states in uracil in order to show that the VUV-probe can only ionize population in S_1 and S_2, and that ionization from S_0 is not measured, even if it is assumed that the molecule is occupying a 'hot' ground state. This illustrates why a VUV-probe is needed in order to do a proper weak-field pump-probe experiment.

ezSpectrum 3.0 [86] was used to calculate FC overlaps using the Duschinsky

rotations approximation. They define the FC factors as $\left|\langle\psi_{v_{\text{final}}}|\psi_{v_{\text{initial}}}\rangle\right|^2$, where $\psi_{v_{\text{initial}}}$ and $\psi_{v_{\text{final}}}$ are the initial and final vibrational states. The S_0 and D_0 minima were optimized at the B3LYP/6-31G(d) and UB3LYP/6-31G(d) level of theory, respectively. Frequencies and normal modes were calculated at the same level of theory and used for the FC overlap calculations. In order to obtain the correct character for the D_1 minimum they had to use TDDFT/TDA/CAM-B3LYP/6-31G(d) level, since the B3LYP functional did not give the correct character. For consistency the S_1 minimum was also obtained at the same level of theory. Frequencies and normal modes were calculated at the TDDFT/TDA/CAM-B3LYP/6-31G(d) level of theory for the S_1 and D_1 minima and were used in the FC overlap calculations. The minima and normal modes were calculated with Q-Chem package [74].

FC factors were calculated between S_0 and D_0 and between S_1 and D_1. The results can be see in Fig. B.2, where the UV and VUV-photon energies are also indicated. In Fig. B.2 a) it is clear that the UV and VUV-photon energy are not energetically capable of ionizing from S_0 to D_0, even if the ground state were vibrationally hot. Fig. B.2 b) shows the FC factors between S_1 and D_1 which indicate that the UV-photon energy is insufficient to ionize from S_1 without excess vibrational energy, making it a poor probe of S_1. In contrast, the VUV-photon has more than enough energy to ionize S_1 to D_1 from its lowest vibrational level, and is a good probe of S_1. The VUV-photon is in a unique position to enable us to fully probe any dynamics in S_1, but is still 'blind' to ground state dynamics.

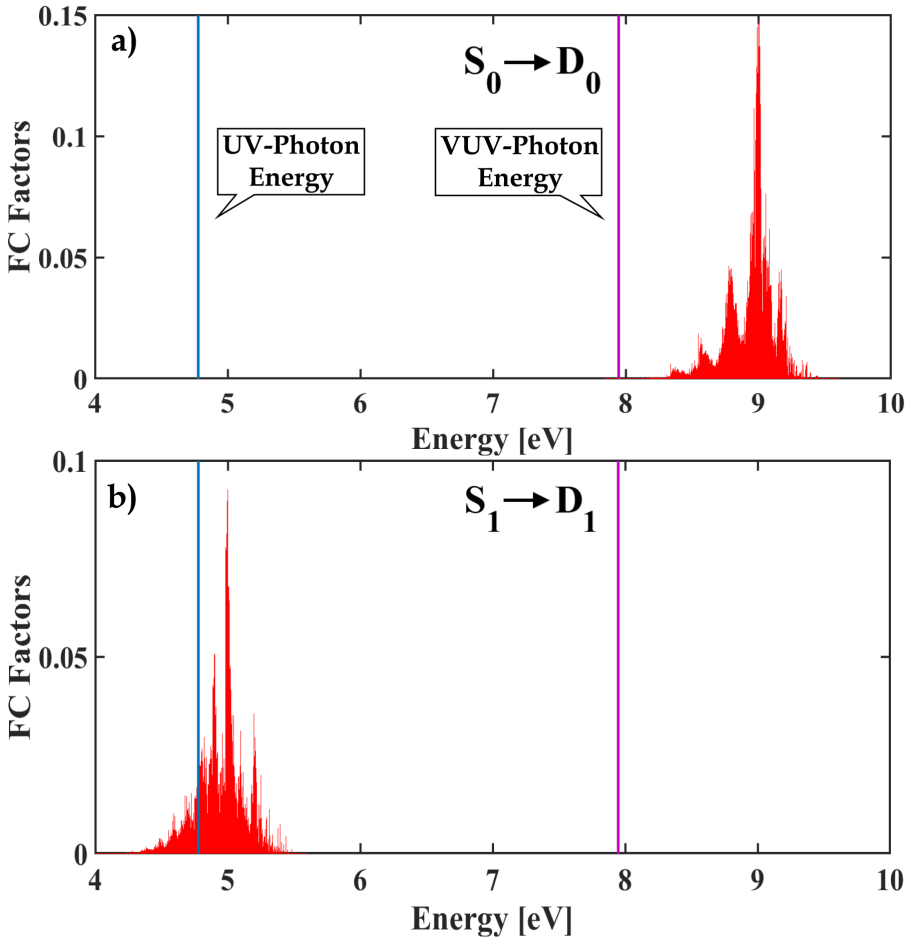

Figure B.2: FC Factors between a) S_0 and D_0 b) S_1 and D_1. The UV- and VUV-photon energies are labels and are indicated by the blue and magenta vertical lines respectively.

Appendix C

Differential Pumping Calculation

In this Appendix I explore the idea of removing the 500 μm CaF_2 window that separates the argon gas cell from the interaction chamber and replacing it with a differential pumping scheme.

C.0.1 Characterization of our Current Pumps

In order to characterize our vacuum system I utilize methods outlined in [174]. The vacuum system consists of a Welch 1397 mechanical roughing pump, and a Alcatel - Annecy 5150 CP molecular turbo pump.

A Welch 1397 has a pumping speed of 8.33 L/s (500 L/min). I operate below 100mTorr, so I am in the molecular flow regime. Therefore, the conductance of the tubing between the roughing pump and the vacuum chamber for air at $20°C$ is

$$C = 12\frac{D^3}{L}[\text{Ls}^{-1}] = 12\frac{\text{cm}}{\text{s}}\frac{(3.81\text{ cm})^3}{1828\text{cm}} = 0.363[\text{L/s}], \tag{C.1}$$

where D is the diameter of the tubing, and L is the length of the tubing. For the vacuum chamber $D = 1.5" = 0.0381$ m and $L = 60' = 18.28$ m. The net speed of our system at the chamber is

$$S = \left(\frac{1}{S_p} + \frac{1}{C}\right)^{-1} = \left(\frac{1}{8.33\text{ L/s}} + \frac{1}{0.363\text{ L/s}}\right)^{-1} = 0.348[\text{L/s}] \tag{C.2}$$

where S_p is the speed of the pump and C is the conductance of the tubing.

The turbo molecular pumps pumping speed for nitrogen is 140 L/s.

C.1 One Stage Differential Pumping System

The following is for a one stage system, where I have the argon gas cell at P_0 = 300 Torr and a small aperture between that and the high vacuum chamber at P_2 = 1 $\times$ 10^{-6} Torr.

The throughput for the system is

$$Q = P_2 S, \tag{C.3}$$

where S = 140 L/s, and the conductance of the sampling region that provides this throughput is

$$C = \frac{Q}{P_0 - P_2} = \frac{P_2 S}{P_0 - P_2}. \tag{C.4}$$

The flow through the aperture is in the viscous flow regime (since the argon gas cell is at 300 Torr), so

$$A = \frac{C}{20}[\text{cm}^2] = \frac{1}{20}\left(\frac{P_2 S}{P_0 - P_2}\right)[\text{cm}^2]. \tag{C.5}$$

Solving for the radius of the aperture

$$r = \frac{1}{100}\sqrt{\frac{A}{\pi}} = \frac{1}{100}\sqrt{\frac{1}{20\pi}\left(\frac{P_2 S}{P_0 - P_2}\right)}[\text{m}]. \tag{C.6}$$

For a system with S = 140 L/s the aperture size is r = 860 nm. This is obviously too small to transmit the VUV light into the main chamber.

C.2 Two Stage Differential Pumping System Calculation

The following is for a two stage system, where we have the argon gas cell at P_0 = 300 Torr and a small aperture between that and the intermediate chamber at P_1 = 13 mTorr, and another small aperture between that and the high vacuum chamber at P_2 = 1 $\times$ 10^{-6} Torr. The pumping speed in the high vacuum chamber is S_2 = 140 L/s and the pumping speed in the intermediate chamber is flexible and can be between S_1 = 0.348 - 140 L/s. A schematic of this system can be seen in Fig. C.1.

The throughput of the pump on the lowest pressure chamber is

$$Q_2 = P_2 S_2. \tag{C.7}$$

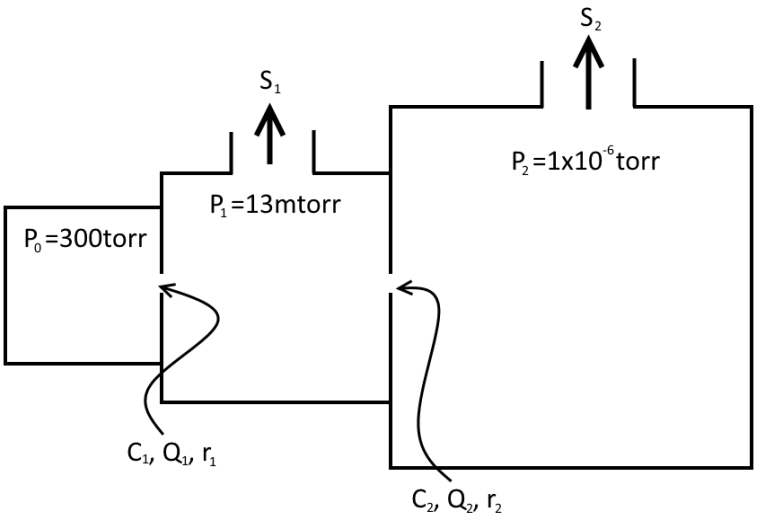

Figure C.1: 2 Stage Differential Pumping Drawing

The conductance C_2 of the aperture separating the region of pressure P_1 from the region of pressure P_2 must maintain the throughput

$$C_2 = \frac{Q_2}{P_1 - P_2} = \frac{P_2 S_2}{P_1 - P_2}. \tag{C.8}$$

We are in the molecular flow regime, so the area of the aperture is

$$A_2 = \frac{P_2 S_2}{P_1 - P_2} \left[3.7 \left(\frac{T}{M} \right)^{1/2} \right]^{-1} [\text{cm}^2], \tag{C.9}$$

where T is the temperature in Kelvin, and M is the mass of the gas in AMU. The radius of the aperture is

$$r_2 = \frac{1}{100} \sqrt{\frac{A_2}{\pi}} = \frac{1}{100} \sqrt{\frac{1}{\pi} \frac{P_2 S_2}{P_1 - P_2} \left[3.7 \left(\frac{T}{M} \right)^{1/2} \right]^{-1}} [\text{m}]. \tag{C.10}$$

The throughput for the pump on the intermediate chamber is

$$Q_1 = P_1 S_1, \tag{C.11}$$

and the conductance C_1 of the aperture separating the region of pressure P_1 from

the region of pressure P_0 must maintain the throughput

$$C_1 = \frac{Q_2}{P_0 - P_1} = \frac{P_1 S_1}{P_0 - P_1}. \tag{C.12}$$

The area of the aperture separating the argon gas cell from the intermediate region is

$$A_1 = \frac{C_1}{20}[cm^2]. \tag{C.13}$$

The radius of this aperture is

$$r_1 = \frac{1}{100}\sqrt{\frac{1}{20\pi}\left(\frac{P_1 S_1}{P_0 - P_1}\right)}[m]. \tag{C.14}$$

For a system with S_2 = 140 L/s and S_1 = 140 L/s the aperture sizes are r_1 = 98 μm and r_2 = 180μm. These sizes are still too small to transmit the generated VUV without adding extra imaging optics to the beam. For this differential pumping to be a viable option for eliminating the CaF_2 window between the chambers I would need a larger pump with $\sim$ 3000 L/s pumping speed. I have diffusion pump available to us that can pump with this speed, but, as mentioned in Chapter 2, pump oil cracks in the presence of VUV light and coats our optics. Therefore, if I wanted to pursue a system with no windows between the argon gas cell and the interaction chamber I would have to invest in a much larger turbo molecular pump.